DTU Library

Nature-inspired double corrugated geometry for enhanced heat transfer

Navickaité, Kristina

Publication date:
2019

Document Version
Publisher's PDF, also known as Version of record

[Link back to DTU Orbit](#)

Thermoelectrical Generators / Superconducting Components
High Temperature Polymer Electrolyte Membrane Fuel Cells

Energy Conversion
Magnetism
Electrochemistry
Defect Chemistry

Colloidal Chemistry/Electrochemistry
Polymer Solar Cells
Solid State Physics
Electron Microscopy
Ceramic Membranes
Solid Oxide Fuel Cells
Shaping Processes / Electron Microscopy / Solid State Physics / Computational Materials Design
Modelling / Heterostructures
Solid Oxide Electrolysis Cells
Computational Materials Design
X-Ray and Neutron Scattering
High Temperature Polymer Electrolyte Membrane Electrolysis Cells
Fuel Cells and Hydrogen Test Center
Shaping Processes / Defect Chemistry
Electrochemical Flue Gas Purification
Batteries / Hydrogen Storage
Synthesis / Colloidal Chemistry / Heterostructures / X-Ray and Neutron Scattering
Magnetic Refrigeration
Energy Storage
Sintering
Synthetic Fuels
Fuel Cells
Magnetism
Synthesis
Modelling
Sintering

Department of Energy Conversion and Storage
Technical University of Denmark
Risø Campus
Frederiksborgvej 399
4000 Roskilde
Denmark
www.energy.dtu.dk

ISBN 978-87-92986-82-5

Technical University of Denmark

DTU

Nature-Inspired Double Corrugated Geometry for Enhanced Heat Transfer

Kristina Navickaitė
Department of Energy Conversion and Storage
Ph.D. Thesis, December 2018

Thermoelectrical Generators / Superconducting Components
High Temperature Polymer Electrolyte Membrane Fuel Cells

Energy Conversion
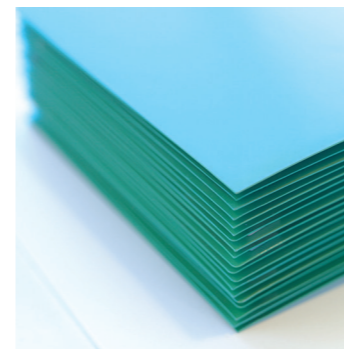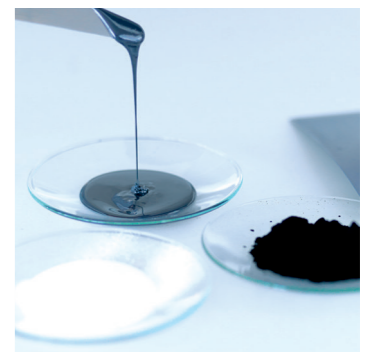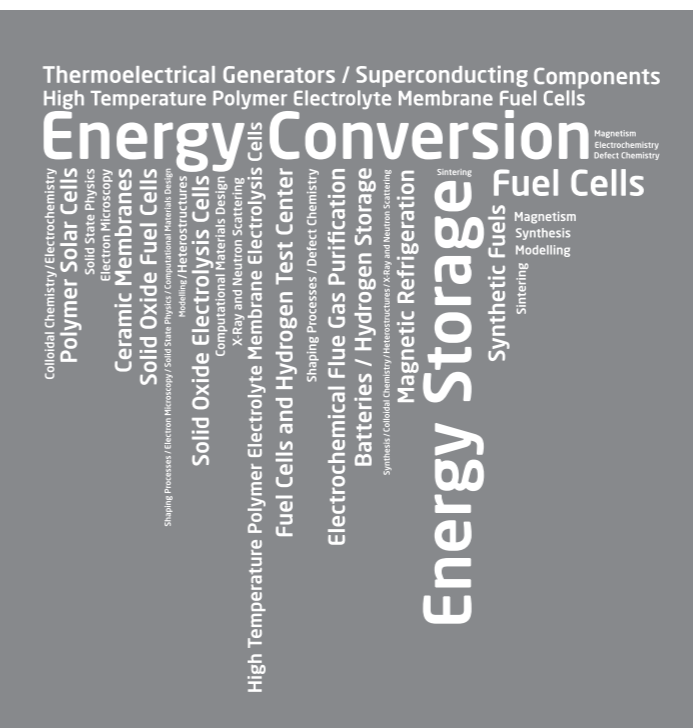
Energy Storage

DTU Energy
Department of Energy Conversion and Storage

Technical University of Denmark
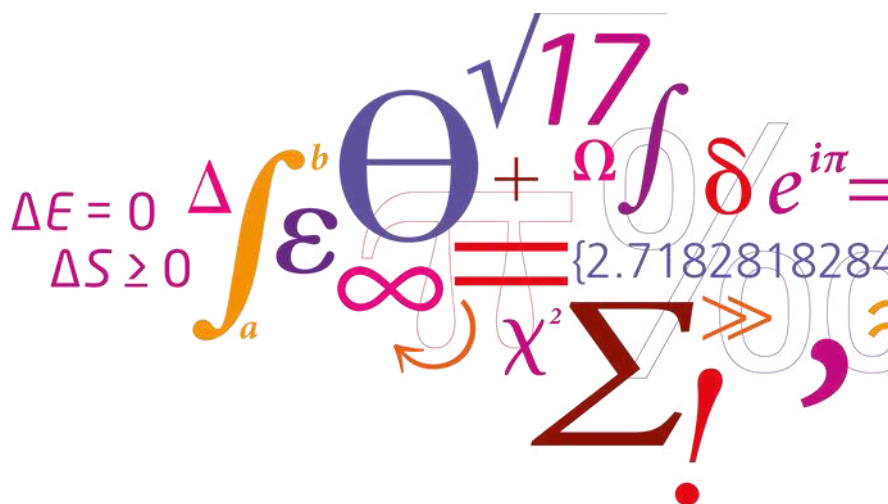
Nature-inspired double corrugated geometry for enhanced heat transfer

PhD Thesis

Kristina Navickaitė

December 14th, 2018

DTU Energy
Department of Energy Conversion and Storage

Acknowledgement

This PhD project was an open door to variety of opportunities and challenges. It was a continuous process of learning, creating and improvising. I am very thankful for the opportunity to work with and be inspired by excellent scholars. Thus, I would like to express my sincere gratitude first to my advisers Kurt Engelbrecht and Christian Bahl. I am grateful for their guidance, lessons and support during three years of PhD studies. They were guiding me through all the challenges and obstacles that I have faced. Their valuable insights and pieces of advice elucidated my further decisions and workflow. I am thankful for their comprehensive support, inspiration and for showing me, how powerful can be a creative mind. Of course, I am endlessly grateful to them for harmonic working environment that was created and maintained during these three years.

I am thankful to the head of the former Section for Electrofunctional Materials, where I started my PhD studies, Nini Pryds, for his support and encouragement. My work at DTU should have been unimaginably harder without Anita Voss's help with all bureaucracy. Thus, I express my sincere gratitude to her. I am also grateful to the head of the new Section for Continuum Modelling and Testing, where I finish my PhD studies, Rasmus Bjørk, for his lessons and motivational sense of humour. I am also thankful to the secretary of this Section Connie Munch Westergaard.

This PhD thesis should have been significantly different without help that I received during my external stays at Royal Institute of Technology KTH, Sweden and at University of Parma, Italy. I would like to thank for all the valuable discussions and helping hands when needed to prof. Björn Palm, Behzad Abolhassani Monfared, prof. Sara Rainieri, prof. Fabio Bozzoli, Andrea Mocerino, and Luca Cattani.

I also would like to express my gratitude to all my colleagues, who became also my friends, through the time of my PhD studies. Their help dealing with both numerical simulations and experiments was very important. I really appreciate all the discussions and their opinion on my work. I learn faster this way. Anders, Andrea, Cathrine, Dan, David, Derek, Florian, Henrique, Jan, Jørgen, Kaspar, Stefano D., Stefano S., Tian, I say honest and big "Thank you".

Obviously, no achievements could be constituted without support of important and dear people. I am honestly grateful to my parents and sisters for their support. I appreciate very much encouragement, support and help received from Michael, Konstantinas, Rokas, Henning, Fabian and Gabriel. I am thankful to everyone, who was supporting and inspiring me through all three years of PhD studies and more. I cannot name all of those people, but I am sure, they know how grateful I am.

Finally, I would like to thank to all of my co-authors separately. I am thankful for the great amount of their efforts to collaborating on preparing quality publications. I am also grateful for their kind permission to use some of the published figures in this thesis.

Abstract (in English)

The PhD project "Improving the efficiency of heat pump and cooling technologies" is focused on research on efficiency improvements for heat pumps driven by the magnetocaloric effect (MCE). Magnetic refrigeration (MR) at room temperature is rather new; however a relatively mature technology in comparison with other caloric approaches. Nevertheless, the efficiency of the current state-of-the-art devices is not sufficient to bring this fascinating technology to commercialization. Therefore, many research efforts are devoted to improving the performance of magnetocaloric heat pumps through advances in the systems and materials. In this PhD project, major attention is paid to two components of magnetocaloric heat pumps, namely heat transfer and regenerator construction, which have significant importance to the performance of such devices.

The main working body in this kind of heat pumps is a solid regenerator of magnetocaloric material (MCM). The size and shape of the particles of MCMs as well as the number of layers in a regenerator play an important role in the performance of magnetocaloric heat pumps. Therefore, regenerators must be carefully constructed. Even a slight deviation of the Curie temperature between layers of MCMs leads to significant reduction of performance. In order to avoid the fatal failure, the designed regenerators are tested in smaller scale testing devices before using them in large-scale machines. This PhD thesis reports experimental results of eight regenerators, which were tested in a small-scale versatile testing device developed at Technical University of Denmark. Experiments on a regenerator with fifteen layers of MCM were conducted using a medium-scale active magnetic refrigeration (AMR) device at KTH Royal Institute of Technology. The tested regenerators varied in regenerator geometry, shape and size of particles as well as number of layers of MCM and amount of epoxy used for bonding particles. Experimental results revealed that epoxy bonding improves the mechanical integrity of the MCM in regenerators; however, it compromises their performance. Moreover, experiments proved that AMRs must be layered carefully in order not to jeopardize the performance. It was also found that a packed bed with spherical particles perform significantly better than similar beds with irregular particles from the efficiency standpoint.

The temperature difference established by the solid MCM regenerator is usually relatively small – around 25 – 40 K. Thus, it is challenging to assure an efficient heat transfer process in systems equipped with a conventional heat exchanger (HEX). Therefore, a novel solution for more efficient HEX is necessary. A nature-inspired tubular geometry for enhanced heat transfer is presented in this PhD thesis. The vascular counter-flow HEX, found in some fishes, was emulated and the obtained double corrugated tubes were numerically and experimentally analysed. The surface equations for these tubes were derived in a way that enables effortless adjustments of the diameter, equivalent to a straight tube, aspect ratio of the radial axes and the corrugation period. Either a constant hydraulic diameter, D_h, or a constant cross-section area, A_c, is maintained at any point along the flow channel of the designed geometry. An ellipse and a super-ellipse were used as a base geometry for double corrugated tubes, periodically converging to a circle or a perfect super-ellipse, respectively.

Computational fluid dynamics (CFD) analysis was carried out for the designed double corrugated tubes. The boundary conditions for CFD were constant surface temperature, constant pressure drop; and fully hydraulically developed flow with constant properties. Moreover, the modelling was performed at low temperature difference between the inlet and the tube wall, considering the possible application where only small temperature difference is available, such as heat pumps, or underfloor heating system. The CFD results showed that ellipse-based double corrugated tubes with constant D_h are generally more efficient than the same type tubes with the supper ellipse-based, or any double corrugated tubes with constant A_c. Major findings of the CFD analysis were the following:

1. Thermal performance of double corrugated tubes increases with increasing Reynolds number or decrease of corrugation period.

2. Higher aspect ratio leads to better thermal performance, as well as, severe reduction of a flow rate (for constant pressure drop).

3. The global thermo-hydraulic performance, evaluated at constant pressure drop, increases with increasing corrugation period.

Seven ellipse-based double corrugated tubes that demonstrated the best performance according to CFD results were manufactured from an aluminium alloy using selective laser melting technology. Five double corrugated tubes with constant D_h and two with constant A_c were tested in a tube-in-shell counter-flow heat exchanger using potable water as the working fluid in a range of Reynold numbers from 1000 to 2500. Correlations for the Nusselt number and friction factor for each tube are proposed and the experimental results show that Nusselt number increases up to 500 % in corrugated tubes compared to a straight tube while the friction factor increases less than 17 times. The global thermo-hydraulic performance, evaluated for the same pumping power, of the double corrugated tubes is up to 160 % higher than for a straight tube. The performance of tested double corrugated tubes is compared to other state-of-the-art geometries. The experimental results confirmed numerical predictions and demonstrated that double corrugated tubes with constant D_h have significantly higher thermal performance compared to constant A_c. However, the latter tubes exhibit lower increase in f when comparing the same aspect ratio and corrugation period. The global thermo-hydraulic performance is higher for double corrugated tubes with smaller corrugation period and for tubes with constant D_h.

Finally, an efficient AMR should have a high heat transfer rate and low pressure drop across the flow channel. The double corrugated tubes also demonstrated that they have these characteristics. Therefore, several experimentally tested tubes were analysed in a one-dimensional AMR model as a pattern for porous regenerator structure of a solid AMR. The numerical results obtained for double corrugated tubes were compared to results of regenerators with packed spheres and cylindrical micro-channel matrix. It is demonstrated that double corrugated tubes provide nearly two times higher cooling power than beds with packed spheres at the same value of Coefficient of Performance (*COP*). In other words, double corrugated tubes with certain geometrical characteristics provide same cooling power at higher *COP* than packed sphere at the same operating conditions.

Resumé (dansk)

Ph.d-projektet "Improving the efficiency of heat pump and cooling technologies" ("Forbedring af effektiviteten af varmepumpe og kølingteknologier") omhandler forskning i effektivitetsforbedringer af varmepumper baseret på den magnetokaloriske effekt (MCE). Magnetisk køleteknologi (MR) ved stuetemperatur er forholdsvist nyt; men dog en relativt moden teknologi i sammenligning med andre kaloriske køleknologier. Alligevel er effektiviteten af de nuværende state-of-the-art enheder endnu ikke tilstrækkelig til kommercialisering af denne fascinerende teknologi. Der er derfor er mange forskningsaktiviteter dedikeret til forbedring af ydeevnen af magnetokaloriske varmepumper. I dette ph.d-projekt lægges der stor vægt på to komponenter af de magnetokaloriske varmepumper; nemlig varmeoverførsel og regeneratorsammensætning, som begge har stor betydning for ydeevnen af denne type af varmepumper.

Den vigtigste funktionelle komponent i denne type varmepumpe er en regenerator bestående af magnetokalorisk materiale (MCM). Størrelsen og formen af MCM partiklerne samt antallet af lag i regeneratoren spiller en væsentlig rolle for ydeevnen af den magnetokaloriske varmepumpe. Regeneratoren skal derfor konstrueres omhyggeligt. Selv en lille afvigelse af Curie temperaturen for lagene af MCM medfører en betydelig reduktion i ydeevne. For at undgå fatale fejl testes regeneratorerne i mindre testenheder før de avendes i faktiske maskiner. Denne ph.d.-afhandling rapporterer eksperimentelle resultater af otte regenerator materialer, som blev testet i en magnetokalrisk teststand udviklet ved Danmarks Tekniske Universitet. Målinger på en regenerator med femten lag MCM blev udført ved anvendelse af en mellemstor aktiv magnetisk køle (AMR) enhed ved KTH i Stockholm. De testede regeneratorer varierede i geometri, form og størrelse af partikler, såvel som antal lag af MCM og mængde epoxy anvendt til a holdepartiklerne sammen. Eksperimentelle resultater viste, at epoxybinding forbedrer den mekaniske integritet af MCM i testede regeneratorer, men kompromitterer imidlertid ydeevnen. Desuden viste eksperimentelle resultater, at upræcis lagdelingen af AMR'eren medførte forringet ydeevne. Ydermere, viste de at regeneratorer bestående af pakkede sfæriske partikler havde signifikant højere effektivitet end tilsvarende regeneratorer med uregelmæssige partikler.

Temperatursforskellen, der opbygges af MCM regeneratoren, er normalt forholdsvis lille, omkring 25 – 40 K. Det er således udfordrende at sikre en effektiv varmeveksling i systemer udstyret med en konventionel varmeveksler. Derfor er en ny løsning til mere effektiv HEX nødvendig. En natur inspireret, rørformet geometri til forbedret varmeveksling præsenteres i denne ph.d.-afhandling. Den vaskulær modstrøms varmeveksler som findes i nogle typer fisk blev efterlignet, og de opnåede dobbeltkorrugerede rør blev analyseret numerisk og eksperimentelt. Ligningerne der beskriver fladerne af disse rør blev udledt på en måde, der muliggør ændringer af diameteren, svarende til hvis røret var lige, forholdet imellem største og mindste diameter og korrugeringsperioden. Enten en konstant hydraulisk diameter, D_h, eller et konstant tværsnitsareal, A_c, opretholdes på et hvilket som helst sted langs strømretningen i den konstruerede geometri. Som basisgeometri blev en ellipse og en superellipse anvendt. Således bevæger rørene sig imelleml henholdsvis en cirkel eller en perfekt superellipse.

Computational fluid dynamics (CFD) blev anvendt til at analysere de designede dobbeltkorrugerede rør. Randbetingelserne for CFD var konstant overfladetemperatur, konstant trykfald og konstant hydraulisk strømning af væske. Desuden blev modelleringen udført med en lille temperaturforskel mellem indløb og rørets yderside, med henblik på den mulige anvendelse i for eksempelvis varmepumper eller gulvarmesystemer, hvor kun en lille temperaturforskel er tilgængelig. CFD-resultaterne viste, at de ellipsebaserede dobbeltkorrugerede rør med konstant D_h generelt er mere effektive end tilsvarende type superellipsebaserede rør eller dobbeltkorrugerede rør med konstant A_c. De vigtigste resultater af CFD-analysen er følgende:

1. Den termiske ydeevne af dobbeltkorrugerede rør stiger med stigende Reynolds-tal eller aftagende korrugeringsperiode.

2. Øget forhold imellem største og mindste diameter fører til bedre termisk ydeevne, og en betragtelig reduktion af strømningshastighed (ved konstant trykforskel).

3. Den globale termohydrauliske ydeevne stiger med stigende korrugeringsperiode ved konstant trykfald.

Syv ellipsebaserede dobbeltkorrugerede rør, som baseret på CFD-resultaterne udviste den bedste ydeevne, blev fermstillet af en aluminiumlegering ved anvendelse af selektiv laser-smeltteknologi. Fem dobbeltkorrugerede rør med konstant D_h og to med konstant A_c blev testet i en modstrømsvarmeveksler med et rør i en ydre skal. Drikkevand blev brugt som arbejdsvæske ved en række Reynolds-tal fra 1000 til 2500. Korrelationer for Nusselt-tal og friktionsfaktor for hvert rør udledes. De eksperimentelle resultater viser, at Nusselt-tallet øges med op til 500 % i korrugerede rør sammenlignet med lige rør, mens friktionsfaktoren stiger mindre end 17 gange. Den globale termohydrauliske ydeevne af de dobbeltkorrugerede rør er op mod 180 % højere end for et lige rør ved samme pumpeeffekt. Ydeevnen af de testede dobbeltkorrugerede rør sammenlignes med andre state-of-the-art geometrier. De eksperimentelle resultater stemte overens med de numeriske forudsigelser og viste, at dobbeltkorrugerede rør med konstant D_h har signifikant højere termisk ydeevne sammenlignet med dem med konstant A_c. De sidstnævnte rør udviser imidlertid en lavere stigning i friktionsfaktor, når man sammenligner samme diameter forhold og korrugeringsperiode. Den globale termohydrauliske ydeevne er højere for dobbeltkorrugerede rør med mindre korrugeringsperiode og for rør med konstant D_h.

Endelig bør en effektiv AMR have en høj varmeoverførselshastighed og lavt trykfald over strømningskanalen. De dobbeltkorrugerede rør viste også, at de har disse egenskaber. Derfor blev flere eksperimentelt testede rør analyseret i en endimensionel AMR-model som et eksempel på en porøs regeneratorstruktur. De numeriske resultater opnået for dobbeltkorrugerede rør blev sammenlignet med resultater af tilsvarende regeneratorer med tætpakkede kugler og en matrix af cylindriske mikrokanaler. Det vises, at dobbeltkorrugerede rør næsten medfører en fordobling af kølekraften i forhold til regeneratorer med pakkede kugler ved tilsvarende effektivitet (COP). Dobbeltkorrugerede rør med visse geometriske egenskaber giver med andre ord samme køleeffekt ved højere COP end pakkede kugler under de samme betingelser.

List of publications

The list of articles published/submitted in international peer-reviewed journals:

Enhanced heat transfer in tubes based on vascular heat exchangers in fish: experimental investigation.
Navickaitė, Kristina; Mocerino, Andrea; Cattani, Luca; Bozzoli, Fabio; Bahl, Christian; Liltorp, Klaus; Zhang, Xiaodan; Engelbrecht, Kurt.
In: International Journal of Heat and Mass Transfer, Submitted. P.1.

Elliptical double corrugated tubes for enhanced heat transfer.
Navickaitė, Kristina; Cattani, Luca; Bahl, Christian; Engelbrecht, Kurt.
In: International Journal of Heat and Mass Transfer, Vol. 128, 2019, p. 363-377. P.2.

Experimental and numerical comparison of multi-layered La(Fe,Si,Mn)$_{13}$H$_y$ active magnetic regenerators.
Navickaitė, Kristina; Bez, Henrique Neves ; Lei, Tian; Barcza, Alexander; Vieyra, Hugo ; Bahl, Christian; Engelbrecht, Kurt.
In: International Journal of Refrigeration, Vol. 86, 2018, p. 322-330. P.3.

Passive characterisation and active testing of epoxy bonded regenerators from room temperature magnetic refrigeration.
Lei, Tian; Navickaitė, Kristina; Engelbrecht, Kurt; Barcza, Alexander; Vieyra, Hugo ; Nielsen, Kaspar Kirstein; Bahl, Christian.
In: Applied Thermal Engineering, Vol. 128, 2017, p. 10-19. P.4.

Operational test of bonded magnetocaloric plates.
Bahl, Christian; Navickaitė, Kristina; Neves Bez, Henrique; Lei, Tian; Engelbrecht, Kurt; Bjørk, Rasmus; Li, Ke; Li, Zhenxing; Shen, Jun; Dai, Wei; Jia, Jiche; Wu, Yuanyuan; Long, Yi; Hu, Fengxia; Shen, Baogen.
In: International Journal of Refrigeration, Vol. 76, 2017, p. 245-251. P.5.

From a magnet to a heat pump.
Navickaitė, Kristina; Neves Bez, Henrique; Bahl, Christian; Engelbrecht, Kurt.
In: Journal of Sustainable Architecture and Civil Engineering, Vol. 14, 2016, p. 73-79. P.6.

The list of articles published conference proceedings:

Experimental investigation of fifteen-layer epoxy-bonded La(Fe,Mn,Si)$_{13}$H$_y$ active magnetic regenerator.
Navickaitė, Kristina; Monfared, Behzad; Palm, Björn; Bahl, Christian; Engelbrecht, Kurt.
Proceedings of the 8th International Conference on Caloric Cooling, Darmstadt, Germany. C.1.

Passive heat transfer enhancement in 3D corrugated tube.
Navickaitė, Kristina; Noël, Derek; Bahl, Christian; Engelbrecht, Kurt.
Paper presented at 9th World Conference on Experimental Heat Transfer, Fluid Mechanics and Thermodynamics (ExHFT-9 2017), Foz Do Iguaçu, Brazil. C.2.

Epoxy-bonded La(Fe,Mn,Si)$_{13}$H$_y$ as a multi layered active magnetic regenerator.
Neves Bez, Henrique; Navickaitė, Kristina; Lei, Tian; Engelbrecht, Kurt; Barcza, Alexander; Bahl, Christian.
Proceedings of the 7th International Conference on Magnetic Refrigeration at Room Temperature. International Institute of Refrigeration, 2016. C.3.

List of Figures

List of Tables

Nomenclature

Abbreviations

AEA	Alternating ellipse axis
AMR	Active magnetic regenerator
BC	Boundary conditions
CFD	Computational fluid dynamics
DCT	Double corrugated tube
EAC	Ellipse-based double corrugated tube with cross-section area held constant
EDH	Ellipse-based double corrugated tube with hydraulic diameter held constant
EDS	Energy dispersive microscopy
FOPT	First order phase transition
HEX	Heat exchanger
HST	Helical screw-tape
MCE	Magnetocaloric effect
MCM	Magnetocaloric material
MR	Magnetic refrigeration
SEAC	Super-ellipse-based double corrugated tube with cross-section area held constant
SEDH	Super-ellipse-based double corrugated tube with hydraulic diameter held constant
SEM	Scanning electron microscope
SLM	Selective laser melting
SOPT	Second order phase transition
TC	Thermocouple
VSM	Vibrating sample magnetometer

Variables

A	Area, [m²]
AR	Aspect ratio, [-]
a_s	Specific area, [m^{-1}]
a, b	Major axis, minor axis, [m]
C	Multiplicative constant, [-]
cff	Correction factor for friction factor, [-]
cfn	Correction factor for Nusselt number, [-]
COP	Coefficient of Performance, [-]
c_p	Isobaric specific heat capacity, [J/(kg K)]
c_H	Isomagnetic specific heat capacity, [J/(kg K)]
D	Diameter, [m]
De	Dean number, [-]
err	Error, [%]
f	Friction factor, [-]
H	Magnetic field, [T]
h	Convective heat transfer coefficients, [W/(m² K)]
$\bar{h}$	Average convective heat transfer coefficients, [W/(m² K)]
K	Multiplicative constant, [-]
k	Thermal conductivity, [W/(m K)]
l	Length, [m]
m	Mass, [kg], Reynolds exponent, [-]
$\dot{m}$	Mass flow rate, [kg/s]
N	Number of measurement, [-]

n	Normal vector, [-], ellipse shape factor, [-]
Nu	Nusselt number, [-]
$\overline{Nu}$	Average Nusselt number, [-]
NTU	Number of transfer unit, [-]
P	Perimeter, [m]
p	Period, [m], pressure, [Pa]
PEC	Performance evaluation criterion, [-]
Pr	Prandtl number, [-]
Q_{cool}	Cooling power, [W]
q	Net heat transfer, [W]
R	Radius, [m]
R_w	Thermal resistance, [m K/W]
Re	Reynolds number, [-]
S	Least square function
S_q	Surface roughness, [m]
s	Entropy, [J/K]
T	Temperature, [K]
t	Time, [s], parameter [-]
U	Overall heat transfer coefficient, [W/ (m² K)], utilisation, [-]
u	Velocity (field), [m/s]
V_h	Housing volume, [m³]
v_f	Fluid velocity, [m/s]
W	Pumping power, [W]
x, y, z	Cartesian coordinates, [-]
Y	Twist ratio, [-]

Greek letters

α	Reynolds exponent, [-]
β	Prandtl exponent, [-]
γ	Correction coefficient, [-]
Δ	Difference, [-]
ε	Efficiency, [-], porosity, [-], uncertainty, [%]
η	Efficiency, [-]
θ^*	Relative temperature, [-]
μ	Dynamic viscosity, [Pa s]
v	Frequency, [Hz]
ξ	Vorticity, [-]
ρ	Density, [kg/m³]
σ_{est}	Standard error of estimate, [-]

Subscripts

ad	Adiabatic
C	Curie
c	Cross-section, coarse
$disp$	Dispersive
E	Ellipse
e	Epoxy
$estim$	Estimate

exp	Experimental
ele	Electron
f	Fluid, fine
H	Constant magnetic field
h	Hydraulic
hot	Hot
i	Inlet, inner
lam	Laminar
lat	Lattice
lm	Log mean
m	Magnetic, mean
max	Maximum
o	Outlet, outer
p	Particle
SE	Super-ellipse
s	Surface, solid
span	Difference (span)
stat	Static
tot	Total
turb	Turbulent
W	Constant pumping power
w	Wall
x	Axial position
Δp	Constant pressure drop
0	Reference
1	Tube side
1.1	Tube side inlet
1.2	Tube side outlet
2	Shell side
2.1	Shell side inlet
2.2	Shell side outlet
2nd, AMR	Second law of thermodynamic for active magnetic regenerator

Table of content

1. Introduction to a general problem of magnetocaloric heat pump

1.1. Outline of the PhD thesis

This PhD thesis presents results of research devoted to improve efficiency of the technology of heat pumps driven by magnetocaloric effect (MCE). Two main issues that compromise the efficiency of such a device were analysed. Namely, solid active magnetic regenerators (AMR) and heat transfer.

The thesis is structured in five chapters. Chapter 1 is divided into four subsections that provide analysis of previous research work done in the fields of magnetic refrigeration and passive heat transfer enhancement. Chapter 2 presents modelling and experimental results of novel geometry for enhanced heat transfer that was created at the Department of Energy Conversion and Storage, Technical university of Denmark (DTU). A performance comparison of the presented geometry to other state-of-the-art geometries is also provided. Chapter 3 presents results of a numerical analysis using a one-dimensional AMR model to investigate double corrugated pattern of a porous structure of a solid AMR. Chapter 4 presents experimental results obtained on various solid AMRs. The tested regenerators varied in particle size, shape, number of layers and amount of epoxy. Finally, conclusions of this PhD thesis and suggestions for future research are given in Chapter 5.

1.2. Basics of magentocaloric effect and materials

The magnetocaloric effect (MCE) is a physical response of a magnetocaloric material (MCM) to a change of applied magnetic field [1]. This phenomenon was discovered by French and Swiss physicists Weiss and Piccard and first was used in near absolute-zero-degree applications [2]. Later, after the discovery of gadolinium (Gd), it was demonstrated that the MCE could be used in near room temperature applications [3]. This encouraged an invention of a heat pump, operating near room temperature, that is driven by MCE [4] and attracted significant interest from scientific community.

In principle all magnetic materials exhibits temperature changes depending on variation of a magnetic field. This phenomenon occurs due to coupling of the magnetic sublattice with the magnetic field that changes the magnetic entropy part of a solid, s_m, [5] as given in Eq. 1-1.

$$s_{tot}(T, H) = s_m(T, H) + s_{lat}(T) + s_{ele}(T)$$
Eq. 1-1

Where s is specific entropy of a solid, T is temperature, H is magnetic field and subscripts *tot*, *m*, *lat* and *ele* denote total, magnetic, lattice and electron, respectively. One can see that only magnetic component of the s_{tot} is a function of both magnetic field and temperature, while other two components depend only on temperature[1]. This results into change of s_m in the solid material when magnetic field is varied. In Figure 1-1, it can be seen that magnetic spins of the solid are highly disordered when magnetic field is absent. When the non-zero magnetic field is applied (material is magnetized), magnetic spins of the solid align in ordered manner. This process causes the isothermal entropy change (Δs_m), however, the s_{tot} must remain constant. Therefore, as the response to decrease of s_m, the s_{lat} and s_{ele} increases, leading to adiabatic temperature increase of the solid material (ΔT_{ad}). Once the magnetic field is removed (material is demagnetized) magnetic spins return into disordered state and the temperature of the material changes by opposite ΔT_{ad}. MCE is classified into ordinary and inverse. Ordinary MCE results in negative Δs_m and positive ΔT_{ad} when the magnetic field is increased (as described above), and inverse MCE demonstrates positive Δs_m and negative ΔT_{ad} with increased magnetic field [2,5]. Every MCM exhibits the highest MCE at its Curie temperature, T_C.

---

[1] Both s_{lat} and s_{ele} only weekly depend on magnetic field, thus can be considered as functions of the absolute temperature only [60].
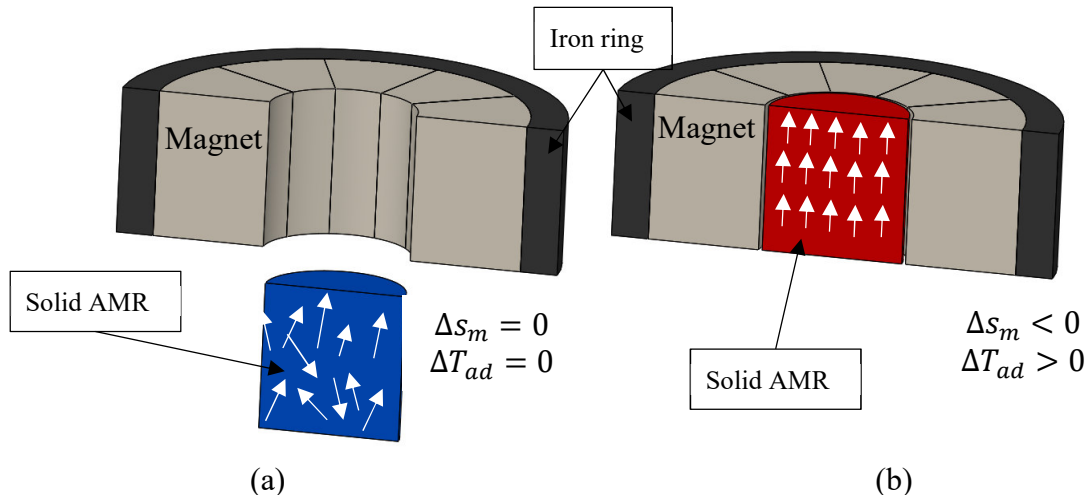
Figure 1-1. Alignment of magnetic spins in a solid AMR that exhibits ordinary MCE when (a) magnetic field is zero and (b) non-zero.

Heat, generated during the magnetization process, can be removed by applying flow of a heat transfer fluid through a solid regenerator. By cycling a solid AMR in and out of the magnetic field and managing the flow, temperature difference (span), ΔT_{span}, between hot and cold reservoirs is established. It is obvious that the most efficient thermodynamic cycle must be employed in order to obtain maximum possible efficiency of such a device. A beautiful explanation of the thermodynamic theory of the MCE is given in Ref. [2,5,6] thus it will be omitted in this thesis.

The MCE are grouped according to the continuity of the magnetic phase transition to first-order and second-order materials. The latter group of MCE show continuous phase transition between the non-magnetic and magnetic phases. That results into moderate entropy change over a broad temperature range. The benchmark material in this group is Gd that provides MCE of ~ 3 K at 1 T [5]. It is important to note that MCE effect is not a linear function of a magnetic field. Gd is extensively used in most of the developed AMR devices, despite the fact that it is extremely expensive [2].

First-order phase transition (FOPT) materials show very narrow and sharp discontinuous entropy change as a function of the temperature and exhibits giant MCE [7], which can be as high as 6.5 K at 1 T [5]. Besides a very narrow working temperature region, FOPT materials are accompanied by other sever drawbacks, such as magnetic and thermal hysteresis and material brittleness caused by volume changes during the phase transition [8,9]. These issues compromise performance of magnetocaloric devices. For instance, volume changes of MCM during cyclical operation eventually cause mechanical disintegration of solid regenerators. Smaller particles, which occur due to fraction of the solid AMR, clog flow channels inside regenerators reducing the performance of devices and, at the end, causing the vital failure of apparatuses [10,11]. To prevent particles from displacement and breakage, they could be coated with ductile material or epoxy [10–13]. One of the obvious shortcomings here is that introduction of non-magnetic material in a solid AMR leads to reduction of the performance due to reduced amount of MCM in a regenerator and reduced thermal properties of a selected coating material. In Chapter 4, the effect of epoxy bonding on performance of a solid AMR is presented. As one of other possible solution to increase mechanical stability of solid AMR, porosity was proposed [14]. Porous structure of a solid AMR increase space between neighbouring particles and removes grain boundaries. Therefore, particles can exhibit volume change during cyclical operation without damaging each other. However, porosity alone is not sufficient solution for maintaining mechanical stability of a solid AMR for long-term applications.

A detailed explanation of thermal and magnetic hysteresis in MCM is given in Ref. [15], thus it will be omitted in this thesis. Nevertheless, it is important to mention that hysteresis can be eliminated in some FOPT materials by slightly changing their chemical composition [16]. This also would lead to a reduction of the MCE, which still would be higher than for SOPT [16].

As it was mentioned above, FOPT materials have a very narrow region of working temperature, i.e. where the giant MCE is observed. This region for FOPT materials is approximately four times smaller than for SOPT materials [8] being ~ 7 K of half maximum of Δs_m [16]. For practical use of FOPT materials, this region must be above 25 K [10]. The necessary working temperature range can be obtained by layering MCE with slightly different T_C [11,17,18]. However, it is not trivial and one has to take a very good care in selecting the T_C of neighbouring layers. It was shown that even a slight deviation in the T_C distribution along a regenerator would lead to significant reduction in performance [19]. In order to obtain 90 % of the cooling power of infinitely layered bed, the recommended temperature span between two neighbouring layers is 2.5 K for FOPT materials such as La(Fe,Mn,Si)$_{13}$H$_y$ [19]. Moreover, selection of the suitable T_C also depends on the objective of a designed regenerator. For example, to achieve maximum temperature span one should select materials with the largest MCE in the working temperature region. On the other hand, the highest Carnot efficiencies could be obtained using materials that have T_C higher than the average temperature of a layer during a cycle [20]. However, it is rather difficult to manufacture materials with precise T_C values due to different challenges, such as stability of chemical composition [21] or ability to tune the T_C. Recently it was experimentally demonstrated that inaccuracy in T_C, when layering regenerators, could be compensated by adjusting mass fraction of each layer [22]. The effect of layering FOPT materials on performance of regenerators is discussed in details in Chapter 4.

1.2.1. AMR geometries

Performance of any AMR device strongly depends on the selected geometry of an AMR. It is desired to have a high heat transfer and low pressure drop, so that high cooling power with high coefficient of performance (*COP*) could be obtained. However, a fine AMR geometry provides high cooling power, but results in low efficiency because of high pressure drop [1]. Due to relatively simple manufacturing, the most widely reported experimentally tested AMR geometries are packed beds with spherical or irregular shaped particles and parallel plates [23–32].

In theory, sufficiently thin, approx. 0.1 mm thickness, parallel plates should demonstrate high efficiency due to lower pressure drop and viscous dissipation in comparison with packed beds [33]. However, it is very challenging to manufacture such thin plates. Furthermore, numerical investigations have revealed that there is an optimal length of an AMR with parallel plates that depends on porosity of the AMR [23]. Moreover, plates must be evenly spaced with narrow flow channels. It was numerically demonstrated that inhomogeneous spacing of plates would significantly reduce the performance of an AMR bed [34].

On the other hand, numerical studies have shown that a shorter packed bed AMR with sufficiently small spherical particles (in a size range of 0.07 to 0.17 mm) can operate with similar efficiency as an AMR with parallel plates [23]. Again, it is technically very difficult to produce such small spheres. An experimental study has showed that too big sphere diameter compromise the performance of an AMR [23]. Another study demonstrated experimentally that AMR beds with spherical particles significantly outperform beds with parallel plates [35]. Here, the tested geometries had same amount of MCM material, porosity and heat transfer surface, thus differences in performance were caused only by geometries themselves [35].

Performance of regenerators with parallel plates could be improved by enhancing surface of plates. An experimental investigation showed that corrugation with a specific angle increases performance of parallel plate regenerators [36]. Seven passive regenerators (with no magnetic field applied) with dimpled, two types of corrugated and smooth plates with four different spacing were investigated numerically and experimentally [36]. The corrugated plate regenerator with 90º of included angle provided highest temperature span over the same range of utilisation, *U*. Utilisation is a dimensionless parameter giving a ratio between thermal capacity of fluid pushed through a

regenerator during one fluid blow and thermal capacity of a regenerator [1]. It is defined in Eq. 4-1, given in Chapter 4.

A comprehensive numerical study on various different AMR geometries was presented in Ref. [33]. There circular and rectangular micro-channels, packed screen bed along with packed sphere beds and parallel plates were investigated. Regenerators with square pins [35] and packed cylinders [25] were tested experimentally. None of these geometries outperformed packed sphere beds.

A possibility to manufacture regenerators using selective laser melting [37] or laser beam melting [38] opened an opportunity to investigate different geometries, such as fin-shaped rods or wavy channels. It was proved that laser melting and quenching does not affect magnetocaloric properties of MCM. However, quenching after annealing causes internal strains [37].

As mentioned above, a successful AMR geometry should provide higher heat transfer with lower pressure drop. Therefore, a double corrugated geometry is proposed as a flow pattern for a porous structure of an AMR. Two double corrugated tubes with different geometrical characteristics were selected for numerical investigation. The chosen tubes were studied experimentally in a counter-flow heat exchanger in order to determine their thermal performance. The obtained results were implemented into one-dimensional AMR model. The double corrugated tubes and prove of concept are presented in Chapter 2. Chapter 3 presents results of numerical investigation of AMR with double corrugated flow structure.

1.3. Overview on magnetocaloric prototype devices

Development of magnetocaloric prototype devices started with the demonstration of the first magnetic heat pump in 1975 [3,4]. To this day, a variety of the state-of-the-art magnetocaloric devices has been reported. They are grouped in linear motion and rotary devices depending on how AMRs and magnets are moved with respect to each other.

Development of a magnetocaloric device is a challenging and complex process, thus with each developed machine only a small improvement could be seen. Here several magnetocaloric devices are reviewed in chronological order with specific emphasis on their performance and improvements that were applied. Devices that were used in this PhD project are presented in more details. More extensive reviews of existing devices are given in Ref. [1,39].

1.3.1. The *Test machine*

The *Test machine*, developed at DTU, is a versatile small-scale linear motion device. It was designed for a purpose to characterize MCM regenerators in a fast and inexpensive way, regardless of geometry, material, particle size, or heat transfer fluid [40,41]. The *Test machine* was used for characterisation of AMR with 1 to 9 layers of MCM that are presented in Chapter 4.

From Figure 1-2 (a), one can see that the actual device is built inside a temperature-controlled cabinet. A Halbach cylinder permanent magnet generates 1.1 T magnetic field inside its bore (ø 40 mm) and is mounted in a fixed position. Figure 1-2 (b) shows schematics of the *Test machine*. A small regenerator is moved in and out of the magnetic field by a stepper motor. The heat transfer fluid is pushed through a regenerator by a displacer, controlled by other stepper motor. The hot side forced convection heat exchanger is placed above a tested regenerator and is connected to the hot reservoir that maintains constant hot side temperature.
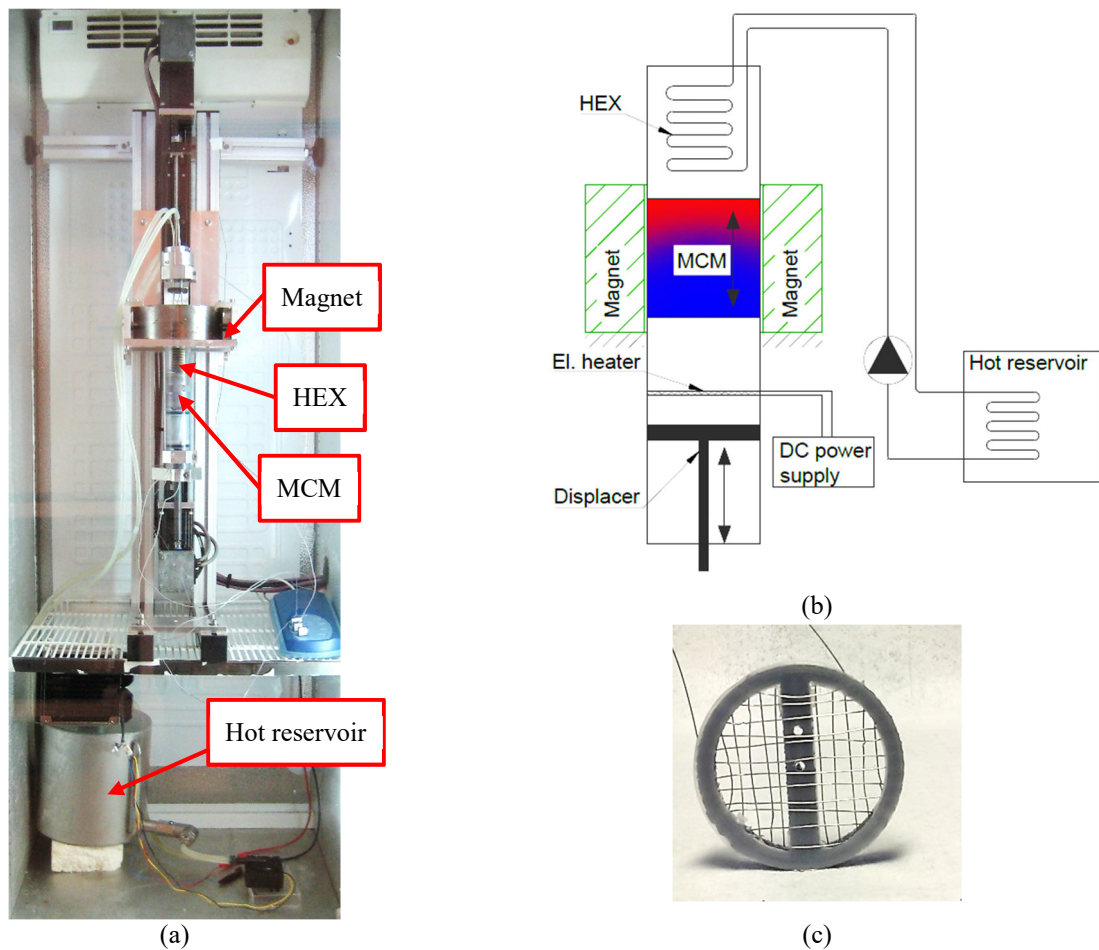
Figure 1-2. (a) The *Test machine*. This figure is a slightly modified version of the figure presented in Ref. [42]. (b) Schematic of the *Test machine* This figure is a slightly modified version of the figure presented in Ref. [32]. (c) A heater with two holes for mounting thermocouples.

Figure 1-2 (c) shows a heater build from heat resistant wire that is mounted at the cold side for cooling load experiments. The Aim TT i EL302P power supply with the stated power accuracy of ± 0.9 % is used for controlling power of the heater. The temperature measurements are taken with E-type calibrated thermocouples. The operational conditions can be changed by varying velocity and amplitude of the displacer.

1.3.2. Magnetic device at University of Ljubljana

A linear motion magnetic device for a quick and simple testing of different AMR materials was designed at University of Ljubljana [1,25,43]. The unique design of the device allows operating the machine with one or two AMR beds. Four pieces of permanent magnet are assembled with a soft ferromagnetic material in the "8" shape. The maximum flux that the magnet assembly provides is 1.15 T. The maximum operational frequency of the device is 0.9 Hz [1]. The fluid flow through regenerators is controlled by electric actuator that is connected to two pistons at both ends of regenerators. The speed and a stroke of the actuator can be adjusted. The hot end temperature is controlled by a heat exchanger connected to a thermostatic chamber. An electrical heater is installed at the end of the cold end for simulating cooling load.

The device was operated with FOPT [25,43] and SOPT [43] materials. Different geometries of the regenerators were also investigated using this machine [25]. The maximum no-load temperature span was obtained with parallel plates of Gd with 0.25 mm spacing. The zero-span specific cooling power obtained for this geometry was 39.7 W/kg [1,25]. AMRs with four and seven layers of

LaFeCoSi material demonstrated 20 K no-load temperature span. The maximum specific cooling load at 8 K temperature span was 15 W/kg for both FOPT regenerators [1,43]. The geometry of later regenerators were stacked parallel plates with 0.5 mm thickness and 0.2 mm spacing.

1.3.3. Large-scale rotary device at Astronautic Corporation of America

Large-scale magnetic rotary device was developed at Astronautic Corporation of America [26]. The magnet assembly, providing maximum 1.44 T field, is rotated over twelve beds arranged circumferentially. The fluid flow system is unidirectional and there is no mixing of inlet and outlet fluid. The system is designed in a way that all twelve beds are coupled in pairs. This means that one bed in a couple is magnetized and experiences cold fluid blow, while its partner is demagnetized and experiences hot fluid flow. Four beds are (de)magnetized at the same time and experience (hot) cold fluid blow. The remaining two couples are blocked for fluid flow and are in transition for (de)magnetization process. An electrical heater is mounted at the cold outlet of the system for simulating cooling load. The hot side is connected to a temperature-controlled bath before entering the hot side of AMRs. Volume of each packed bed is 30 cm^3.

The performance of the device was evaluated using the six layers of FOPT material [26]. In total 1.52 kg of LaFeSiH were used. The MCM had form of spheres that were in a size range of 0.177 to 0.246 mm. To the best of knowledge of the author of this thesis, it is the smallest size range of spherical particles that have been experimentally used in AMR devices reported up to this day. A small diameter of spherical particles or flow channels in an AMR bed is desired, because it increases heat transfer surface and, thus performance of an AMR system. The packed beds, used in this large-scale rotary device were epoxy-bonded [26]. An average porosity of the beds was 37 %. The heat transfer fluid used in the system was water with a slight amount of an anticorrosion inhibitor. The operational frequency was 4 Hz. The cooling load obtained at zero-span was 3042 W and 2090 W at 12 K of temperature span at flow rate of 21.2 l/min.

1.3.4. A magnetic rotary device at University of Victoria

The second-generation rotary device PM II, designed at University of Victoria, has three nested Halbach cylinders [44]. The inner cylinder is kept stationary while the intermediate and the outer ones are counter-rotated. This arrangement of the magnet assembly provides sinusoidal field waveform and stationary field vector as well as zero low-field. Moreover, the intermediate and the outer magnets could be co-rotated and create a field wave form as in first rotary device PM I [44]. The maximum field intensity in PM II is 1.54 T. The operational frequency of this device is 0.2 – 0.4 Hz. This machine operates with a single bed of MCM material that is mounted inside the inner magnet. The maximum volume of MCM is 57 cm³. The fluid flow system is designed in a way that the amount of fluid that is not interacting with the regenerator ('dead volume') would be minimized [44]. The fluid flow is oscillating inside the regenerator. However, once it leaves the MCM bed, the flow is converted into unidirectional by employing check valves.

The performance of the PM II machine was demonstrated using packed Gd spheres with size of 0.5 mm and co-rotating the outer magnets. The practically required torque for counter-rotating outer magnets made it impossible to operate the machine in this mode. The maximum obtained no-load temperature span was 33 K for a regenerator with 650 g of Gd. The zero-span cooling power was 96 W at $v = 0.8$ Hz.

1.3.5. Versatile magnetic refrigerator demonstrator at the University of Zaragoza

For the purpose of material characterization, a versatile linear motion magnetic refrigerator was developed at the University of Zaragoza [45,46]. Differently from the *Test machine*, this prototype is

organized in horizontal manner and operates with two AMR beds. Due to its design, this device can perform two cycle at the same time, i.e. one AMR is magnetized and experiences the cold fluid flow while the second AMR is demagnetized and experiences the hot fluid flow [46]. The design of this machine provides high flexibility in varying operational parameters such as pushed fluid volume, heat load and mass flow rate [46].

The Halbach permanent magnet provides uniform 1.4 T magnetic field. The AMR beds are moved in and out of the magnet by sliders. The flow system is moved together with the AMR beds. Each bed has volume of 3.19 mm³. The heat transfer fluid is reciprocated by pistons that are moved by a separate slider. The system operating frequency is up to 0.82 Hz. Series of experiments have been performed with this device using 32 g Gd spheres of the size of 0.2 – 0.4 mm. The maximum reported no-load temperature span was 19.3 K at $U = 0.19$ and maximum obtained cooling power was 6 W at zero temperature span and $U = 1.1$ [46]. The maximum COP was 0.7 for the later operational conditions and $v = 0.3$ Hz.

1.3.6. *MAGGIE*

MAGGIE (Mechanical Alternatives Giving Greatly Improved Efficiency) is the second-generation rotary magnetocaloric prototype developed at DTU. One can see from Figure 1-3 that *MAGGIE* had a vertical magnet that is generating magnetic field of maximum 1.13 T and flow system arrangement. The magnet rotates around the cylindrical regenerator bed divided into 11 compartments, which is mounted on an iron core [47]. The first DTU prototype had 24 beds [48] as well as most of the other magnetocaloric rotary devices. However, it was learned from practice, that having uneven number of cassettes with MCM would misbalance magnetic forces. Thus, the torque required to rotate a magnet would be lower. This good practice was first implemented into the design of *MAGGIE*. The heat transfer fluid flow system was designed so that unidirectional external flow and reciprocating flow through the MCM beds is ensured [49]. Poppet valves, actuated by a cam ring, ensure timing of the fluid flow with the magnet rotation.
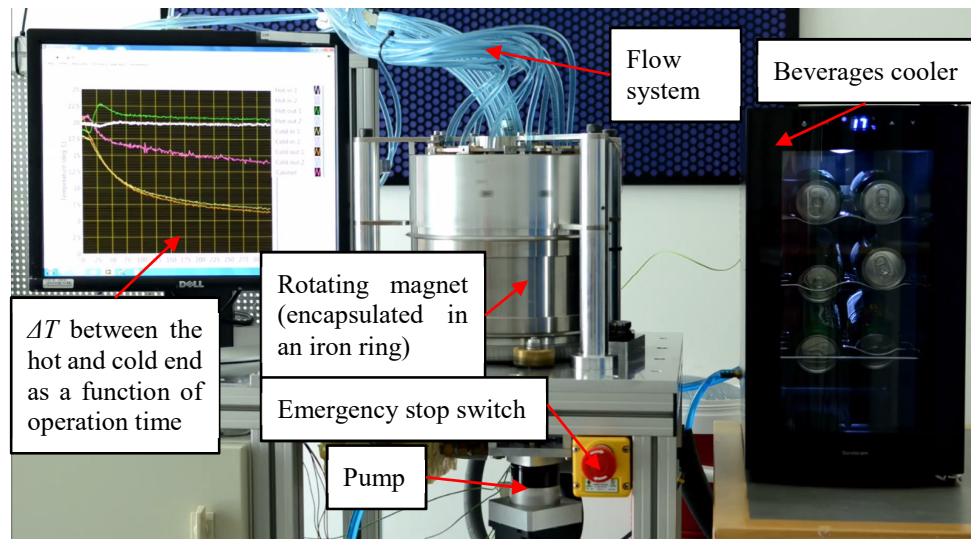
Figure 1-3. *MAGGIE* during the demonstration of performance.

In total 1.7 kg of Gd and Gd alloys with different T_C are used in *MAGGIE*. The MCMs were arranged in four layers. More details about the used MCM and its arrangement in the regenerator beds as well as selection and characterization are given in Ref. [49,50].

Experimental results obtained with *MAGGIE* revealed the significance of flow balancing on the performance of magnetocaloric prototypes. It was shown that flow imbalances reduce ΔT up to 17 % [50,51]. *MAGGIE* provides the second law efficiency of $\eta_{2^{nd},AMR} = 18$ % at $\Delta T = 15.5$ K, $COP = 3.6$

at operating frequency of $\nu = 0.61$ Hz with balanced flow [52]. Analysis of the efficiency of *MAGGIE* showed that significant part of losses are due to pressure losses in external components and it could be improved in future designs [52]. Moreover, efficiency of any AMR device could be improved by changing shape of packed beds from spherical to corresponding parallel plates. However, this would be technically very challenging [52].

1.3.7. Magnetic refrigerator at the POLO Laboratories of UFSC

A rotary magnetic refrigerator consisting eight pairs of MCM beds was constructed at the POLO Laboratories of the Federal University of Santa Catarina (UFSC) [53,54]. The machine is designed so that an assembly of a permanent NdFeB magnet that provides magnetic flux of 1 T is rotated inside regenerator beds that are mounted on the inside diameter of an iron stator [53]. Usually, AMR beds are exposed to the highest and lowest magnetic field one at the time. In this machine, the regenerator beds are coupled, i.e. two pairs of the regenerator beds are simultaneously magnetized and experience cold fluid blow, two pairs of them are demagnetized and experience hot fluid flow and four remaining couples are closed for flow. Differently from other designs, the rotary valves were mounted only on a hot end, thus the heat generation at the cold end is eliminated [53]. Operational frequency of this prototype can be up to $\nu = 8$ Hz [53].

This magnetic prototype demonstrated the second law efficiency $\eta_{2^{nd},AMR}$ of 1.16 % with *COP* of 0.54. These performance parameters were obtained at $\nu = 0.8$ Hz and flow rate of 150 L/h. The cooling power of 80.4 W with $\Delta T = 7.1$ K was obtained at the same operating conditions [53]. The losses analysis for this devise was carried out as well. It revealed that the biggest part of the power is consumed by a valve system [55]. The maximum reported *COP* for this machine was 2.46 at $\Delta T = 4$ K and the maximum $\eta_{2^{nd},AMR}$ was 3.7 % at $\Delta T = 6$ K, considering the same operational conditions with flow rate of 150 L/h and $\nu = 0.4$ Hz [55]. The necessity for a novel design of regenerator beds with objective to reduce pressure drop inside them was concluded after the losses analysis [55].

1.3.8. Rotary magnetic refrigerator at the University of Salerno

The first Italian rotary magnetic prototype *8Mag* was developed at the Refrigeration Lab of the University of Salerno [27]. This apparatus consists 8 AMR beds that are placed on a metal ring with 45° spacing. The machine operates with 1.2 kg of Gd spheres that are 0.4 – 0.5 mm size. The magnetic circuit has the double "*U*" shape and is arranged in a two-pole magnetic system. In this arrangement, the maximum obtainable flux density is 1.25 T. The motor that rotates the magnetic system can operate in the range of 0.1 – 1 Hz, however, due to the coupling of the regenerators, the frequency of AMR cycle is doubled [27]. An electrical heater is installed at the cold end for simulating cooling load. The fluid flow is managed by a rotary valve, which is installed inside the magnetic system in order to increase compactness of the system.

To investigate the performance of this apparatus, several tests, using Gd, were conducted at constant operational frequency of 0.5 Hz and fluid flow rate 0.083 kg/s with varying hot end temperature and cooling load. The maximum temperature span at no-load test conditions was 11.3 K. Maximum cooling load at zero-span was approximately 200 W. The maximum *COP* obtained with this machine was 1.8 at 163 W thermal load conditions and hot end temperature of 295 K [27].

1.3.9. *MagQueen*

The large-scale magnetocaloric heat pump *MagQueen* was recently developed at DTU. The experimental validation of this machine is currently in progress. However, the intriguing design details and novelty of the machine were reported in Ref. [56,57]. Figure 1-4 shows fully assembled

MagQueen. One can see that the machine is organized in three layers: (top) magnetocaloric layer, (middle) flow system layer and (bottom) electronics layer.
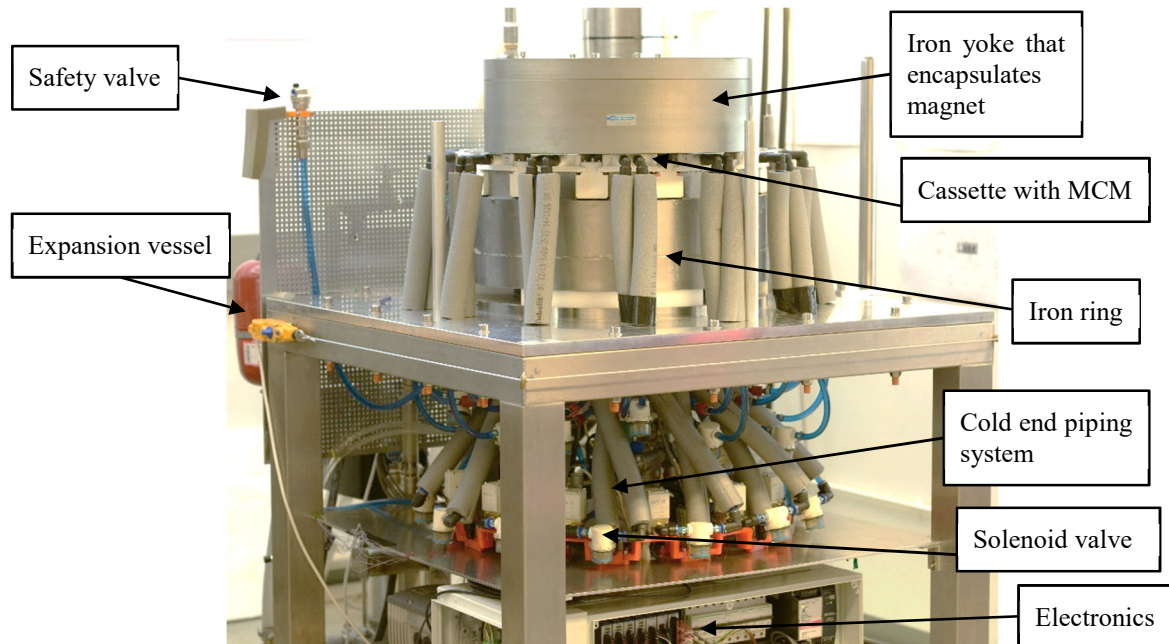
Figure 1-4. Fully assembled *MagQueen.*

The engineering solution on the design of the magnet assembly and shape of the cassettes of MCM is innovative [58,59]. The two kidney-shape magnets, encapsulated into an iron yoke, are rotated over 13 trapezoidal shaped-cassettes. The design of the magnet allows to create high and low magnetic field regions in a circular arrangement by using moderate volume of magnetic material [58]. The trapezoidal shape of the cassettes allows favourable exploitation of changes in fluid viscosity. The cassettes are tapered in a way that the cross-section area for the cold fluid would be larger than for the hot fluid, thus pressure drop across the regenerator would be minimized. It was shown numerically, that trapezoidal regenerator shape allows to obtain a slightly higher *COP* value [19,57].

Epoxy-bonded spherical particles with an average diameter of 450 μm are constructed into 10 layers in each cassette. In total 2.8 kg of La(Fe,Mn,Si)$_{13}$H$_y$ is used. The maximum generated magnetic field is 1.6 T. The flow of heat transfer fluid is managed by 26 solenoid valves. This machine was designed to deliver approximately 1.5 kW of heating power at *ΔT* of 25 – 30 K with *COP* of 5.

1.3.10. The prototype at KTH Royal Institute of Technology

Figure 1-5 presents the medium-scale rotary magnetic device at KTH Royal Institute of Technology (KTH). A little bit more detail description of this device is provided here since a part of experiments, described in Chapter 4, were conducted using this machine. However, the full description of the machine and the adjustments done in order to improve its performance are given in Ref. [60,61].

<div align="center">(a)   (b)</div>
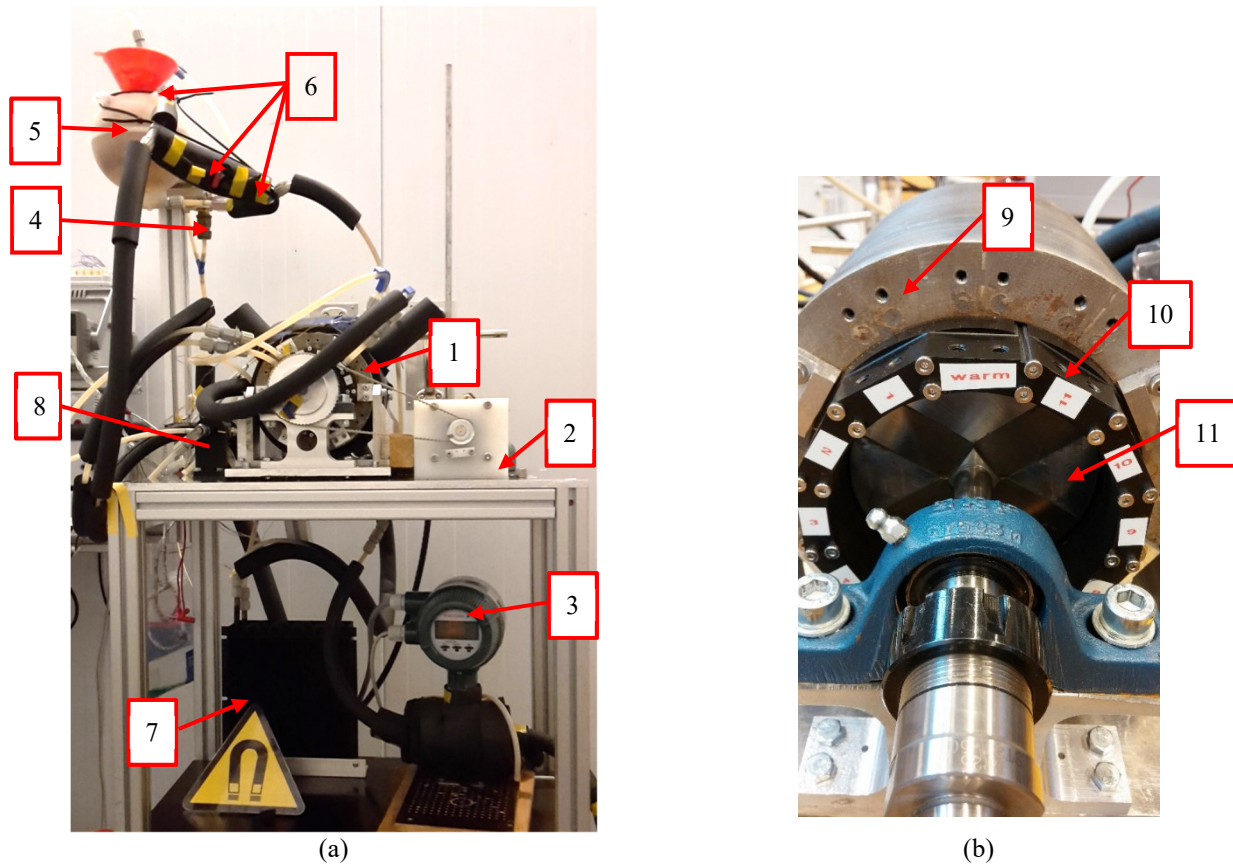
Figure 1-5. (a) A medium-scale rotary device. 1 – the iron yoke with the regenerator and the magnet inside; 2 – the stepper motor; 3 – the flow meter; 4 – the safety valve (4 bar); 5 – the expansion vessel, 6 – shut-off valves; 7 – the forced convection heat exchanger; 8 – the rotary valve [31]; (b) The assembly of the iron yoke (9), the regenerator housing (10) and the permanent magnet (11) used in the medium-scale device at KTH Royal Institute of Technology.

The regenerator (10) consists of 12 separated beds, mounted on the rotating magnet (11), which provides 0.75 T magnetic field. This system is mounted into the stationary iron yoke (9). The magnet is rotated by the electric motor (2). A shaft rotating the magnet is also connected to the rotary valve (8). This allows precise timing of a heat transfer fluid flow though (de)magnetized MCM beds.

Figure 1-6 presents the schematic of the device. One can see that regenerator beds are connected in series in the hydraulic circuit, i.e. the warm fluid is pushed through demagnetized beds where it cools down before entering magnetized beds, where it heats up and is pushed towards the heat exchanger (7). A cartridge heater is installed at the cold side for simulating cooling load experiments. The device is placed in a climate chamber, which allows precise control of a hot side temperature. The operational frequency of the magnetic prototype can be adjusted by changing rotational speed of the stepper motor. The fluid flow can be varied by changing frequency of the fluid pump.
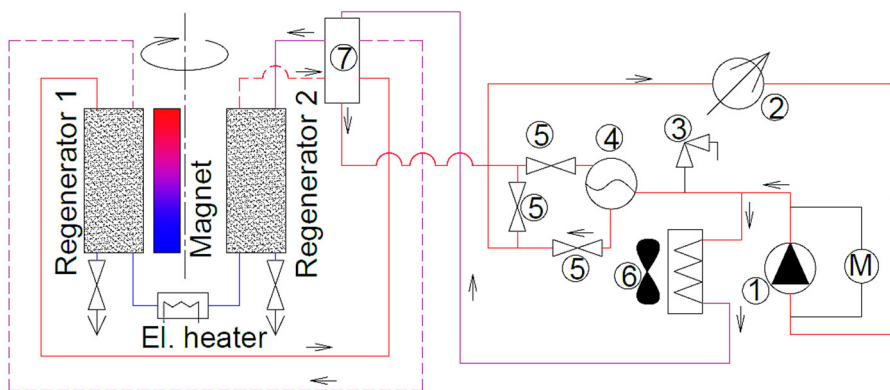
Figure 1-6. A schematic drawing of the flow system of the device: (1) pump; (2) flow meter; (3) safety valve set at 4 bar; (5) shut-off valves; (6) forced convection heat exchanger; (7) rotary valve. The shut-off valve (5), mounted in the connecting line is always closed. The full lines present pipes through which flow is flowing at the denoted moment of a cycle. The dashed lines present pipes that are free of flow at the same moment of a cycle. This figure is a slightly modified version of the figure presented in Ref. [31].

The regenerator housing is 15 cm long and has inner volume of 31.2 cm³ per bed. At each side of every regenerator bed, a fine mesh is mounted in order to prevent small particles from contaminating the hydraulic circuit. Even though, the machine is design having 12 regenerator beds, with some adjustments it can operate with 2, 4 or 6 beds [60]. As it was pointed out in Ref. [61], the pressure drop increases this much in the long and narrow regenerator beds of this machine that the potential of FOPT materials is eliminated. However, it was shown numerically that increased porosity of the packed beds would reduce viscous dissipation and, thus, cooling capacity would increase [61].

It was demonstrated by numerous experimental and numerical work that efficiency of a magnetic heat pump can be improved by optimizing geometry of regenerator beds [23,33,35–37,47,62–64]. One more way to improve efficiency of a magnetic heat pump is to use better heat exchangers. Research efforts on heat transfer enhancement are reviewed in the following section.

1.4. Overview on passive techniques for heat transfer enhancement

High heat transfer rate is limited to many different constrains such as low temperature difference, fluid properties and flow conditions, and development of thermal boundary layers. For many years, enormous research efforts have been devoted to find solutions providing enhanced heat transfer at reasonable input of additional energy such as required pumping power. All the techniques developed for the purpose of higher heat transfer are grouped in active, passive and combined [65]. Active techniques require external energy input such as electrostatic field, fluid vibration, injection and similar [65]. Passive techniques, on the other hand, disturb thermal boundary layers by deforming heat transfer surfaces in various ways, i.e. creating artificial roughness, extending surfaces, using additives such as nanoparticles, or inducing secondary flow by using coils or twisted tapes [65]. Combined techniques are so-called because they combine several techniques together. The main purpose of this section is to review passive techniques, used separately or in combination with each other, for heat transfer enhancement investigated numerically and experimentally.

Numerical and experimental investigation demonstrated gain in convective heat transfer using nanofluids with various nanoparticles suspended in variety of base fluids [66–71]. Mostly Cu, Al_2O_3 and TiO_2 nanoparticles were investigated for this application. One could think about other materials that have high thermal conductivity and are good candidates as nanoparticles, e.g. silica [68] or materials consisting high amount of carbon. It was experimentally shown that heat transfer decrease when nanofluid with SiO_2 nanoparticles were used, while nanofluid with Al_2O_3 nanoparticles

demonstrated significantly better thermal performance in the same test apparatus [68]. It was concluded that SiO_2 nanoparticles entangle to micro or macro roughness of a tube and increase flow resistance, thus heat transfer decreased [68]. Another interesting observation is that there is almost no increase in friction factor, when using small concentrations of nanoparticles [70].

More widely investigated passive heat transfer enhancement techniques are various surface deformations and inserts. Unlike nanofluids, surface deformations cause higher friction factor in comparison to a smooth surface. Nevertheless, the latter approach demonstrates much greater thermal performance than nanofluids. For example, artificially roughened tubes [72–75] provide higher overall efficiency, η, (Eq. 1-2) i.e. gain in heat transfer is greater than gain in friction factor [72,74,75].

$$\eta = \frac{Nu/Nu_0}{f/f_0} \qquad \text{Eq. 1-2}$$

Where Nu is Nusselt number, f is friction factor and superscript 0 denotes a reference geometry.

Twisted-tapes and helical-screw tapes also show significantly greater efficiency than smooth tubes [76–80]. Moreover, it was demonstrated that regularly spaced twisted-tape elements provide higher overall efficiency than full length twisted-tapes due to lower increase in friction factor [77]. It was also numerically demonstrated that greater overall efficiency was obtained for combination of twisted-tape and nanofluids comparing with results obtained for nanofluids only [71].

Spirally fluted tubes [81–84], spirally, helically, cross-spirally or transversally corrugated tubes [85–92] have been extensively studied numerically and experimentally. These kinds of surface deformation provide enhanced heat transfer at a reasonable increase in friction factor by periodically breaking thermal boundary layers, inducing swirl flow and, thus, fluid mixing. Corrugation height, e, corrugation period, p, and corrugation angle, φ, are sufficient parameters to describe tube corrugation. Different types of corrugation show superior efficiency at different flow conditions. For instance, helically corrugated tubes demonstrated up to 300 % higher thermal efficiency with increase in flow resistance up to 93 % when Reynolds number, Re, is low [90]. However, higher thermal efficiency of cross-spirally corrugated tubes has been obtained with increasing Re, while Nusselt number, Nu, of spirally corrugated tubes was 66 % higher than for a straight tube regardless of Re [92]. Corrugated tubes were also investigated in combination with various inserts [93–98] and in form of coils [99,100]. It was concluded that combination of several techniques performs better than each method separately. Interestingly, it was demonstrated that Nu for coils with smooth and corrugated walls is of the same magnitude at low Dean number, De. However, coils with corrugated walls demonstrate superior heat transfer to similar coils with smooth walls once De exceeds a critical value [100].

It was demonstrated theoretically that heat transfer could be enhanced if an angle between flow velocity and temperature profiles would be increased [101]. This was obtained by alternating ellipse axis (AEA) approach [102–104]. It was numerically [103,104] and experimentally [102] demonstrated that AEA tubes provides higher thermal efficiency at the same pumping power. Moreover, it was concluded that this kind of surface deformation prevents system from fouling [102]. These results confirms conclusions of numerical simulations [105], stating that surface corrugation focuses particles into the centre of a flow, thus they are removed with a flow.

Extended and corrugated geometries have been investigated in a form of plates [106,107] and micro- or mini-channels [108–113]. Results from both numerical and experimental investigations proved that enhanced surfaces provide higher convective heat transfer due to induced mixing in fluids. It was also demonstrated that properly arranged pins on cooling plates provide uniform and more efficient cooling along the surface of a cooling plate [106].

All the methods and approaches to enhance thermal efficiency of heat transfer elements reported above are based on engineering knowledge and intuition, as well as limits of massive manufacturing techniques available to this day. Nevertheless, heat transfer problems have been also analysed from a different perspective. Topology optimization have been used for analysis of systems of thermofluids [114–119]. Detailed reviews of topology optimized and nature-inspired structures are given in Ref. [120,121]. Here it is only emphasised that shapes of topology optimized heat sinks reminds more organic structures, such as tree branches, snowflakes or leaves, rather than conventional engineering solutions. It was demonstrated that topology optimization also can be used in latent heat thermal energy storage applications [117]. A three-dimensional topology optimization approach was strongly encouraged by revealing that some non-intuitive design features cannot be captured with a two-dimensional approach, which have significant effect on a performance of a system [117]. Results of experimental investigations also proved that topology optimized heat sinks perform significantly better at operational conditions they were optimized for, in comparison to conventional pin fin heat sinks [118].

Furthermore, there are many other engineering solutions that first were developed in nature, e.g. thermal insulation in a form of fur and blubber [122]. Thus, a lesson of enhanced heat transfer was taken from nature in this PhD project and performance of a novel double corrugated geometry based on a vascular counter-flow heat exchanger found in fishes was analysed. Results of numerical and experimental investigation on the emulated geometry are presented in Chapter 2.

2. Double corrugated geometry

In this chapter, the novel double corrugated geometry that was inspired by nature is presented. Firstly, a short explanation of the idea and inspiration source is given in Section 2.1. Section 2.2 provides the detailed explanation of the analysed geometries. The approach of numerical modelling and the obtained results are presented in Section 2.3. Experimental analysis and obtained results are presented in Section 2.4.

It must be clarified that the double corrugated tubes were designed and modelled at the Technical University of Denmark. For the first time, the initial modelling results and the concept of double corrugated tubes were presented in the International Conference on Experimental Heat Transfer, Fluid Mechanics and Thermodynamics. The original papers *C.2. Passive heat transfer enhancement in 3D corrugated tube* is included in this thesis. Latter, the full set of results obtained with the *CFD* was published in the International Journal of Heat and Mass Transfer. The original paper *P.2. Elliptical double corrugated tubes for enhanced heat transfer* is included in this thesis. The experimental investigation on selected double corrugated tubes was done in collaboration with the University of Parma, Italy. The experimentally obtained data were analysed using the technique, modified and validated by the group from the University of Parma. The design and construction of the used test setup was done in collaboration of both parties. The author of this thesis carried out the experiments and interpretation of the results, while the group from the University of Parma conducted the data reduction and analysis. The paper, presenting experimental results, is under revision at the International Journal of Heat and Mass transfer. The paper *P.1. Enhanced heat transfer in tubes based on vascular heat exchangers in fish: experimental investigation* is included in this thesis. A part of the experimental results is going to be presented at International Conference REMOO Energy 2019.

Finally, it is worth to mention that the patentability of the concept of the double corrugated tubes was investigated. An invention discloser was filed and the clearance and opinion search was conducted at the designated office. There, it was found a patent filled in 1953 by E. Jantsch [123], in which a similar concept of flow deformation for enhanced heat transfer was presented. Even though, it was still possible to file a patent application on the concept of double corrugated tubes, it would have been difficult to formulate claims that did not interfere ones made by Jantsch. Therefore, the patenting procedure on the double corrugated tubes was stopped. Jantsch [123] proposed deforming a straight tube by a specially designed device. He claimed that the fluid flow was "effectively kneaded" by the deformed geometry, thus heat transfer increased. However, no evidence of Jantsch's invention being tested or reported elsewhere could be found.

2.1. Inspiration

No engineer could ever be as good as nature is. Nature provides fascinating examples of various advanced solutions for problems that are faced daily in many engineering applications. Using the biomimetics [122] approach, engineers have replicated and successfully applied some of these nature-inspired solutions.

A particular interest in this thesis is paid to heat transfer processes occurring in nature and developed solutions. Mostly, heat is preserved inside an organism by different kind of insulation material, such as fur, feathers or blubber. It is very rare that high heat transfer would be required in nature. Artic birds give few examples of the enhanced heat transfer [124]. Blood vessels, entering feet of these birds, form a counter-flow heat exchanger that allows feet to operate at lower temperature than rest of birds' body [124]. Several type of fishes, such as lamnidae sharks, billfishes and tunas, have also developed a regional counter-flow heat exchanger so their body could be warmed in one or several specific spots such as fins, eyes or the brain [125]. Thus, these fishes could dive deeper and hunt in colder waters than those without a regenerative heat exchanger. The whole-body endothermy

was found in opahs [126]. This is due to high efficiency counter-flow heat exchanger found in fish gills. It is a compact, very complex, and tightly bundled in alternating manner, collection of blood vessels. This arrangement allows the cold oxygenated blood to be warmed by deoxygenated blood before previous enters the fish's body. Then, warmed blood is circulated all over the body. Therefore, opahs can maintain their body temperature ~ 5 °C higher than temperature of surrounding water [126].

The counter-flow heat exchangers found in the fishes mentioned above were taken as an inspiration for a novel geometry for enhanced heat transfer. The blood vessels arrangement and geometry were analysed from the cross-section and 3D tomography images provided in Ref. [126,127]. It became clear that the shape of the flow path is changing the aspect ratio across the flow channel. However, the cross-section area of the flow channel should remain the same in order to prevent overstressing the heart [128]. With these ideas, the geometry of double corrugated tubes was generated. The geometry of these tubes is based on elliptical cross-section that changes the aspect ratio along the flow channel while maintaining either constant hydraulic diameter, D_h, or constant cross-section area, A_c. More details about the geometry and its classification are given in Section 2.2. The presented geometry periodically impinges thermal boundary layers preventing them from development. In this way, the heat transfer is enhanced with a moderate increase in pressure drop.

2.2. Geometry

The geometry of double corrugated tubes (DCTs), presented in this thesis, emulates a vascular heat exchanger, found in several fish species. The objectives for the geometry were as following:
1. D_h or A_c must be maintained constant along the flow channel;
2. Tube diameter, D_h, corrugation period, p and aspect ratio, AR, should be easily modified;
3. Construction of the geometry using CAD software should be non-demanding.

These requirements implied that the designed geometry must be described by surface equations. It is also clear that two different set of equations are necessary to describe surface of DCTs with holding constant D_h and A_c. Additionally, DCTs with two different base geometries were constructed and analysed. Namely, an ellipse and a super-ellipse were selected as the base geometries. An elliptical cross-section shape of the DCTs was initially chosen in order to replicate more accurately the vascular heat exchangers. It is noticeable that at high AR the flow channels in ellipse-based tubes become strongly squeezed. Furthermore, a fluid flow suffers great pressure losses when p is small. Therefore, a super-ellipse cross-section was additionally investigated since it would allow constructing less squashed flow channels of DCTs while replicating the vascular geometry rather accurately. Thus, pressure drop should be lower for the latter case while providing enhanced heat transfer and thus, higher overall efficiency. The parametric equation of an ellipse in Cartesian coordinates is given in Eq. 2-1.

$$\begin{cases} x = \pm a \ cos^{\frac{2}{n}} t \\ y = \pm b \ sin^{\frac{2}{n}} t \end{cases} \quad 0 \leq t \leq \frac{\pi}{2} \qquad \text{Eq. 2-1}$$

Where a and b are the semi-major and semi-minor axes of the ellipse, respectively and n is an ellipse shape factor and t is a parameter with no geometrical interpretation.

It must be mentioned that ellipse shape factor, n, may be any positive number. Thus, a wide variety of super-ellipse shapes can be generated. One can see from Figure 2-1 that an application-sensible shape can be obtained when n is in a range from 2 to 3, where the shape is an ordinary ellipse when $n = 2$ and a rectangular with rounded corners when $n = 3$. Note that Figure 2-1 represents super-ellipses with the highest aspect ratio, AR, analysed in this thesis. Figure 2-1 (b) shows quarter of cross-sections of several super-ellipses with various n values between 2 and 3. It is seen that $n = 2.5$ gives

a good representation of a super-ellipse, thus it was selected for the further analysis. From Figure 2-1 (b), it is also seen how the scaling factor γ affects the cross-section of a supper ellipse.
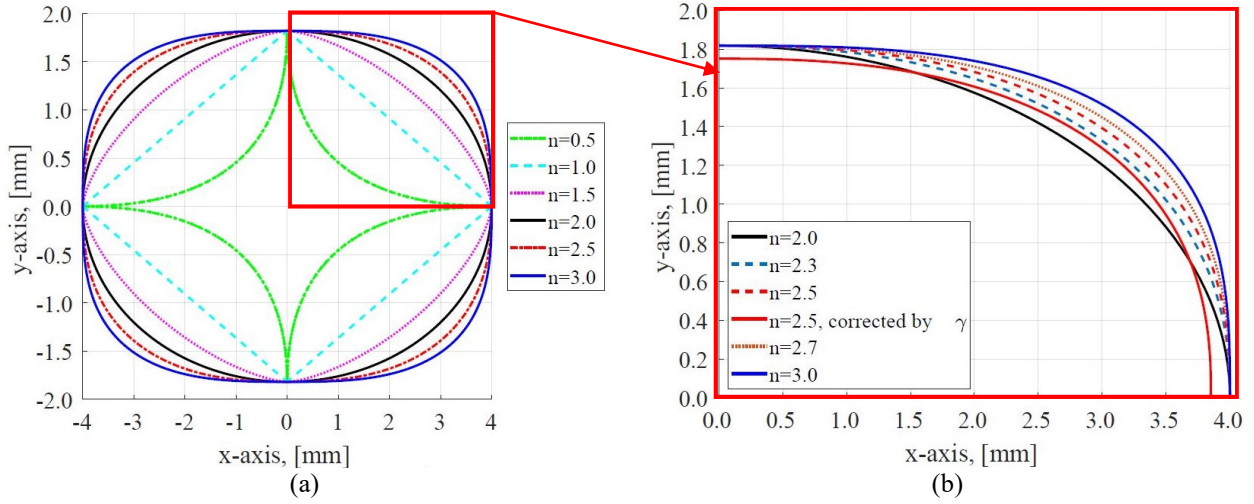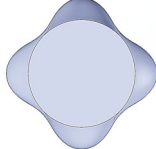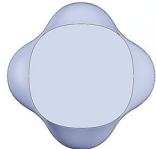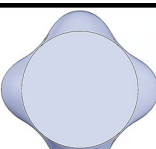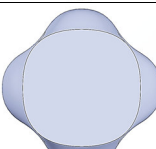
Figure 2-1. Shapes of a super-ellipses as a function of n with $AR = 2.2$ (a) a full cross-section when n is in a range from 0.5 to 3.0 and (b) a quarter of a cross-section when n is in a range from 2.0 to 3.0.

The four sets of surface equations have been derived as given in Table 2-1. The DCTs are grouped according to the base geometry and the characteristic parameter that is held constant. This result in four groups: (1) EDH for ellipse-based DCTs with constant D_h; (2) EAC for ellipse-based DCTs with constant A_c; (3) SEDH for super-ellipse-based DCTs with constant D_h; and (4) SEAC for super-ellipse-based DCTs with constant A_c.

Table 2-1. Surface equations of double corrugated tubes with different base geometries and D_h or A_c held constant.

Base geometry		Constant hydraulic diameter	
Ellipse		$\begin{cases} x = \dfrac{R}{2}AR^{\left(sin\left(\frac{2\pi}{p}z\right)\right)} + \dfrac{R}{2} \\ y = \dfrac{R}{2}AR^{\left(-sin\left(\frac{2\pi}{p}z\right)\right)} + \dfrac{R}{2} \end{cases}$	Eq. 2-2
Super-ellipse		$\begin{cases} x = \left(\dfrac{R}{2}AR^{\left(sin\left(\frac{2\pi}{p}z\right)\right)} + \dfrac{R}{2}\right)\gamma \\ y = \left(\dfrac{R}{2}AR^{\left(-sin\left(\frac{2\pi}{p}z\right)\right)} + \dfrac{R}{2}\right)\gamma \end{cases}$	Eq. 2-3
Base geometry		Constant cross-section area	
Ellipse		$\begin{cases} x = R\left(AR^{\left(sin\left(\frac{2\pi}{p}z\right)\right)}\right) \\ y = R\left(AR^{\left(-sin\left(\frac{2\pi}{p}z\right)\right)}\right) \end{cases}$	Eq. 2-4
Super-ellipse		$\begin{cases} x = \left(R\left(AR^{\left(sin\left(\frac{2\pi}{p}z\right)\right)}\right)\right)\gamma \\ y = \left(R\left(AR^{\left(-sin\left(\frac{2\pi}{p}z\right)\right)}\right)\right)\gamma \end{cases}$	Eq. 2-5

Where R is a radius of an equivalent straight tube, AR is an aspect ratio between the x and y axes, p is the corrugation period, z is tube length in a flow direction and γ is a scaling factor for super-

ellipse-based tubes given in Eq. 2-6. The scaling factor $\gamma = 0.963$ was used to ensure constant D_h and A_c of the super-ellipse-based DCTs, reported in this thesis.

$$\gamma = n^{\left(\frac{2-n}{2^{(1.44\,n)}}\right)}$$

Eq. 2-6

It is noticeable that a circle and a super-ellipse of the same radius R, have different D_h and A_c. In order to create a super-ellipse with similar D_h and A_c values as ones of a circle, a scaling factor γ is introduced. Thus, it is possible to construct a super-ellipse-based double corrugated tube having same D_h and A_c values by referring to an equivalent R of a straight tube.

The single expression of γ was used for generating SEDH and SEAC tubes since the hydraulic diameter is a linear function of γ and the cross-section area is a quadratic function of γ. This is seen from Eqs. 2-7 - 2-14. A cross-section of an ellipse is given in Eq. 2-7. When the scaling factor γ is applied, Eq, 2-7 becomes as given in Eq. 2-8. After some arithmetic operations and simplification, it is seen that a cross-section area of a super-ellipse is a quadratic function of a scaling factor γ as it is given in Eq. 2-9.

$$A_{c,E} = \pi\,x\,y$$

Eq. 2-7

$$A_{c,SE} = \pi\,(x\gamma)\,(y\gamma)$$

Eq. 2-8

Where a subscript *SE* denotes super-ellipse.

$$A_{c,E} = \frac{A_{c,SE}}{\gamma^2}$$

Eq. 2-9

The perimeter of an ellipse, P_E, is given in Eq. 2-10 [129].

$$P_E \approx 2\pi\,\sqrt{\frac{1}{2}(x^2 + y^2)}$$

Eq. 2-10

When γ is applied here, Eq. 2-10 becomes as given in Eq. 2-11.

$$P_{SE} \approx 2\pi\,\sqrt{\frac{1}{2}((x\gamma)^2 + (y\gamma)^2)}$$

Eq. 2-11

Then, the relation between P_E and P_{SE} is as given in Eq. 2-12; demonstrating that perimeter of a super-ellipse is a linear function of γ.

$$P_E = \frac{P_{SE}}{\gamma}$$

Eq. 2-12

Finally, hydraulic diameter of any non-circular geometry is expressed as given in Eq. 2-13.

$$D_h = \frac{4A_c}{P}$$

Eq. 2-13

Substituting Eqs. 2-9 and 2-12 into Eq. 2-13, it is seen that a hydraulic diameter of a super-ellipse is a linear function of γ, as it is shown in Eq. 2-14. Therefore, a single scaling factor γ could be used for corrections.

$$D_{h,SE} = \gamma D_{h,E} \qquad \text{Eq. 2-14}$$

The DCTs were generated in *SolidWorks* using the *Parametric equation* tool for defining the longitudinal surface of these tubes. The *Lofted Boss/Base* feature was used to generate a solid body using the *Guide curves* (surface equations) and given *Profiles* (start and end geometries). It must be mentioned that an option to draw an ordinary ellipse (with $n = 2$) already exist in *SolidWorks*. However, a super-ellipse shape must be provided manually. It is seen in Eq. 2-1, that whenever $2/n$ is a non-natural number, a solution of Eq. 2-1 has an imaginary part, which is ignored by *SolidWorks*. Thus, a drawing a full cross-section ($0 \le t \le 2\pi$) of a super-ellipse cannot be generated. Therefore, a quarter of a cross-section of a super-ellipse, which is in the first quadrant of Cartesian coordinates, was drawn in *SolidWorks*. Then it was mirrored on x- and y-axes, as it is shown in Figure 2-2. In this way, a full cross-section of a super-ellipse was obtained for every super-ellipse-based double corrugated tube.
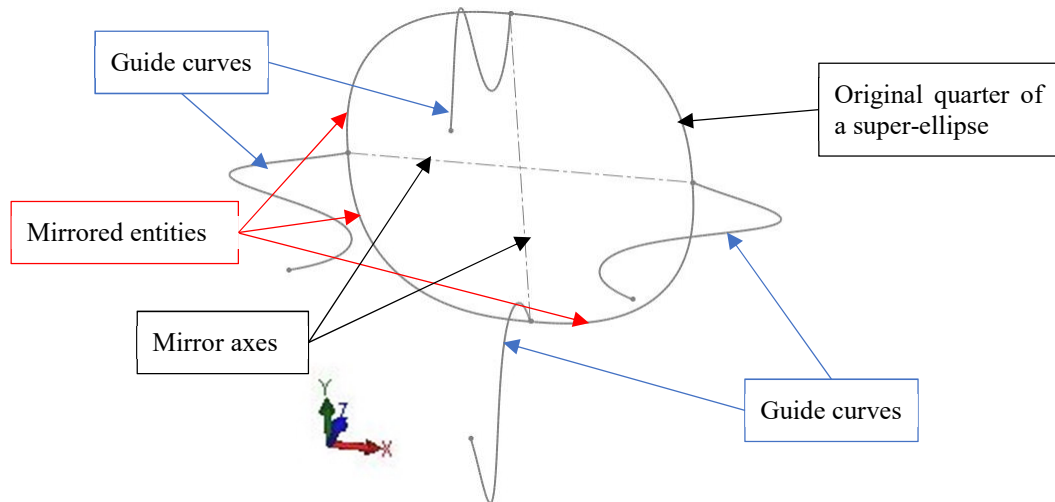
Figure 2-2. SEDH $AR = 2.2$ p =7.5 mm base geometry generated in *SolidWorks* using *Parametric equations* tool.

Double corrugated tubes are based on an elliptical cross-section with x and y axes. The AR of x and y is changing in the longitudinal direction z, while D_h or A_c is maintained constant. A closer look at Eqs. 2-2 – 2-5 reveals that x and y axes each half of the period, p, became equal forcing DCTs to their initial base shape. Thus, EDH and EAC tubes each half of a period have a circular cross-section; and SEDH and SEAC tubes have a shape of a symmetrical super-ellipse.

It must be mentioned that the equations, given in Table 2-1, as well as *SolidWorks* only approximate the desired geometry. The maximum deviation from the constant D_h or constant A_c is $\pm$ 4 % due to inaccuracies inherited from the surface equations. The maximum $\pm$ 7 ‰ of inaccuracy is calculated for tubes with constant A_c and $\pm$ 1 ‰ with constant D_h due to geometry approximations in *SolidWorks*. Table 2-2 shows inaccuracies of geometries built in *SolidWorks* that were used for numerical analysis. Note that data of few geometries are provided in Table 2-2 in order to avoid clutter. It is seen that inaccuracies decrease with increasing p or decreasing AR. Moreover, the DCTs designed to hold the D_h constant show significantly lower inaccuracy in value of D_h than in A_c and vice versa. This means that the derived surface equations fulfils the initial requirements they were designed for. It is also noticeable that super-ellipse-based tubes demonstrate lower change in both D_h and A_c than

ellipse-based. Since the maximum inaccuracy in constructed geometry was ± 5 %, it is considered to be acceptable. Thus, hydraulic diameter and cross-section area of DCTs are considered constant for further analysis.

Table 2-2. Inaccuracies in several double corrugated tubes generated due to geometry approximation in *SolidWorks*.

Tube name	p, mm	Distance with respect to p	A_c, mm²	P, mm	D_h, mm	Max. inaccuracy in D_h, %	Max. inaccuracy in A_c, %
EDH AR = 1.2	5	0	19.62	15.71	5.00	0.00	0.00
		1/6	19.78	15.86	5.00	-0.14	0.81
		2/6	19.75	15.84	5.00	-0.16	0.66
		3/6	19.69	15.73	5.00	0.23	0.36
		4/6	19.78	15.85	4.99	-0.08	0.81
		5/6	19.80	15.86	4.99	-0.04	0.91
		1	19.62	15.71	5.00	0.00	0.00
	7.5	0	19.62	15.71	5.00	0.00	0.00
		1/6	19.78	15.86	5.00	-0.14	0.81
		2/6	19.80	15.86	4.99	-0.04	0.91
		3/6	19.63	15.71	5.00	0.05	0.05
		4/6	19.77	15.85	5.00	-0.13	0.76
		5/6	19.80	15.86	4.99	-0.04	0.91
		1	19.62	15.71	5.00	0.00	0.00
	50	0	19.62	15.71	5.00	0.00	0.00
		1/6	19.79	15.86	4.99	-0.09	0.86
		2/6	19.79	15.86	4.99	-0.09	0.86
		3/6	19.63	15.71	5.00	0.05	0.05
		4/6	19.79	15.86	4.99	-0.09	0.86
		5/6	19.78	15.86	5.00	-0.14	0.81
		1	19.62	15.71	5.00	0.00	0.00
EDH AR = 2.2	5	0	19.62	15.71	5.00	0.00	0.00
		1/6	21.66	18.04	4.80	-4.02	9.42
		1/4	23.11	19.11	4.84	-3.27	15.10
		2/6	23.29	18.60	5.00	0.26	15.76
		3/6	21.87	16.80	5.21	4.06	10.29
	7.5	0	19.62	15.71	5.00	0.00	0.00
		1/6	21.90	18.15	4.83	-3.50	10.41
		2/6	22.81	18.44	4.95	-0.96	13.99
		3/6	21.17	16.41	5.16	3.19	7.32
	50	0	19.62	15.71	5.00	0.00	0.00
		1/6	22.18	18.21	4.87	-2.53	11.54
		2/6	22.21	18.21	4.88	-2.40	11.66
		3/6	19.73	15.75	5.01	0.30	0.56
EAC AR = 2.2	5	0	19.62	15.71	5.00	0.00	0.00
		1/6	19.95	17.28	4.62	-8.17	1.65
		1/4	20.24	17.80	4.55	-9.83	3.06
		2/6	20.58	17.49	4.71	-6.14	4.66
		3/6	20.71	16.18	5.12	2.43	5.26
SEDH AR = 2.2	5	0	19.54	15.74	4.97	-0.60	-0.41
		1/6	21.76	17.90	4.86	-2.73	9.83
		1/4	23.04	18.86	4.89	-2.23	14.84
		2/6	23.10	18.48	5.00	0.09	15.06
		3/6	21.63	16.95	5.10	2.13	9.29
SEAC AR = 2.2	5	0	19.58	15.76	4.97	-0.52	-0.20
		1/6	20.02	17.18	4.66	-7.17	2.00
		1/4	20.33	17.69	4.60	-8.67	3.49
		2/6	20.53	17.40	4.72	-5.85	4.43
		3/6	20.56	16.28	5.05	1.11	4.57

In Figure 2-3, the top view of the designed double corrugated tubes with different base geometries and AR is presented. Generally, DCTs with A_c constant have shorter major-axes than tubes with D_h constant, when comparing tubes with the same AR. The difference in the length of the major-axes becomes more noticeable with increased AR. This results in more strongly deformed flow channels along the z direction. Therefore, it is expected to have higher increase in heat transfer in DCTs with constant D_h accompanied by higher friction factor than in ones with constant A_c.

	AR = 1.2	*AR* = 1.4	*AR* = 1.6	*AR* = 1.8	*AR* = 2.0	*AR* = 2.2
EDH	5,56	6,02	6,53	7,04	7,54	8,01
SEDH	5,35	5,75	6,23	6,75	7,19	7,73
EAC	5,53	5,99	6,34	6,73	7,12	7,47
SEAC	5,32	5,75	6,11	6,42	6,95	7,11
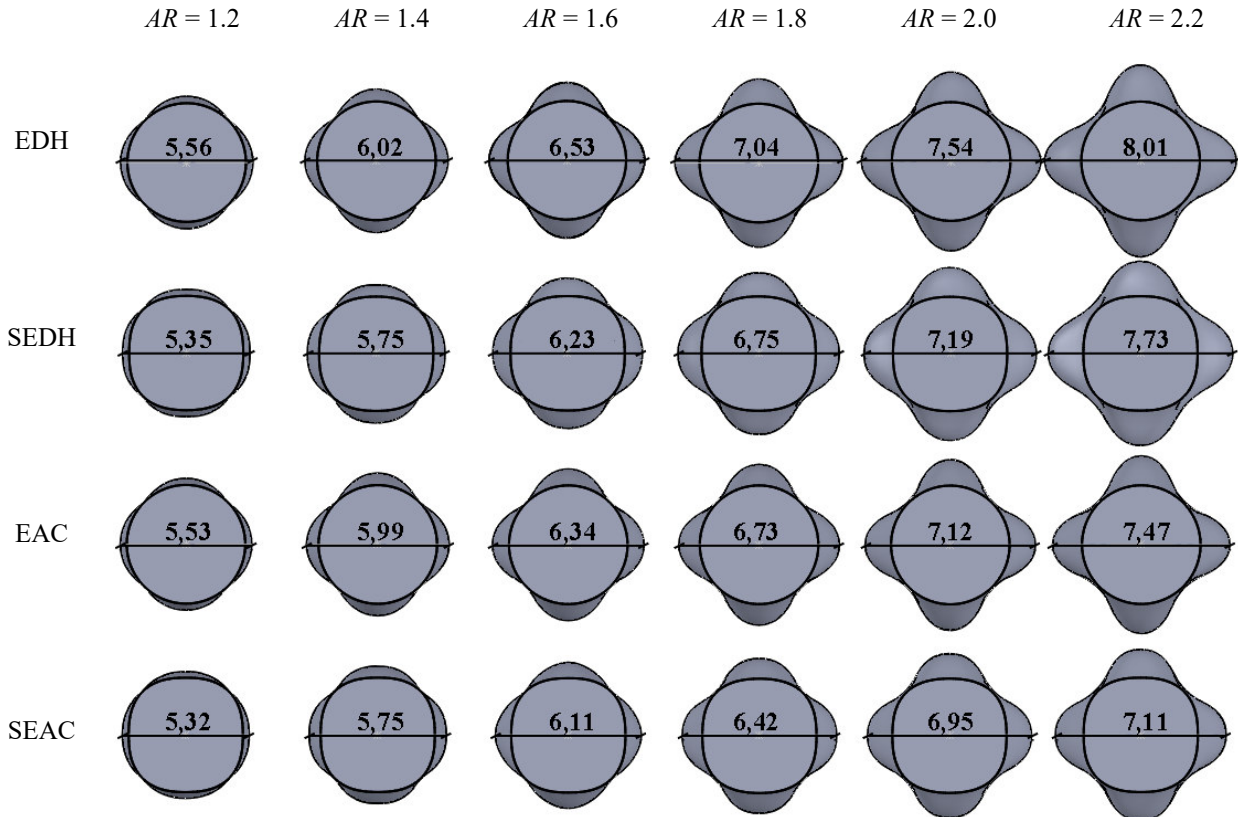
Figure 2-3. Top view of double corrugated tubes with different base geometry and aspect ratio.

All of the double corrugated tubes, presented in Figure 2-3, were constructed with period, p, of 5, 7.5, 10, 20, 40 and 50 mm for numerical analysis using commercially available CFD software *Comsol Multiphysics*. Several selected tubes were constructed with p of 75, 100, 150 and 200 mm for more detail analysis. Figure 2-4 presents the double corrugated tubes that were manufactured for experimental investigation. From Figure 2-4, it is seen how a period length affects the corrugation of tubes.

(a) (b) (c) (d) (e) (f) (g) (h)
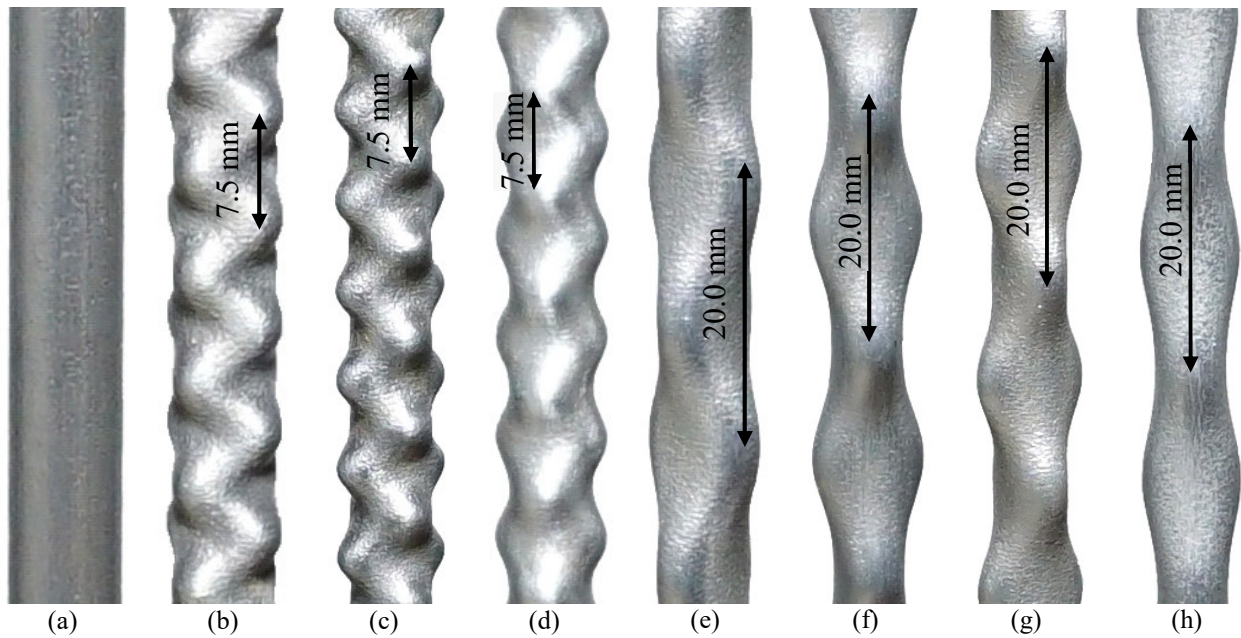
Figure 2-4. The 3D printed tubes (a) the straight tube, (b) EDH *AR* = 1.6 *p* = 7.5 mm, (c) EDH *AR* = 2.0 *p* = 7.5 mm, (d) EAC *AR* = 2.0 *p* = 7.5 mm, (e) EDH *AR* = 1.6 *p* =20.0 mm, (f) EDH *AR* = 2.0 *p* = 20.0 mm, (g) EDH *AR* = 2.2 *p* = 20.0 mm, (h) EAC *AR* = 2.2 *p* = 20.0 mm.

Detailed presentation of the developed CFD model and the obtained results of CFD analysis are presented in Section 2.3. The discussion on the approach of experimental analysis and selection of the tubes as well as obtained results is given in Section 2.4.

2.3. Numerical modelling

The designed double corrugated tubes were numerically analysed using the CFD software *Comsol Multiphysics*. The purpose of the modelling was to evaluate the performance of the double corrugated tubes and compare it with the performance of an equivalent straight tube at the same working conditions. The obtained modelling results served as the criterion for selecting the best performing tubes for the experimental investigation.

2.3.1. Boundary conditions and governing equations

From the application point of view, enhanced heat transfer techniques are on high demand in industries where medium or high viscosity fluids are used, such as food industry [130]. There fluid flow is necessarily laminar. Additionally, the flow of heat transfer fluid in an AMR regenerator is also always laminar since very small flow channels that normally are in a size range of few hundred microns [6,62]. However, the heat transfer fluid used in the AMR technology is mostly aqueous solution of a corrosion inhibitor, i.e. ethylene glycol or ENTEK FNE, which was used as the heat transfer fluid for testing AMR geometries, presented in Chapter 4. These solutions normally contain a small amount of an anticorrosion inhibitor, thus, water was selected as heat transfer fluid for CFD modelling. Laminar flow regime was considered for CFD analysis of the DCTs. Furthermore, fully developed flow condition was analysed in order to separate effects on heat transfer caused by the entry region and the double corrugated geometry. In order to implement the fully developed laminar flow, the periodic pressure drop, *Δp*, boundary condition (BC) was applied. Therefore, the performance of the DCTs was analysed at constant pressure drop. Finally, the SIMPLE algorithm was used to couple the steady-state equations for non-isothermal flow. The incompressible fluid flow with constant

properties at constant wall temperature, T_w, was analysed. The governing equations were formulated in Cartesian coordinates. Then, continuity, momentum conservation and energy equations are formulated as in Eqs. 2-15, 2-16 and 2-17, respectively. Note, that energy equation is formulated neglecting pressure work and viscous dissipation.

$$\nabla \cdot \boldsymbol{u}=0 \qquad\qquad \text{Eq. 2-15}$$

Where **u** is the fluid velocity vector.

$$-\rho\,(\boldsymbol{u} \cdot \nabla\boldsymbol{u})= \nabla p - \mu\nabla^2\boldsymbol{u} \qquad\qquad \text{Eq. 2-16}$$

Where ρ is fluid density, μ is fluid dynamic viscosity and p is the pressure field.

$$\rho c_p\boldsymbol{u}\,\nabla T= \nabla\cdot(k\,\nabla T) \qquad\qquad \text{Eq. 2-17}$$

Where c_p is fluid specific heat capacity, T is temperature, k is fluid thermal conductivity.

The inner side of the tubes was modelled, meaning that only a fluid domain was considered. In practice, a layer of a real fluid is always attached to a solid wall and has zero velocity [131]. To model this phenomenon, a non-slip BC was imposed as given in Eq. 2-18.

$$\boldsymbol{u}\cdot\boldsymbol{n}=\boldsymbol{U}\cdot\boldsymbol{n} \qquad\qquad \text{Eq. 2-18}$$

Where **U** is the velocity vector of a solid and **n** is the unit normal to the surface of the solid.

Finally, *Comsol Multiphysics* uses finite element method for solving heat transfer in fluids problems. The second order element discretisation for velocity field and linear discretisation for the pressure field, P2+P1, was applied. All the modelled cases were solved using *PARDISO* solver with relative tolerance of 10^{-6}. The initial modelling conditions are summarised in Table 2-3. The visualisation of the implemented BCs is provided in Figure 2-5.

Table 2-3. The initial conditions for CFD modelling.

D_h, [mm]	ρ, [kg/m³]	$\Delta p/l$, [Pa/m]	T_i, [K]	T_w, [K]	c_p, [J/(kg K)]	μ, [Pa s]	k, [W/(m K)]	Pr, [-]
5	1000	[246; 164; 82; 16]	303	281	4183	8 e-4	0.603	5.5
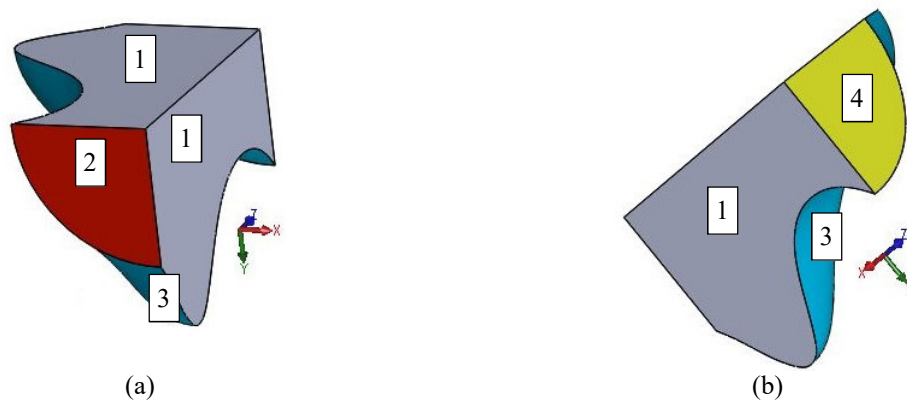
Figure 2-5. Visualization of the boundary conditions applied on the modelled geometries. (a) 1 is symmetry boundary conditions; 2 is inlet with T_i, 3 is wall temperature, T_w. (b) 4 is outlet.

When comparing DCTs with an equivalent straight tube, the length of the tubes was hold constant rather than an area of a heat transfer surface. It is important to emphasise that the surface

area, A_s, of DCTs increases up to 34 % compared to equivalent straight tubes. From Figure 2-6, it is seen that surface increases more for DCTs with constant D_h than for those with constant A_c. The surface area for super-ellipse-based DCTs show the same tendency as for ellipse-based DCTs. The maximum increase in A_s is for EDH and SEDH type of tubes, then follows EAC and lastly SEAC showing values of 34 %, 26 % and 25 %, respectively. In order to maintain Figure 2-6 readability, DCTs with $p < 50.0$ mm were omitted from the figure. Moreover, the ratio between A_s and A_{s_0} show asymptotical decrease with increasing p.
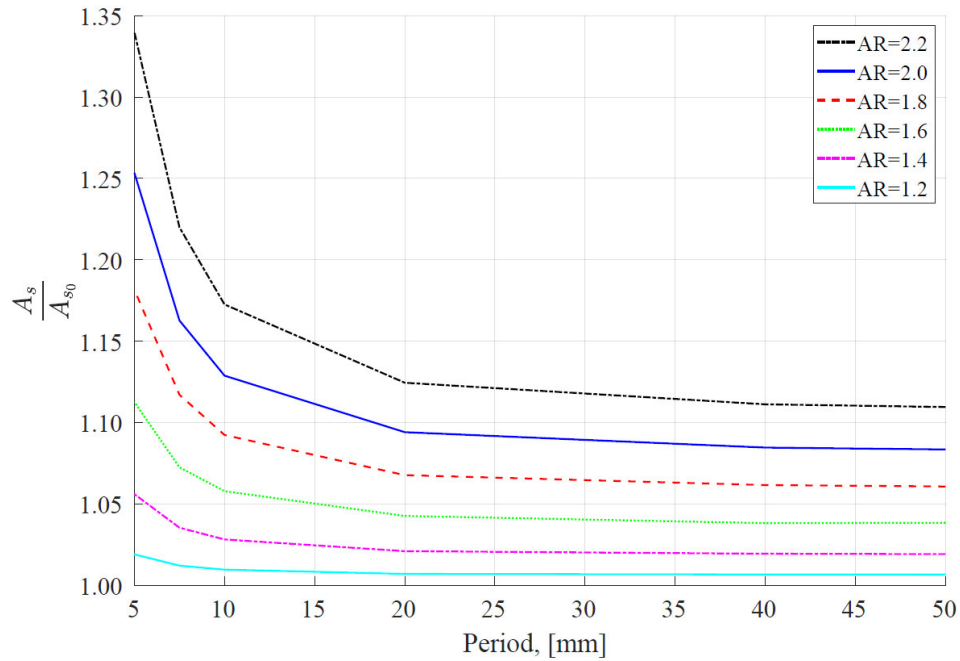
(a)
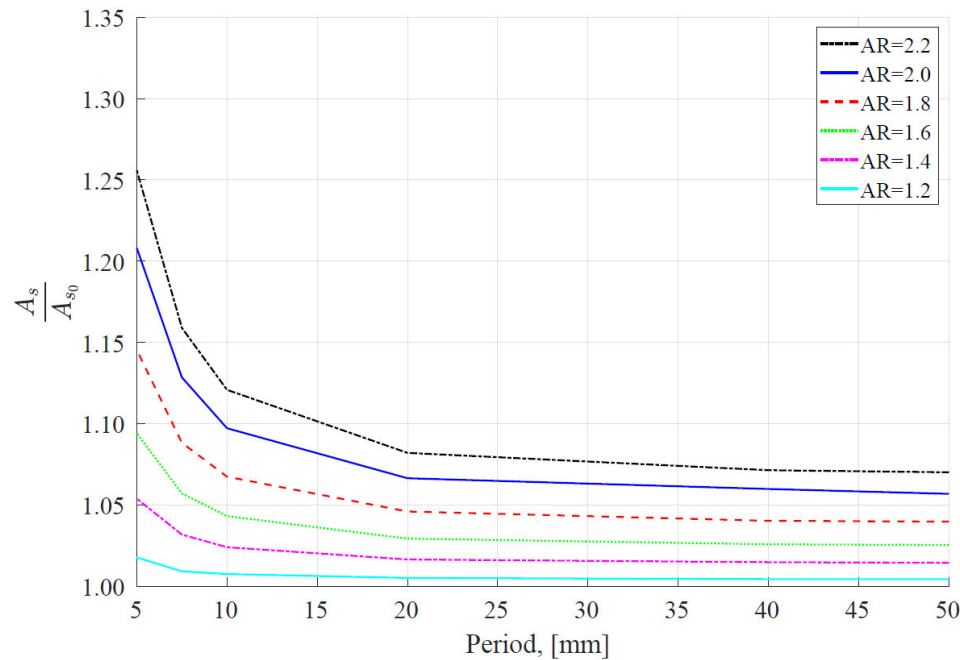
(b)

Figure 2-6. Ratio of A_s/A_{s0} for (a) EDH tubes and (b) EAC tubes.

Few Δp values were used to model several selected DCTs while other BCs remained unchanged. One can note from Table 2-3, that the imposed temperature difference between the inlet and the wall of a tube is rather low. Selection of such a small temperature difference lies in the nature of the considered applications. As mentioned in Section 1.2, the temperature difference created by an AMR is rather low, energy, provided by many renewable sources, is available at low temperature too, e.g. heat recovery from wastewater.

In summary, fully hydraulically developed laminar incompressible flow with constant properties was modelled with constant surface temperature conditions.

2.3.2. Mesh and model validation

The geometry of DCTs implies that numerical analysis should be carried out using a 3D model. Therefore, a full-length model of each tube would require huge computational resources. Thus, several measures were considered to increase computational efficiency. One of them is a symmetry BC. Every DCT has two symmetry planes along the z-axis. Consequently, a quarter of a cross-section of each tube was modelled using the symmetry BC. Another possibility to lower computational cost is a periodic BC. It was shown that for the analysis of a fully thermally and hydraulically developed flow, it is sufficient to model a single period of a geometry of interest [132,133]. However, only fully hydraulically developed fluid flow is considered in this thesis. Nevertheless, to find out whether one period of a corrugated tubes is sufficient for thermal analysis, few double corrugated tubes with different AR and p were modelled with varying number of their periods. Several lengths of a straight tube were modelled for comparison. The obtained modelling results were compared with the analytical solutions calculated for each modelled case as presented in Figure 2-7.
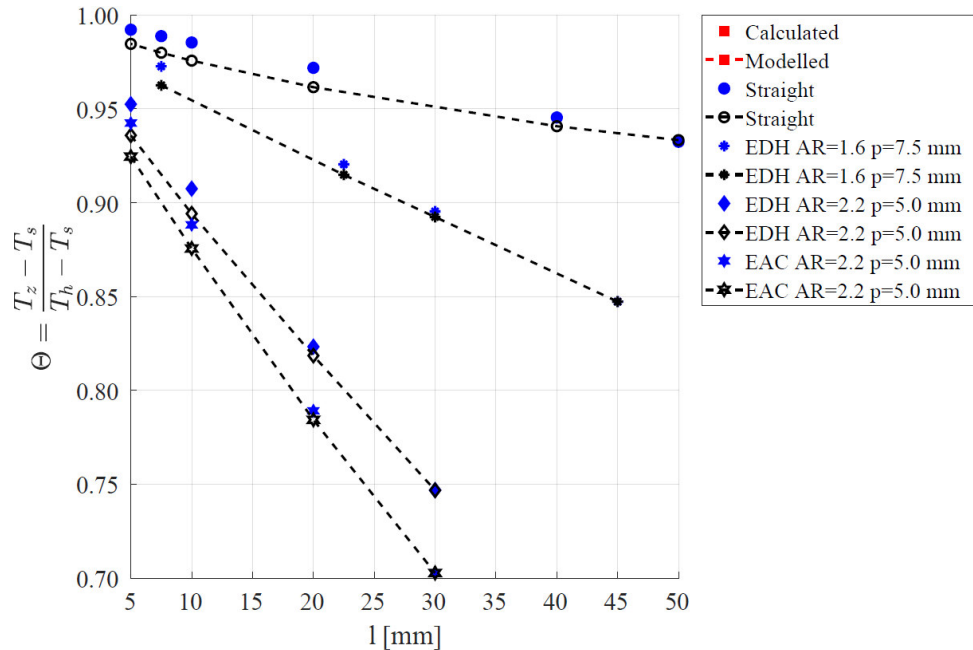
Figure 2-7. Temperature difference at the outlet of an ellipse-based DCTs and a straight tube at different modelled number of periods or lengths.

In order to find an analytical solution of an outlet temperature, T_o, of each investigated tube at intermediate length between its inlet and outlet, it is necessary to know a local heat transfer coefficient, $\bar{h}$, given in Eq. 2-23. The coefficient $\bar{h}$ was obtained from the modelling results of the longest analysed

case for each tube. Then, T_o was integrated for every point of interest within a corresponding tube length. The dimensionless temperature, θ^*, was calculated as given in Eq. 2-19 [134].

$$\theta^* = \frac{T_o - T_w}{T_i - T_w}$$

Eq. 2-19

Where T is temperature, and subscripts i, o and w are inlet, outlet and wall, respectively.

In Figure 2-7, it is seen that analytically calculated and modelled values agree reasonably well. The maximum difference between calculated and modelled T_o is 0.39 K in the worst case. It must be explained, that the slight disagreement at the short length of the analysed tubes is due to the nature of heat transfer. It is well-known that the temperature in a flow direction decays exponentially. An average local heat transfer coefficient is also much higher at the entry of a tube and decreases in non-linear manner. Consequently, integration for T_o using lower $\overline{h}$ value, provides somewhat elevated results. Nevertheless, it was concluded, that one period of a geometry of interest is sufficient to conduct thermal analysis as well. Thus, one period of a quarter of a cross-section of each DCT and a corresponding length of an equivalent straight tube were modelled for thermo-hydraulic investigation.

Another promising finding, seen in Figure 2-7, is potential of the double corrugated tubes to transfer heat more efficiently. The temperature gradient is significantly steeper for DCTs than for an equivalent straight tube. This implies that heat transfer is intensified in DCTs.

A mesh sensitivity analysis was carried out for a straight tube and each DCT that has the highest AR and shortest p at each group. A swept mesh with two boundary layers, BL, and tetrahedral elements was used to mesh all the tubes for this investigation. An average Nusselt number, $\overline{Nu}$, defined in Eq. 2-25, was selected as the control quantity to evaluate a mesh. Relative errors, err, of $\overline{Nu}$ were calculated as using Eq. 2-20 [135].

$$err = 100 \left| \frac{\overline{Nu_c} - \overline{Nu_f}}{\overline{Nu_f}} \right|$$

Eq. 2-20

Where subscripts c and f denote the coarsest and the finest meshes, respectively.

In order to evaluate the element number used for constructing a mesh consistently for all the analysed tubes, a concept of element density was used. It is clear that volume of an analysed geometry changes with its AR and p values. Several different sizes of meshes for each tube with the element density from 800 to 4372 el./mm³ were analysed. Figure 2-8 shows that mesh-independent solutions were reached when mesh resolution was between 2000 and 3000 el./mm³ depending on the tube type. It must be mentioned that a mesh finer than 2500 el./mm³ was used for modelling all the tubes. Moreover, the relative errors in using the finest and the selected mesh were less than 0.5 %, concluding that the accuracy of numerical models was sufficient for further analysis. Note that the reported err value was the maximum obtained for all the analysed tubes.
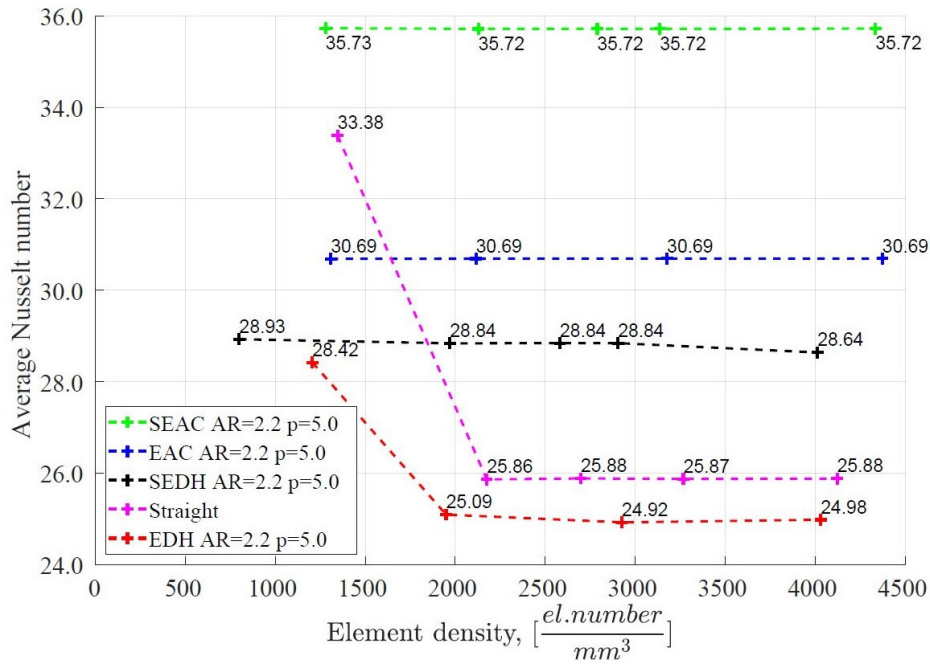
Figure 2-8. The results of the study of mesh independency.

After the mesh sensitivity analysis, it was investigated whether two BLs are sufficient for a precise analysis of near wall fluid flow. Thus, simulations of a straight tube with five, seven and ten BL were conducted. After applying error analysis routine as described above, it was concluded that higher number of BL does not provide a more accurate solution. The maximum obtained error was *err* = 0.006 %. Thus, it was concluded that two BLs are sufficient for further analysis. Figure 2-9 shows the isometric view of a quarter of a cross-section of EDH *AR* = 2.2 *p* = 5.0 mm tube after being meshed in *Comsol Multiphysics*.
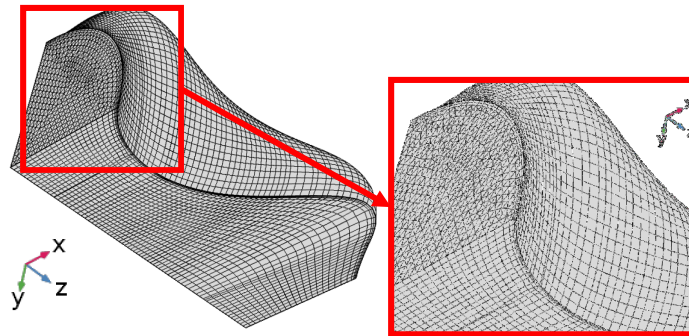
Figure 2-9. The isometric view of the EDH *AR* = 2.2 *p* = 5.0 mm tube after being meshed in *Comsol Multiphysics*. The boundary layers are shown in the zoomed in view.

The developed model was validated against the analytical solution of *Re* for a straight tube. Figure 2-10 demonstrates that the developed model is stable in a wide range of *Re*. It also demonstrates the perfect agreement between modelling results and analytical solution.
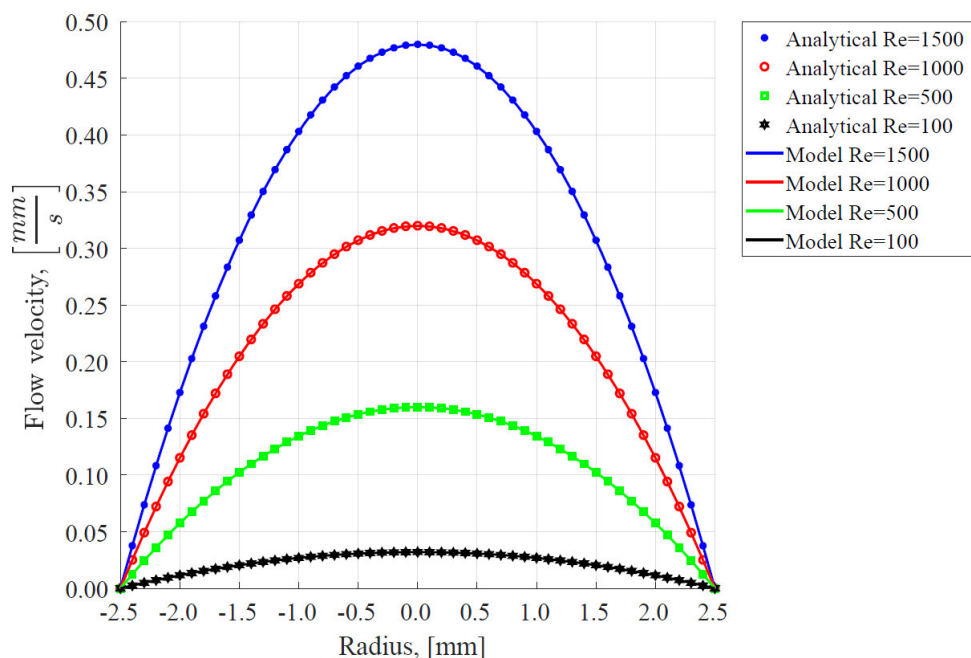
Figure 2-10. Model validation against analytical solution.

Finally, the modelling results agrees within 10 % of accuracy with the classical Hausen correlation at high *Re*, given in Eq. 2-21, for $\overline{Nu}$ at thermal entry region combined with fully hydraulically developed flow [136]. Moreover, the model agrees excellently with the Hausen correlation at low *Re*. $\overline{Nu}$ for the straight tube was calculated as described in Section 2.3.3. Thus, it was concluded, that the developed model is valid and suitable for further analysis.
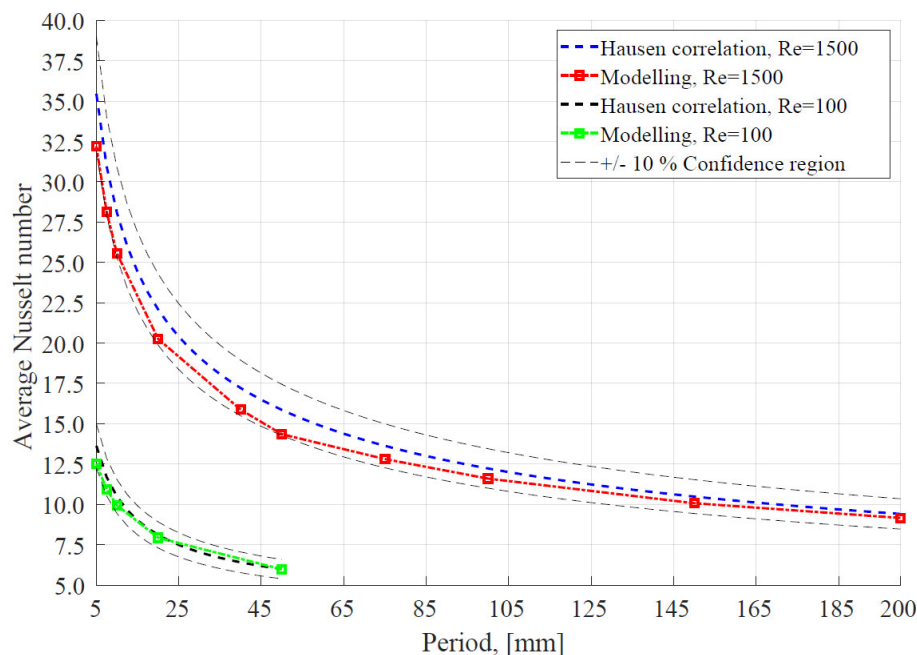
Figure 2-11. A comparison of modelling results obtained for a straight tube with a Hausen correlation.

$$\overline{Nu} = 3.66 + \frac{0.0668 \left(\frac{D_h}{l}\right) Re \, Pr}{1 + 0.04 \left(\left(\frac{D_h}{l}\right) Re \, Pr\right)^{2/3}}$$

Eq. 2-21

Where l is tube length, Pr is Prandtl number.

In addition, the mass and energy balances were calculated for every modelled case. The maximum obtained inaccuracy was less than 0.16 %. This means that all the developed models are sufficiently accurate.

2.3.3. Data analysis

The main input to the model was a length normalised pressure drop, Δp, i.e. all the modelling results were obtained for constant pressure drop. Then, the main outputs were the flow rate and the resulting temperature profile. These results were used to evaluate thermo-hydraulic performance of the DCTs in terms of average Nusselt number, $\overline{Nu}$, number of transfer units, NTU, method and performance evaluation criterion, $PEC_{\Delta p}$, that was evaluated at constant pressure drop. A comparison of a mass flow rate, $\dot{m}$, and required pumping power, W, was also performed.

It must be mentioned that the comparison of the performance of DCTs was carried out using nominal geometry. It is commonly accepted that a nominal geometry, in this case a straight tube, is used for evaluating the heat transfer enhancement in augmented geometries [137]. This becomes especially convenient when the analysed geometry could be used as a direct replacement for conventional solutions [137]. Indeed, the ellipse-based DCTs could be mounted in an existing tube-in-shell heat exchanger without any additional adjustments or fittings since their inlet and outlet shape is circular. On the other hand, the shape of inlets and outlets of the super-ellipse-based DCTs could be easily modified into a circular shape with a small reduction in length of a corrugated section before manufacturing tubes.

Parameters for the thermo-hydraulic analysis were calculated as defined in Eqs. 2-22 – 2-34. First off all, the net rate of outflow of thermal energy, q, was calculated as given in Eq. 2-22.

$$q = \dot{m} \, c_p (T_i - T_o)$$

Eq. 2-22

The average convective heat transfer coefficient, $\overline{h}$, was calculated as given in Eq. 2-23.

$$\overline{h} = \frac{q}{A_s \Delta T_{lm}}$$

Eq. 2-23

Where ΔT_{lm} is the log mean temperature difference, given in Eq. 2-24.

$$\Delta T_{lm} = \frac{\Delta T_o - \Delta T_i}{\ln \left(\frac{\Delta T_o}{\Delta T_i}\right)}$$

Eq. 2-24

Where $\Delta T_{o,i}$ is temperature difference between temperature of a tube wall, T_w, and the bulk temperature, T, at the tube outlet, o, and inlet, i, respectively.

Average Nusselt number, $\overline{Nu}$, was calculated as given in Eq. 2-25.

$$\overline{Nu} = \frac{\overline{h}D_h}{k_f} \qquad \text{Eq. 2-25}$$

Where k_f is thermal conductivity of water.

In order to avoid possible confusion, an explanation, how the BC of constant Δp was implemented, is provided here. The laminar fluid flow was selected for CFD analysis of the DCTs. This implies that Re must be not higher than 2100 [131] or 2300 [134] in a straight tube. In addition, it was not known beforehand how the double corrugation would affect fluid flow and what flow regime it would cause. It was reported in literature, that not suitable mathematical description of the flow regime prevents CFD models from convergence [102]. Therefore, the fluid flow with maximum Re of 1500 in a straight tube was selected for CFD analysis in this work. Then the friction factor in a straight tube, f_0, was calculated as given in Eq. 2-26 [131].

$$f_0 = \frac{64}{Re} \qquad \text{Eq. 2-26}$$

Then the corresponding pressure drop, Δp, was calculated for each modelled length, l, of a straight tube as given in Eq. 2-27. The obtained Δp values were applied for all the modelled DCTs with respect of their period, p, (modelled lengths).

$$\Delta p = f_0 \frac{\rho u_m^2 l}{2D_h} \qquad \text{Eq. 2-27}$$

Where u_m is a mean flow velocity.

As mentioned above, one of the outputs of the model, was a mass flow rate, $\dot{m}$. Then, mean flow velocity, u_m, was calculated as defined in Eq. 2-28 and the resulting friction factor in DCTs as given in Eq. 2-29.

$$u_m = \frac{\dot{m}}{A_c \, \rho} \qquad \text{Eq. 2-28}$$

$$f = \frac{2 \, \Delta p \, D_h}{\rho u_m^2 l} \qquad \text{Eq. 2-29}$$

In order to determine the potential of DCTs for enhancing heat transfer, number of transfer units, NTU, method was used for analysis, which is defined in Eq. 2-30.

$$NTU = -\ln(1 - \varepsilon) \qquad \text{Eq. 2-30}$$

Where ε is efficiency of a heat exchanger, which was calculated using Eq. 2-31.

$$\varepsilon = \frac{q}{q_{max}} \qquad \text{Eq. 2-31}$$

Where q_{max} is maximum possible heat transfer, which was calculated using Eq. 2-32.

$$q_{max} = \dot{m}c_p(T_i - T_s) \qquad \text{Eq. 2-32}$$

The global performance of the DCTs at constant pressure drop conditions was analysed using the performance evaluation criterion $PEC_{\Delta p}$, defined in Eq. 2-33 [65,103,137].

$$PEC_{\Delta p} = \frac{\overline{Nu}\Big/\overline{Nu_0}}{\left(f\big/f_0\right)^{1/3}}$$

Eq. 2-33

Where $\overline{Nu_0}$ is the average Nusselt number of a straight tube, based on simulation results and calculated using Eq. 2-22 – 2-25 and f_0 is the Darcy-Weisbach friction factor for a straight tube, given in Eq. 2-26.

The pumping power, W, required to maintain fluid flow of a given $\dot{m}$ at constant Δp was calculated using Eq. 2-34.

$$W = \frac{\dot{m}}{\rho}\Delta p$$

Eq. 2-34

For presentation purposes, the obtained modelling results were normalized with the results obtained for a corresponding length of an equivalent straight tube. Moreover, only selected results are presented and discussed in Section 2.3.4 in order to avoid clutter.

2.3.4. Results

The double corrugated tubes, regardless of their base shape, were analysed from two hydraulically different points of view, i.e. holding either hydraulic diameter constant, or cross-section area. The main characteristic of *hydraulic diameter* is that the pressure drop (momentum) of a flow is maintained constant [131]. Thus, the pressure drop should remain the same along the fluid flow in DCTs with D_h constant, resulting in varying mean flow velocity, u_m, at different cross-sections of these tubes. On the other hand, the constant cross-section area implies that u_m must remain the same along the flow channel, since the mass flow rate is constant. Thus, the pressure drop should fluctuate at different cross-sections of the DCTs with A_c constant. Figure 2-12 illustrates relative mean flow velocity, $u_{m,z}/u_m$, at point of interest, l_z, along the tube length, l. *Spline* function (in *Matlab*) was used for plotting purposes. It was found that the DCTs with same geometrical parameters but different base shape demonstrate similar behaviour from hydraulic point of view. The most intense velocity fluctuations were observed for DCTs with the highest aspect ratio, AR. Therefore, double corrugated tubes with varying periods were selected for presentation in Figure 2-12. As expected, DCTs with constant D_h demonstrate throttling effect on the flow velocity. A small fluctuation of the relative flow velocity is seen also for DCTs with constant A_c. This is due to geometrical inaccuracy reported in Section 2.2. It is noticeable that the fluctuations, caused by the geometrical inaccuracies, are the most intense in EAC and SEAC tubes with short p and high AR values.
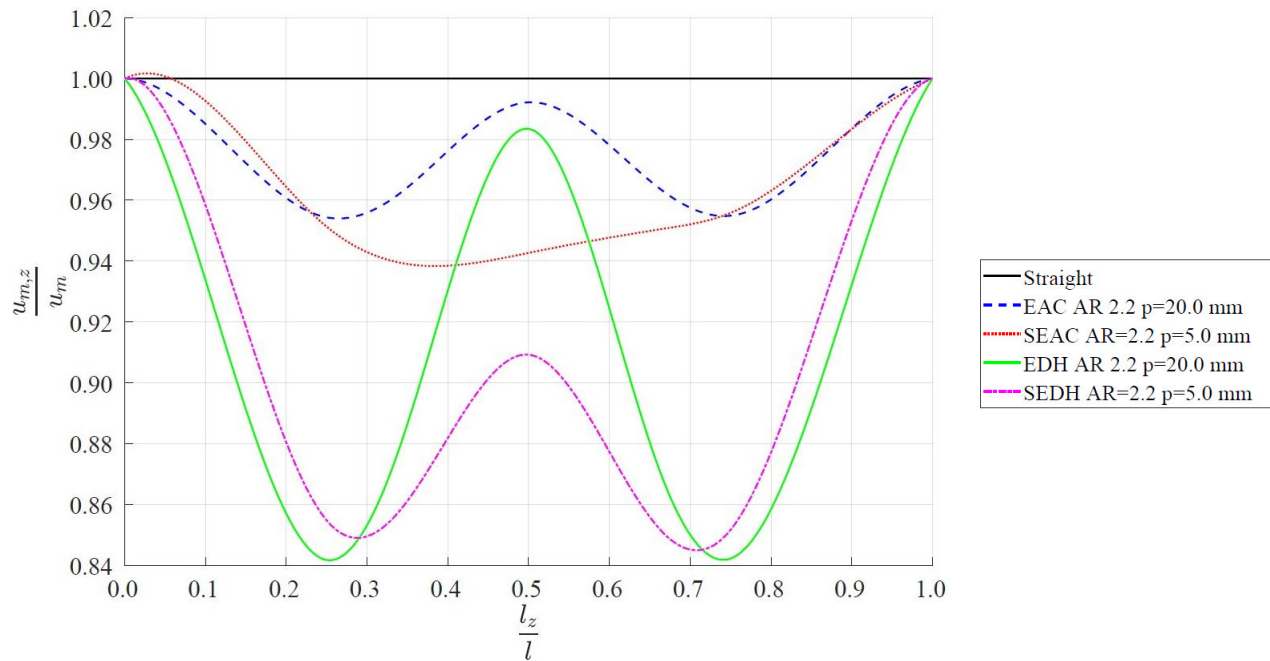
Figure 2-12. Relative mean flow velocity along the relative tube lengths.

The double corrugated geometry infringes the thermal boundary layers as well. This interruption causes fluid layer mixing and prevents thermal boundary layers from development. Note that the actual flow behaviour in DCTs is not well understood yet and here *fluid mixing* is used to describe an interruption of boundary layers rather than fluid transport in radial direction or stirring. Consequently, the heat transfer is enhanced over the entire channel of the fluid flow at increased flow resistance. In order to visualize this effect Figure 2-13 demonstrates the heat flux through the wall of EAC $AR = 2.2$ $p = 5.0$ mm and the equivalent straight tube at constant Δp. It is clear that, differently from a straight tube in Figure 2-13 (b), the heat transfer occurs through all the length of the EAC tube, while this phenomenon is the most intense at the inlet of the straight tube and gradually evanesces along the flow. It is also important to note, that the mass flow rate, $\dot{m}$, of the straight tube is more than four time higher than in the EAC tube. This proves that double corrugation efficiently enhances heat transfer with a penalty of reduced flow rate.

(a)
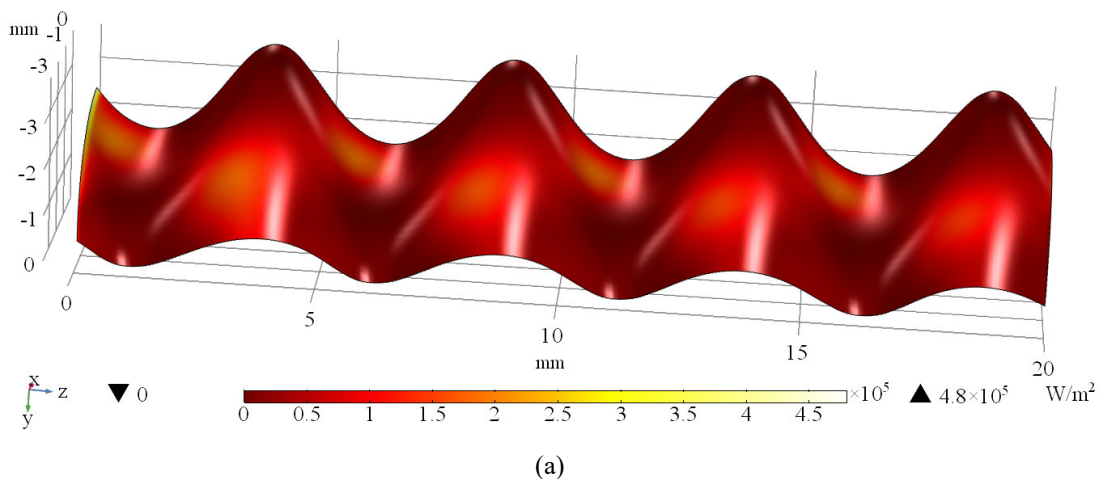
Figure 2-13. Heat flux through the wall of (a) EAC $AR = 2.2$ $p = 5.0$ mm tube (4 periods), $\dot{m} = 0.96$ kg/h, $\Delta p = 12.29$ Pa and (b) the equivalent straight tube with $l = 20$ mm, $\dot{m} = 4.24$ kg/h, $\Delta p = 12.29$ Pa.
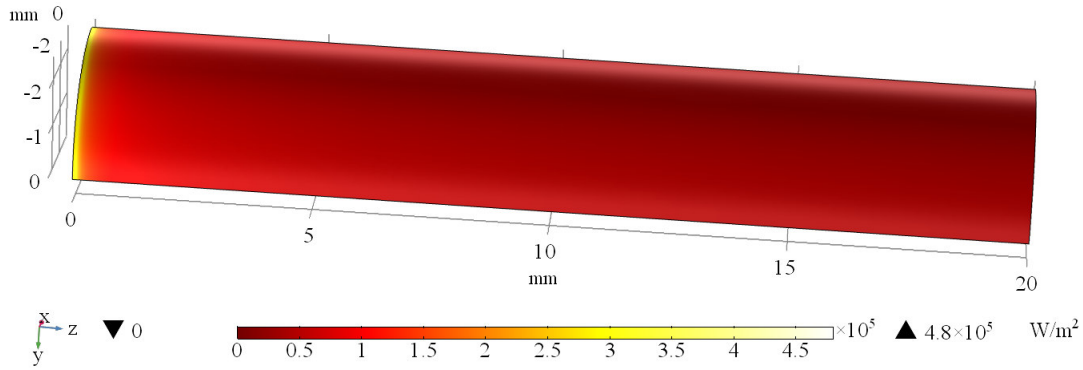
(b)

Figure 2-13. Continuation from the previous page.

Figure 2-14 demonstrates that the thermal gradient in an axial direction in double corrugated tubes is more inclined than in the equivalent straight tube indicating higher heat transfer in the previous case. Moreover, the sharp jump of the temperature difference at approx. $R_x/R = 0.5$ shows that wall corrugation actually pushes warmer fluid towards the tube wall. It should be noted, that the temperature profile was evaluated at the converging axes (y – axis) for both double corrugated tubes as it is seen in Figure 2-15 (b-1) and (c-1).
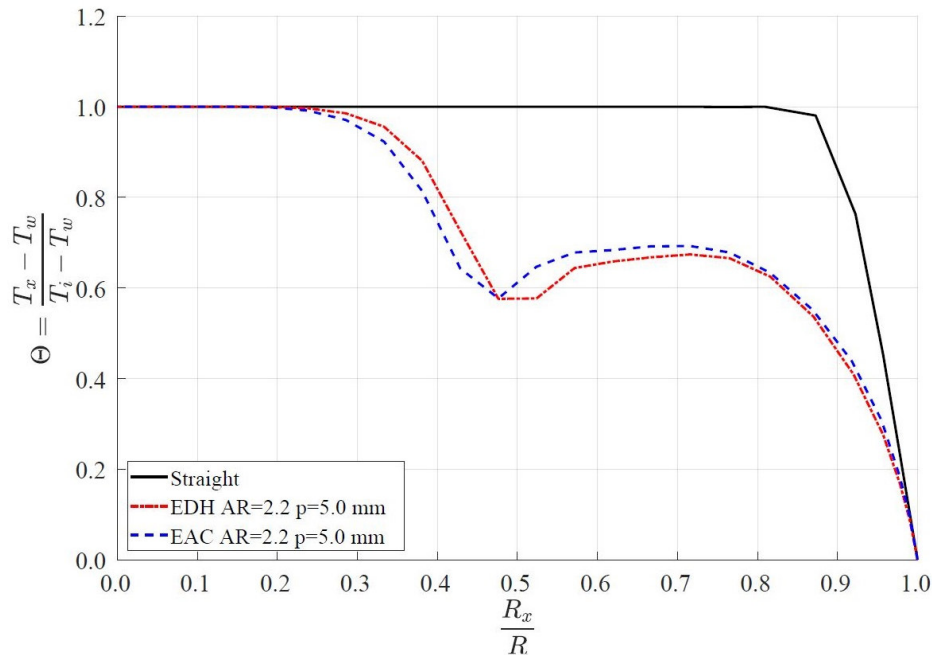
Figure 2-14. Temperature profile at the outlet of the straight, EDH AR = 2.2 p = 5.0 mm and EAC AR = 2.2 p = 5.0 mm.

From the 3D temperature and velocity fields, shown in Figure 2-15, it can be seen that double corrugated geometry contorts flow and induces fluid mixing, while flow in the straight tube is undisturbed. It is also noticeable from Figure 2-15 (b) and (c) that EAC and EDH tubes with the same geometrical characteristics affect fluid flow in the same manner. It must be mentioned that super-ellipse-based DCTs have the same effect on the fluid flow as corresponding ellipse-based DCTs. Thus, 3D temperature and velocity fields for these tubes were omitted from Figure 2-15. On the other hand, longer period causes less intense fluid mixing (Figure 2-15 (d)) and the flow behaviour becomes similar to behaviour in the equivalent straight tube.
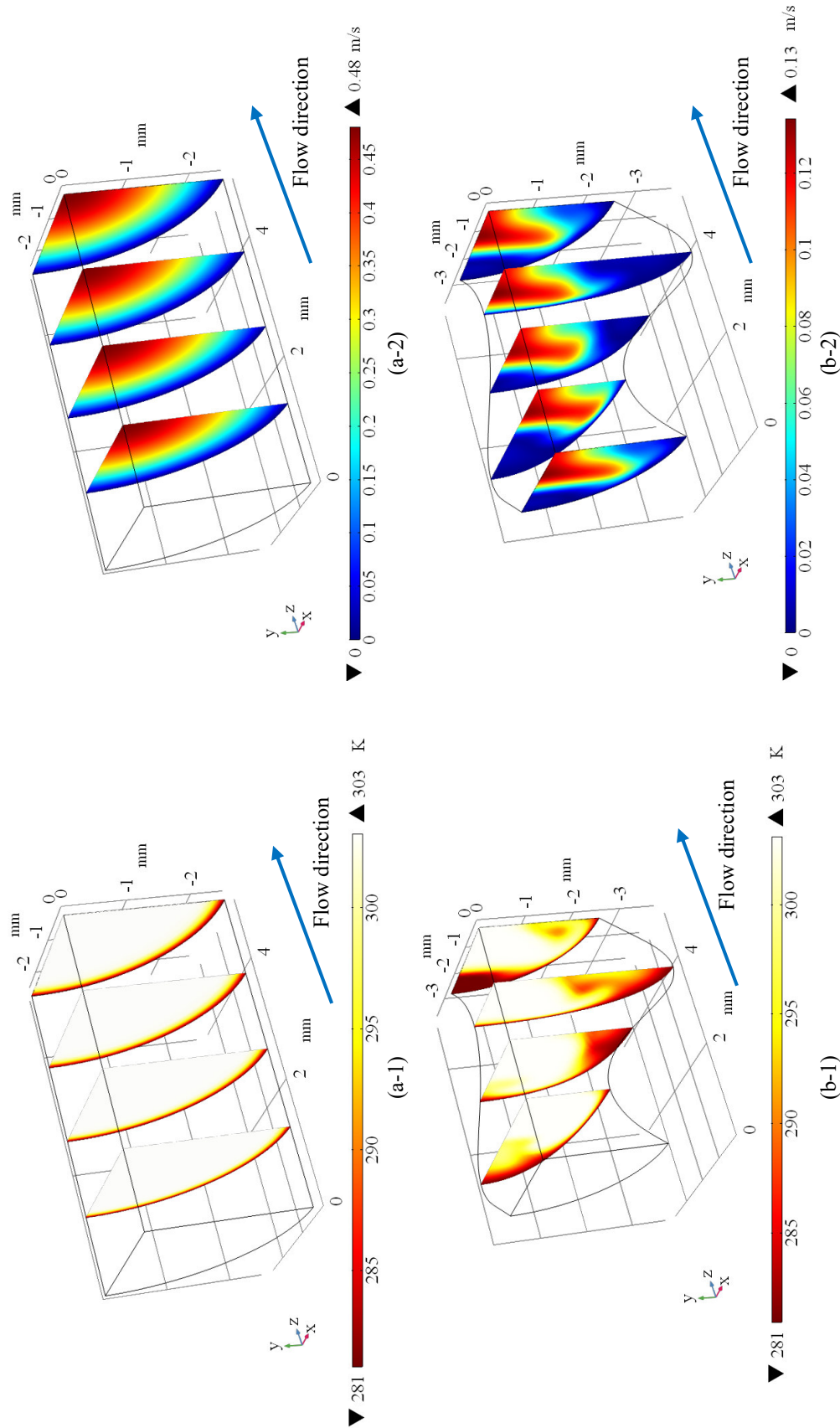
Figure 2-15. 3D temperature (1) and velocity (2) fields at $\Delta p/l = 246$ Pa/m (a) a straight tube $l = 5.0$ mm; (b) EAC $AR = 2.2$ $p = 5.0$ mm; (c) EDH $AR = 2.2$ $p = 5.0$ mm; (d) EDH $AR = 2.2$ $p = 10.0$ mm.
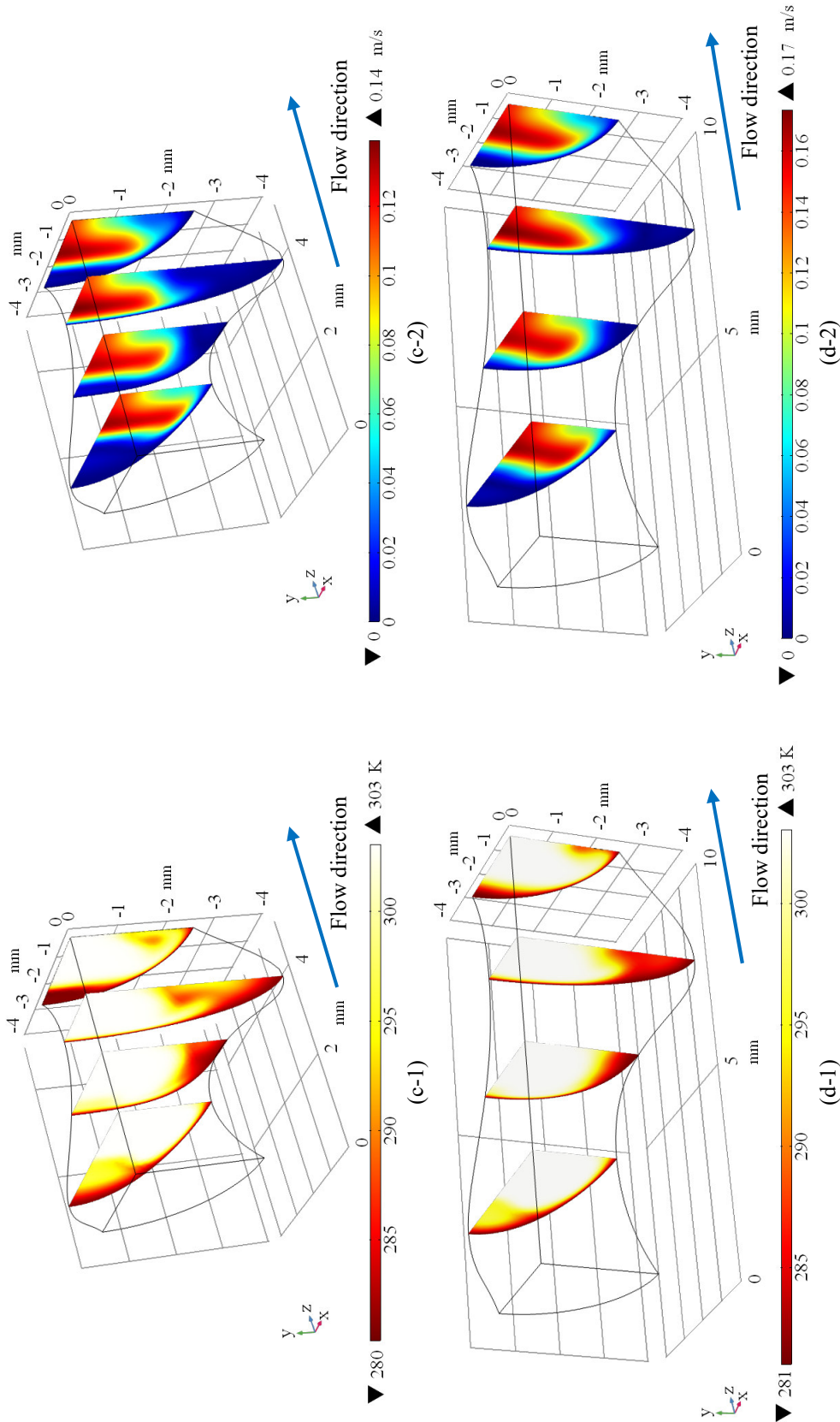
Figure 2-15. Continuation from previous page.

Figure 2-16 demonstrates that ratio of $\overline{Nu}$ increases with increasing AR and decreasing p values for DCTs and it is generally more than 20 % higher than for an equivalent straight tube. One can see that all the DCTs, presented in Figure 2-16, demonstrate higher or almost equal (EDH $AR = 1.6$ $p \leq$ 10.0 mm) thermal efficiency as an equivalent straight tube with less than a half of a pumping power required in the latter one. It is noticeable that super-ellipse and ellipse-based DCTs with same geometrical characteristics demonstrated nearly the same thermal performance. Furthermore, DCTs with constant D_h slightly outperform tubes with constant A_c when $p < 10.0$ mm considering the same AR value. Finally, the sharp decrease of the $\overline{Nu}$ ratio in the range from $p = 5.0$ mm to $p = 10.0$ mm and steep further increase is attributed to mixing of fluid flow. As it was demonstrated in Figure 2-15, fluid flow mixing becomes less intense when p is longer causing lower enhancement of heat transfer. Thus, the ratio of $\overline{Nu}$ decreases with increase of p until a critical value of p is reached. From that point, even a slight disturbance of thermal boundary layers caused by the geometry of DCTs is sufficient to noticeably increase ratio of $\overline{Nu}$, since the heat transfer gradually diminishes along the flow in relatively long straight tubes, as it was shown in Figure 2-13.
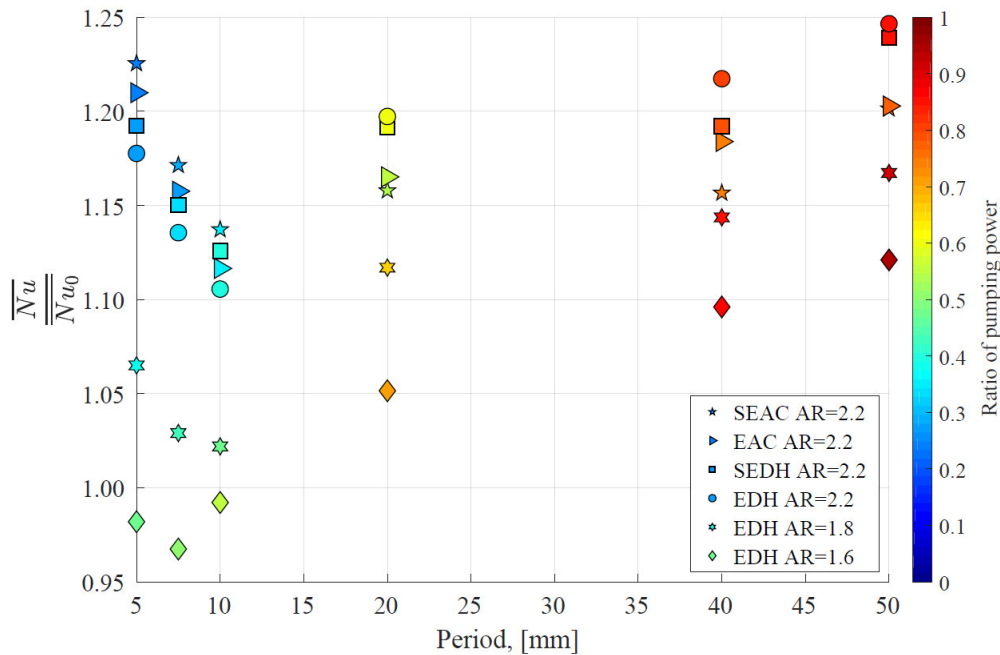
Figure 2-16. Ratio of $\overline{Nu}/\overline{Nu_0}$ as a function of a period, p, at $\Delta p/l = 246$ Pa/m.

Figure 2-17 shows the ratio between mass flow rate in DCTs, $\dot{m}$, and in equivalent straight tubes, $\dot{m}_0$, as a function of p, for the same DCTs, reported in Figure 2-16. Interestingly, the most severe mass flow reduction is obtained for DCTs with constant A_c, even though their geometry is somewhat smoother than of DCTs with constant D_h, as mentioned in Section 2.2. Again, it was found that DCTs with both ellipse and super-ellipse-based geometries perform similarly when comparing the same geometrical features.

Figure 2-18 demonstrates that DCTs are more than five times thermally more efficient than an equivalent straight tube at the constant Δp. It is also seen that DCTs provide up to 50 % higher thermal efficiency than an equivalent straight tube even when p values exceeds 40 mm. It is worth mentioning that, at this point, the length and hydraulic diameter ratio is $l/D_h \geq 8$, noting that from this point DCTs become relatively straight and no strong flow disturbance is expected.
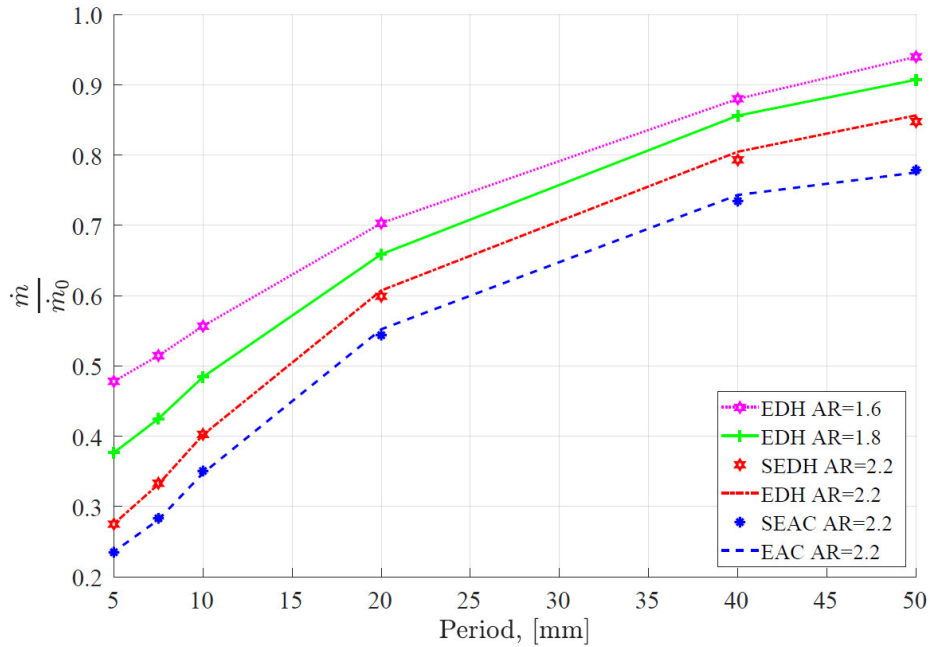
Figure 2-17. Ratio of $\dot{m}/\dot{m}_0$ as a function of a period at $\Delta p/l = 246$ Pa/m.
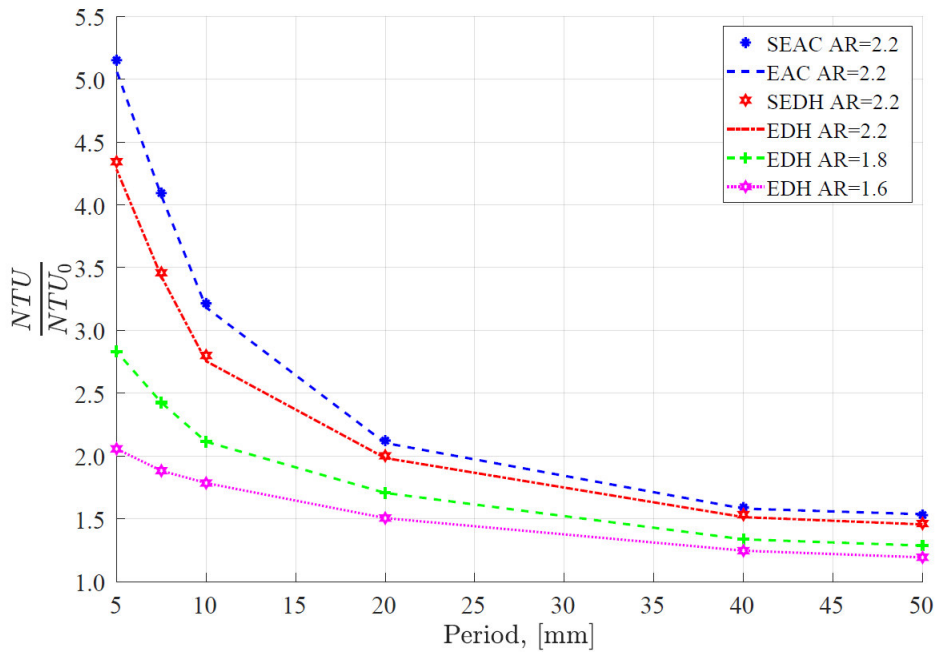
Figure 2-18. Ratio of NTU/NTU_0 as a function of a period at $\Delta p/l = 246$ Pa/m.

Figure 2-19 demonstrates the global performance $PEC_{\Delta p}$. One can see that DCTs with $AR = 2.2$ and $p = 5.0$ mm provide approximately half of efficiency of an equivalent straight tube requiring only 20 to 30 % pumping power of the same straight tube. It is also noticeable that the global efficiency of DCTs increase with increase in p and exceeds 1, which means that the DCTs are as efficient as an equivalent straight tube at Δp constant. It is interesting to note that EDH type of tubes with $AR = 2.2$ demonstrate similar $PEC_{\Delta p}$ values with around 15 % lower pumping power compared with EAC and SEAC tubes with $AR = 2.2$. These results demonstrate that DCTs are potentially significantly more efficient than an equivalent straight tube.
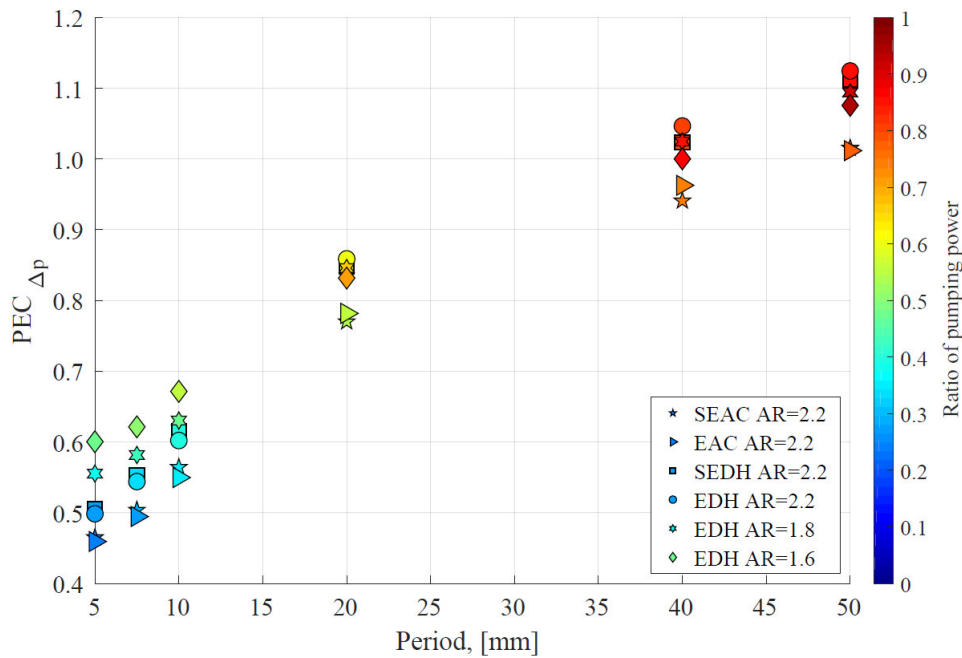
Figure 2-19. $PEC_{\Delta p}$ as a function of a period and ratio of pumping power at $\Delta p/l$ = 246 Pa/m.

Figure 2-20 demonstrates $PEC_{\Delta p}$ as a function of Re in EDH tubes with varying AR and p. Note that $PEC_{\Delta p}$ was evaluated at constant Δp conditions. However, several sets of simulations were carried out with different $\Delta p/l$ values, given in Table 2-3. It is clear from Figures 2-19 and 2-20 that the highest efficiency is demonstrated by EDH tubes with AR = 1.6 and p values up to 10.0 mm. It is interesting to note that the ratio of pumping power, W/W_0, decreases to 40 % with increasing Re while still providing more than 60 % of efficiency of an equivalent straight tube.
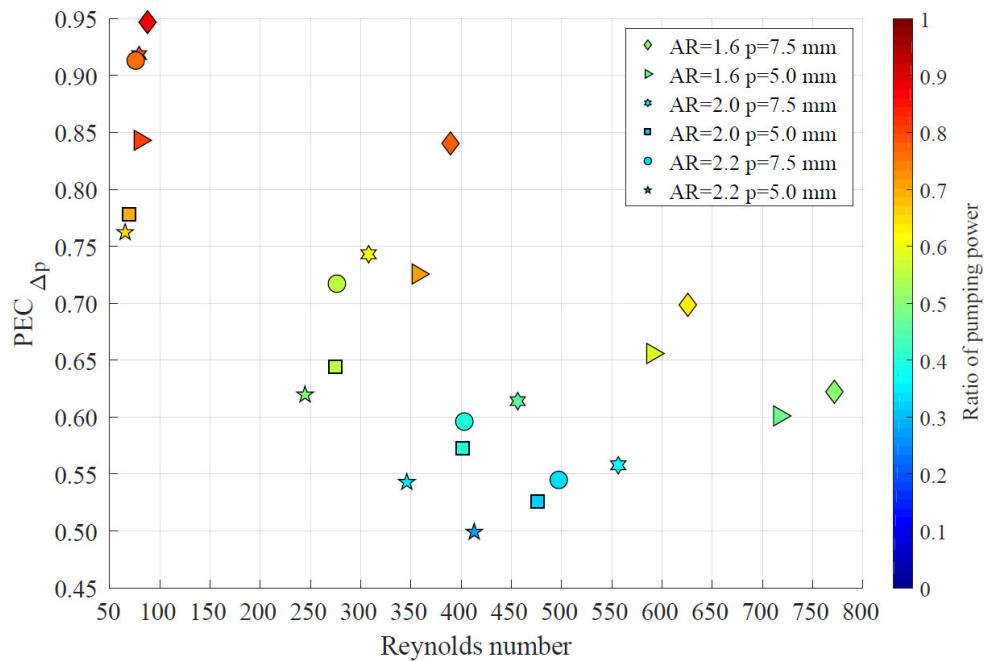
Figure 2-20. $PEC_{\Delta p}$ as a function of Re in EDH tubes.

The results of numerical study demonstrated that the investigated double corrugated tubes are more efficient than an equivalent straight tube. In case DCTs demonstrate same performance as an

equivalent straight tube at the same working conditions, the benefit of using DCTs is increased compactness of a heat exchanger.

Finally, the results obtained from CFD analysis served as a measure for selecting the tubes for an experimental investigation. However, some of the best numerically performing tubes could not be manufactured due to technological limitations. Nevertheless, seven ellipse-based double corrugated tubes with varying *AR* and *p* were 3D printed using selective laser melting (SLM) technique. The manufactured tubes are shown in Figure 2-4. The detail description of the experimental procedure and data analysis as well as results are presented in Section 2.4. The super-ellipse-based DCTs were not manufactured since their thermo-hydraulic performance, obtained numerically, was similar to ellipse-based DCTs.

2.4. Experimental results

2.4.1. 3D printed tubes and the test setup

Seven double corrugated tubes and an equivalent straight tube were 3D printed in $AlSi_{10}Mg$ powders. The relative density of the final product after the SLM process was 99.5 %. The external surface of all the 3D printed tubes was manually polished using fine sand paper. The geometrical parameters of the experimentally investigated tubes are summarised in Table 2-4. Note that the number of periods of DCTs is an integer and the length of corrugated section for all the DCTs has the length of 238.5 mm for DCTs with *p* = 7.5 mm and 240 mm for DCTs with *p* = 20.0 mm. The remaining length up to 10 mm was used to create a straight passage for connecting DCTs into an experimental setup.

Table 2-4. The geometrical data of the experimentally investigated tubes.

No	Tube name	AR	p, mm	l, mm	$A_{s,i}$, mm²	$A_{s,o}$, mm²	D_h, mm	δ, mm
1	EDH AR=1.6 p=7.5 mm	1.6	7.5	250	4195.4	5873.3	5	1
2	EDH AR=2.0 p=7.5mm	2.0	7.5	250	4525.2	6349.8	5	1
3	EAC AR=2.0 p=7.5 mm	2.0	7.5	250	4177.3	5782.7	5	1
4	EDH AR=1.6 p=20.0 mm	1.6	20.0	250	4087.5	5526.9	5	1
5	EDH AR=2.0 p=20.0 mm	2.0	20.0	250	4280.2	5893.9	5	1
6	EDH AR=2.2 p=20.0 mm	2.2	20.0	250	4396.8	6028.2	5	1
7	EAC AR=2.2 p=20.0 mm	2.2	20.0	250	4236.0	5850.9	5	1
8	Straight	-	-	250	3925.0	5495.0	5	1

The chemical composition of the used alloy was investigated using energy dispersive spectroscopy (EDS). The roughness of inner surface of a cut from a straight tube was measured using LEXT OLS4100 3D Measuring Laser Microscope. The obtained data were analysed with *SPIP* software to calculate root mean square surface roughness, S_q.

Figure 2-21 shows the view of wall section of EAC *AR* = 2.2 *p* = 20.0 mm tube obtained by scanning electron microscope (SEM) with EDS. From this picture, it is seen that the thickness of the tube wall is rather uniform despite the curvature of the tube geometry. Note, that the dark spots on the sample are mostly residues from cutting process and dusts. It is possible that some of them are small cavities, resulting in lower relative density of the alloy [138]. However, thermal conductivity was rather uniform across the tube wall thus it was considered constant.
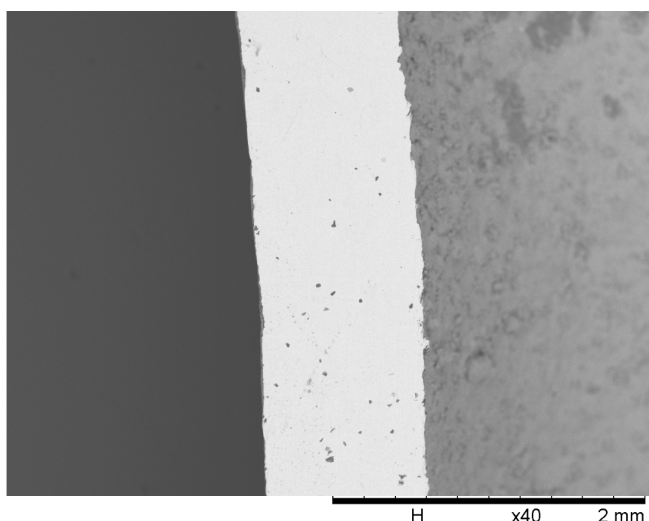
Figure 2-21. Typical microstructure of EAC $AR = 2.2$ $p = 20.0$ mm. The plane is parallel to the longitudinal axis of the tube.

Figure 2-22 presents the results from the EDS analysis. It can be seen that the alloy did not contain impurities. The measurement inaccuracy were 3.7, 0.4 and 0.1 % for aluminium, silicon and magnesium, respectively. It must be mentioned that the chemical composition of the alloy was uniform with no spots of agglomerated single elements. That demonstrated a high quality of the alloy.

(a) (b)
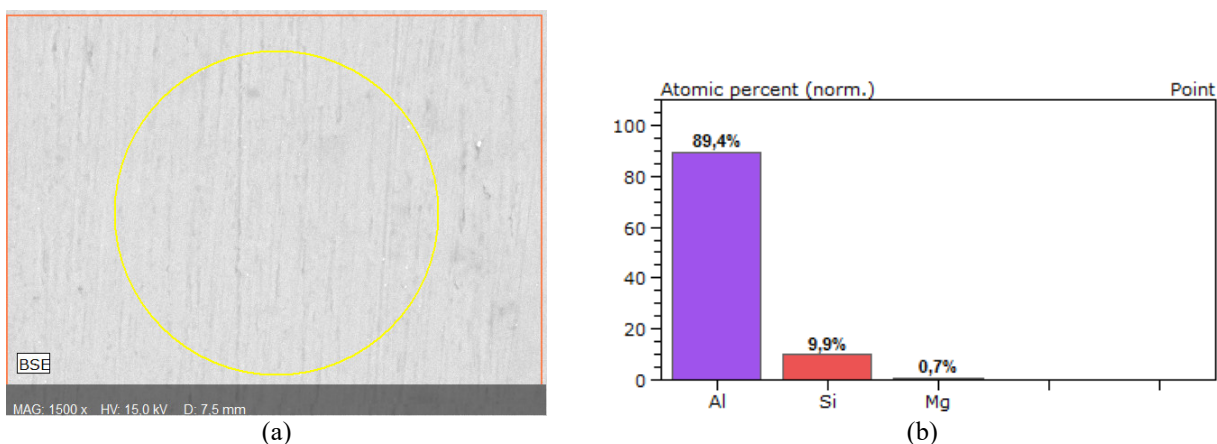
Figure 2-22. Results of EDS analysis of the sample from EAC $AR = 2.2$ $p = 20.0$ mm tube. (a) The analysed area on a wall; the plane is parallel to the longitudinal axis of the tube; (b) chemical composition of the alloy.

The surface roughness was measured on a sample cut from a straight tube along the flow direction. Figure 2-23 shows the 3D image of the inner surface of the tube. A rectangular area 0.62 × 6.56 mm was evaluated according the standard ISO 4287. It was found that S_q was 0.013 mm with the maximum difference between the highest and the lowest measured points of 145.6 ± 13 μm.
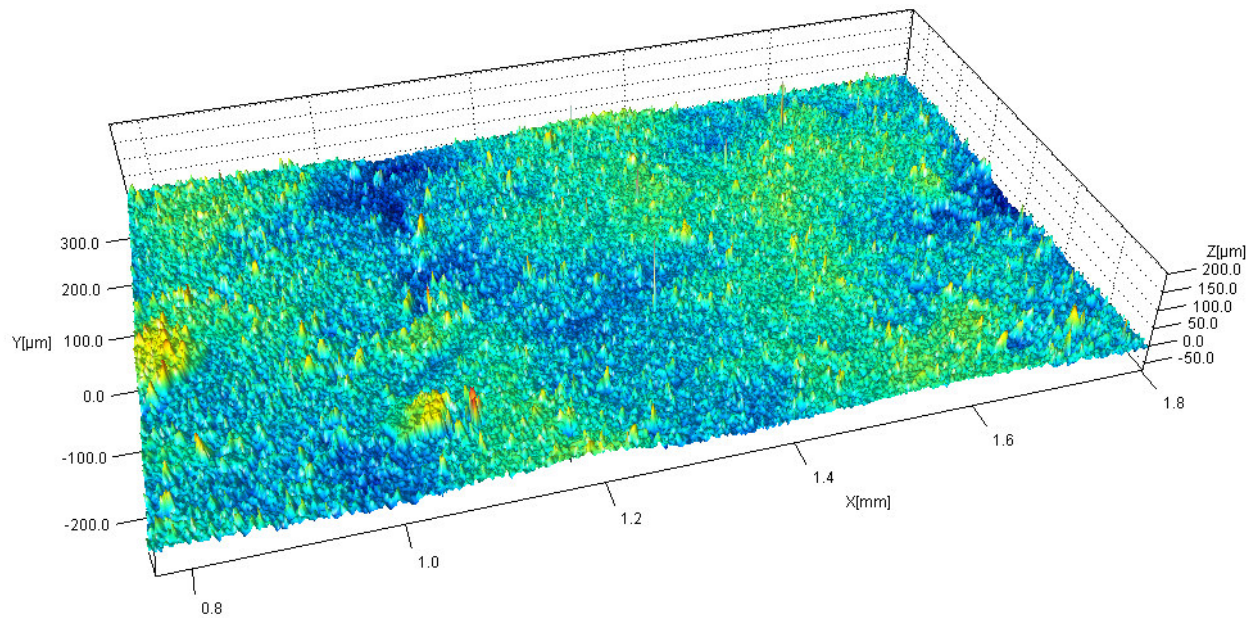
Figure 2-23. 3D image of a representative part of the analysed area; the plane is parallel to the longitudinal axis.

Note that a small representative part of the analysed area is shown in Figure 2-23, in order to increase its readability. The obtained S_q value was used to determine the friction factor using the Colebrook's equation [131]. It is noticeable that the Colebrook's equation correlates the friction factor within 10 % of accuracy due to number of uncertainties caused by surface roughness and experimental data [131,139]. It is also noticeable that it is rather difficult to evaluate precisely surface roughness of any tube due to various factors, such as welding spots, uneven distribution of geometrical objects on a surface, etc. However, Colebrook's equation provides reasonably accurate values of friction factor even if the relative surface roughness is strongly overestimated [139]. The detail explanation of the analysis of experimental data is given in Subsection 2.4.2.

The 3D printed tubes were experimentally investigated in a counter-flow heat exchanger in a water – water system. The experiments were conducted in a moderate range of *Re* from 1000 to 2500. The test setup is presented in Figure 2-24. The shell side consisted of two nylon connectors (3) and a steel tube with outer diameter of 20 mm. Four manifolds for connecting the plastic hoses and inserting T-type thermocouples (TC) at the ends of the tube side (1) and the shell side (2). The TCs were connected to an NI Ice point reference. The temperature measurements were logged using LabView and the experimental uncertainty was ± 0.1 K. Each tubes was mounted and sealed with silicone into a tube holder (6) on each side of a tube and mounted inside the shell. These holders were used in order to centre the tested tubes inside the shell as well as prevent leakage from the shell side to the tube side and vice versa. The system was checked for leakage before each set of experiments.
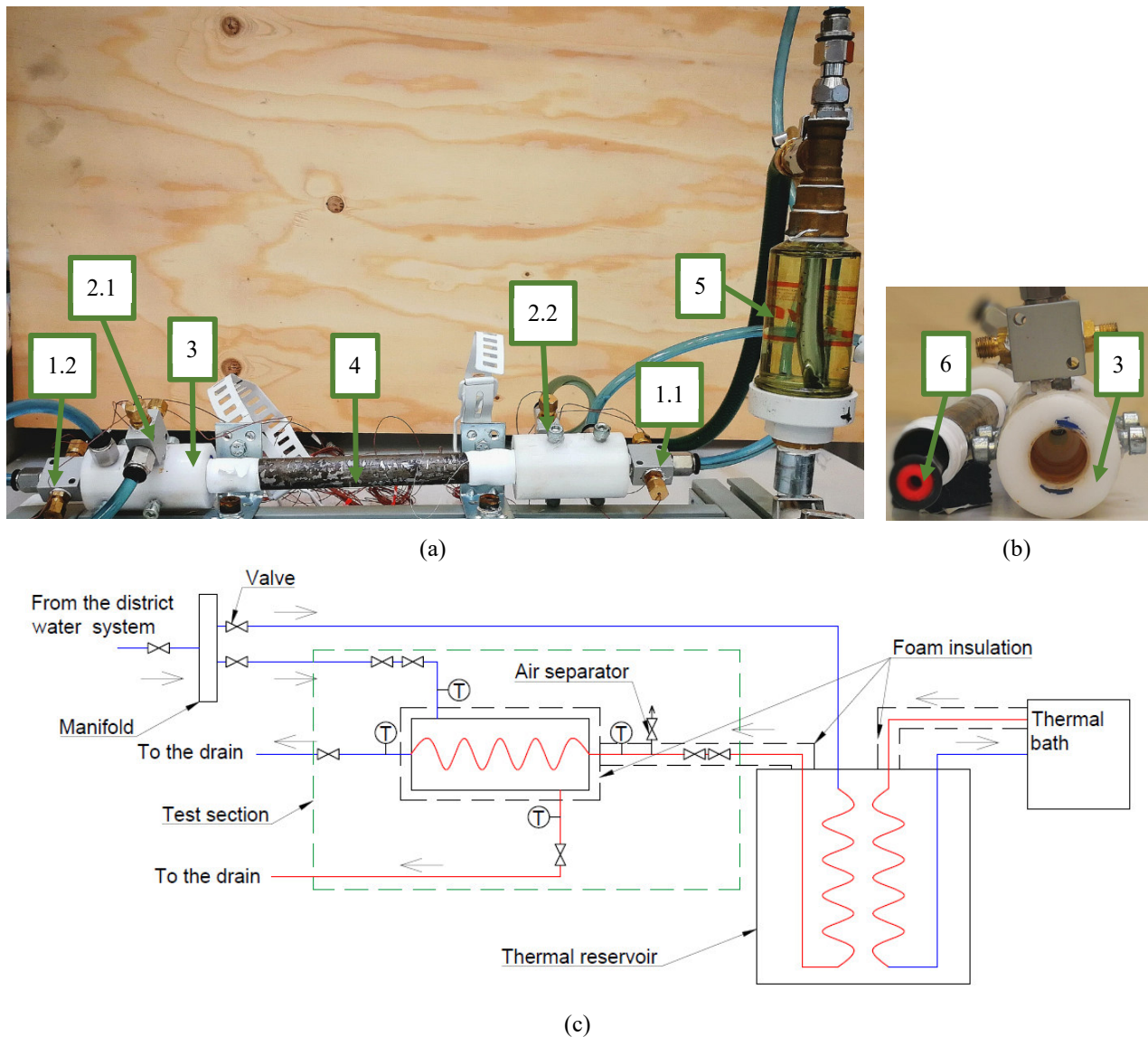
Figure 2-24. A photograph of (a) a counter-flow heat exchanger; (b) a nylon connector of the shell side (3) and a tube holder (6); (c) a schematics of the test setup [128].

City water was used in the test rig. From Figure 2-24 (c), it is seen that the test rig was connected to a tap through a manifold separating the water flow into two streams. One stream was directed to a shell side (cold stream), while other was pushed through a copper coil heat exchanger in a thermal reservoir. There, the stream was heated up (hot stream) and pushed to a tube side. Temperature in a thermal reservoir was maintained by a thermal bath. Shut-off valves on the inlet and outlet of the tube and the shell sides were used to control the water flow. To ensure the air-bubble free flow the air separator was installed before the tube inlet (1.1).

The range of *Re*, within which the thermal measurements were conducted, was limited by several reasons. First off all, the steady state could not be reached when hot stream *Re* was higher than 2500. Secondly, stratification of the temperature on both sides occurred when *Re* was lower than 700 and 1000 at the tube and the shell side, respectively. Finally, the highest possible *Re* for the shell side was around 5000 without compromising accuracy of the mass flow rate measurements.

The pressure drop was measured at isothermal conditions using a differential manometer. The uncertainty of the differential manometer was ± 10 Pa.

2.4.2. Analysis of experimental data

The modified Wilson plot technique was used for evaluating the performance of the tubes. Therefore, series of experiments were conducted with holding the flow rate of the shell side constant while varying the flow rate on the tube side and vice versa. Each experimentally obtained data set consisted of mass flow rates, $\dot{m}$, on both the tube and the shell side, and inlet and outlet temperatures, T, for both sides. The data were analysed considering D_h as a characteristic length. The thermal and hydraulic behaviour of the tested tubes was analysed in terms of Nusselt number, Nu, and friction factor, f, using Eqs. 2-29 and 2-35 – 2-51.

As it was emphasised in Subsection 2.3.3, the comparison of the DCTs was done using geometrical data of an equivalent straight tube. The penalty for the enhanced surface was evaluated via the experimentally measured friction factor. Finally, the maximum enhancement of the surface area of the experimentally investigated DCTs was less than 16 %, thus it is of less importance.

The average overall heat transfer coefficient, U, is determined in Eq. 2-35.

$$U = \frac{q}{A_o \Delta T_{lm}}$$

Eq. 2-35

Where A_o is an outer heat transfer surface of an investigated tube and q is the net heat flow rate defined in Eqs. 2-36 and 2-37 for the tube side and the shell side, respectively.

$$q_1 = \dot{m}_1 c_{p,1}(T_{1.1} - T_{1.2})$$

Eq. 2-36

$$q_2 = \dot{m}_2 c_{p,2}(T_{2.2} - T_{2.1})$$

Eq. 2-37

Where $\dot{m}$ is mass flow rate and c_p is specific heat capacity. Subscripts 1 and 2 denote the tube and the shell sides, respectively. 1.1 and 1.2 refer to inlet and outlet of the tube side, respectively. 2.1 and 2.2 refer to inlet and outlet of the shell side, respectively.

It must be noted that the shell side was extremely susceptible to temperature stratification at low flow rates. Moreover, the temperature difference between the inlet and the outlet was rather small, thus extra care was taken to ensure the reliability of the measurements.

In order to evaluate thermal performance of the examined tubes, one should determine Nusselt number for the tube side, Nu_1, which is expressed in Eq. 2-38.

$$Nu_1 = \frac{h_1 D_h}{k_f}$$

Eq. 2-38

From Eq. 2-38, it is clear that in order to find Nu_1 it is necessary to know h_1. It is not possible to determine precise value of the later term. However, the relation between the convective heat transfer coefficients on the tube and the shell sides, h_1 and h_2, respectively, is determined in Eq. 2-39.

$$\frac{1}{U A_o} = \frac{1}{h_1 A_i} + R_w + \frac{1}{h_2 A_o}$$

Eq. 2-39

Where R_w is thermal resistance of a tube wall, which is calculated using Eq. 2-40.

$$R_w = \frac{ln(D_0/D_i)}{2 \pi l k_w}$$

Eq. 2-40

Where D_i and D_o are the inner and the outer diameters of a tube, respectively. k_w is the thermal conductivity of the wall material, which is 150 W/(m K) [138]. R_w is considered constant over a tube length at the operational conditions.

Both terms h_1 and h_2 are unknown and of the same order of magnitude and it is difficult to know a priori which one is higher. Thus, the parameter estimation technique for an inverse data processing was used to determine the two unknowns [140]. Both h_1 and h_2 can be simultaneously correlated in terms of Nu using the Colburn equation [136]. Then Nu_1 and Nu_2 are determined as in Eqs. 2-41 and 2-42, respectively.

$$Nu_1 = C_1 Re^{\alpha_1} Pr^{\beta_1} \qquad\qquad \text{Eq. 2-41}$$

$$Nu_2 = C_2 Re^{\alpha_2} Pr^{\beta_2} \qquad\qquad \text{Eq. 2-42}$$

Where C is the multiplicative constant, α is the Re exponent and β is Pr exponent, which was assumed equal to 0.33 [134,136], since the only working fluid was water and Pr value did not vary significantly during the experiments.

In order to estimate both h_1 and h_2 simultaneously, the parameter estimation approach was applied by minimizing the least squared errors between estimated and experimentally measured U [140]. Then the function, for which the least square approach was applied, is given in Eq. 2-43.

$$S(C_1, \alpha_1, C_2, \alpha_2) = \sum_{j=1}^{N} \left[(U)_{exp,j} - (U)_{estim,j} \right]^2 \qquad\qquad \text{Eq. 2-43}$$

Where N is the number of experiments, done by varying mass flow rate on the tube and the shell sides. Subscripts *exp* and *estim* denote experimentally obtained and estimated values of U, respectively. Then, U_{estim} was calculated using Eq. 2-44.

$$U_{estim} = \frac{1}{A_o} \left(\frac{D_{h,i}}{k_f A_i} \cdot \frac{1}{C_1 Re^{\alpha_1} Pr^{0.33}} + R_w + \frac{D_{h,o}}{k_f A_o} \cdot \frac{1}{C_2 Re^{\alpha_2} Pr^{0.33}} \right)^{-1} \qquad \text{Eq. 2-44}$$

Where Re was considered as independent variable, C_1, C_2, α_1 and α_2 were considered as unknown variables. Terms, referring to fluid properties and geometrical data, were treated as knowns.

The accuracy of the estimated U values was determined by the parametric bootstrap method where U_{exp} was substituted by the distribution given in Eq. 2-45 [141,142].

$$U_{exp} = U_{estim} \cdot (1 + \varepsilon) \qquad\qquad \text{Eq. 2-45}$$

Where ε represents a uniformly distributed random noise with zero mean and variance σ. The variance σ was considered equal to the uncertainty related to the temperature difference, measured at a tube side between the inlet and the outlet. As the starting value, U_{exp} was re-sampled from its probability distribution and the U_{estim} was estimated using Eq. 2-44. This was repeated many times and the obtained results were analysed using standard statistical methods for evaluating 95 % confidence intervals. The parametric bootstrap method also presents the uncertainty of the estimation procedure. The error propagation was evaluated considering uncertainties [143] in estimation technique, temperature measurements, fluid properties and mass flow rate that were 2.5 %, 2 % and 5 %, respectively [128]. Therefore, reported uncertainties are overall uncertainties of Nu.

Full pressure drop in the testing region is expressed in Eq. 2-46.

$$\Delta p = f \frac{\rho u_m^2}{2D_h} L + \xi \frac{\rho u_m^2}{2} \qquad \text{Eq. 2-46}$$

Where the first term on the right hand side presents the frictional pressure drop and the second term presents the concentrated pressure drop. ξ is vorticity [144].

Concentrated pressure drop occurred due to the configuration of the test rig. It was caused by variations of the cross-section of the flow channel through the used fittings. For this reason, the concentrated pressure must be the same for all the investigated tubes. In order to evaluate the frictional pressure losses that were caused by the geometry of the examined tubes only, the concentrated pressure must be subtracted from Eq. 2-46. This was done by evaluating ξ, which is unique for every flow regime [144] despite changes of the geometry of the examined tubes.

The data, obtained for the straight tube were analysed in order to determine values of ξ for laminar and turbulent flow regimes. In order to evaluate the term of frictional losses in any straight tube, one should know the friction factor, f. For this reason, two classical expressions of f were applied depending on the flow regime. The Darcy friction factor, f, given in Eq. 2-26, was used in laminar flow regime and Colebrook correlation, given in Eq. 2-47 [131] was used in transitional and turbulent flow regimes. For clarity reasons, the subscript in Eq. 2-26 is changed from 0 to lam, denoting laminar flow regime. Thus, the Eq. 2-26 can be written as Eq. 2-48.

$$\frac{1}{\sqrt{f_{turb}}} = -2.0 \, log \left(\frac{S_q/D_h}{3.7} + \frac{2.51}{Re\sqrt{f_{turb}}} \right) \qquad \text{Eq. 2-47}$$

Where the relative roughness $S_q/D_h = 0.0026$ was used for solving the Colebrook equation for f. The *Matlab* routine, presented in Ref. [145] was employed to solve Eq. 2-47.

$$f_{lam} = \frac{64}{Re} \qquad \text{Eq. 2-48}$$

It must be noted, that the experimental data on pressure measurements had to be sorted manually into laminar and turbulent flow regimes. However, it is not possible to draw a clear line between laminar and turbulent flow regimes. In this thesis, the laminar flow regime was considered for flow with $Re \leq 2000$ [131] and turbulent $Re > 3500$ regimes. The data in between laminar and turbulent regimes were considered as transitional flow. It must be emphasised that the Colebrook equation was used to determine f also in transitional flow regime. Then, knowing f, the frictional pressure loss was calculated and subtracted from Eq. 2-46, resulting in term of concentrated pressure drop. From this point, the values of ξ were determined for laminar and turbulent flow regimes using least square fit method. Then, the experimentally obtained friction factor, f, was evaluated for all the examined tubes, considering only the frictional pressure loss component in Eq. 2-46. The experimentally obtained and corrected for concentrated pressure drop f values then were fitted to the form given in Eq. 2-49 [130].

$$f = KRe^m \qquad \text{Eq. 2-49}$$

Where K is the multiplicative constant and m is the Re exponent.

The uncertainty of the fitted f values, using the nonlinear regression approach, was evaluated in terms of standard error of estimate, σ_{est}, given in Eq. 2-50 [146].

$$\sigma_{est} = \sqrt{\frac{\Sigma(f_{exp} - f_{est})^2}{N - 2}} \qquad \text{Eq. 2-50}$$

The global performance of the experimentally investigated double corrugated tubes was evaluated calculating PEC_W at constant pumping power, W, as given in Eq. 2-51.

$$PEC_W = \frac{Nu/Nu_0}{\left(f/f_0\right)^{1/3}}$$

Eq. 2-51

Note, that subscript 0 here refers to data, only experimentally obtained for the straight tube. The results are presented in Subsection 2.4.3.

2.4.3. Experimental results

The experimentally obtained results for DCTs are presented in terms of correlations of Nu and f. The global performance is presented in terms of PEC_W evaluated at constant pumping power conditions. In order to compare the performance of DCTs with other state-of-the-art geometries, two experimental studies on alternating ellipse axis (AEA) tubes [102] and tubes fitted with helical screw-tape (HST) [78] were selected, since the most suitable range of Re. The Nusselt number correlations for the AEA and HST tubes are given in Eqs. 2-52 and 2-53, respectively, as reported in Ref. [102] and Ref. [78], respectively. Moreover, the Nu_{AEA} correlation is valid in a range of Re from 500 to 5000 and was obtained for tubes with $p/D_o = 2$ and aspect ratio of 1.6 [102]. The experimentally investigated DCTs have p/D_o ratio of 1.1 to 2.9 and AR values of 1.6, 2.0 and 2.2.

$$Nu_{AEA} = 0.0615 Re^{0.76} Pr_f^{1/3} \left(\frac{Pr_f}{Pr_w}\right)^{0.11}$$

Eq. 2-52

$$Nu_{HST} = 0.017 Re^{0.996} Pr \, Y^{-0.5437}$$

Eq. 2-53

Where Y is the twist ratio. The best performing helical screw-tape had $Y = 1.95$ [78], therefore, this value was used to compare thermal performance of DCTs to HST tube.

Hydraulic performance of the DCTs was compared to AEA and HST tubes in term of friction factor. The correlations for f in latter tubes are given in Eqs. 2-54 and 2-55, respectively, as reported in Ref. [102] and Ref. [78], respectively.

$$f_{AEA} = 1.54 Re^{-0.32}$$

Eq. 2-54

$$f_{HST} = 10.7564 Re^{-0.387} Y^{-1.054}$$

Eq. 2-55

It must be emphasised that none of the studies, selected for comparison, reported correlations for Nusselt number and friction factor of their reference geometry. Therefore, the Nu and f correlations, obtained for the straight tube in this thesis were used instead. In addition, the Pr of the working fluid used for obtaining the correlations as well as the Pr_w value were not reported either. Therefore, Pr, experimentally obtained for the DCTs, was used in Eqs. 2-52 and 2-53, acknowledging the increased uncertainty of the comparison. Finally, the ratio of Pr_f/Pr_w was considered to be 1. For these reasons, the thermal and hydraulic performance of DCTs was compared to performance of AEA and HST tubes separately rather than comparing their PEC_W.

The test rig and experimental procedure was validated against the classical Nu correlation for the combined entry region in laminar flow regime. Namely, the Sieder – Tate correlation was used for this reason. It is expressed in Eq. 2-56 [134].

$$Nu_{Sieder-Tate} = 1.86 \left(\frac{Re \, Pr}{L/D_h} \right)^{1/3} \left(\frac{\mu}{\mu_w} \right)^{0.14} \qquad \text{Eq. 2-56}$$

Where μ is dynamic viscosity of water. The ratio μ/μ_w is considered to be 1, since the temperature difference between the inlet and outlet measured in the straight tube is approximately 10 °C and the change in viscosity is negligible.

Figure 2-25 demonstrates that the classical Sieder – Tate correlation and the *Nu* correlation, obtained experimentally, agree with accuracy of 5 %, showing that the experimental method and procedure of data analysis were reliable.
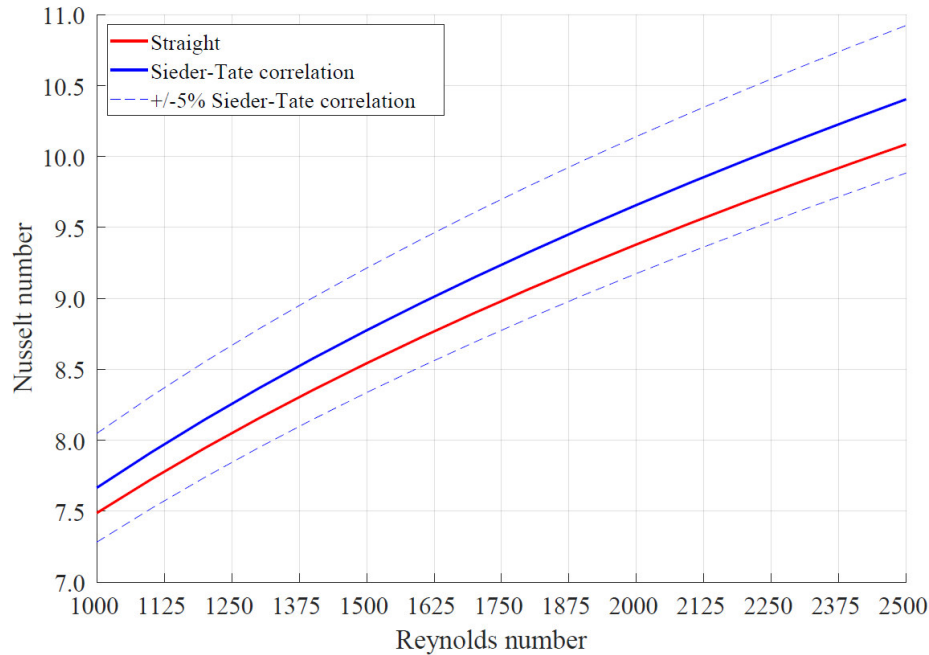
Figure 2-25. Comparison of *Nu* correlation obtained from experimental data for a straight tube and the Sieder – Tate correlations as a function of *Re*.

Finally, the agreement between experimentally measured and correlated data were checked in terms of overall heat transfer coefficient, *U*. One can see from Figure 2-26, that experimental data and obtained correlations agree very well regardless of *Re* on both the tube and the shell side for double corrugated tubes. Nevertheless, by paying closer attention to Figure 2-26 (c), it is seen that the agreement between correlated and experimentally obtained data for EAC AR = 2.0 *p* = 20.0 mm is lower than for DCTs with p = 7.5 mm. Moreover, the agreement between measured and correlated data is also lower for the straight tube as it is seen in Figure 2-26 (d). As it is seen in Figure 2-26, the latter tubes showed lower overall heat transfer coefficient, *U*, in comparison with the DCTs with *p* = 7.5 mm. Therefore, it is mainly attributed to a rather small temperature difference between the inlet and the outlet of these tubes that was caused by experimental limitations. Nevertheless, the experimental procedure and the method of analysis were considered reliable.
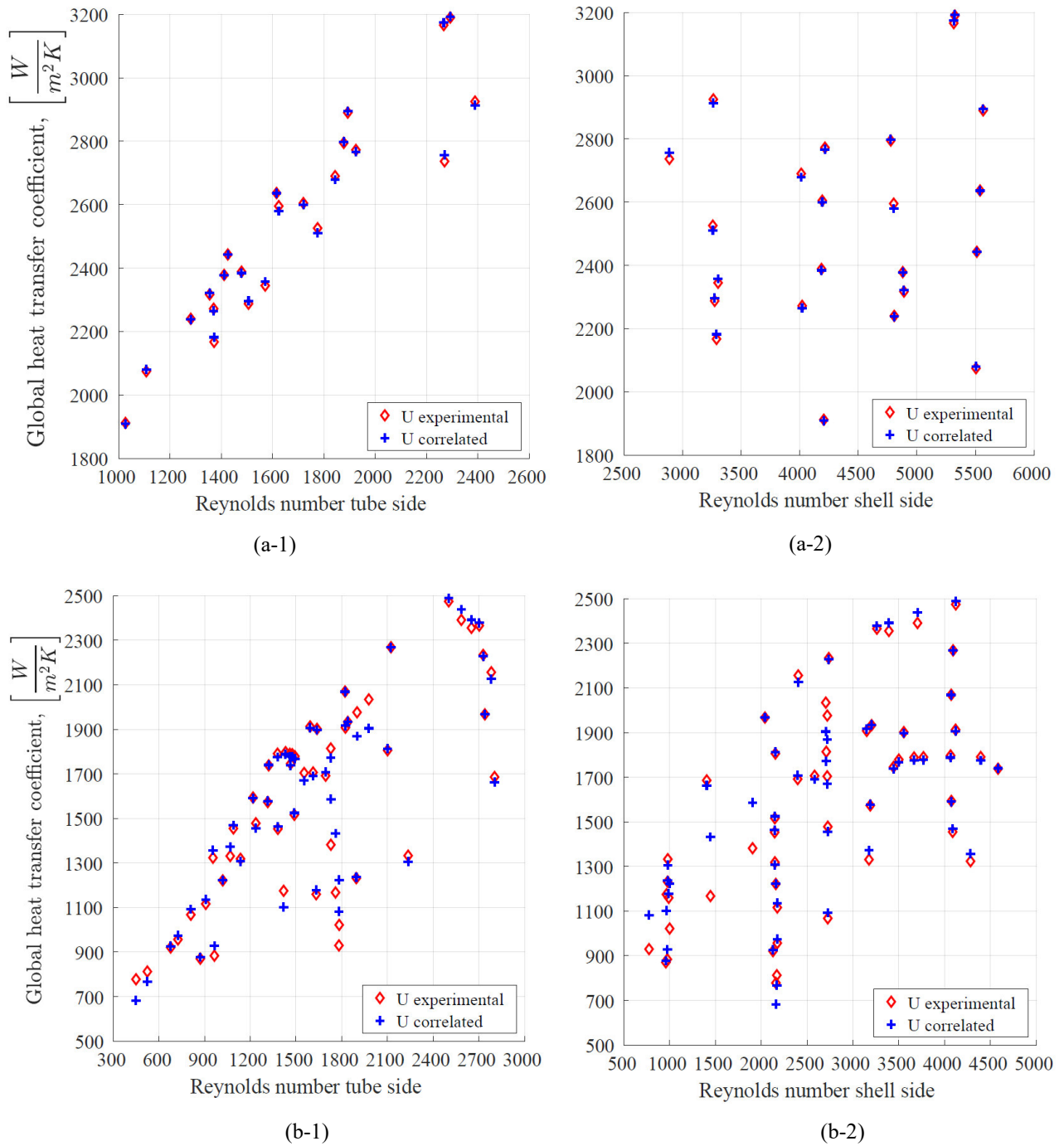
Figure 2-26. Global heat transfer coefficient, *U*, measured experimentally and calculated using the obtained correlations for Nusselt number for (1) the tube side and for (2) the shell side as a function of *Re* in (a) EDH *AR* = 1.6 *p* = 7.5 mm; (b) EAC *AR* = 2.0 *p* =7.5 mm; (c) EAC *AR* = 2.2 *p* =20.0 mm; (d) the straight tube.
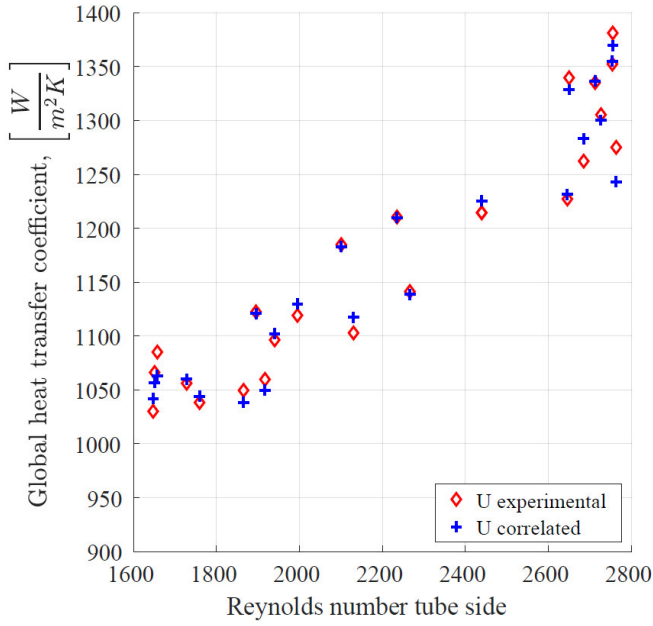
(c-1)
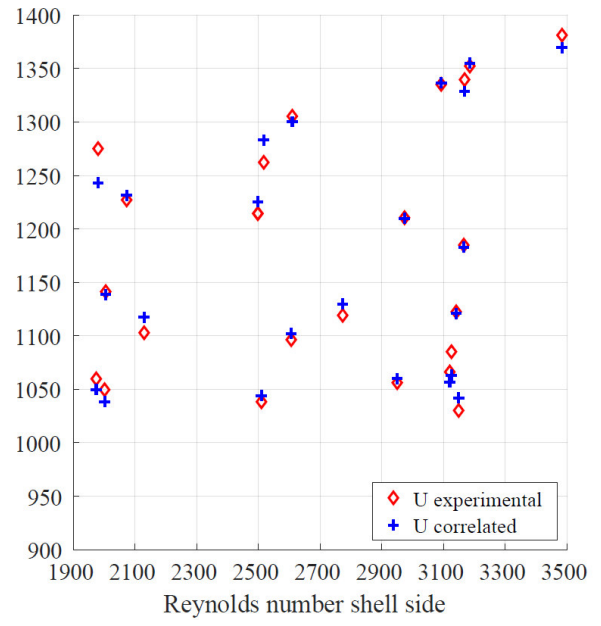
(c-2)
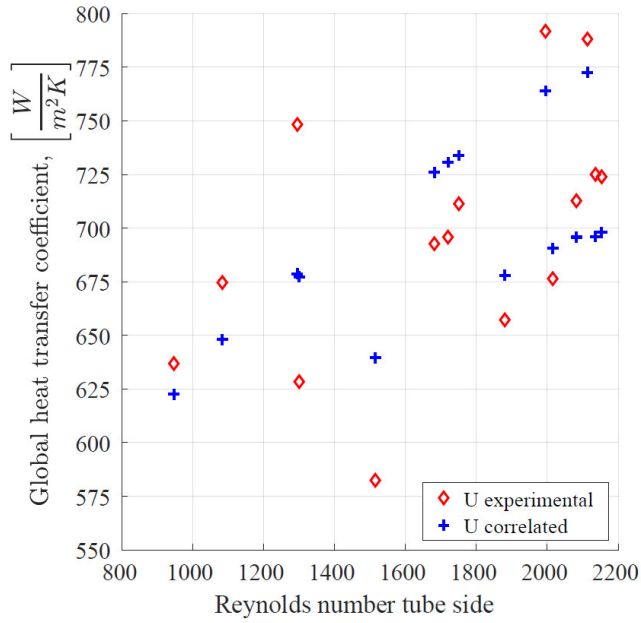
(d-1)
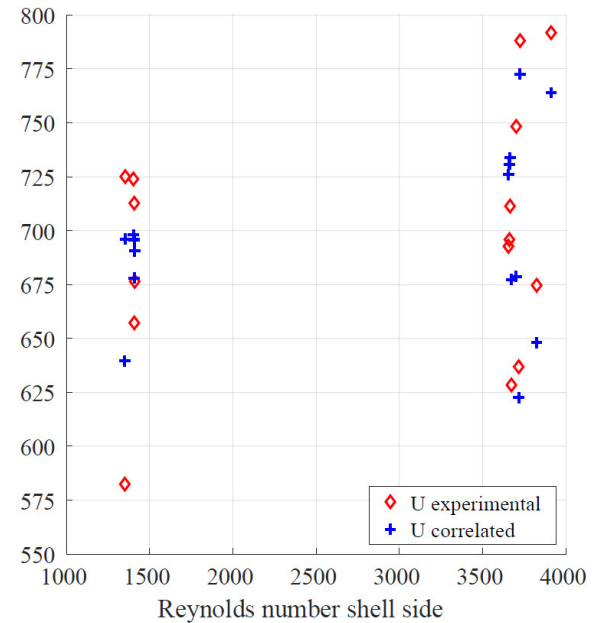
(d-2)

Figure 2-26. Continuation from the previous page.

The experimentally obtained coefficients for correlating *Nu* inside the examined tubes are given in Table 2-5. The uncertainties for *Nu* are also presented there.

Table 2-5. Experimentally obtained correlation coefficients for calculating Nu inside the tubes and Nu uncertainty.

Tube name	C_1	α_1	ε_{Nu}
EDH AR=1.6 p=7.5	0.039	0.88	± 8.0 %
EDH AR=2.0 p=7.5	0.16	0.77	± 8.5 %
EAC AR=2.0 p=7.5	0.012	1.01	±11.0 %
EDH AR=1.6 p=20.0	0.056	0.75	± 9.0 %
EDH AR=2.0 p=20.0	0.037	0.76	± 11.0 %
EDH AR=2.2 p=20.0	0.016	0.91	± 9.0 %
EAC AR=2.2 p=20.0	0.056	0.69	± 10.0 %
Straight	0.52	0.33	±14.0 %

Figure 2-27 presents the experimentally obtained Nu values for DCTs. The uncertainties, reported in Table 2-5, are not plotted together in order to keep clearness of the figure. One can see that EDH tubes clearly outperform EAC tubes comparing similar geometrical characteristics. This proves that approach to hold the D_h constant provides higher heat transfer than constant A_c. From Figure 2-27, it is clear that DCTs with shorter corrugation periods outperforms those with longer periods. Another interesting observation is that AR is of lower importance than p when comparing thermal performance. Nevertheless, significance of AR for DCTs with $p = 7.5$ mm depends on Re. One can see that at lower Re DCTs with higher AR provide higher heat transfer, when considering short corrugation period, while this is opposite at Re higher than 2200. Finally, special attention is paid to EDH $AR = 2.2$ $p =20.0$ mm tube, which demonstrates different behaviour than expected. Its performance is in between EDH $p = 20.0$ mm tubes with $AR = 1.6$ and $AR = 2.0$. This is attributed to geometrical inaccuracies inherited from manufacturing process as well as design in *SolidWorks*. The inaccuracy of the inner surface of this tube caused by manufacturing process could not be evaluated using a non-destructive method.
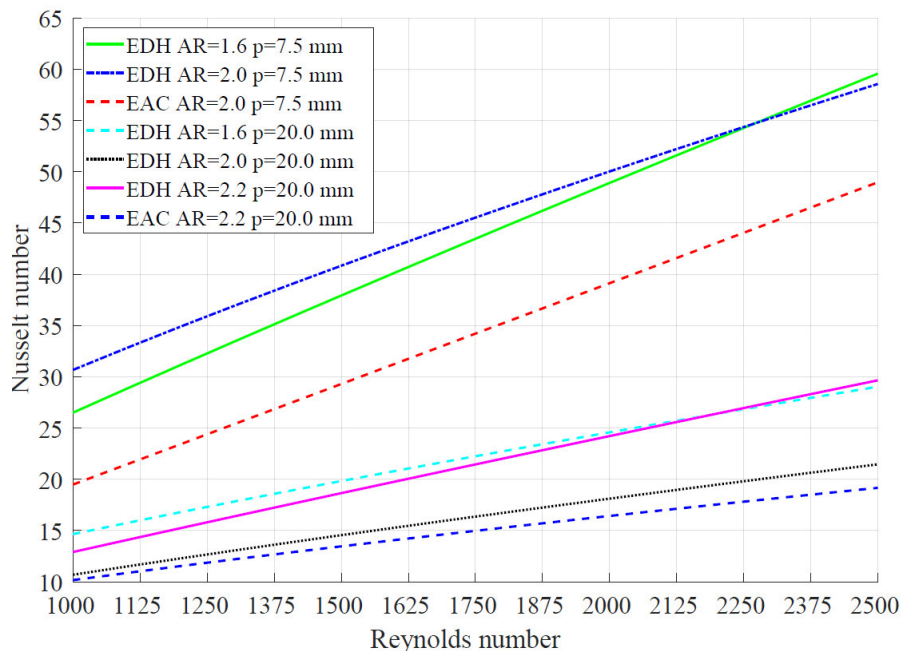
Figure 2-27. Nusselt number distribution for the tube side. Here $Pr = 3.5$.

Figure 2-28 demonstrates the DCTs are up to 500 % more thermally efficient than the straight tube. One can see that EDH tubes with $p = 7.5$ mm perform twice as well as DCTs with $p = 20.0$ mm. It is interesting to observe that the tube EAC $AR = 2.0$ $p = 7.5$ mm shows the strongest dependence on Re comparing to other DCTs. The thermal efficiency of this tube approaches EDH tubes with similar geometrical characteristics with increasing Re.

It is noticeable that all of the DCTs with p =7.5 mm demonstrate up to twice as high thermal efficiency as the AEA tube. On the other hand, performance of DCTs with p = 20.0 mm is lower than for the AEA tube. However, it is up to 300 % higher than for the straight tube.

However, HST tube significantly outperformed all the DCTs and the AEA tubes. It must be mentioned that the Nu correlation for the HST tube was obtained at constant heat flux condition. On the other hand, Nu_0 correlation was obtained in the counter-flow heat exchanger with water-water system. This imply that due to nature of heat transfer, Nu is higher at constant heat flux conditions than at constant surface temperature. Therefore, the thermal efficiency of the HST tube is to some extent over predicted.
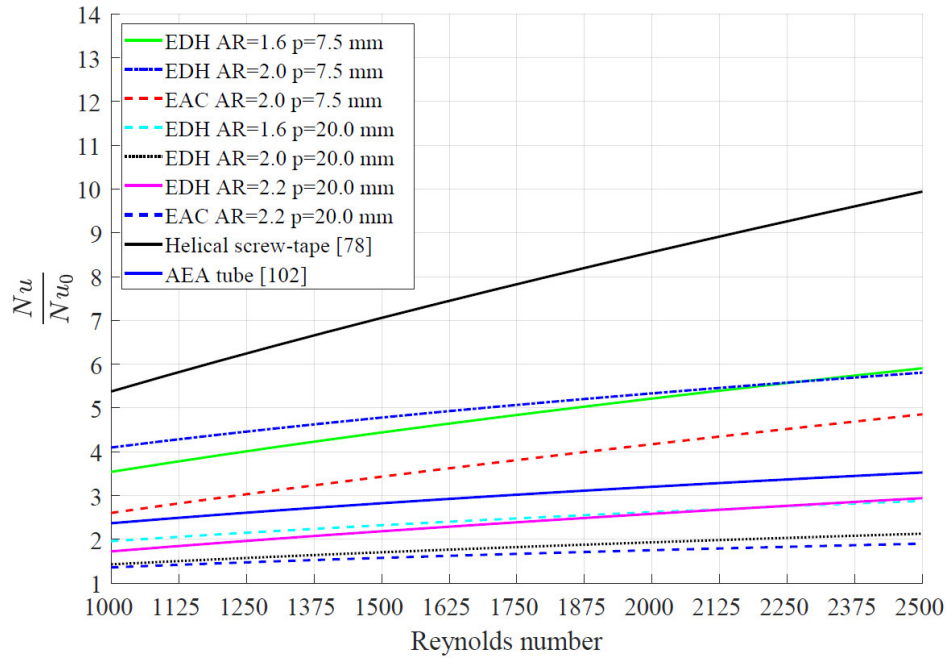
Figure 2-28.The ratio of Nu/Nu_0 as a function of Re.

Figure 2-29 presents a comparison of experimentally measured friction factor for the straight tube with theoretical correlations. Namely, Darcy – Weisbach, given in Eq. 2-29, Colebrook, given in Eq. 2-47, and Petukhov, given in Eq. 2-57, [134] correlations were used for comparison. It must be mentioned that the latter correlation is valid in Re range from 3000 to $5 \cdot 10^6$. One can see that the friction factor, obtained experimentally and corrected for the concentrated pressure drop, demonstrates an excellent agreement with the theoretical correlations. It must be mention that ξ values, calculated for laminar and turbulent flows, are in excellent agreement with theoretical values, presented in literature [144]. The values are $\xi = 1.3$ for the turbulent regime and $\xi = 2.9$ for the laminar regime. Note that in Figure 2-29, a *spline* curve was used to represent f in the transition region (2000 $< Re \leqslant 3500$) for plotting purposes when comparing friction factor in the straight tube to DCTs.

$$f_{Petukhov} = (0.790 \, ln \, Re - 1.64)^{-2} \qquad \text{Eq. 2-57}$$

From Figure 2-29 one can see that the friction factor, obtained experimentally and not corrected for the concentrated pressure drop, is significantly higher than the corrected one. This means that the concentrated pressure drop term in Eq. 2-46 was dominating in the experimental rig. However, it was not surprising, since the length of the experimentally investigated tubes was rather short. It also demonstrates that the inner surface of the 3D printed tubes was rather smooth. In order to make the frictional pressure drop dominating, one could consider investigating either significantly longer tubes, or ones having much rougher inner surface, e.g. concrete. Nevertheless, the length of the tubes,

experimentally investigated in this thesis, was pre-defined by the current technological limitations of SLM technique.
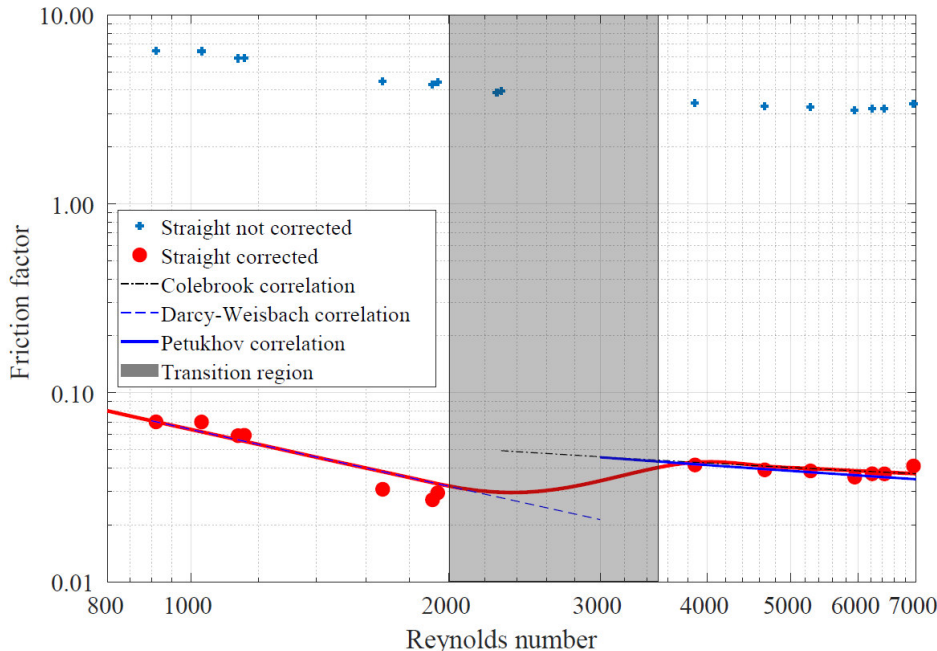
Figure 2-29. Comparison of both not corrected and corrected experimental friction factor with Darcy-Weisbach and Colebrook correlations for laminar and turbulent flow regimes, respectively.

It must be mentioned that several authors have reported that flow transition in enhanced geometries occurs much earlier than in a straight tube [102,130]. The critical Re depends on corrugation intensity and could be as low as 500 [130]. Due to this fact, a single value of ξ =1.3 was used to normalize f for the DCTs, considering that the Re of the experiments was from 1000 to 2500. The obtained results are presented in Figure 2-30 and the obtained coefficients of the data fit with the corresponding uncertainties for the fitting procedure are reported in Table 2-6. One can see that the experimentally obtained data and the data fit agree well.

Table 2-6. Data fit coefficients for friction factor and standard error of estimate.

Tube name	K	γ	σ_{est}
EDH AR=1.6 p=7.5	1.22	-0.17	±1.97 %
EDH AR=2.0 p=7.5	1.17	-0.12	±2.24 %
EAC AR=2.0 p=7.5	0.57	-0.14	±0.83 %
EDH AR=1.6 p=20.0	10.0	-0.57	±0.35 %
EDH AR=2.0 p=20.0	7.66	-0.54	±0.94 %
EDH AR=2.2 p=20.0	5.94	-0.52	±0.73 %
EAC AR=2.2 p=20.0	5.64	-0.55	±0.51 %
Straight (700≤Re <2000)	581	-1.31	±0.81 %
Straight (3500<Re≤6400)	0.21	-0.20	±0.10 %
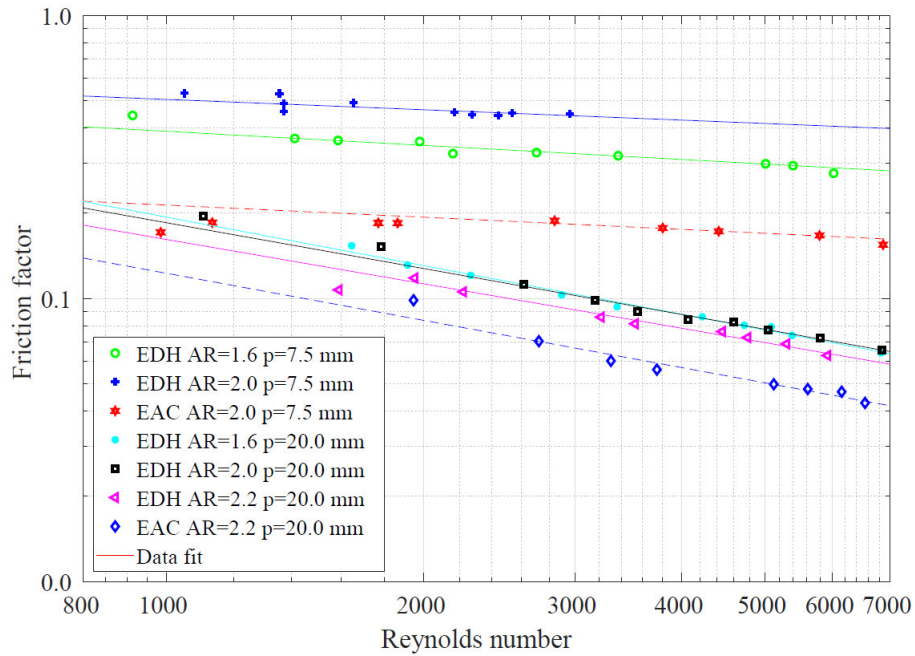
Figure 2-30. The experimentally obtained and corrected for the concentrated pressure drop friction factor, f, (marker points) and proposed data fits for f (lines) as a function of Re for double corrugated tubes.

From Figure 2-30, one can see that the EDH tubes show significantly higher friction factor than EAC tubes with the same geometrical characteristics. It is also noticeable that the impact of AR is more significant on friction factor for DCTs with short p. One can note that f for DCTs with long periods demonstrate stronger dependence on Re. On the other hand, DCTs with short periods demonstrate that f is rather independent on Re. This agrees with literature and show that the critical Re for flow transition is much lower for DCTs. However, the flow visualisation tests are needed in order to conclude the findings with confidence.

Figure 2-31 demonstrate that the f for DCTs in laminar regime increases up to 17 times in comparison to the straight tube. It is noticeable that in EAC $AR = 2.0$ $p = 7.5$ mm tube, the increase in friction factor is similar to DCTs with constant D_h and $p = 20.0$ mm rather than ones with constant D_h and $p = 7.5$ mm. However, all the DCTs with $p = 20.0$ mm demonstrated similar hydraulic behaviour regardless of the base geometry or AR. In comparison with AEA and HST tubes, DCTs with $p = 20.0$ mm demonstrate lower increase in f regardless their AR. However, EDH tubes with $p = 7.5$ mm experience the highest increase in f. It is noticeable that EAC tube with $p = 7.5$ mm shows smaller increase in friction factor than HST tube.

The global performance of the DCTs was evaluated at constant pumping power, W, conditions. From Figure 2-32, one can see global efficiency of the DCTs is up to 160 % higher than of the straight tube. Generally, the PEC_W increases with increase in Re. It is interesting to observe that the EAC $AR = 2.0$ $p = 7.5$ mm tube demonstrates similar performance as EDH $AR = 1.6$ $p = 7.5$ mm. Indeed, at high Re the values of PEC_W for both tubes are almost the same. Another interesting observation is that the global performance of the EDH $AR = 2.0$ $p = 7.5$ mm increases with Re only when a critical Re value is exceeded. Otherwise, it is rather stable and more than two times higher than of the straight tube.
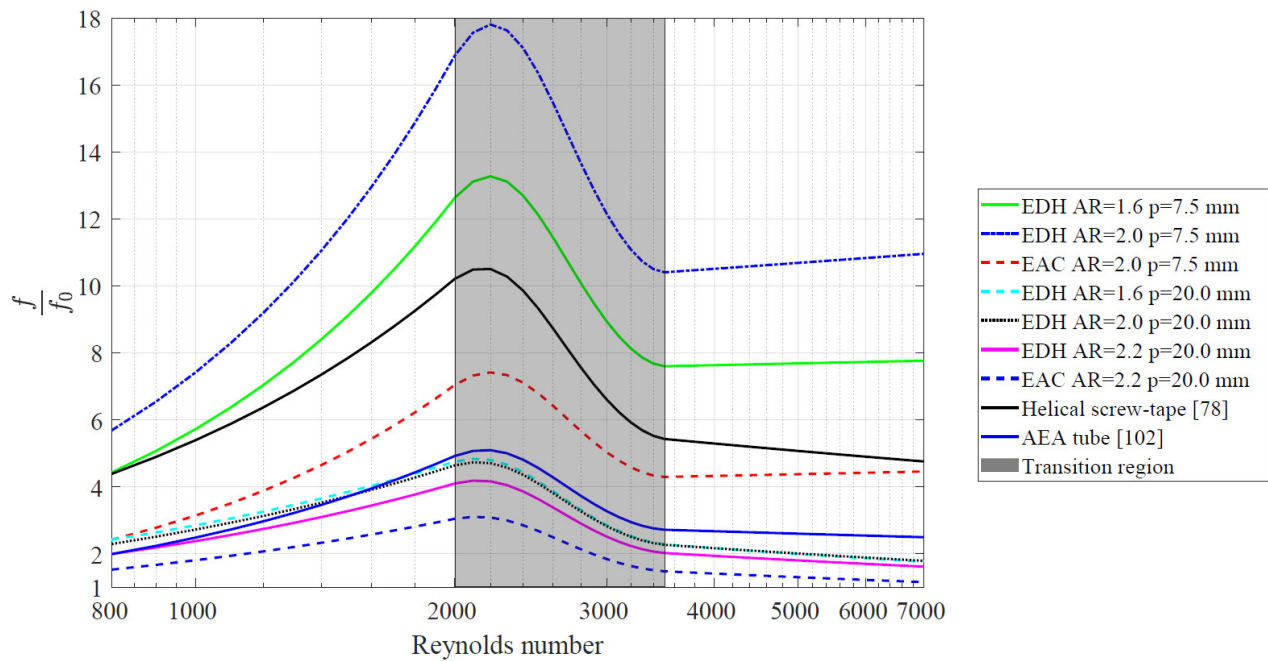
Figure 2-31. The ratio of *f/f₀* as a function of *Re*.
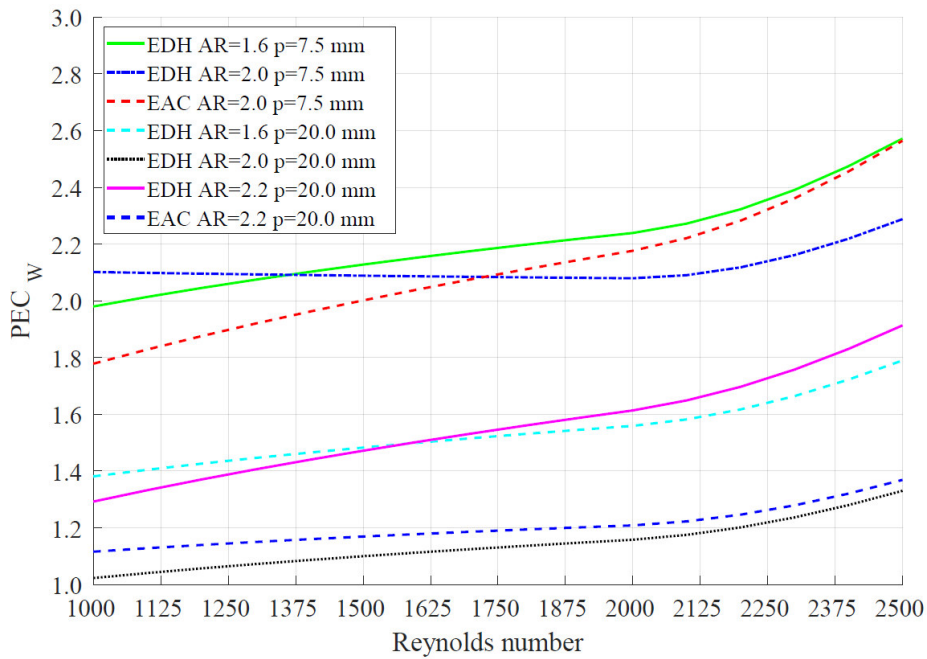
Figure 2-32. *PEC_W* as a function of *Re*.

Finally, the experimental investigation proved that the double corrugated tubes are significantly more efficient than the equivalent straight tube. Moreover, the presented tubes demonstrate higher performance than some other state-of-the-art geometries. Furthermore, the results of numerical modelling were qualitatively proved by the experiments showing that the EDH tubes are generally more efficient than EAC tubes. Moreover, EDH *AR* = 1.6 *p* = 7.5 mm was proved to be among the most efficient DCTs. However, the quantitative comparison of the modelling and experimental results was not carried out due to rather different modelling and experimental conditions.

The experimental results obtained for the DCTs encouraged an idea that performance of an AMR with a double corrugated flow pattern would improve efficiency of a magnetocaloric heat pump. Therefore, a numerical analysis was carried out and the results are presented in Chapter 3.

3. AMR with double corrugated flow structure

It was concluded in Subsection 1.3.10 that the efficiency of magnetocaloric heat pumps could be improved by optimizing geometry of an AMR beds. A great deal of research efforts has been devoted to experimental and numerical investigation of various geometries of AMR beds seeking to map out the optimized parameters such as particle size, length and an aspect ratio of a packed bed in order to improve performance of a magnetocaloric heat pump [25,33,35,37,147].

The experimental results obtained for DCTs, presented in Subsection 2.4.3, have encouraged studying numerically the performance of AMR beds with double corrugated regenerator geometry. All of the DCTs demonstrated higher thermal performance than a straight tube with higher or lower increase in friction factor. It was emphasised in Subsection 1.2.1 and Section 1.3 that performance of a magnetocaloric heat pump can be enhanced by improving a shape of an AMR flow pattern. It is necessary to ensure a low pressure drop in a solid regenerator, while a high heat transfer is provided. In Subsection 1.2.1, it was noted that the high heat transfer rate is obtainable using regenerators with packed spherical particles. However, the pressure drop is very high in this type of regenerators. On the other hand, one can consider using AMR with stacked plates or cylindrical micro-channel matrix, where the pressure drop is lower, so is the heat transfer. Therefore, the double corrugated geometry is proposed as a compromise to both cases. AMR with double corrugated geometry is expected to provide higher heat transfer rate than an AMR with stacked parallel plates or cylindrical micro-channel matrix, and lower pressure drop than an AMR with packed spherical or irregular particles. Therefore, it should provide higher *COP* at the same Q_{cool} in comparison to conventional AMR geometries. A one-dimensional AMR model was used to perform the analysis. A brief overview of the used AMR model is given in Section 3.1. The modelling results are discussed in Section 3.2. It should be noted that 1D AMR modelling results on double corrugated flow patterns are in preparation as a journal publication.

3.1. One-dimensional AMR model

Generally, AMR models are used to predict potential performance of an AMR bed depending on operational conditions, MCM materials and geometry of the AMR itself. Usually, a cooling power, Q_{cool}, over a temperature span, ΔT_{span}, is an output of these models with a possibility to calculate the *COP* [148]. Many different approaches have been reported in literature to model AMRs. A review on numerical AMR models that were developed by 2011, with a focus on various components of AMR models emphasising their effect on modelling results, is given in Ref. [148]. The vast majority of the developed AMR models are one-dimensional [147,149]. Although, two- and three-dimensional models have been presented as well. However, two-dimensional models could be used only for modelling beds with ordered structures, i.e. parallel plates, cylindrical or square channels [23] due to differences in a definition of heat transfer between fluid and a solid.

Regardless of the modelling approach, all the of AMR models must solve mathematically described heat transfer in a solid MCM matrix, which exhibits MCE due to varying magnetic field, coupled with convective heat transfer in fluid. Then, the governing equations, as described first in Ref. [62] and later modified in Ref. [29], are expressed in Eqs. 3-1 and 3-2.

$$\frac{\partial}{\partial x}\left(k_{stat}A_c\frac{\partial T_s}{\partial x}\right) + \frac{Nu\,k_f}{d_h}a_sA_c\left(T_f - T_s\right)$$

$$= A_c(1-\varepsilon)\rho_s\left[c_H\frac{\partial T_s}{\partial t} + T_s\left(\frac{\partial s_s}{\partial H}\right)_{T_s}\frac{\partial H}{\partial t}\right] \qquad \text{Eq. 3-1}$$

$$\frac{\partial}{\partial x}\left(k_{disp}A_c\frac{\partial T_f}{\partial x}\right) - \dot{m}_f c_f \frac{\partial T_f}{\partial x} - \frac{Nu\,k_f}{d_h}a_s A_c\left(T_f - T_s\right) + \left|\frac{\partial P}{\partial x}\frac{\dot{m}_f}{\rho_f}\right|$$
$$= A_c \varepsilon\,\rho_f c_f \frac{\partial T_f}{\partial t}$$

Eq. 3-2

Where k is thermal conductivity, T is temperature, ρ is density, c is specific heat, s is specific entropy, A_c is cross-section area, d_h is hydraulic diameter, a_s is specific area, and ε is porosity, x is axial positon, t is time, $\dot{m}$ is mass flow rate, H is internal magnetic field, Nu is Nusselt number and $\frac{\partial P}{\partial x}$ is pressure drop. The subscripts f, s, $disp$ and $stat$ represents fluid, solid refrigerant, dispersion and static, respectively.

The full model description, applied modifications and discretization of governing equations are given in Ref. [29]. Therefore, it is omitted in this thesis. However, it must be explained that the first term on the left hand side of Eq. 3-1 describes thermal conduction through the AMR bed. Then the second term represents the heat transfer between the fluid and MCM. The energy storage and magnetic work of the MCM are defined by the term on the right hand side. The first term on the left hand side of Eq. 3-2 defines thermal conduction through the fluid, the second term represents the enthalpy flow, the third term defines the heat transfer between the fluid and MCM, and thus it couples both energy equations. Then the viscous dissipation is defined by the fourth term on the left hand side of Eq. 3-2 and the energy storage in fluid is described by the term on the right hand side.

The used 1D AMR model comprises the following assumptions:
• There is no flow leakage or bypass;
• The heat transfer caused by radiation is negligible;
• The MCM is uniformly distributed in the AMR bed;
• The fluid is incompressible;
• No phase change occurs in the fluid;
• The MCM exhibits uniform magnetization and demagnetization;
• Fluid enters an AMR at uniform bulk temperature and uniform velocity profile across the cross-section of an AMR.

The number of time and space nodes used in this study was 4000 and 40, respectively. It was found that accuracy of the numerical solution did not increase by increasing time nodes by 25 % and 50 %. The model reached convergence if the numerical tolerance of $2 \cdot 10^{-4}$ was attained and number of iterations exceeded 500. The 1D AMR model used in this study has previously been validated against SOPT and FOPT as well as multi-layered materials [30,32]. Comparison of results, obtained experimentally and using the 1D model, is provided in Chapter 4.

3.2. Double corrugated flow pattern of an AMR

As it was mentioned in Subsection 1.2.1, from the performance point of view, it is important that the geometry of an AMR would provide high heat transfer and low pressure drop. These characteristics have been demonstrated experimentally in double corrugated tubes and results have been presented in Subsection 2.4.3. Thus, geometry of two double corrugated tubes was selected for comparison with an AMR of packed sphere bed and a cylindrical micro-channel matrix. The comparison was carried out in terms of Q_{cool} and COP. Namely, EDH $AR = 1.6$ $p = 7.5$ mm and EAC $AR = 2.2$ $p = 20.0$ mm tubes were selected for numerical analysis.

A sketch of a modelled AMR bed is given in Figure 3-1. It is seen that the modelled regenerator is rather short and bulky. From the regenerator performance point of view, this kind of geometry favours packed sphere beds with sufficiently fine particles rather than stacked plates or other type of structured channels. This is because a packed sphere bed can provide significantly higher Q_{cool} than a

regenerator with parallel plates and still the pressure drop in the previous regenerator would allow obtaining higher efficiency. Moreover, the shape of this regenerator is similar to a cassette of *MagQueen*, described in Subsection 1.3.9, neglecting tapering of the original design. It is worth to note that the cassettes of *MagQueen* are filled with ten layers of spherical particles made in FOPT material. A sketch of an AMR with a double corrugated geometry is presented in Figure 3-1 (b) – (d). It is seen that the double corrugated channels are stacked in a way that the peak of one channel would be at the same level of the narrowest part of neighbouring channels. In this way, compactness of an AMR is increased with the possibility to obtain porosity as high as $\varepsilon = 0.54$.
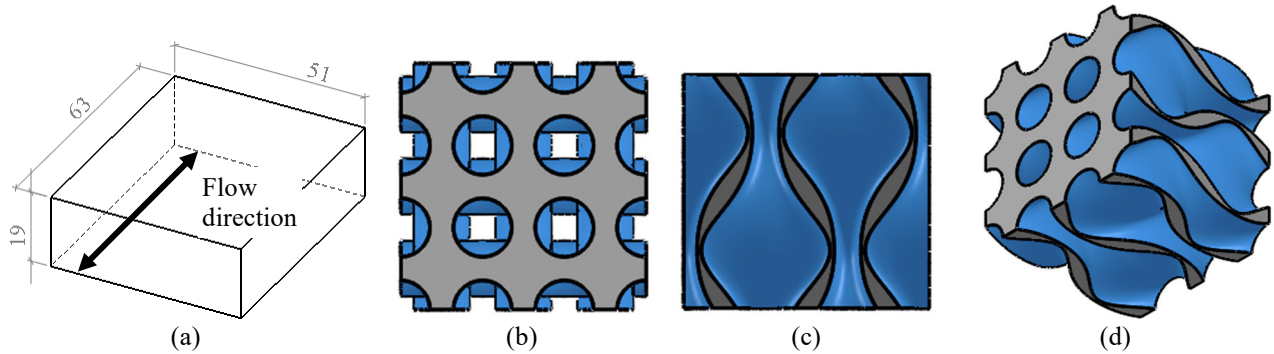
Figure 3-1. The modelled AMR bed. (a) The sketch of the AMR. (b) A fraction of the zoomed in top/bottom view of the AMR with double corrugated geometry (EAC $AR = 2.2\ p = 20.0$ mm). (c) A fraction of a zoomed in side view of Figure 3-1 (a). (d) A fraction of a zoomed in isometric view of Figure 3-1 (a). The solid material is represented by grey colour and flow channels are represented by blue colour.

The input data for the 1D AMR model are reported in Table 3-1. It must be mentioned that all of the analysed geometries were constrained to the same volume of MCM regardless of a porosity. Therefore, mass, m, of MCM varied by 28 % between regenerators with $\varepsilon = 0.36$ and $\varepsilon = 0.54$. The values of the porosity were selected due to limitations of packing spherical particles and double corrugated flow patterns. The minimum porosity of randomly packed uniform size spheres is $\varepsilon = 0.36$ and the maximum possible porosity of packed the double corrugated flow pattern is $\varepsilon = 0.54$.

Table 3-1. Boundary conditions for 1D AMR model.

	Packed sphere bed	Circular micro-channel matrix	Double corrugated channels	
			EDH $AR = 1.6\ p = 7.5$	EAC $AR = 2.2\ p = 20.0$
Length, L, mm			63	
Height, H, mm			19	
Cross-section, A_c, mm²			976	
Material			Gadolinium	
Number of layers			1	
Temp. span, ΔT_{span}, K			25.0	
Hot end temp., T_{hot}, K			300.0	
Cold end temp., T_{cold}, K			275.0	
Heat transfer fluid			Water	
Magnetic field, H, T			1.2	
Operational freq., v, Hz			0.5; 2.0	
Porosity, ε	0.36		0.36;0.54	
Mass of MCM, m, kg	0.311		0.311;0.223	
Particle size, D_p, mm	0.35		-	
Hydraulic diam., D_h, mm	0.13		0.13;0.35	

The performance of all the analysed geometries was grouped according AMR characteristics, i.e. porosity, ε, hydraulic diameter, D_h. Thus, mass, m, of the MCM and the specific heat transfer

surface, a_s, are the same for all the compared geometries. Therefore, the difference of the performance is only due to the different geometry of flow pattern. The performance of the numerically analysed geometries was evaluated at different utilisation, U, which is defined in Eq. 4-1, and at the fixed temperature span of ΔT_{span} = 25 K. The AMR with cylindrical micro-channel matrix, EDH AR = 1.6 p = 7.5 mm and EAC AR = 2.2 p = 20.0 mm were also analysed having different hydraulic diameter of the flow channels. Namely, two values of hydraulic diameter were modelled. These values were pre-defined by current technological limitations of the additive manufacturing techniques to produce AMR with flow channels that are smaller than 0.3 mm in diameter [38] as well as by the hydraulic diameter of flow channels, formed in AMR with packed spherical particles, analysed in this study.

The heat transfer term generally is expressed in terms of convective heat transfer coefficient, h, in one-dimensional models. Classical Nusselt-Reynolds correlations are normally used for this purpose [148]. It is well understood that different correlations must be used for different types of modelled geometries. The correlations used to determine the friction factor and Nusselt number in AMRs with packed spheres and the cylindrical micro-channel matrix are reported in Ref. [29,62]. Correlations for double corrugated tubes were obtained experimentally and reported in Subsection 2.4.3. The later correlations are valid in region of Re from 1000 to 2500. However, the Re in the AMR beds varied from 1 to 125 in this study. Thus, the ratios of Nu/Nu_0 and f/f_0 for the DCTs and the equivalent straight tube were calculated in the laminar flow region, considering a straight tube, (Re from 1000 to 2000). The obtained coefficients were applied as the correction factors for the Nu and f correlations for the cylindrical micro-channel matrix with the assumption that the efficiency of DCTs is the same or very similar in low Re region as it is in the experimentally investigated region. The correction factors for Nu and f for all the experimentally investigated DCTs are reported in Table 3-2. One can see that in general, DCTs, which demonstrate higher thermal efficiency, are also accompanied by higher increase in friction factor. The different behaviour of EDH AR = 2.2 p = 20.0 mm is explained in Subsection 2.4.3. This DCT was not considered as the candidate for the numerical analysis. EDH AR = 1.6 p = 7.5 mm DCT was selected for the analysis because of the highest demonstrated PEC_W. One can note that, for example, for EAC AR = 2.2 p = 20.0 mm the increase in friction factor only 35 % higher than increase in Nusselt number, while for EDH AR = 1.6 p = 7.5 mm it is 52 % higher than increase in Nu in the same Re region. Therefore, these two DCTs that demonstrate rather different PEC_W were selected for the numerical analysis.

Table 3-2. Correction factors for Nu and f for double corrugated tubes.

Tube name	Correction factor for Nu, cfn	Correction factor for f, cff
EDH AR=1.6 p=7.5	4.41	9.12
EDH AR=2.0 p=7.5	4.75	12.05
EAC AR=2.0 p=7.5	3.41	5.05
EDH AR=1.6 p=20.0	2.31	3.82
EDH AR=2.0 p=20.0	1.69	3.70
EDH AR=2.2 p=20.0	2.17	3.25
EAC AR=2.2 p=20.0	1.57	2.44

Figure 3-2 demonstrates the performance of the investigated AMR geometries with the same values of ε and D_h. The performance of these geometries were analysed at two operational frequencies. One can see that generally higher Q_{cool} is obtained at v = 2 Hz. It is also seen that the maximum Q_{cool} of 49 W and 97 W was obtained for EDH AR = 1.6 p = 7.5 mm at v = 0.5 Hz and v = 2 Hz, respectively. The opposite effect is seen for the circular micro-channel matrix, this geometry provides the lowest cooling power with maximum Q_{cool} of 30 W and 50 W at v = 0.5 Hz and v = 2 Hz, respectively. It is also noticeable that optimal U value for obtaining maximum Q_{cool} with EDH AR = 1.6 p = 7.5 mm was shifted to the right side of the axis in comparison to a packed sphere bed and cylindrical micro-channel matrix. However, from Figure 3-2, one can see that even at the same U value, AMRs with double corrugated flow patterns show higher Q_{cool} than conventional AMR geometries. It is interesting

that EAC $AR = 2.2$ $p = 20.0$ mm demonstrated somewhat higher cooling power than AMR with packed spherical particles and cylindrical micro-channel matrix at $v = 0.5$ Hz. However, the opposite effect is seen at $v = 2$ Hz, where the AMR with spherical particles outperformed the one with EAC $AR = 2.2$ $p = 20.0$ mm geometry.

(a)

(b)

Figure 3-2. Cooling power established by the AMR with $\varepsilon = 0.36$ and $D_h = 0.13$ mm at (a) $v = 0.5$ Hz and (b) $v = 2$ Hz.

From Figure 3-3 one can see that the maximum *COP* was established by the AMR with cylindrical micro-channel matrix regardless the operational frequency. However, it is seen that the maximum cooling power, at which a sensible value of *COP* could be established is rather low for both AMR with packed spherical particles and cylindrical micro-channel matrix at $v = 0.5$ Hz. On the other hand, AMR with EAC $AR = 2.2$ $p = 20.0$ mm geometry demonstrated potential to obtain about 5 W higher cooling power at *COP* of 4 than rest of the AMR geometries, as it is seen from Figure 3-3 (a).

Nevertheless, Figure 3-3 (b) shows that the later AMR geometry establishes somewhat lower performance than AMR with packed spherical particles at higher operational frequency of $v = 2$ Hz. It is also seen that AMR with EDH $AR = 1.6$ $p = 7.5$ mm demonstrates the highest cooling power at rather meaningless COP of 1.

(a)

(b)

Figure 3-3. COP as a function of cooling power established by the AMR with $\varepsilon = 0.36$ and $D_h = 0.13$ mm at (a) $v = 0.5$ Hz and (b) $v = 2$ Hz.

COP of the regenerators with $\varepsilon = 0.36$ at constant cooling power of $Q_{cool} = 30$ W and $Q_{cool} = 50$ W is summarised in Table 3-3. It is clear that AMR with EAC $AR = 2.2$ $p = 20.0$ mm has potential to provide higher COP than other investigated geometries, especially at low operational frequency at the same cooling power. However, the required pump work increases at least by 20 % in comparison with a packed sphere bed. An interesting observation is that EAC $AR = 2.2$ $p = 20.0$ mm outperforms the

cylindrical micro-channel matrix at higher Q_{cool}. Indeed, at $v = 2$ Hz and $Q_{cool} = 30$ W the later geometry demonstrates the highest COP of 6.10. However, once Q_{cool} increases up to 50 W at the same operation frequency, COP of the cylindrical micro-channel matrix degrades faster than it does for the packed sphere bed and EAC $AR = 2.2$ $p = 20.0$ mm.

Table 3-3. COP of numerically analysed AMR geometries with $\varepsilon = 0.36$ and $D_h = 0.13$ mm.

AMR geometry	v, Hz	Q_{cool}, W	COP	Utilisation	Δp, bar	Pump work, W
Spherical particles			5.04	0.93	0.460	0.81
Cylindrical micro-channel matrix	0.5	30	5.25	0.93	0.328	0.59
EDH $AR = 1.6$ $p = 7.5$ mm			4.08	0.73	2.361	3.34
EAC $AR = 2.2$ $p = 20.0$ mm			5.70	0.77	0.664	0.99
Spherical particles			5.34	0.19	0.369	0.55
Cylindrical micro-channel matrix	2	30	6.10	0.19	0.271	0.40
EDH $AR = 1.6$ $p = 7.5$ mm			4.15	0.18	2.339	3.63
EAC $AR = 2.2$ $p = 20.0$ mm			5.67	0.18	0.630	0.92
Spherical particles			4.59	0.35	0.847	2.28
Cylindrical micro-channel matrix	2	50	3.95	0.45	0.647	2.29
EDH $AR = 1.6$ $p = 7.5$ mm			3.03	0.33	4.086	10.09
EAC $AR = 2.2$ $p = 20.0$ mm			4.85	0.32	1.124	2.88

Figure 3-4 presents performance of AMR with $\varepsilon = 0.54$ and $D_h = 0.13$. One can see that, in terms of maximum cooling power, AMR with cylindrical micro-channel matrix is outperformed by AMR with double corrugated flow patterns regardless of operational frequency. An interesting point here is that AMR with EDH $AR = 1.6$ $p = 7.5$ mm demonstrates the highest cooling power at lower operational frequency. However, AMR with EAC $AR = 2.2$ $p = 20.0$ mm establishes somewhat higher Q_{cool} than the latter regenerator at $v = 2$ Hz. More interestingly, the maximum cooling power, established by AMR with cylindrical micro-channel matrix and EAC $AR = 2.2$ $p = 20.0$ mm at $v = 0.5$ Hz, despite the changes in porosity of AMR, is rather similar to one reported in Figure 3-2 (a). It must be mentioned that the porosity of AMR affects mass of MCM per regenerator. Any difference in mass of MCM per regenerator leads to changes in obtainable cooling power. Moreover, it is noticeable that for higher porosity of AMR, the utilisation, necessary to obtain maximum Q_{cool}, increased almost twice, indicating that the required pump work is higher, as it is seen from Tables 3-3 and 3-4. However, AMR with EDH $AR = 1.6$ $p = 7.5$ mm showed slight decrease in Q_{cool} at $v = 0.5$ Hz. Moreover, it is noticeable that the maximum cooling power, established by AMR with cylindrical micro-channels and EAC $AR = 2.2$ $p = 20.0$ mm increases up to 24 % and 13 %, respectively, at $v = 2$ Hz once porosity of an AMR is increased by 50 %. On the other hand, maximum cooling power, established by AMR with EDH $AR = 1.6$ $p = 7.5$ mm decreases, by 20 % at the same conditions.
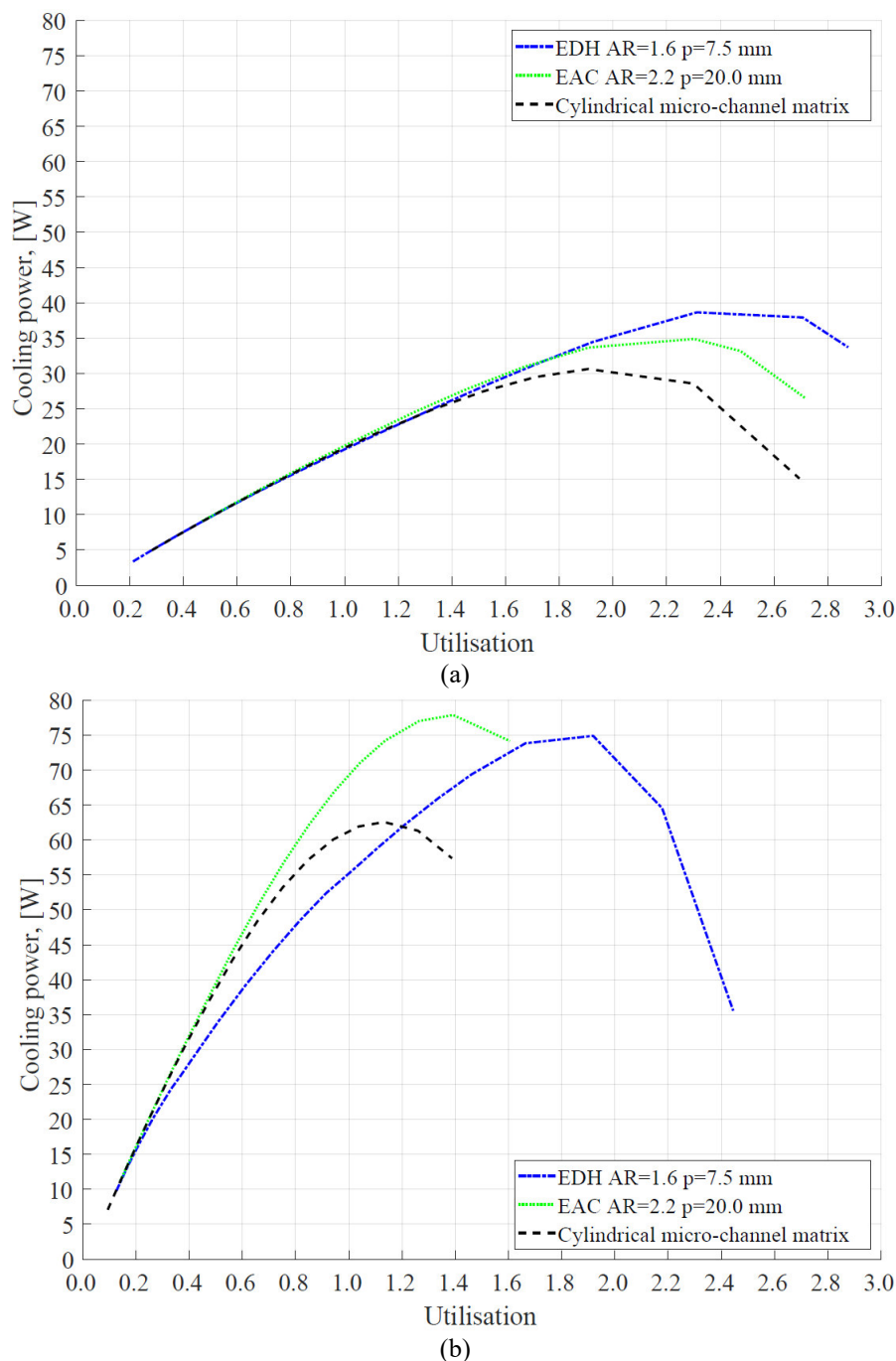
Figure 3-4. Cooling power established by the AMR with $\varepsilon = 0.54$ and $D_h = 0.13$ mm at (a) $v = 0.5$ Hz and (b) $v = 2$ Hz.

Figure 3-5 shows that, among AMR with $\varepsilon = 0.54$ and $D_h = 0.13$ mm, cylindrical micro-channel matrix establishes the highest *COP* regardless of operational frequency. Nevertheless, the AMR with EAC *AR* = 2.2 *p* = 20.0 mm demonstrates *COP* of 3.49 at $Q_{cool} = 70$ W and $v = 2$ Hz when $\varepsilon = 0.54$ and $D_h = 0.13$ mm, while this operational point is not achievable using AMR with, cylindrical micro-channel matrix. Moreover, AMR with packed spherical particles establishes *COP* of 3.08 at $Q_{cool} = 70$ W and $v = 2$ Hz, when $\varepsilon = 0.35$ and $D_h = 0.13$ mm, as it is seen from Figure 3-3. This indicates that AMR with EAC *AR* = 2.2 *p* =20.0 mm is more efficient from both performance and economical aspects considering the same hydraulic diameter of the flow channels. In other words, AMR with EAC *AR* = 2.2 *p* = 20.0 mm demonstrates potential to achieve higher *COP* using smaller amount of MCM. However, the analysed AMR with packed spherical particles has a technical advantage since it is easier to manufacture spherical particles that have required size of $D_p = 0.35$ mm, than an AMR with

$D_h = 0.13$ mm. Nevertheless, producing spherical particles that have uniform size, as it is assumed in this model, is challenging. Thus, theoretically predicted performance of any AMR is always somewhat higher in comparison with one, obtained experimentally.
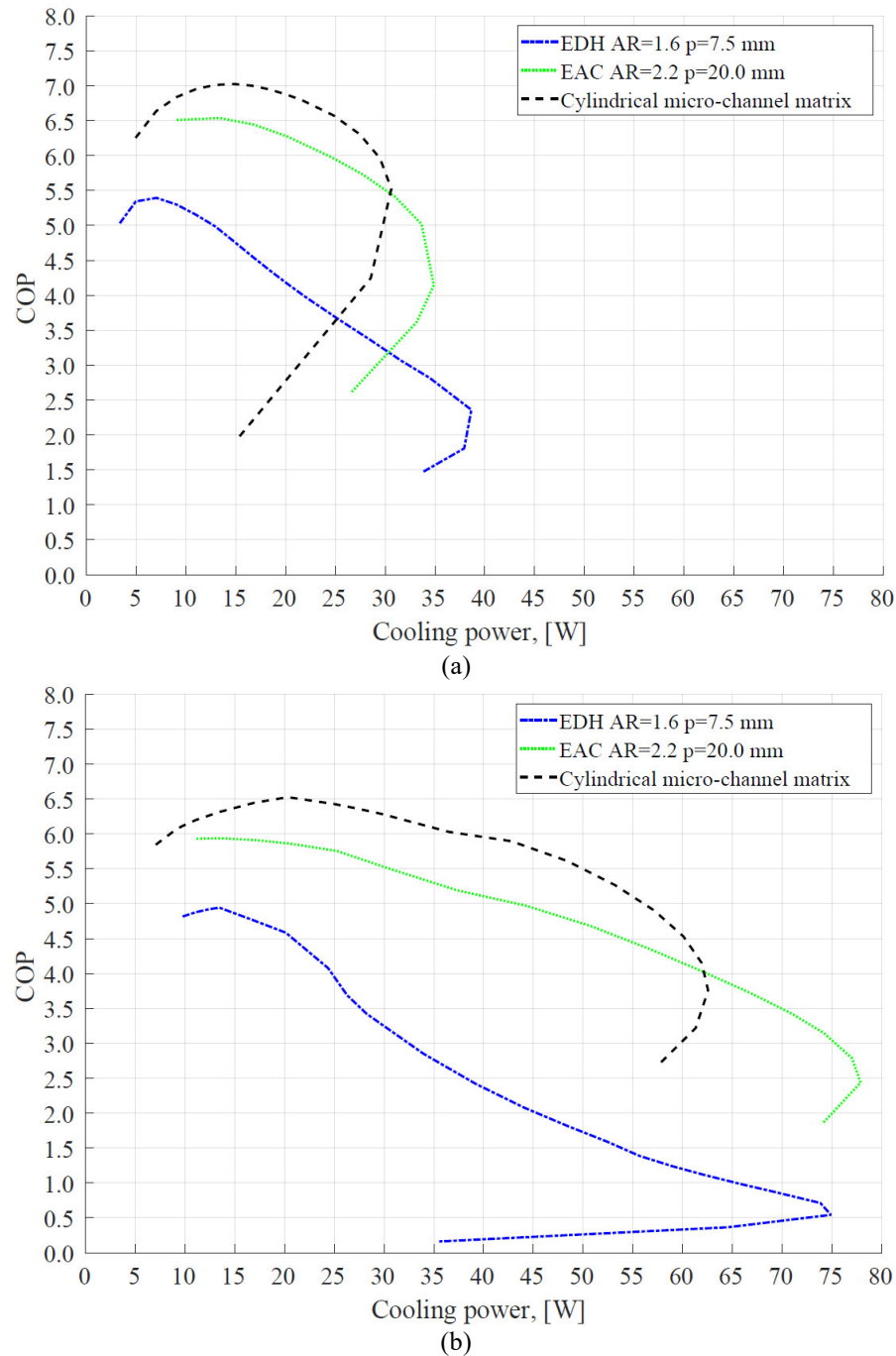
Figure 3-5. *COP* as a function of cooling power established by the AMR with $\varepsilon = 0.54$ and $D_h = 0.13$ mm at (a) $v = 0.5$ Hz and (b) $v = 2$ Hz.

Numerical results, obtained for AMR with $\varepsilon = 0.35$ and $D_h = 0.13$ mm, are summarized in Table 3-4. There it is seen that AMR with cylindrical micro-channel matrix shows slightly higher *COP* values at same Q_{cool} in comparison with AMR with double corrugated flow channels. Nevertheless, certain operational conditions, e.g. $Q_{cool} = 70$ W, is not possible to achieve using previous AMR geometry, where AMR with EAC $AR = 2.2$ $p = 20.0$ mm demonstrates sensible *COP* value of 3.49.

Table 3-4. *COP* of numerically analysed AMR geometries with $\varepsilon = 0.54$ and $D_h = 0.13$ mm.

AMR geometry	v, Hz	Q_{cool}, W	*COP*	Utilisation	Δp, bar	Pump work, W
Cylindrical micro-channel matrix	0.5	30	5.76	1.80	0.304	0.76
EDH *AR* = 1.6 *p* = 7.5 mm			3.22	1.63	2.483	5.55
EAC *AR* = 2.2 *p* = 20.0 mm			5.51	1.61	0.662	1.48
Cylindrical micro-channel matrix	2	30	6.28	0.38	0.26	0.54
EDH *AR* = 1.6 *p* = 7.5 mm			3.25	0.44	2.526	5.79
EAC *AR* = 2.2 *p* = 20.0 mm			5.53	0.37	0.623	1.31
Cylindrical micro-channel matrix	2	60	4.54	0.94	0.642	3.37
EDH *AR* = 1.6 *p* = 7.5 mm			1.20	1.14	6.645	39.67
EAC *AR* = 2.2 *p* = 20.0 mm			4.15	0.81	1.348	6.12
EDH *AR* = 1.6 *p* = 7.5 mm	2	70	0.87	1.49	8.53	66.05
EAC *AR* = 2.2 *p* = 20.0 mm			3.49	1.02	1.69	9.56

AMR with $\varepsilon = 0.54$ and $D_h = 0.35$ mm was analysed in order to see how an increase in a hydraulic diameter of flow channels affects the performance of AMR with double corrugated flow geometry. Figure 3-6 demonstrates that maximum cooling power of such an AMR decreases at least by 50 % in comparison with AMR with $\varepsilon = 0.54$ and $D_h = 0.13$ mm. One can see that maximum Q_{cool} is obtained with EDH *AR* = 1.6 *p* = 7.5 mm regardless of the operational frequency. Moreover, the maximum Q_{cool}, established by AMR with EDH *AR* = 1.6 *p* = 7.5 mm, is more than two times higher in comparison with other AMR geometries. Nevertheless, both double corrugated geometries demonstrate superior cooling power to the cylindrical micro-channel matrix.

From Figure 3-7 one can see that AMR with EDH *AR* = 1.6 *p* = 7.5 mm significantly outperforms other regenerators with $\varepsilon = 0.54$ $D_h = 0.35$ mm in terms of maximum cooling power and obtainable *COP*, regardless of the operational frequency. It is interesting to note that AMR with EDH *AR* = 1.6 *p* = 7.5 mm and $\varepsilon = 0.54$ and $D_h = 0.35$ mm provides $Q_{cool} = 40$ W at *COP* = 4.94. In comparison, AMR with cylindrical micro-channel matrix provides the same cooling power at *COP* = 5.95, when $\varepsilon = 0.54$ and $D_h = 0.13$ mm, and at *COP* = 5.55, when $\varepsilon = 0.36$ and $D_h = 0.13$ mm. As it was mentioned above, it is rather challenging to manufacture AMR with $D_h = 0.13$ mm. On the other hand, it was demonstrated experimentally that using laser beam melting technique one could manufacture AMR with D_h as small as 0.30 mm [38]. This provides an additional technical advantage to AMR with EDH *AR* = 1.6 *p* = 7.5 mm over an AMR with cylindrical micro-channels with $D_h = 0.13$ mm. Moreover, the mass of MCM is 28 % lower in AMR with $\varepsilon = 0.54$ than in one with $\varepsilon = 0.36$. Therefore, AMR with EDH *AR* = 1.6 *p* = 7.5 mm and $\varepsilon = 0.54$ has as well an economical advantage, since it would provide same cooling power at similar *COP* using less MCM.
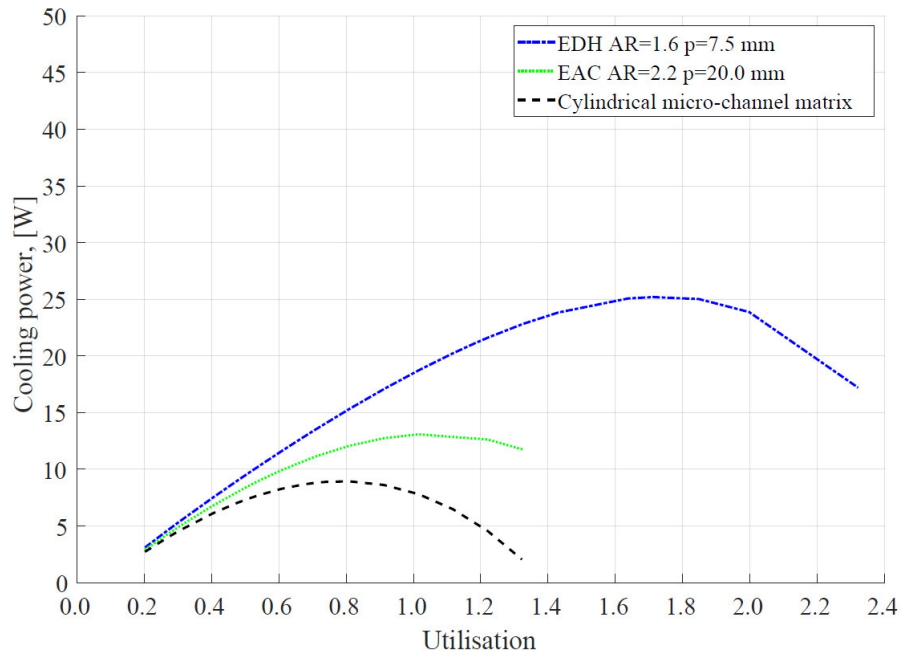
(a)
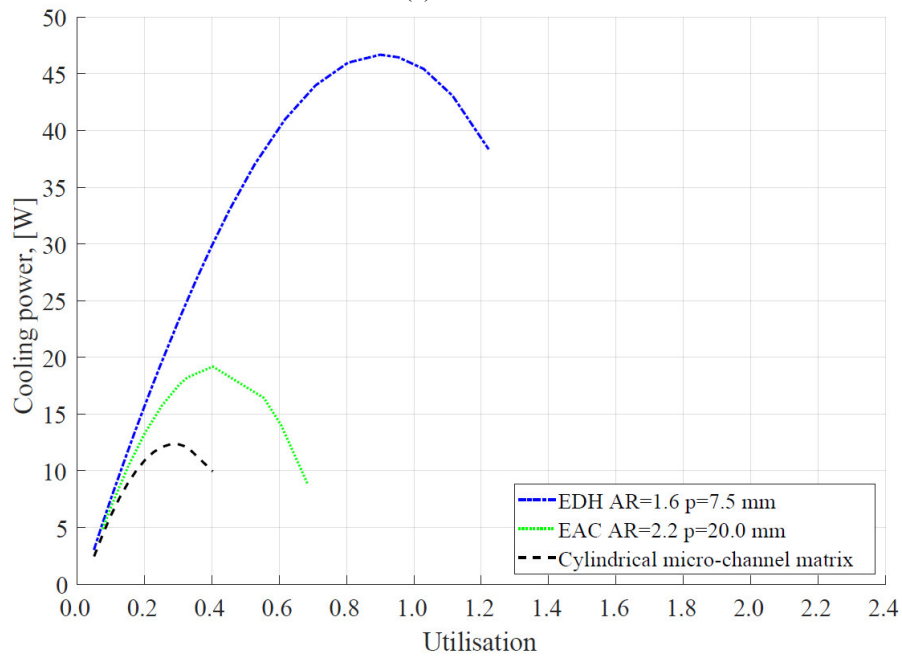
(b)
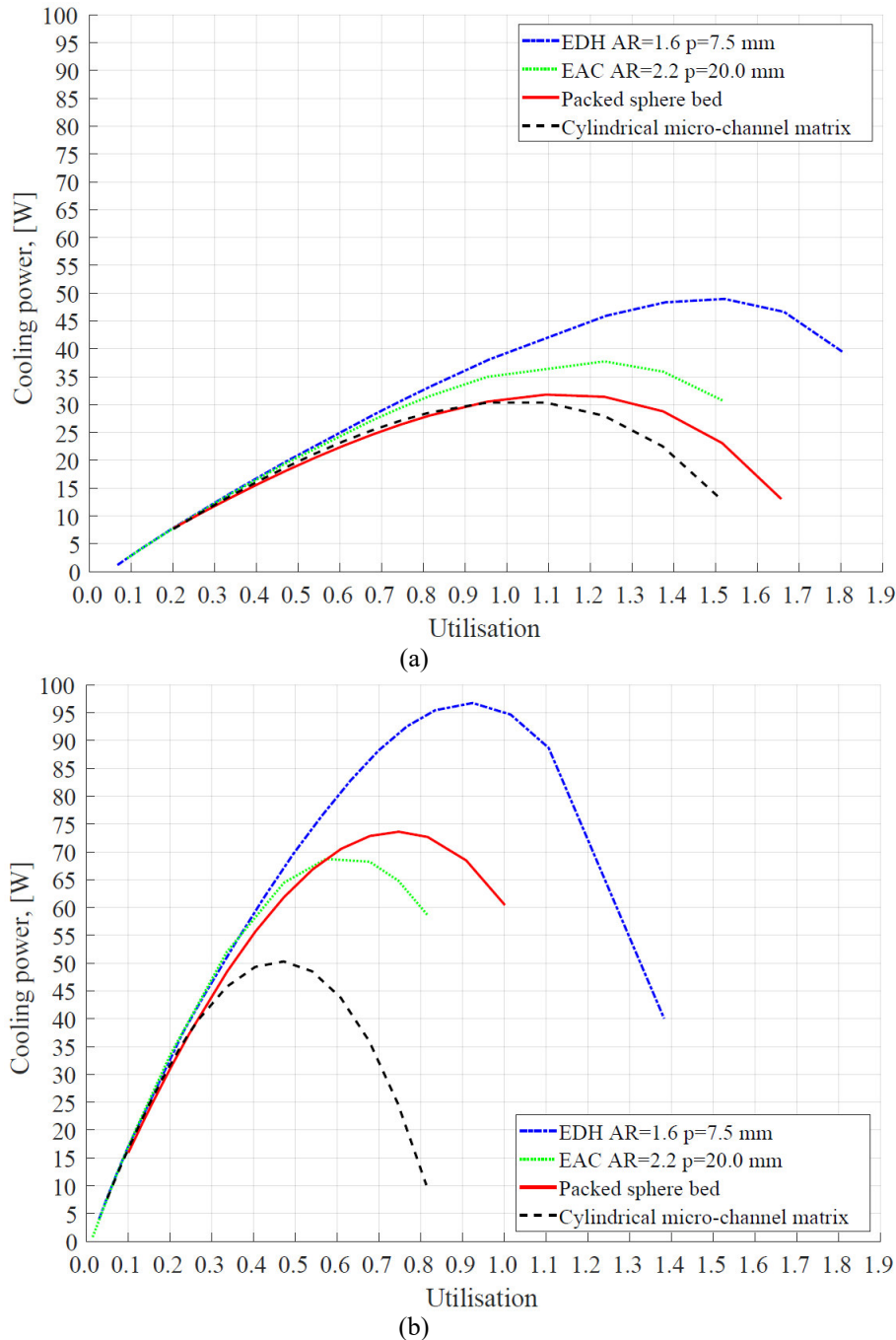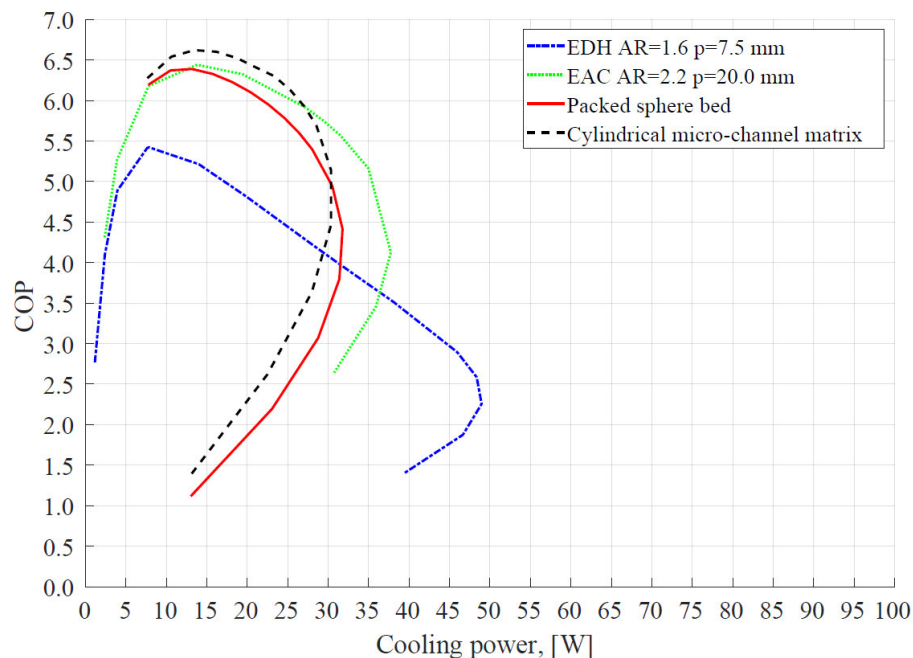
Figure 3-6. Cooling power established by the AMR with $\varepsilon = 0.54$ and $D_h = 0.35$ mm at (a) $v = 0.5$ Hz and (b) $v = 2$ Hz.

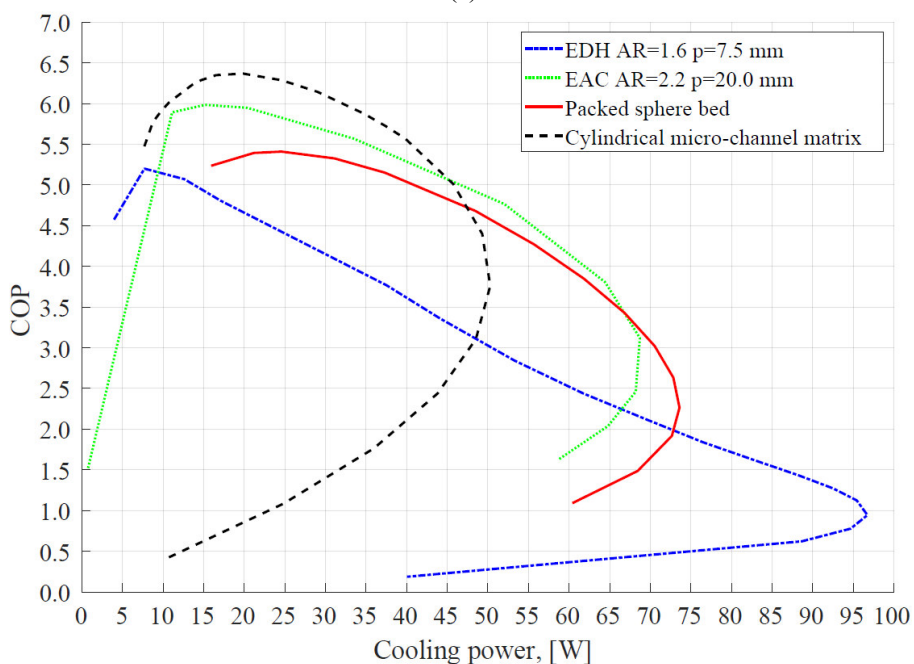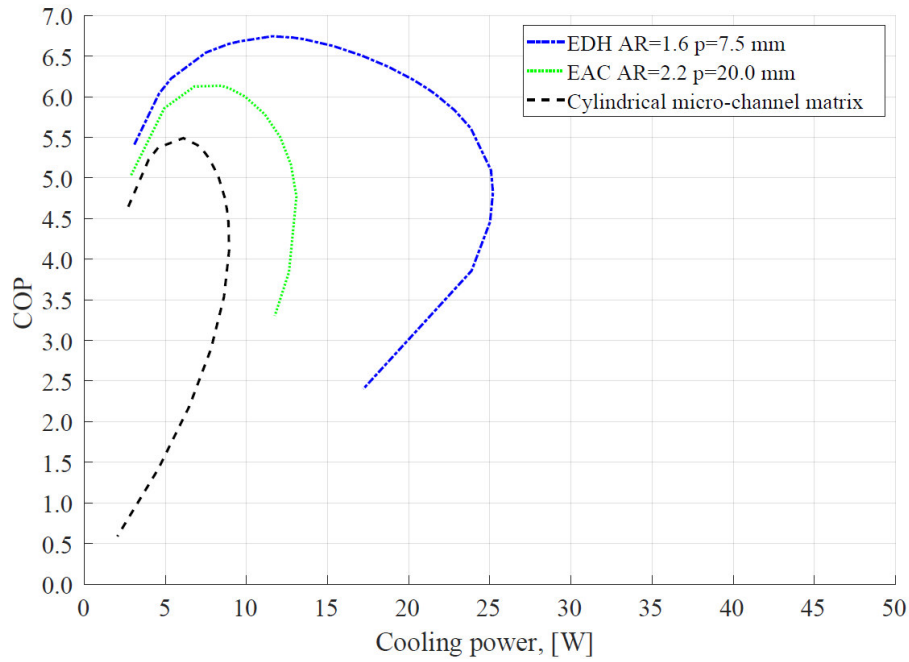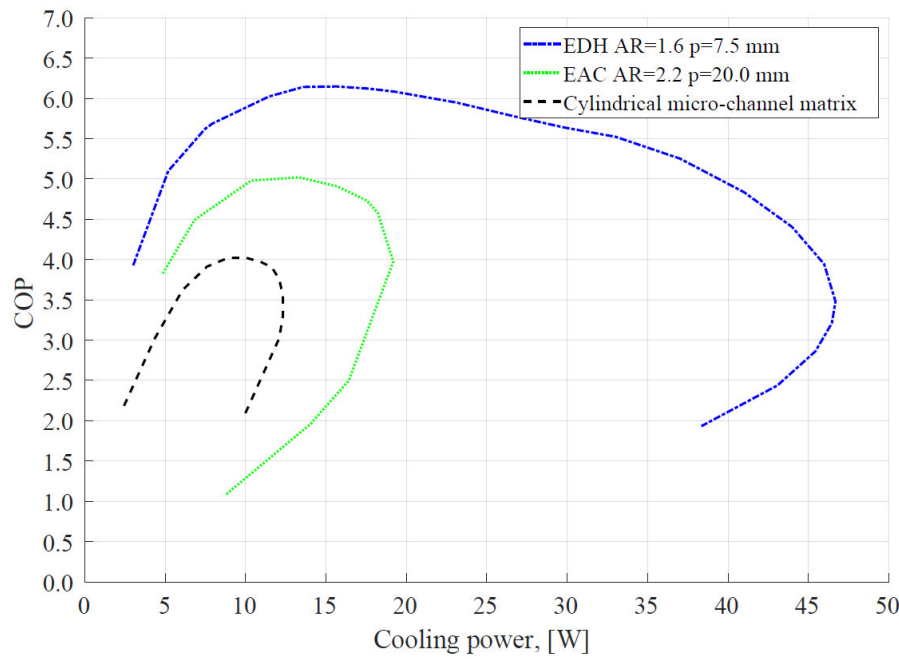Figure 3-7. *COP* as a function of cooling power established by the AMR with $\varepsilon = 0.54$ and $D_h = 0.35$ mm at (a) $v = 0.5$ Hz and (b) $v = 2$ Hz.

The performance for the AMR with coarser geometry was also compared in terms of fixed Q_{cool} and *COP*. The obtained results are presented in Table 3-5. Several values of Q_{cool} were selected for this analysis. The maximum obtainable Q_{cool} with cylindrical micro-channel matrix was 8 W, then 13 W and 19 W were selected for comparison of the performance of the AMRs with different double corrugated flow patterns. One can see that EDH *AR* = 1.6 *p* = 7.5 mm demonstrates significantly higher *COP* at the same Q_{cool} in comparison with the cylindrical micro-channel matrix or EAC *AR* = 2.2 *p* = 20.0 mm flow pattern. However, required pump work increases significantly for AMR with double corrugated flow geometry comparing to a cylindrical micro-channel matrix.

Table 3-5. *COP* of numerically analysed AMR geometries with $\varepsilon = 0.54$ and $D_h = 0.35$ mm.

AMR geometry	v, Hz	Q_{cool}, W	*COP*	Utilisation	Δp, bar	Pump work, W
Cylindrical micro-channel matrix	0.5	8	5.12	0.58	0.014	0.01
EDH *AR* = 1.6 *p* = 7.5 mm			6.58	0.43	0.092	0.06
EAC *AR* = 2.2 *p* = 20.0 mm			6.13	0.48	0.028	0.02
Cylindrical micro-channel matrix	2	8	3.95	0.13	0.013	0.01
EDH *AR* = 1.6 *p* = 7.5 mm			5.69	0.11	0.092	0.06
EAC *AR* = 2.2 *p* = 20.0 mm			4.66	0.12	0.027	0.02
EDH *AR* = 1.6 *p* = 7.5 mm	0.5	13	6.73	0.68	0.147	0.14
EAC *AR* = 2.2 *p* = 20.0 mm			4.87	0.99	0.057	0.08
EDH *AR* = 1.6 *p* = 7.5 mm	2	13	6.11	0.17	0.144	0.14
EAC *AR* = 2.2 *p* = 20.0 mm			5.02	0.20	0.045	0.05
EDH *AR* = 1.6 *p* = 7.5 mm	2	19	6.09	0.24	0.211	0.29
EAC *AR* = 2.2 *p* = 20.0 mm			4.09	0.39	0.090	0.20

The comparison of the Figures 3-2 – 3-7 suggests that considering possible technological limitations of manufacturing an AMR bed, performance could be enhanced by employing a suitable double corrugated geometry as a flow pattern for a porous AMR structure. It is interesting that the performance of an AMR with a double corrugated flow pattern strongly depends on combination of corrugation intensity, i.e. length of period and aspect ratio, and porosity of an AMR as well as hydraulic diameter of flow channels. As it is seen from results of this study, too intense double corrugation would even degrade the performance of an AMR with a fine geometry. On the other hand, the same corrugation intensity would strongly improve the performance of an AMR with coarser geometry. Moreover, as it is seen in Figure 3-7 and Table 3-5, that even a slight increase in heat transfer using intense corrugation, would enhance performance of an AMR. Nevertheless, higher improvement of the performance of an AMR using less intense corrugation is seen in case of finer AMR geometry. Moreover, as mentioned in Subsection 1.2.1, performance of an AMR strongly depends on combination of flow structure and shape of the AMR itself. Short and bulky regenerators favour packed beds of spherical or crushed particles, while long and skinny ones perform better with geometries, having structured flow channels, i.e. parallel plates, cylindrical micro-channel matrix, or double corrugated micro-channel matrix.

In addition, the initial results of this study suggests that *PEC* criterion is not relevant for selecting a flow pattern based on double corrugated geometry. *PEC* criterion was initially developed for evaluating global performance of enhanced geometries at the same operational conditions as for a reference geometry [65]. This criterion, after some modifications, could be used for evaluating performance of enhanced geometries at constant: pumping power; flow rate; heat transfer surface area; heating duty, and etc. [65]. However, none of these evaluation criteria provides boundary conditions, suitable for AMR application. For example, *PEC* with constant heating duty condition would lead to reduced length of an enhanced geometry. This is not applicable when performance of different AMR is compared. Moreover, *PEC* criterion has been developed for evaluating an enhanced heat transfer rate over increase in friction factor, i.e. an enhanced geometry is considered to be more efficient than a reference geometry if the previous demonstrates greater increase in Nusselt number than it is in friction factor. On the other hand, AMR geometries are compared in terms of constant cooling power. Thus, a more performance efficient AMR would demonstrate higher *COP* at the same Q_{cool}.

Finally, it is seen that the double corrugated geometry has a potential to be applied as a flow pattern for a porous AMR structure. However, a more comprehensive analysis is required in order to find an optimal set of parameters for constructing AMR beds with double corrugated flow patterns. Different aspect ratios of a regenerator as well as different length should be considered in future work. Moreover, different hydraulic diameters of the flow channels as well as various porosities should be considered in order to find the threshold of performance using different corrugation intensities.

4. Experimental investigation of active magnetic regenerators

As mentioned in Chapter 1, FOPT materials can provide larger MCE and thus, increase the efficiency of magnetic heat pumps. Nevertheless, application of FOPT materials is not a straightforward process. It requires a detailed investigation before implementing FOPT into an expensive large-scale machine such as a heat pump. Moreover, as it was emphasised in Section 1.2.1 and demonstrated in Chapter 3, geometrical characteristics of an AMR have a strong influence on the performance of a magnetocaloric heat pump in terms of cooling power and *COP*. One should take care of a precise temperature span between layers of MCM and amount of epoxy used for bonding particles into a regenerator as well as geometrical characteristics of the MCM.

In this chapter, results of an experimental investigation of various AMR are presented. It is structured in four sections, describing three different geometries of the tested regenerators. The tested regenerators were manufactured using FOPT materials. These materials were shaped into different flow structures. The experimental routine, described in Section 4.1, was similar for all the presented regenerators regardless of the used apparatus. Only the fifteen-layer regenerator was tested at KTH Royal Institute of Technology using the medium-scale rotary device, described in Subsection 1.3.10. The experimental results obtained in collaboration with a research group at KTH were published as conference proceedings in the International Conference on Caloric Cooling. The original article *C.1. Experimental investigation of fifteen-layer epoxy-bonded La(Fe,Mn,Si)$_{13}$H$_z$ active magnetic regenerator* is included in this thesis. All the other regenerators were characterized using the *Test machine* at DTU, described in Subsection 1.3.1. The experimental results on an AMR with stacked parallel plates are presented in Section 4.2. Section 4.3 is divided into two subsections that are focused on AMR with irregular particles. Section 4.4 is devoted to AMR with packed spherical particles. These results were published in peer-reviewed scientific journals. The corresponding articles: *P.3. Experimental and numerical comparison of multi-layered La(Fe,Si,Mn)$_{13}$H$_y$ active magnetic regenerators*, *P.4. Passive characterisation and active testing of epoxy bonded regenerators from room temperature magnetic refrigeration*, *P.5. Operational test of bonded magnetocaloric plates*, *P.6. From a magnet to a heat pump* and *C.3. Epoxy-bonded La(Fe,Mn,Si)$_{13}$H$_y$ as a multi layered active magnetic regenerator*, are included in this thesis.

4.1. Experimental procedure

In order to obtain a high performance of an AMR, several operational parameters must be carefully determined. Namely, they are the hot end temperature, T_{hot}, utilisation, U, and an operational frequency, v. The utilisation is defined in Eq. 4-1.

$$U = \frac{m_f c_{p_f}}{m_s c_{p_s}}$$

Eq. 4-1

Where m_f is fluid mass pushed through regenerator during one blow, m_s is mass of solid, c_p is specific heat capacity and subscripts f and s denote fluid and solid respectively. The utilisation is defined using the background value of c_{p_s} rather than the peak value. The heat transfer fluid used for all the experiments presented in this study was 2 vol. % aqueous solution of an anticorrosion inhibitor ENTEK FNE. Note that demineralised water was used as a base of the solution.

It is shown later in this chapter, that a slight deviation in any of these parameters compromises performance of any regenerator. Therefore, an experimental routine for determining the optimal operational conditions for any AMR was established. It generally consists of few steps, described further, that are applicable to any device and regenerator to be tested. The optimal value for each of the operational parameters is found varying one of them while holding other two constant.

Firstly, a series of experiments at no-load conditions are conducted varying utilisation at constant T_{hot} and v. Then, the U value, where the peak performance of an AMR was established, is selected and held constant as well as T_{hot}. From this series of experiments, the optimal value of the operational frequency is determined. Once optimal values of U and v are ascertained, a set of experiments to find the optimal T_{hot} is conducted. It is noticeable that the peak performance of each MCM is observed a few degrees above the Curie temperature, T_C, of the material [150]. Once a set of the optimal operational parameters is found, cooling load tests are carried out varying applied power, P, and holding T_{hot} and U constant. One should note that optimal utilisation point at no-load tests is not the same as for cooling-load tests. Thus, several different U values should be investigated at varying cooling load.

Determination of operational frequency and utilisation is an apparatus-specific task. The main differences between determining later parameters using the *Test machine* and the medium-scale prototype at KTH are explained further. The utilisation and the operational frequency of experiments using the later machine were controlled by setting the desired parameters in the software controlling the pump and the stepper motor.

On the other hand, the utilisation and the frequency of a process are controlled by changing a stroke and speed of a displacer in the *Test machine*. However, it is not straightforward to manipulate the operational frequency, when using this apparatus. It must be noted that frequency does change whenever utilisation or fluid velocity, v_f, of an process are changed. Thus, the determination of operational parameters using the *Test machine* was equivalently modified to optimisation of a stroke and speed of the displacer for finding optimal utilisation and fluid velocity, respectively. Thus, the first two steps of an experimental routine using the *Test machine* changed into determination of a displacer stroke, while holding T_{hot} and displacer velocity constant. Then displacer velocity is determined, while holding displacer stroke and T_{hot} constant. The rest of the procedure remains unchanged. Nevertheless, the experimental results, obtained with the *Test machine*, are presented in terms of utilisation. This enables a straightforward comparison of the investigated AMRs.

Finally, it must be noted that the testing routine was carried out in monotonically increasing manner of utilisation, hot end temperature and applied power, unless it is stated otherwise.

4.2. AMR with parallel plates

A $La_{0.85}Ce_{0.15}Fe_{11.25}Mn_{0.25}Si_{1.5}$ ingot was crushed into particles with maximum size of 350 μm. These particles, mixed with 5 wt. % of phenolic resin, were formed into plates using the hot pressing technique. The plates had dimension of 40 mm in height, 25 mm in width and 0.5 mm thickness. The plate manufacturing process as well as material characterisation are fully described in Ref. [28]. The plates were manufactured using a single MCM with a Curie temperature of 288 K and stacked to form a regenerator. A metal wire with the diameter of 0.25 mm was used as a spacer for creating fluid channels. It was previously demonstrated experimentally that the optimal plate spacing in order to obtain higher temperature span was 0.2 – 0.3 mm for this manufacturing routine [36]. Figure 4-1 (a) presents the stack of 25 plates used to build a regenerator, shown in Figure 4-1 (b). Mass of each plate was on average 2 g, thus the mass of the regenerator was 50 g. One can see that the height of flow channels varied due to uneven thickness of the plates. It was demonstrated numerically that uneven plate spacing leads to significant reduction of the performance of regenerators with parallel plates [151]. It must be mentioned that the plates were manually sanded in order to remove high edges that remained after hot pressing procedure. However, the plates had a slight curvature around the perimeter as it is seen in Figure 4-2. The surface profile measurements were done using a Cyberscan Vantage laser profilometer with resolution of 0.01 μm. Note that the white spots in Figure 4-2 were caused by shiny surface of the exposed particles that dissipated the laser beam.

(a)   (b)
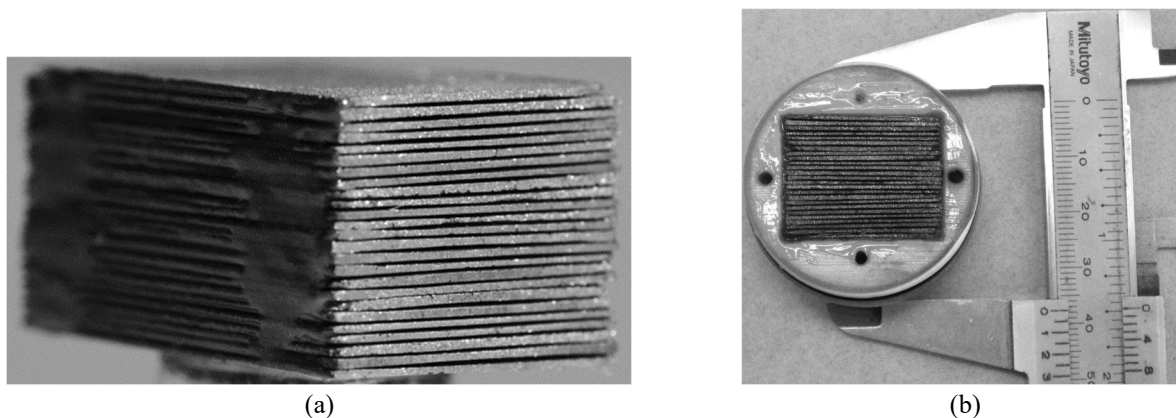
Figure 4-1. The AMR with stacked parallel plates (a) before and (b) after mounting into a plastic housing. Both pictures are slightly modified versions of the pictures presented in Refs. [28,42], respectively.
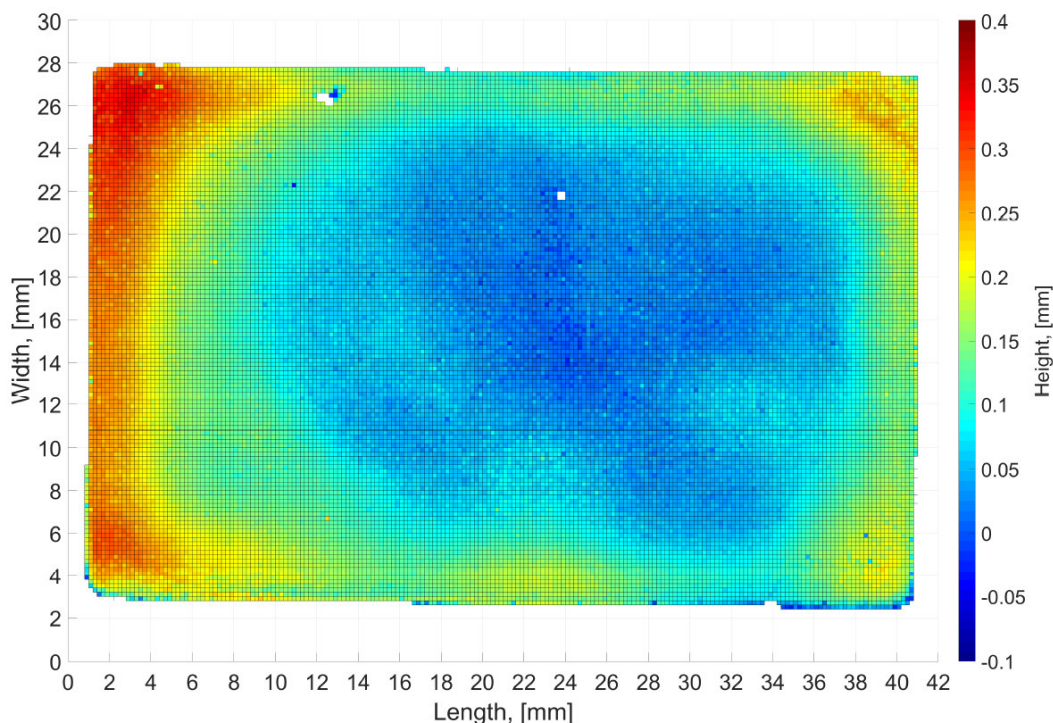
Figure 4-2. The surface of a sanded plate used in the stacked parallel plate regenerator, shown in Figure 4-1.

The regenerator was tested at no-load conditions only. The first series of experiments was started at T_{hot} = 290 K varying utilisation. Figure 4-3 shows that the optimal utilisation value was determined to be U = 0.23. It must be noted that the optimal fluid velocity, v_f, was found to be 7 mm/s. It is seen that the performance of the regenerator was highly sensible to utilisation.
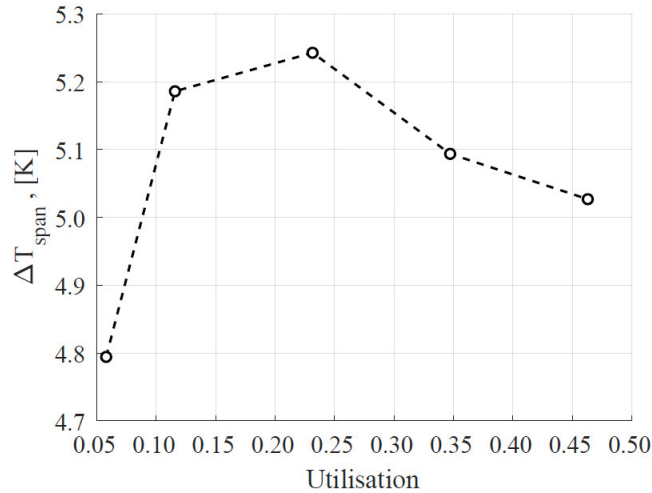
Figure 4-3. No-load temperature span, ΔT_{span}, as a function of an utilisation, U, at $T_{hot} = 290$ K. This figure is a slightly modified version of the figure published in Ref. [28].

Figure 4-4 shows that the maximum temperature span of 6.5 K was obtained at $T_{hot} = 291.8$ K, $U = 0.23$ and $v_f = 7$ mm/s. This low performance might be attributed to many different reasons. Firstly, the amount of resin used to bond the crushed particles was rather high and led to significant reduction of thermal properties of the manufactured plates [28]. Moreover, uneven flow channel thickness negatively affected the performance of the regenerator. Nevertheless, the performance of AMRs, produced using hot pressing technique, could be significantly improved by producing multi-layered plates as it was successfully demonstrated by side-by-side tape casting technique [152]. An amount of resin used for plate manufacturing also could be optimized. Lastly, manufacturing process should be improved in order to produce thinner and flatter plates [28].
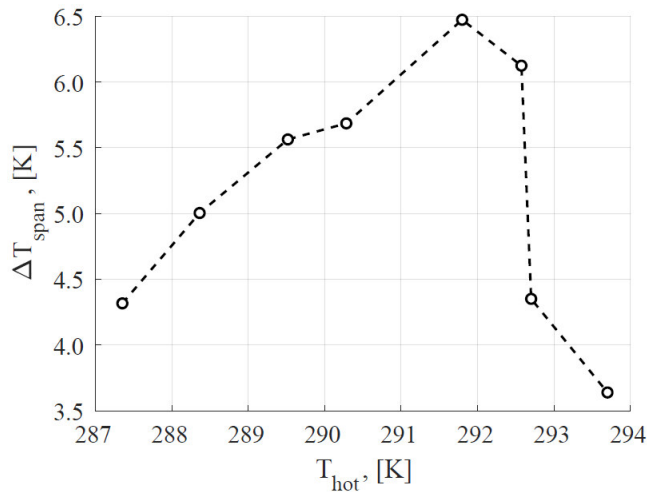
Figure 4-4. No-load temperature span, ΔT_{span}, as a function of a hot end temperature, T_{hot}, at $U = 0.23$. This figure is a slightly modified version of the figure published in Ref. [28].

Finally, a relatively low temperature span is rather common for single-layered FOPT materials. Similar performance using the same device was also observed for single layer LaFeCoSi and LaCaSrMnO materials [153,154]. The temperature span established by LaFeCoSi material was increased by layering the regenerator [153]. It was also strongly emphasised that one should take a good care when selecting Curie temperatures of the MCM for a multi-layered regenerator.

4.3. AMRs with irregular particles

Several independent experimental studies were conducted on AMRs with packed irregular particles during this PhD project. The tested AMRs varied in number of layers, particle size, amount of epoxy and Curie temperatures of AMRs. Moreover, the two different machines were used for experimental investigation. Besides, AMRs having comparable characteristics were tested using the *Test machine*, while the distinct regenerator was tested using the device at KTH. Therefore, the obtained results are grouped according the device used for experimental investigation.

4.3.1. AMR tested with the Test machine

Active magnetic regenerators with packed irregular particles, made of $La(Fe,Si,Mn)_{13}H_y$, were provided by Vacuumschmelze GmbH. Those AMR were constructed in two, five and nine layers of MCM. Irregularly shaped particles in a size range between 250 μm and 450 μm were epoxy bonded into a plastic housing. The dimensions of the housing were 40 mm height and 30 mm and 34 mm internal diameter for two-layered AMRs and five- and nine-layered AMRs, respectively.

It must be emphasised that the experimental study on AMRs with irregular particles was conducted in two steps. Firstly, four AMRs were constructed having two layers of $La(Fe,Si,Mn)_{13}H_y$ with different T_C between layers. The amount of epoxy in those regenerators varied from 1 wt. % to 4 wt. %. The aim of this part of the study was to find the minimum amount of epoxy, required to maintain mechanical integrity of an AMR bed, without compromising its performance.

The second step of the study was experimental characterisation of AMR beds with five and nine layers of FOPT material. Those regenerators were constructed using the same MCM with different T_C between the layers. The amount of epoxy that was found to be optimal amount in the first step of the study was used to bond MCM. Curie temperature of the material used in the investigated AMR was measured as reported in Refs. [30,32].

Figure 4-5 presents one of the AMR tested in this study. It must be noted that all of the AMRs with irregular particles looked identically. Therefore, pictures of one regenerator are presented here.

(a)   (b)
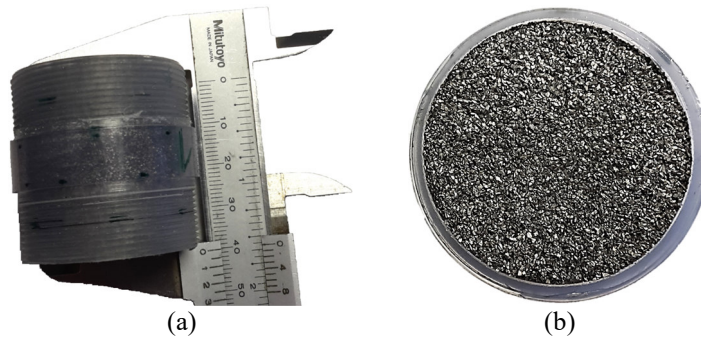
Figure 4-5. The AMR with five layers before testing a) side view; b) top view.

The characteristics of the tested regenerators are given in Table 4-1. The porosity, ε, reported there is calculated as given in Eq. 4-2.

$$\varepsilon = 1 - \frac{\dfrac{m_s}{\rho_s} + \dfrac{m_e}{\rho_e}}{V_h} \qquad \text{Eq. 4-2}$$

Where V_h is the total inner volume of the AMR housing. The subscripts s and e denote solid and epoxy, respectively. The values for ρ_s and ρ_e were 7000 kg/m³ and 1250 kg/m³, respectively [32].

From Table 4-1 one can see that the porosity of the AMRs varied within 7 %. The regenerator with the smallest amount of epoxy had the highest porosity, while the one with the biggest amount of

epoxy had the lowest porosity. It must be noted that the AMRs with five and nine layers had significantly higher mass of MCM in comparison to regenerators having two layers. This is because the volume of the housing of the previous AMRs was significantly larger. From Table 4-1 it is also seen that the mass fraction of MCM with a certain T_C varied rather strongly between layers. This is also seen in Figure 4-6.

Table 4-1. The characteristics of the experimentally investigated AMR with irregular particles.

Number of layers	Overall mass of MCM, m, g	Mass fraction of each MCM layer in the regenerator, wt. %	Porosity, ε, vol. %	Mass fraction of epoxy, wt. %
Two	94.1	53.0; 47.0	50	1
	93.1	53.7; 46.3	48	2
	93.0	52.5; 47.5	45	3
	91.2	54.0; 46.0	43	4
Five	122.9	23.6; 19.6; 19.8; 17.4	47	2
Nine	126.0	13.2; 11.9; 10.5; 10.4; 10.7; 11.5; 11.7; 10.4; 9.9	45	

Figure 4-6 shows the distribution of Curie temperatures along the tested regenerators with respect to mass fraction of each layer and the reference lines representing the ideal regenerators for AMR with two, five and nine layers. One can see that the thickness of the layers in the samples was slightly varying. It must be emphasised that the samples with two layers and varying amount of epoxy had similar MCM fraction resulting in slightly thicker layer with the lowest T_C. Note that the temperature span between the cold (a layer with the lowest T_C) and the hot (a layer with highest T_C) ends was T_{span} = 3.3 K for the AMRs with two layers and T_{span} = 14.7 K for five- and nine-layered AMRs. The regenerator with nine layers had intermediate T_C comparing to five-layered AMR.
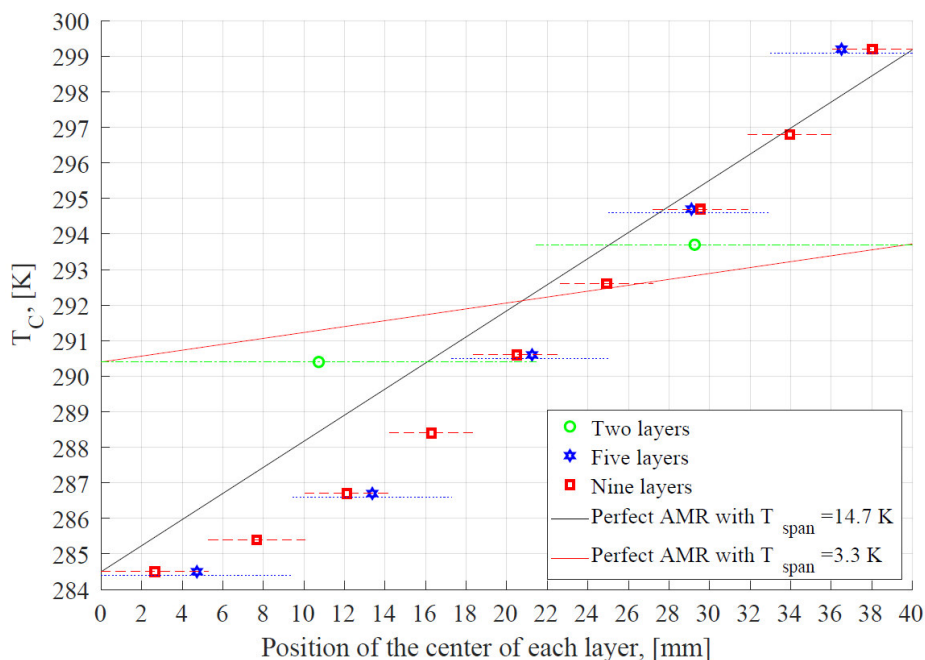
Figure 4-6. A Curie temperature distribution along the AMRs with irregular particles.

It must be mentioned that the regenerators and in particular the properties of the used MCM are fully described in Refs. [8,155]. Findings of this study and experimental investigation of the regenerator with packed spheres, presented in Section 4.4, served for a purpose of designing regenerator beds for *MagQueen*, described in Subsection 1.3.9.

4.3.1.1. Effect of epoxy bonding

It is seen from Table 4-1 that the AMRs with two layers and different amount of epoxy just slightly varied from each other. Therefore, the procedure for finding optimal operational parameters for the regenerators was carried out only for one sample. Namely, it was the AMR with 2 wt. % of epoxy. It must be mentioned, that the regenerator with 1 wt. % of epoxy could withstand only three tests until losing its mechanical integrity. Thus, the AMR with 2 wt. % was used for determining the optimal operational parameters. It was found to be $U = 0.45$ and $v_f = 8.2$ mm/s. The remaining samples were examined at different T_{hot} holding the same operational parameters as for the AMR with 2 wt. % of epoxy. The operational frequency was approximately 0.15 Hz [32].

Figure 4-7 demonstrates the performance of the AMRs with two layers and different amount of epoxy. Note that the regenerator with 1 wt. % of epoxy was excluded from the figure because of the breakage. One can see from Figure 4-7 that the regenerator with the lowest amount of epoxy established the highest ΔT_{span} of 13.6 K. The lowest temperature span ΔT_{span} of 12.2 K was obtained with the sample having 4 wt. % epoxy. One can also see that the difference between T_{hot}, where the maximum ΔT_{span} was observed, was shifted by 0.9 K between the regenerators with 2 and 4 wt. %. However, T_{hot}, where the peak performance of the regenerator with 3 wt. % of epoxy was obtained, was somewhat similar to the sample with 2 wt. % of epoxy. This can be explained by the difference in mass of MCM among the regenerators as well as the mass fraction of each layer in the AMRs. One can see from Table 4-1, that the regenerators with 2 and 3 wt. % of epoxy are more similar to each other than to the sample with 4 wt. % of epoxy. Several authors have observed numerically and experimentally that even a slight deviation in mass fraction of MCM or T_C affects the performance of an AMR significantly [19,22,43].
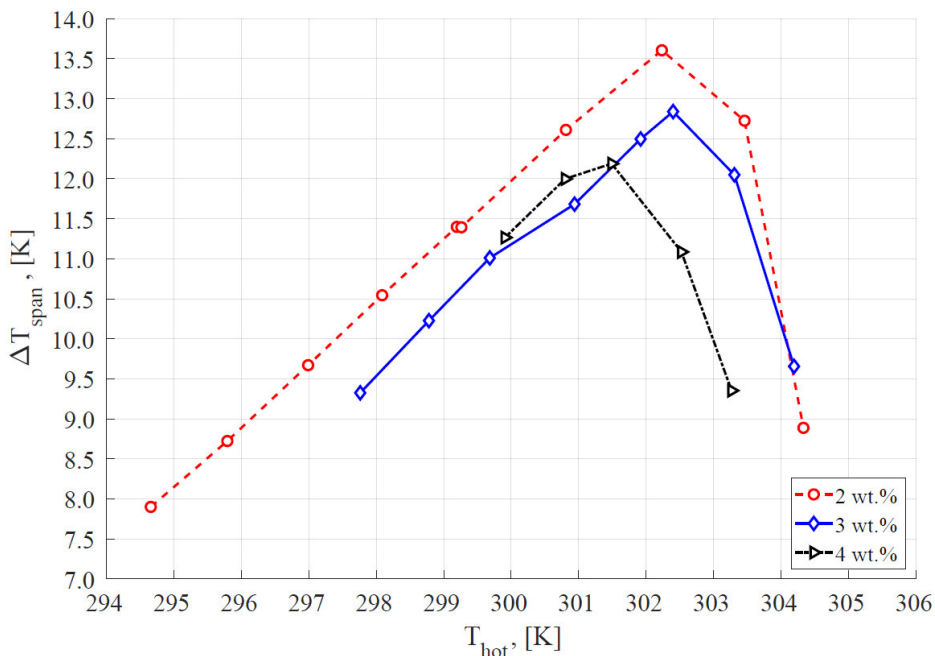
Figure 4-7. No-load temperature span, ΔT_{span}, as a function of a hot end temperature, T_{hot}, for the AMRs with two layers and varying amount of epoxy, at $U = 0.45$ and $v_f = 8.2$ mm/s. This figure is a slightly modified version of the figure published in Ref. [42].

It is obvious that even a slight amount of epoxy degrades the performance of the tested AMRs. However, as it was observed form the sample with 1 wt. % of epoxy, a certain amount of a bonding agent is required in order to assure mechanical properties of a regenerator. It was concluded, in this step of the study, that 2 wt. % is a sufficient amount of epoxy in order to maintain the mechanical stability of the regenerator without significantly compromising the performance.

4.3.1.2. Effect of layering MCM

The optimal fluid velocity for the AMR with five and nine layers was find to be 21.7 mm/s and 22.7 mm/s, respectively [32]. Figure 4-8 presents the temperature span, ΔT_{span}, as a function of utilisation, U. It must be noted that the same fluid mass was pushed through both regenerators, however differences in utilisation are due to slightly different mass of the AMRs. One can see that the utilisation merely has a significant effect on performance of the regenerators in the range from $U = 0.3$ to $U = 0.9$, unlike as for the single layered AMR, presented in Section 4.2. This kind of behaviour of multi-layered regenerator was also observed by other authors [8]. It could be explained as an effect of varying specific heat capacity of the solid, c_{p_s}. It is highly dependent on temperature [155]. Therefore, at the same T_{hot} every single layer in the regenerator has different c_{p_s}, resulting in varying U for each layer. As it was mention in Section 4.1, U is calculated using the background value of c_{p_s}, determined for the whole regenerator rather than a single layer. Consequently, the range of U, where the peak of no-load performance is observed for multi-layered regenerators, becomes broader. It is also interesting to note that the performance of the AMRs with five and nine layers is rather similar. The maximum no-load temperature span ΔT_{span} of 20.9 K and 20.7 K was observed for the regenerator with five and nine layers, respectively.
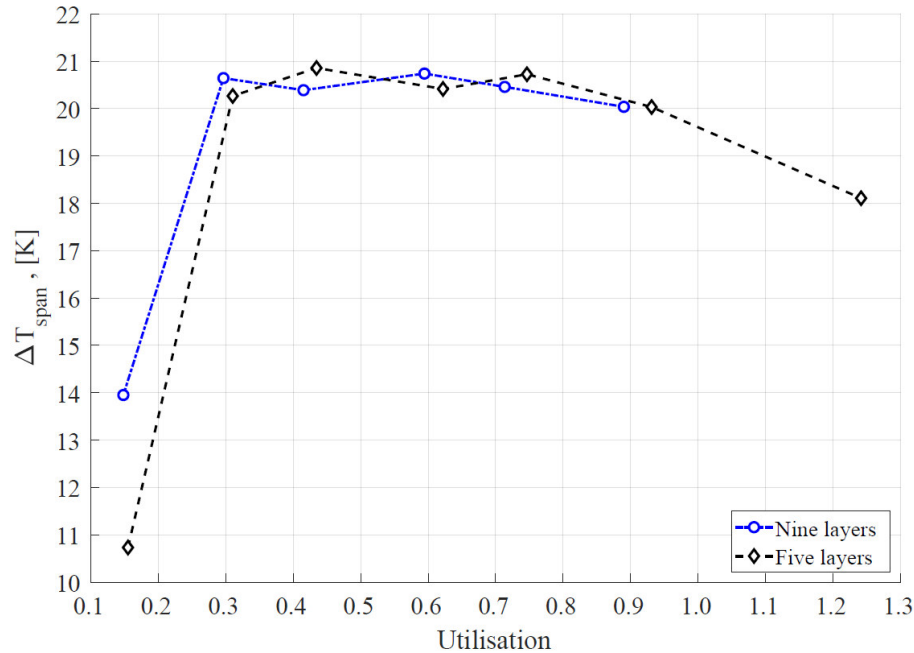
Figure 4-8. No-load temperature span, ΔT_{span}, as a function of an utilisation, U, at $T_{hot} = 303$ K.

It was observed from numerical and experimental investigations that multi-layered regenerators are very sensitive to even slight changes of operational conditions [19,22,43]. From Figures 4-9 and 4-10, it is clear that the tested five- and nine-layered AMRs demonstrated very strong sensitivity to the operational conditions. One can see that the performance of the investigated regenerators strongly depends on T_{hot} as well as on utilisation at higher hot end temperature $T_{hot} = 305.5$ K and the same v_f values of 21.7 mm/s and 22.7 mm/s for five- and nine-layered regenerators, respectively. It is also noticeable that no-load temperature span was approximately 40 % of the temperature span, established at the optimal T_{hot}. This phenomenon shows that the MCM layers with lower T_C in both regenerators were inactive during the operation at higher working temperatures. From Figure 4-10, one also can see that the regenerator with nine layers was more sensitive to changes in operational parameters than one with five layers.
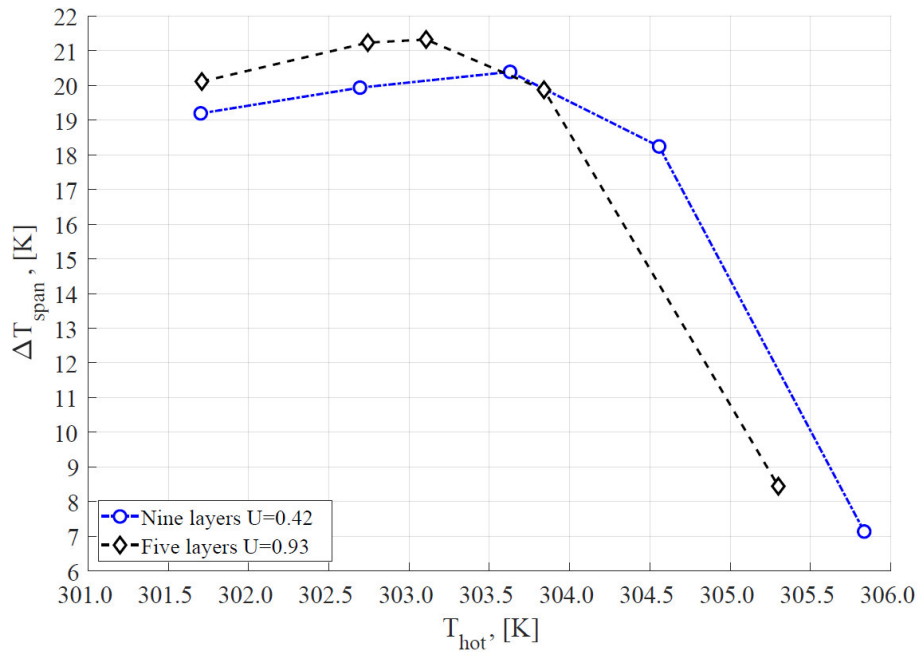
Figure 4-9. No-load temperature span, ΔT_{span}, as a function of a hot end temperature, T_{hot}.
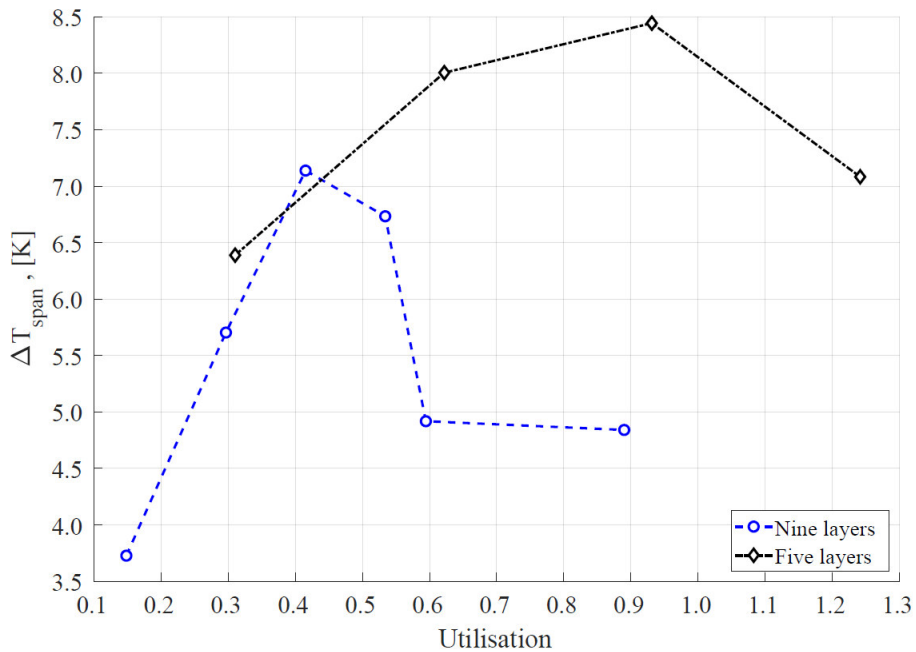
Figure 4-10. No-load temperature span, ΔT_{span}, as a function of an utilisation, U, at $T_{hot} = 305.5$ K.

The no-load performance of the AMRs with five and nine layers was modelled using the one-dimensional model, described in Section 3.1. It must be mentioned that epoxy was not included in the model. It is because the effect of epoxy on performance of an AMR is of the same magnitude as the inaccuracy of the model itself [32]. Figure 4-11 demonstrates comparison of the experimental and numerical results. It is seen that the numerical model predicts performance of the regenerators very well in terms of the peak temperature span. On the other hand, the model predicted slightly broader range of working temperature. However, this difference between the numerical and experimental results can be attributed to various imperfections of the physical regenerators. One should remember that numerical models are incapable of capturing imperfections inherited from fabrication process, such as uneven porosity or uneven particle size.
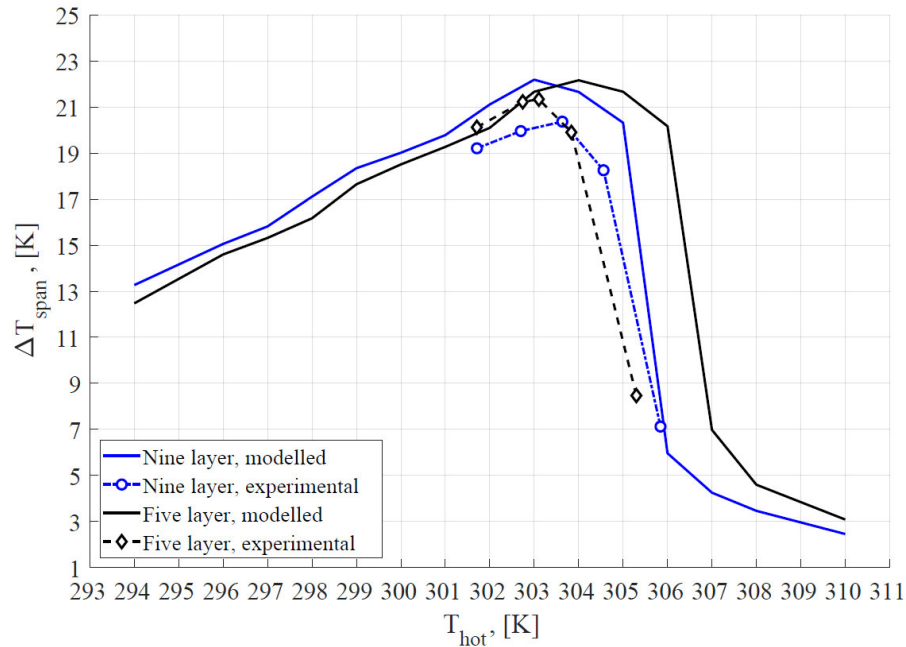
Figure 4-11. Comparison of the results obtained experimentally and numerically using the one-dimensional model, presented in Section 3.1.

The five- and nine-layered regenerators were tested against cooling load, Q_{cool}. It was observed that performance of both regenerators was rather similar. Thus, only results of the regenerator with five layers are presented. Figure 4-12 demonstrates that the maximum specific cooling power obtained with the AMR with five layers is 26.9 W/kg at zero temperature span at $U = 0.75$. Note that the cooling load results are presented in terms of specific cooling power due to different mass of the tested regenerators. In order to enable a direct comparison of performance of different regenerators, the applied cooling power, Q_{cool}, had to be converted to the specific cooling power. Form Figure 4-12, one can see that the intermediate utilisation of $U = 0.75$ was found to be the optimal value for maximum performance at cooling load tests. This phenomenon shows that the fluid flow rate at $U = 0.75$ was sufficient to transfer the generated heat from the heated cold end through the AMR bed and maintain the working temperature close to the transitional temperature of each layer of MCM. It is noticeable that the specific cooling power decreases drastically at high temperature span. Similar behaviour of FOPT and SOPT materials was observed by other authors [43,156,157] as well. This is because the working temperature exceeds the Curie temperature of the used materials and high MCE is no longer observed. The specific cooling power obtained over the temperature span ΔT_{span} of 15 K was 17.6 W/kg and 11.4 W/kg for the five- and nine-layered AMR, respectively, at the utilisation of $U = 0.75$ and $U = 0.59$, respectively.
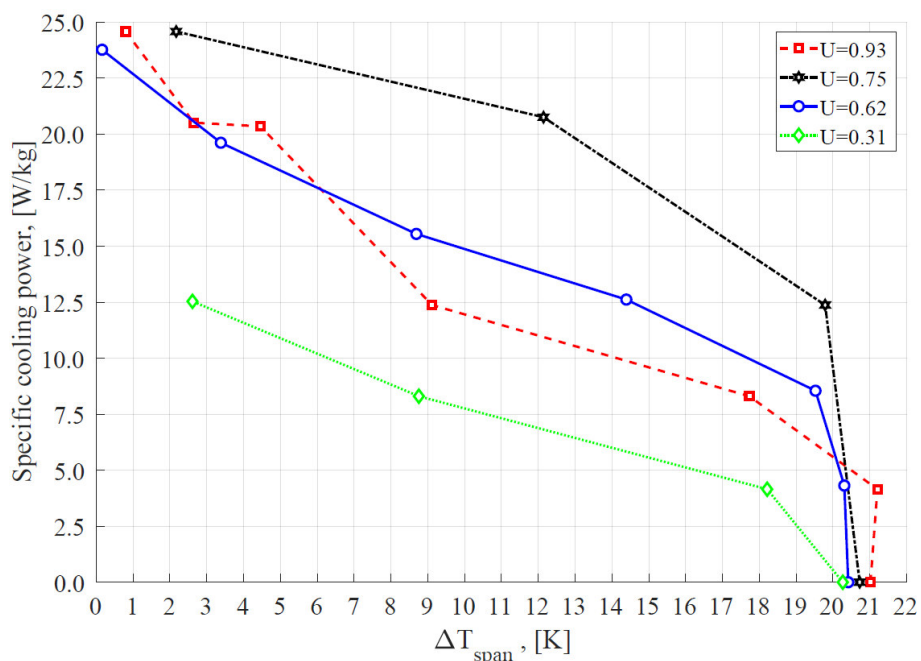
Figure 4-12. Specific cooling load applied on the regenerator with five layers as a function of a temperature span, ΔT_{span}, at T_{hot} = 303 K.

It must be mentioned that the experimental investigation of the regenerators with five and nine layers took around six months. During this period, it was noticed that the performance of the AMRs started degrading. Figure 4-13 shows the decrease in performance of the AMR with five layers at U = 0.75 and $_{Thot}$ = 303 K. One can see that the maximum specific cooling power obtained at the temperature span ΔT_{span} of 15 K was 8.6 W/kg at the same utilisation of U = 0.75 and hot end temperature T_{hot} of 303 K. This is approximately 50 % of the initial performance.

An interesting observation in Figure 4-13 is that a higher no-load temperature span was obtained twelve days after the initial cooling load test. This kind of phenomenon is observable at the beginning of degradation process. The mechanical disintegration of an AMR is the consequence of breakdown of MCM particles. They break into smaller particles and causes rearrangement of flow channels inside the porous structure. At the beginning of degradation, a slight rearrangement of flow structure could lead to slightly higher heat transfer performance. Eventually, the flow channels would be clogged by loose particles causing the vital failure of an AMR [10]. The mechanical breakage of particles also causes changes in different Curie temperatures of each piece of the broken particle [155]. The disintegration of the tested AMR finally led the full leakage of the system and flow bypass around the MCM. The degradation tests could not be performed on the nine-layered AMR. The regenerator reached the last stage of the degradation by the time experiments could be carried out. After the five- and nine-layered regenerators were dried using compressed air that also cleaned them from loose particles, the measurements of magnetic properties of the materials were carried out. Small amount of MCM from the top and the bottom of each regenerator were scraped and analysed using vibrating sample magnetometer (VSM) [32]. No changes in magnetic properties were observed.
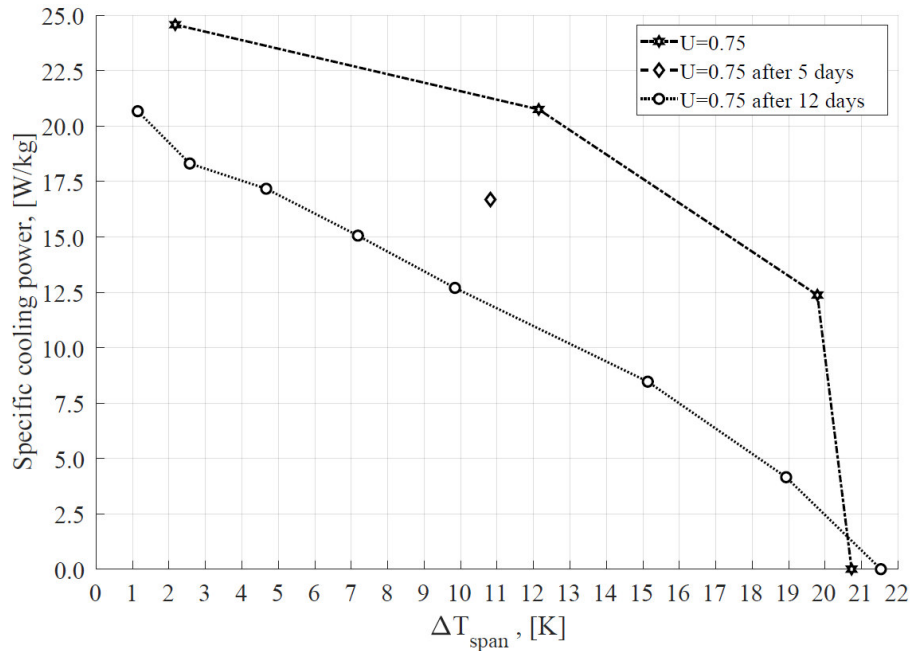
Figure 4-13. Comparison of the initial and repeated performance of the regenerator with five layers at $U = 0.75$ and T_{hot} = 303 K. This figure is a slightly modified version of the figure published in Ref. [32].

Finally, it was observed that the regenerators with five and nine layers tend to lose particles, mostly from the top layer, during cycling, while the AMR with two layers of MCM and 2 wt. % of epoxy did not show similar behaviour. The total mass that the regenerators with five and nine layers lost during the testing was 4.2 and 2.2 g, respectively. The magnetic forces that the five- and nine-layered regenerators exhibited were higher than for the regenerators with two layers. Thus, it would be recommended to use slightly higher amount of epoxy for bonding particles in multi-layered AMRs.

4.3.2. AMR tested with the medium-scale prototype at KTH

The AMR with fifteen layers of irregularly shaped La(Fe,Mn,Si)$_{13}$H$_y$ particles was tested using the medium-scale magnetocaloric device at KTH. The particle size was in the range from 600 to 800 µm. Those particles were bonded into a plastic housing using 2.3 wt. % of epoxy by Vacuumschmelze GmbH. As it is seen in Figure 4-14, two beds, 90° apart, of the housing were filled with particles. The height of the housing was 150 mm and the cross-section of each bed was 207 mm².
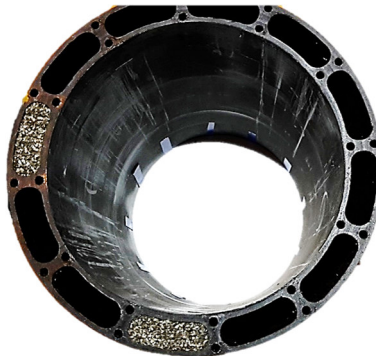
Figure 4-14. The regenerator housing with two beds filled with fifteen layer of La(Fe,Mn,Si)$_{13}$H$_y$. This figure is a slightly modified version of the figure published in Ref. [31].

The Curie temperatures of the used material were sorted manually [158]. All the particles were poured in a thermal bath at the certain temperature. Then a magnetic field was applied to attract

particles having that specific Curie temperature. The magnet then was brushed in order to detach loosely attracted particles. The particles that remained on the magnet were brushed to a plastic container. The temperature of the thermal bath then was lowered by one degree and the procedure was repeated [158]. It must be mentioned that T_C values, obtained using this method, would be different from ones, measured using VSM. This is because manually sorted particles were the most magnetic at a given temperature and magnetic field. On the other hand, using VSM, the Curie temperature is determined at the temperature, when material shows no magnetization at low magnetic field. Nevertheless, here, Curie temperature was used only for planning experiments since the MCM for building the AMR was reused from previous studies and the most important details was to maintain consistency in temperature span between neighbouring layers when constructing the AMR. Moreover, in case of determining too high or too low T_C of the used MCM, the peak performance at no-load experiments of the investigated regenerator would be shifted to the left or right side of the axis of the hot end temperature, T_{hot}, respectively, with respect to the expected value of T_{hot}.

Figure 4-15 represents Curie temperature distribution along the tested regenerators with respect of the mass fraction of MCM in each layer. It was assumed that both regenerators were identical with the same distribution of MCM, epoxy and porosity. The Curie temperature of the used MCM was in the range from 278 K to 292 K. The T_C step was 1 K between neighbouring layers. One can see that the regenerators were nearly perfect. Only two layers were constructed with lower mass fraction, namely the sixth and the last layers had mass fraction of 6.36 % and 2.10 % respectively. All other layers were evenly distributed along the regenerator and had mass fraction of 7.04 %.
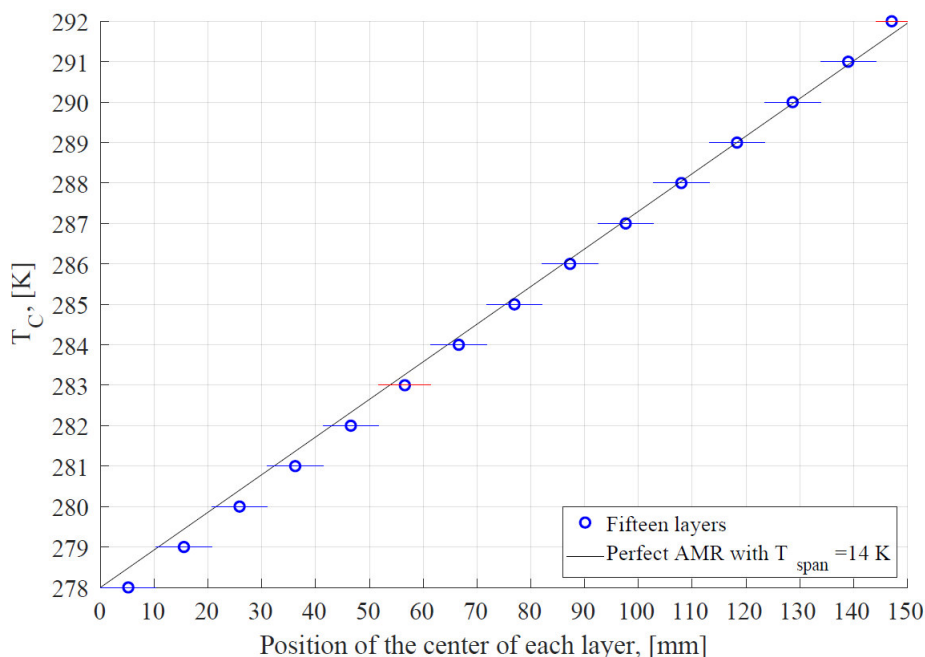
Figure 4-15. Curie temperature distribution along the fifteen-layered AMR. Red lines represent layers containing smaller mass fraction of La(Fe,Mn.Si)$_{13}$H$_y$.

The porosity of the AMRs was estimated according to the data provided by Vacuumschmelze GmbH using Eq. 4-2 and measured experimentally as described in Ref. [31]. The measured porosities of each regenerator were 40.9 % and 41.2 %, while the estimated value was 38.9 %. It must be noted that regenerators were considered identical for porosity estimation. Several reasons could have caused variation in measured values of porosity as well as difference from estimated value. Namely, inaccuracies in measurement technique, uneven distribution of epoxy and MCM in the regenerators as well as other inaccuracies in manufacturing process were considered as contributing factors.

It was demonstrated in Paragraph 4.3.1.2, that utilisation in a certain range does not have an impact on the maximum no-load temperature span established by a multi-layered AMR. On the other hand, such an AMR is very sensible to the hot end temperature, T_{hot}. Therefore, the no-load tests on the fifteen-layered AMR were started at constant operational frequency and utilisation, while varying the T_{hot}. It was pointed out in Ref. [1] that the maximum performance of an AMR is obtainable in the utilisation range from $U = 0.2$ to $U = 0.8$. Therefore the $U = 0.5$ was selected as the starting point. The initial value of T_{hot} was 293.3 K and it was lowered for every following test. From Figure 4-16, one can see that the maximum no-load temperature span ΔT_{span} was 15.4 K. Note that the temperature span between cold and hot ends of the regenerators was $T_{span} = 14$ K. However, at $T_{hot} = 291.2$ K the temperature span was only $\Delta T_{span} = 2.6$ K. This sudden decrease of the performance alerted a possible mechanical disintegration of the regenerators. The hypothesis was confirmed at $T_{hot} = 294.3$, where $\Delta T_{span} = 1.1$ K was obtained. Finally, the pressure drop at $U = 0.5$ and $v = 0.5$ Hz increased by 1.5 bar from the initial value. Thus, further experiments at this operational point could not be carried out.
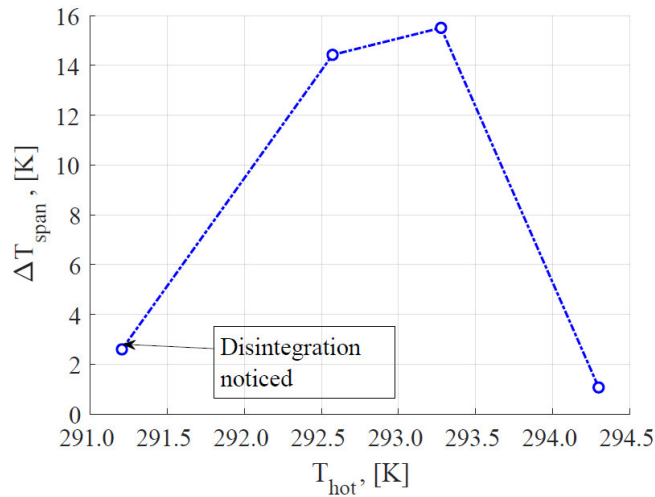
Figure 4-16. No-load temperature span, ΔT_{span} as a function of a hot end temperature, T_{hot}, at $v = 0.5$ Hz and $U = 0.5$.

A series of experiments were conducted to see whether mechanical disintegration progresses in time. Figure 4-17 presents the results obtained initially, during the second test series that were carried out immediately after disintegration was noticed and four days after the initial tests. One can see from Figure 4-17 that the results of the second and the last series were identical. Additionally, the performance at two intermediate utilisation values were tested. One can see that performance at $U = 0.37$ was somewhat better with temperature span of $\Delta T_{span} = 7.8$ K, comparing to other utilisation values. It could be due to temporary flow pattern, caused by loos particles, favouring the performance.
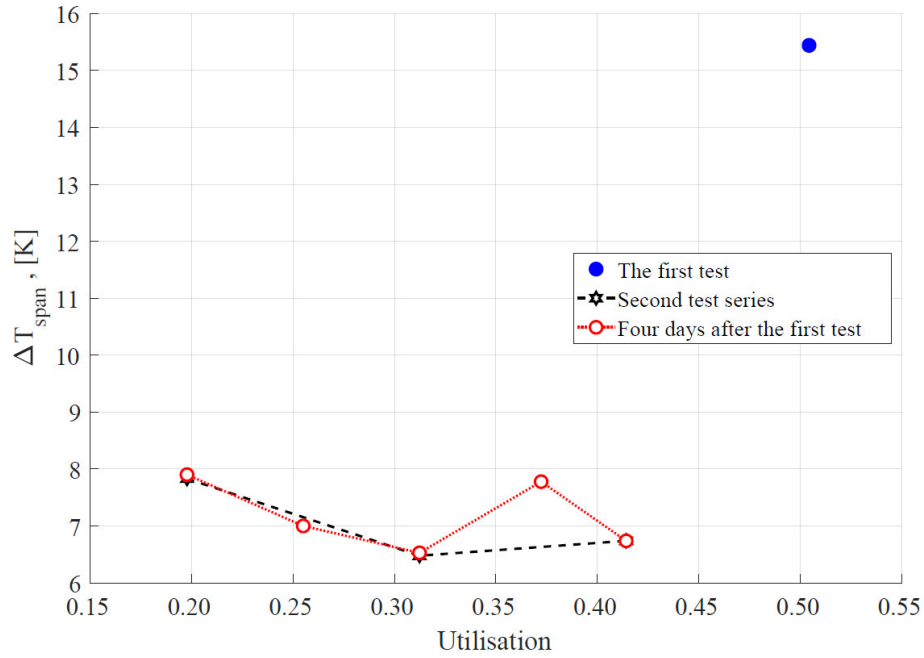
Figure 4-17. No-load temperature span, ΔT_{span}, as a function of an utilisation, U, at $T_{hot} = 292$ K established by the system. This figure is a slightly modified version of the figure published in Ref. [31].

In addition, performance of each regenerator bed was analysed separately. From Figure 4-18, one can see that the regenerators demonstrated significantly different performance from the beginning of the experiments. The initially established temperature span ΔT_{span} at $U = 0.5$ was 16.9 K and 13.9 K of regenerator 2 and 1, respectively. Such differences in performance of the regenerators could have caused by inaccuracies due to manufacturing process. Moreover, it is seen that regenerator 2 established two times higher no-load temperature span than regenerator 1, after mechanical disintegration was noticed.
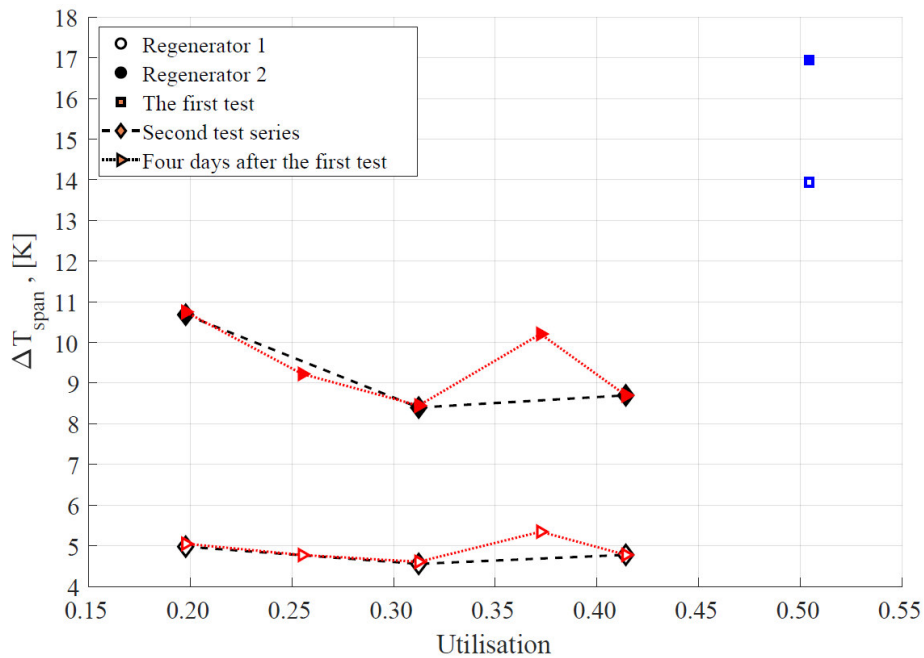
Figure 4-18. A no-load temperature span, ΔT_{span}, as a function of an utilisation, U, at $T_{hot} = 292$ K established by each regenerator separately.

81

Finally, as it was mentioned above, the material used to construct the fifteen-layered regenerators was used previously in the same device. However, the different heat transfer fluid was used. Mechanical disintegration of the material was noticed during those tests as well [60]. It must be emphasised that particles of MCM were not bonded with epoxy for previous testing. Thus, it was possible to separate mechanically degraded particles from the solid ones. The previous experimental work with this MCM could have caused much faster degradation of the AMR beds during the experiments, presented in this thesis.

4.4. AMR with spherical particles

Spherical particles in a size range from 250 to 450 μm were bonded using 2 wt. % of epoxy by Vacuumschmelze GmbH. The regenerator had five layers and it was bonded into plastic housing that was 34 mm in diameter and 40 mm in height. Figure 4-19 represents the packed sphere bed before and after the experimental investigation. From Figure 4-18 (b), one can see that significant amount of the MCM was lost during the experiments. This is attributed to the same phenomenon exhibited by the AMRs with irregular particles and described in Paragraph 4.3.1.2. The total mass lost during the testing was 2.8 g.

<div align="center">(a)   (b)</div>

Figure 4-19. The AMR with five layers of packed spheres (a) before and (b) after testing in the *Test machine*.

The characteristics of the regenerator with packed spherical particles are given in Table 4-2. It is seen that the layer with the smallest T_C was almost half of the thickness of the remaining layers.

Table 4-2. The characteristics of the experimentally investigated AMR with spherical particles.

Number of layers	Overall mass of MCM, m, g	Mass fraction of each MCM layer in the regenerator, wt. %	Porosity, ε, vol. %	Mass fraction of epoxy, wt. %
Five	140.3	12.6; 22.4; 21.3; 22.2; 21.6	39	2

From Figure 4-20, one can see the distribution of Curie temperature along the regenerator depending on the mass fraction of each layer. Despite the significantly shorter first layer, the material distribution follows a straight line. One can see that the temperature span between the first and the second, as well as between two last layers was significantly higher than among the middle layers. However, the temperature span between the cold and the hot ends was $T_{span} = 8.5$ K.
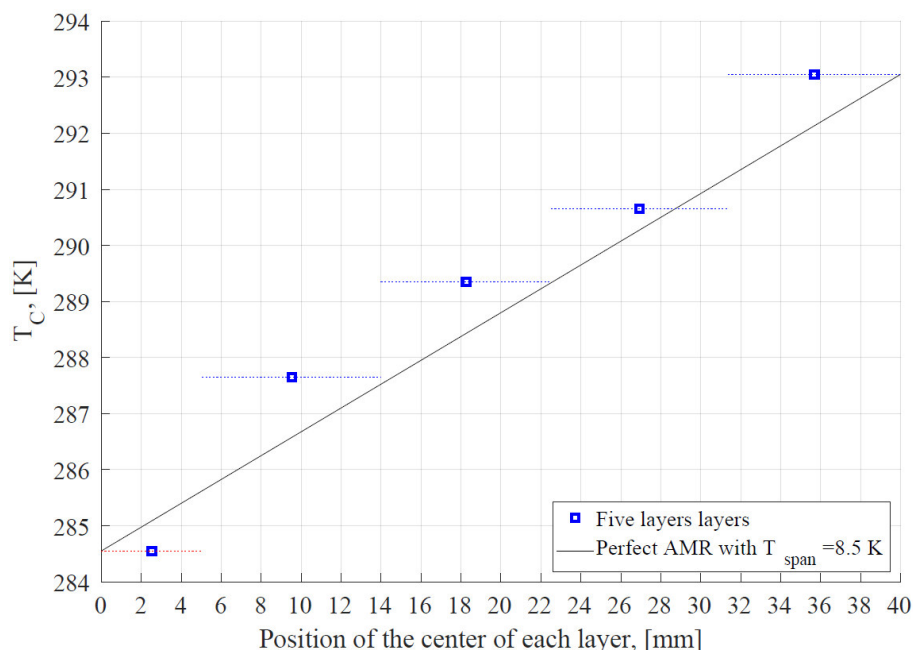
Figure 4-20. Curie temperature distribution along the five-layered AMR with spherical particles. The red line represents the layer containing the smallest mass fraction of La(Fe,Mn.Si)$_{13}$H$_y$.

The regenerator was extensively tested at various conditions. Figure 4-21 (a) demonstrates the no-load performance at two different hot end temperatures, T_{hot}. It is seen that the established no-load temperature span, ΔT_{span}, was independent on utilisation, U, regardless of the hot end temperature, T_{hot}. However, it is seen that the working temperature had a significant influence on the performance of the regenerator. The maximum temperature span ΔT_{span} was 16.2 K at $U = 0.64$ and 0.75, when the hot end temperature, T_{hot}, was 299 K. The ΔT_{span} was 13.8 K at $U = 0.37$, when T_{hot} was 296 K. Figure 4-21 (b) presents that the performance of the regenerator fluctuated within 0.9 K at different values of fluid velocity. Note that the slight difference in ΔT_{span} at $U = 0.53$ and $v_f = 22.7$ mm/s was attributed to the experimental uncertainties rather than different behaviour of the AMR. Figure 4-21 (c) shows no-load temperature span, established by the AMR at $U = 0.53$ and $v_f = 11.3$ mm/s against varying T_{hot}. One can see that the regenerator was highly sensitive to the working temperature. The maximum no-load temperature span was approximately $\Delta T_{span} = 16.9$ K at $T_{hot} = 298.7$ K.

The results of experimental investigation against cooling load at two different hot end temperature, T_{hot}, are presented in Figure 4-22. One can see that regardless of the value of T_{hot}, the highest specific cooling load was obtained at $U = 0.75$. Despite the fact that the no-load temperature span was approximately 2.5 K lower at $T_{hot} = 296$ K than at $T_{hot} = 299$ K, the regenerator established higher specific cooling load at the same utilisation values at $T_{hot} = 296$ K. Another interesting point seen from Figure 4-22 (b) is that the AMR provided around 25 W/kg of specific cooling load at $\Delta T_{span} = 11$ K regardless of U at $T_{hot} = 296$ K, while at $T_{hot} = 299$ K, regenerator performance strongly depended on U, as it is seen from Figure 4-22 (b).
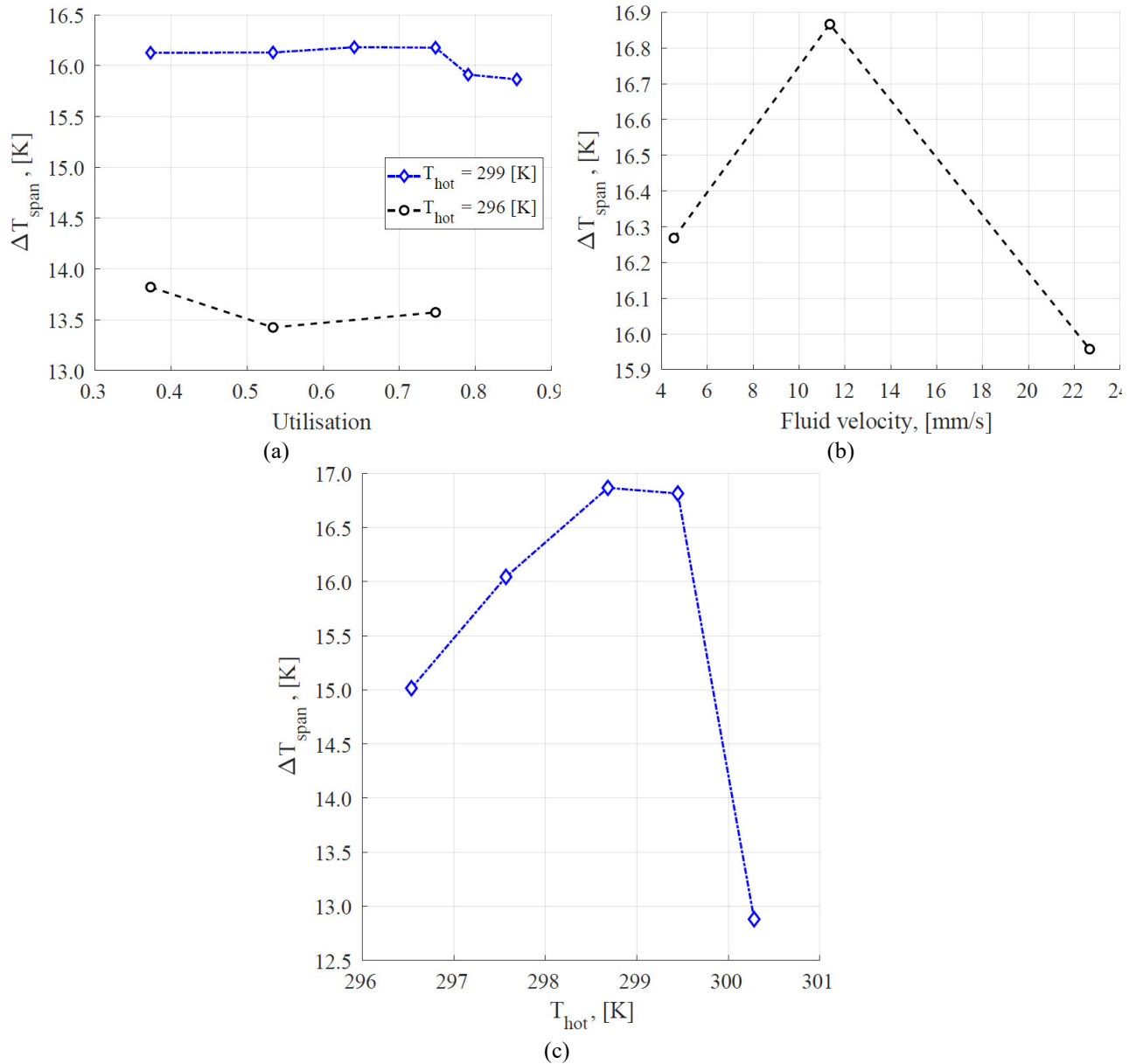
Figure 4-21. (a) No-load temperature span, ΔT_{span}, as a function of an utilisation, U, at $v_f = 22.7$ mm/s. (b) No-load temperature span, ΔT_{span}, as a function of a fluid velocity, v_f, at $U = 0.53$ and $T_{hot} = 299$ K. (c) No-load temperature span, ΔT_{span}, as a function of a hot end temperature, T_{hot}, at $U = 0.53$ and $v_f = 11.3$ mm/s.
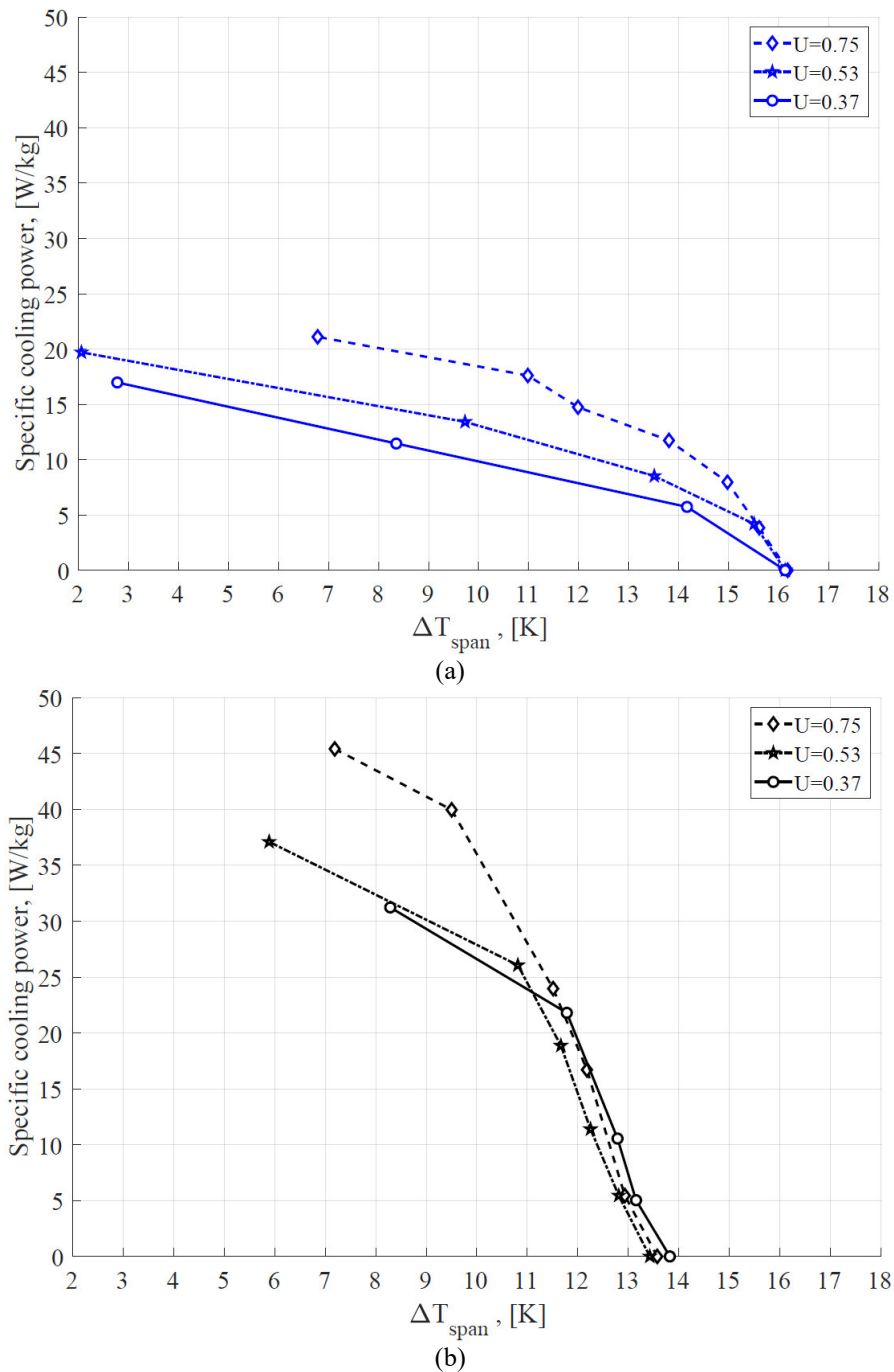
Figure 4-22. Specific cooling load applied on the regenerator with packed spheres as a function of a temperature span, ΔT_{span}, at $v_f = 22.7$ mm/s and (a) $T_{hot} = 299$ K and (b) $T_{hot} = 296$ K.

In order to explore possibilities to establish higher specific cooling load with the packed spheres regenerator, a series of test at constant cooling power of 40 W/kg and $U = 0.75$ were conducted, while varying the hot end temperature, T_{hot}. As it is seen from Figure 4-23, the established temperature span, ΔT_{span}, at both no-load and at applied cooling load conditions shows similar response to the changes in the hot end temperature, T_{hot}. However, the region of the hot end temperature, where sensible temperature span can be established under cooling load, was shifted by approximately 3 K to the left side of the axis. This is because, at given conditions, the working temperature is close to the transition temperature of the material, that allows the regenerator to establish a high performance.
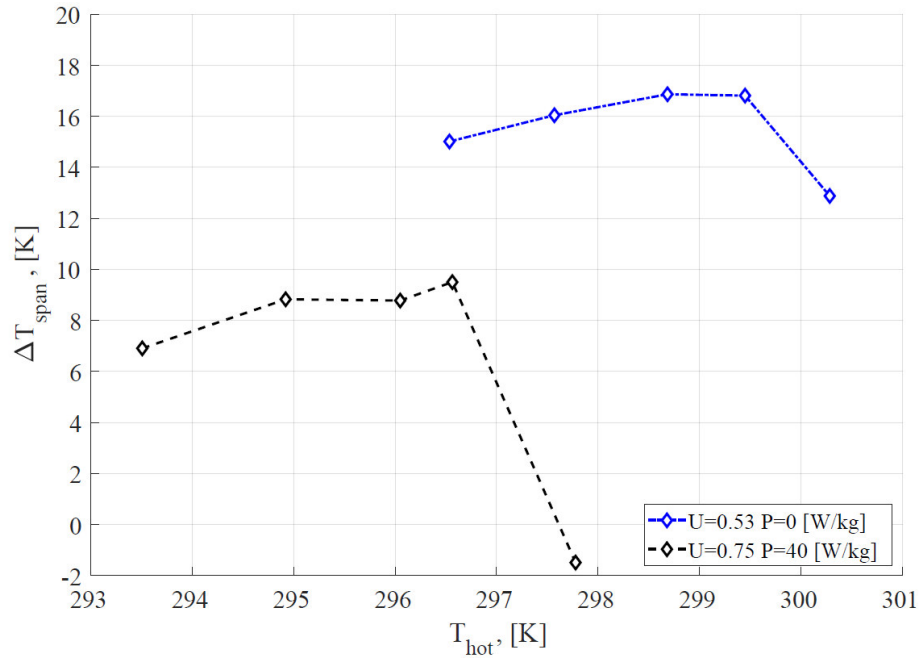
Figure 4-23. Temperature span, ΔT_{span}, as a function of a hot end temperature, T_{hot}, at $v_f = 22.7$ mm/s.

Finally, the performance of the regenerator with packed spherical particles was modelled using the one-dimensional model presented in Section 3.1. The simulations were conducted at no-load conditions as well as applying different cooling load at various hot end temperatures. The results of the numerical analysis are presented in Ref. [30]. It is important to note that the regenerator with packed spheres did not show any sign of mechanical disintegration, caused by breakage of particles, or performance degradation during the testing period.

Experimental results discussed in this chapter demonstrated how sensitive performance of any AMR is. Moreover, MCM are also very brittle. Nevertheless, when carefully designed and manufactured, AMRs can establish high performance. The no-load temperature spans, ΔT_{span}, obtained with five- and nine-layered AMRs are the highest up to date reported performance, obtained for any regenerator tested using the *Test machine*. Moreover, the regenerator with spherical particles, reported in this thesis, established the highest performance under cooling load conditions using the *Test machine*.

5. Conclusions and suggestions for the future research

In this thesis, performance of a heat pump driven by magentocaloric effect was analysed from two aspects. Namely, they were heat transfer and performance of active magnetic regenerators with different geometrical solutions. As it was summarised in Chapter 1, many researchers have concluded that the efficiency of a magnetocaloric heat pump can be increased by improving performance of active magnetic regenerators. Moreover, efficiency of heat exchangers is also of high importance in such a device. Enhanced heat transfer between a heat pump and ambient would allow obtaining higher efficiency at required operational conditions.

For this reason, nature was taken as a source of inspiration for a novel engineering solution. Attention to enhanced heat transfer cases, occurring in nature, was paid. Therefore, several species of fish have been analysed due to their ability to maintain regional or whole body endothermy. It was found that blood vessels of the fishes are tightly bundled together to form a counter-flow heat exchanger. Moreover, the geometrical shape of the vascular heat exchanger was analysed and replicated by deriving two sets of surface equations for both ellipse-based double corrugated geometry with hydraulic diameter held constant and cross-section area held constant. Later, these sets of equations were modified to provide double corrugated geometry based on super-ellipse.

The thermo-hydraulic characteristics of the designed tubes were investigated numerically and experimentally. CFD software was employed in order to perform numerical analysis of the double corrugated tubes at constant pressure drop conditions. Moreover, boundary conditions for the CFD analysis were selected in a way that the operational conditions of an active magnetic regenerator would be partially implemented, i.e. laminar flow regime and small temperature difference between the inlet and the wall a double corrugated tube. The results of numerical investigation showed that the double corrugation disturbs thermal boundary layers, thus the heat transfer is enhanced. Moreover, it was demonstrated that only half of the pumping power is required for double corrugated tubes to deliver the same or higher thermal efficiency as an equivalent straight tube. It was also seen that the thermal efficiency of double corrugated tubes increases with increasing Reynolds number as well as corrugation intensity. It is worth to mention that the CFD simulations did not show a significant difference in performance of the double corrugated tubes with different base geometries.

Based on CDF results, several double corrugated tubes were selected for the experimental investigation. These tubes were 3D printed in aluminium alloy. The novel geometry was mounted into a tube-in-shell counter-flow heat exchanger. The working fluid was city water. The experimental procedure was limited in a range of Reynolds number from 1000 to 2500. The temperature difference between the hot and cold inlets was limited to be approximately 40 °C.

The obtained experimental results qualitatively proved the findings of CFD simulations. Moreover, correlations for Nusselt number and friction factor for each analysed tube were derived from the experimentally obtained data. It was demonstrated that the thermal performance of the double corrugated tubes is up to five times higher than of the straight tube and it increases with increasing Reynolds number. The double corrugated tubes demonstrated up to 160 % higher global thermo-hydraulic performance, evaluated at constant pumping power.

The obtained experimental results for double corrugated tubes encouraged investigating this geometry as a flow pattern for a porous structure of an active magnetic regenerator. As it was emphasised in Chapter 1, it is crucial to improve geometry of these regenerators in order to obtain higher heat transfer and lower pressure drop. In this thesis, Chapter 4, it was also demonstrated experimentally that there are many factors that compromises the performance of an AMR. One of them is geometrical characteristics of the magnetocaloric material. It was observed, that the highest no-load temperature span, with respect to the Curie temperature spacing of the regenerators, was established by the AMR with five layers of packed spherical particles. On the other hand, AMRs with the same size irregular particles and similar Curie temperature of the magnetocaloric material demonstrated somewhat lower no-load performance. Moreover, the latter regenerators showed

mechanical disintegration of the material. Furthermore, it was demonstrated that the performance of active magnetic regenerators is highly dependent on particle size as well. The particles size of the AMR with fifteen layers was approximately twice as big as the particles of the AMRs with five and nine layers of MCM. The former regenerator established significantly lower no-load temperature span than the latter ones, with respect to the Curie temperature spacing.

Of course, other factors, such as epoxy bonding and Curie temperature step between two neighbouring layers, also showed significant importance on the performance of the investigated AMR. Thus, it is rather difficult to carry out a fair comparison of the performance of these regenerators. Nevertheless, geometry of a flow structure of an AMR is of high importance.

For this reason, the experimental results obtained for double corrugated tubes were implemented into a one-dimensional AMR model. The purpose of this numerical analysis was to find out whether performance of an AMR could be increased by using double corrugated geometry as their flow structure. Numerical analysis was carried out for the regenerators with two selected double corrugated flow patterns, packed sphere bed and cylindrical micro-channel matrix. The compared regenerators were grouped with respect to characteristics, such as specific surface area and mass of MCM, thus any difference in their performance was caused by geometrical variations.

The numerical results demonstrated that double corrugated patterns have a significant potential to improve the performance of active magnetic regenerators. Moreover, it was found that double corrugated geometry with rather distinct features has different trends in performance. For instance, the AMR with EDH $AR = 1.6$ $p = 7.5$ mm flow pattern demonstrated significantly higher COP than with EAC $AR = 2.2$ $p = 20.0$ mm and cylindrical micro-channel matrix at constant Q_{cool}, $\varepsilon = 0.54$ and $D_h = 0.35$ mm, regardless the operational frequency. On the other hand, higher COP value was observed for the AMR with EAC $AR = 2.2$ $p = 20.0$ mm flow pattern in comparison with other modelled AMR geometries at constant Q_{cool}, $\varepsilon = 0.36$ and $D_h = 0.13$ mm, regardless the operational frequency. Furthermore, it was found that performance evaluation criterion at constant pumping power, PEC_W, is not suitable as a selection criterion for designing AMR with double corrugated flow geometry. The initial numerical results suggested that the ratio between friction factor in a double corrugated and the straight tubes is of high importance when selecting double corrugated flow pattern for an AMR with fine geometry, i.e. a double corrugated tube with the lowest increase in friction factor should be selected. On the other hand, the ratio between Nusselt numbers is of higher importance when an AMR with a coarse geometry is designed. Then, the double corrugated tube with the highest increase in Nu should be selected as the flow pattern for an AMR. Therefore, the double corrugated flow geometry should be optimized according to the operational conditions such as operational frequency of the process, as well as geometrical features of an AMR, such as porosity, hydraulic diameter of the flow channels and geometry of an AMR bed.

Finally, it was demonstrated that a nature-inspired solution for enhanced heat transfer could be successfully applied in thermal engineering applications, such as magnetocaloric cooling. The double corrugated geometry, presented in this thesis, manifested its usefulness as a novel geometry of a heat exchanger as well as flow structure of a solid AMR. Therefore, the performance of a heat pump, driven by magnetocaloric effect, could be significantly improved by employing the double corrugated geometry in both ways simultaneously.

Many questions related to the research on double corrugated geometry remained unanswered during this PhD project. For example, the flow transition tests should be carried out in order to fully understand the flow behaviour in double corrugated tubes. It is important to know at which Reynolds number fluid flow is still laminar and when it becomes turbulent. This enables more detailed and precise performance comparison between double corrugated geometry and conventional solutions.

Due to possibility to use the double corrugated geometry as a flow pattern of an AMR, more detail analysis is necessary in order to fully understand its effect on fluid flow at significantly lower

Reynolds numbers. Moreover, the thermo-hydraulic behaviour of this novel geometry should be investigated in a micro-scale. Nevertheless, the double corrugated geometry should be characterised in a wide range of Reynolds number, including the turbulent flow regime.

It is also interesting to investigate the performance of double corrugated tubes when fluids with higher viscosity are used, e.g. oil, glycerine and similar, as well as nanofluids. One of the sensitive questions regarding heat exchanger applications is fouling. It would be interesting to investigate this phenomenon in double corrugated tubes.

One could consider optimizing the double corrugated tubes in a way that their geometrical features would allow lower pressure drop, while providing equal or higher thermal efficiency as the current geometry of double corrugated tubes.

From the AMR point of view, in order to fully understand the benefits of using double corrugation as flow patterns in AMR geometry, more comprehensive numerical modelling must be carried out taking in consideration different lengths and aspect ratios of an AMR geometry as well as regenerator porosity and size of flow channels. Moreover, performance of the regenerators with double corrugated flow patterns should be investigated experimentally. This could be done using an oscillating flow technique, which would allow testing passive regenerators manufactured in aluminium alloys and without magnetic field. Regenerators with double corrugated flow patterns could be fabricated using additive manufacturing techniques, e.g. laser beam melting.

Finally, performance of multi-layered AMRs with double corrugated flow patterns is of interest. Numerical studies as well as experimental investigation should be carried out. It is of interest to investigated multi-layered AMR with double corrugated flow pattern. Mechanical properties of such structure should be investigated as well.

References

[1] A. Kitanovski, J. Tušek, U. Tomc, U. Plaznik, M. Ožbolt, A. Poredoš, Magnetocaloric energy conversion. From theory to applications, Springer International Publishing, 2015.

[2] A. Smith, C.R.H. Bahl, R. Bjørk, K. Engelbrecht, K.K. Nielsen, N. Pryds, Materials challenges for high performance magnetocaloric refrigeration devices, *Adv. Energy Mater.* 2 (2012) 1288–1318.

[3] G. V. Brown, Magnetic heat pumping near room temperature, *J. Appl. Phys.* 47 (1976) 3673–3680.

[4] Brown, Magnetic heat pump, USA Patent 4392356, 1975.

[5] V.K. Pecharsky, K.A. Gschneidner Jr., Magnetocaloric effect and magnetic refrigeration, *J. Magn. Magn. Mater.* 200 (1999) 44–56.

[6] T.F. Petersen, Numerical modelling and analysis of a room temperature magnetic refrigeration system, *Technical university of Denmark*, 2007.

[7] V.K. Pecharsky, J.K.A. Gschneidner, Giant magnetocaloric effect in $Gd5(Si_2Ge_2)$, *Phys. Rev. Lett.* 78 (1997) 4494–4497.

[8] H. Neves Bez, K. Navickaitė, T. Lei, K. Engelbrecht, A. Barcza, C.R.H. Bahl, Epoxy-bonded $La(Fe,Mn,Si)_{13}H_z$ as a multi layered active magnetic regenerator, in: 7th *Int. Conf. Caloric Cool.*, Torino, Italy, 2016.

[9] E. Brück, O. Tegus, L. Zhang, X.W. Li, F.R. De Boer, K.H.J. Buschow, Magnetic refrigeration near room temperature with Fe_2P-based compounds, *J. Alloys Compd.* 383 (2004) 32–36.

[10] J.K.A. Gschneidner, V.K. Pecharsky, Thirty years of near room temperature magnetic cooling: Where we are today and future prospects, *Int. J. Refrig.* 31 (2008) 945–961.

[11] W.R. Mérida, J.A. Barclay, Monolithic regenearotr technology for low temperature (4 K) Gifford-McMahon cryocoolers, *Advanes Cryog. Eng.* 43 (1998) 1597–1604.

[12] K. Skokov, D.Y. Karpenkov, M.D. Kuz'Min, I.A. Radulov, T. Gottschall, B. Kaeswurm, M. Fries, O. Gutfleisch, Heat exchangers made of polymer-bonded $La(Fe,Si)_{13}$, *J. Appl. Phys.* 115 (2014) 4–6.

[13] J. Lanzarini, T. Barriere, M. Sahli, J.C. Gelin, A. Dubrez, C. Mayer, M. Pierronnet, P. Vikner, Thermoplastic filled with magnetocaloric powder, *Mater. Des.* 87 (2015) 1022–1029.

[14] J. Lyubina, R. Schäfer, N. Martin, L. Schultz, O. Gutfleisch, Novel design of La(Fe,Si)13 alloys towards high magnetic refrigeration performance, *Adv. Mater.* 22 (2010) 3735–3739.

[15] L. von Moos, Hysteresis in magnetocaloric materials. An experimental and modelling approach, *Technical University of Denamrk*, 2014.

[16] V. Basso, M. Küpferling, C. Curcio, C. Bennati, A. Barzca, M. Katter, M. Bratko, E. Lovell, J. Turcaud, L.F. Cohen, Specific heat and entropy change at the first order phase transition of $La(Fe-Mn-Si)_{13}$-H compounds, *J. Appl. Phys.* 118 (2015) 053907.

[17] M.A. Richard, A.M. Rowe, R. Chahine, Magnetic refrigeration: Single and multimaterial active magnetic regenerator experiments, *J. Appl. Phys.* 95 (2004) 2146–2150.

[18] C. Zimm, A. Boeder, J. Chell, A. Sternberg, A. Fujita, S. Fujieda, K. Fukamichi, Design and performance of a permanent-magnet rotary refrigerator, *Int. J. Refrig.* 29 (2006) 1302–1306.

[19] T. Lei, K.K. Nielsen, K. Engelbrecht, C.R.H. Bahl, H. Neves Bez, C.T. Veje, Sensitivity study of multi-layer active magnetic regenerators using first order magnetocaloric material La(Fe,Mn,Si)$_{13}$H$_y$, *J. Appl. Phys.* 118 (2015) 0–8.

[20] B.A. Monfared, B. Palm, Optimization of layered regenerator of a magnetic refrigeration device, *Int. J. Refrig.* 57 (2015) 103–111.

[21] A. Barcza, M. Katter, V. Zellmann, S. Russek, S. Jacobs, C. Zimm, Stability and magnetocaloric properties of sintered La(Fe,Mn,Si)$_{13}$H$_z$ alloys, *IEEE Trans. Magn.* 47 (2011) 3391–3394.

[22] P. Govindappa, P. V. Trevizoli, O. Campbell, I. Niknia, T. V. Christiaanse, R. Teyber, S. Misra, M.A. Schwind, D. van Asten, L. Zhang, A. Rowe, Experimental investigation of MnFeP$_{1−x}$As$_x$ multilayer active magnetic regenerators, *J. Phys. D. Appl. Phys.* 50 (2017) 315001.

[23] J. Tušek, A. Kitanovski, A. Poredoš, Geometrical optimization of packed-bed and parallel-plate active magnetic regenerators, *Int. J. Refrig.* 36 (2013) 1456–1464.

[24] K. Engelbrecht, J. Tušek, K.K. Nielsen, A. Kitanovski, C.R.H. Bahl, A. Poredoš, Improved modelling of a parallel plate active magnetic regenerator, *J. Phys. D. Appl. Phys.* 46 (2013).

[25] J. Tušek, A. Kitanovski, S. Zupan, I. Prebil, A. Poredoš, A comprehensive experimental analysis of gadolinium active magnetic regenerators, *Appl. Therm. Eng.* 53 (2013) 57–66.

[26] S. Jacobs, J. Auringer, A. Boeder, J. Chell, L. Komorowski, J. Leonard, S. Russek, C. Zimm, The performance of a large-scale rotary magnetic refrigerator, *Int. J. Refrig.* 37 (2014) 84–91.

[27] C. Aprea, G. Cardillo, A. Greco, A. Maiorino, C. Masselli, A rotary permanent magnet magnetic refrigerator based on AMR cycle, *Appl. Therm. Eng.* 101 (2016) 699–703.

[28] C.R.H. Bahl, K. Navickaitė, H. Neves Bez, T. Lei, K. Engelbrecht, R. Bjørk, K. Li, Z. Li, J. Shen, W. Dai, J. Jia, Y. Wu, Y. Long, F. Hu, B. Shen, Operational test of bonded magnetocaloric plates, *Int. J. Refrig.* 76 (2017) 245–251.

[29] T. Lei, Modeling of active magnetic regenerators and experimental investigation of passive regenerators with oscillating flow, *Technical university of Denmark*, 2016.

[30] T. Lei, K. Navickaitė, K. Engelbrecht, A. Barcza, H. Vieyra, K.K. Nielsen, C.R.H. Bahl, Passive characterization and active testing of epoxy bonded regenerators for room temperature magnetic refrigeration, *Appl. Therm. Eng.* 128 (2018) 10–19.

[31] K. Navickaitė, B.A. Monfared, D. Martinez, B. Palm, C.R.H. Bahl, K. Engelbrecht, Experimental investigation of fifteen-layer epoxy-bonded La(Fe,Mn,Si)$_{13}$H$_y$ active magnetic regenerator, in: *8th Int. Conf. Caloric Cool.*, Darmstadt, Germany, 2018: pp. 16–20.

[32] K. Navickaitė, H. Neves Bez, T. Lei, A. Barcza, H. Vieyra, C.R.H. Bahl, K. Engelbrecht, Experimental and numerical comparison of multi-layered La(Fe,Si,Mn)$_{13}$H$_y$ active magnetic regenerators, *Int. J. Refrig.* 86 (2018) 322–330.

[33] T. Lei, K. Engelbrecht, K.K. Nielsen, C.T. Veje, Study of geometries of active magnetic regenerators for room temperature magnetocaloric refrigeration, *Appl. Therm. Eng.* 111 (2017) 1232–1243.

[34] K.K. Nielsen, K. Engelbrecht, C.R.H. Bahl, The influence of flow maldistribution on the performance of inhomogeneous parallel plate heat exchangers, *Int. J. Heat Mass Transf.* 60 (2013) 432–439.

REFERENCES

[35] P. V. Trevizoli, A.T. Nakashima, G.F. Peixer, J.R. Barbosa Jr., Performance assessment of different porous matrix geometries for active magnetic regenerators, *Appl. Energy*. 187 (2017) 847–861.

[36] K. Engelbrecht, K.K. Nielsen, N. Pryds, An experimental study of passive regenerator geometries, *Int. J. Refrig.* 34 (2011) 1817–1822.

[37] J.D. Moore, D. Klemm, D. Lindackers, S. Grasemann, R. Träger, J. Eckert, L. Löber, S. Scudino, M. Katter, A. Barcza, K. Skokov, O. Gutfleisch, Selective laser melting of La(Fe,Co,Si)$_{13}$ geometries for magnetic refrigeration, *J. Appl. Phys.* 114 (2013) 043907.

[38] S. Wieland, J. Kagathara, E. Gärtner, V. Uhlenwinkel, M. Steinbacher, Powder, process parameters and heat treatment conditions for laser beam melting of LaFeSi-based alloys, in: *8th Int. Conf. Caloric Cool.*, Darmstadt, 2018: pp. 16–20.

[39] M. Balli, S. Jandl, P. Fournier, A. Kedous-Lebouc, Advanced materials for magnetic cooling: Fundamentals and practical aspects, *Appl. Phys. Rev.* 4 (2017) 021305.

[40] C.R.H. Bahl, T.F. Petersen, N. Pryds, A. Smith, A versatile magnetic refrigeration test device, *Rev. Sci. Instrum.* 79 (2008).

[41] K. Engelbrecht, D. Eriksen, C.R.H. Bahl, R. Bjørk, J. Geyti, J.A. Lozano, K.K. Nielsen, F. Saxild, A. Smith, N. Pryds, Experimental results for a novel rotary active magnetic regenerator, *Int. J. Refrig.* 35 (2012) 1498–1505.

[42] K. Navickaitė, H. Neves Bez, K. Engelbrecht, C.R.H. Bahl, From a magnet to a heat pump, *J. Sustain. Archit. Civ. Eng.* 14 (2016).

[43] J. Tušek, A. Kitanovski, U. Tomc, C. Favero, A. Poredoš, Experimental comparison of multi-layered La-Fe-Co-Si and single-layered Gd active magnetic regenerators for use in a room-temperature magnetic refrigerator, *Int. J. Refrig.* 37 (2014) 117–126.

[44] D.S. Arnold, A. Tura, A. Ruebsaat-Trott, A. Rowe, Design improvements of a permanent magnet active magnetic refrigerator, *Int. J. Refrig.* 37 (2014) 99–105.

[45] D. Velázquez, E. Palacios, C. Estepa, R. Burriel, A versatile magnetic refrigeration demonstartor, in: *6th Int. Conf. Caloric Cool.*, Victoria, Canada, 2014.

[46] D. Velázquez, C. Estepa, E. Palacios, R. Burriel, A comprehensive study of a versatile magnetic refrigeration demonstrator, *Int. J. Refrig.* 63 (2016) 14–24.

[47] D. Eriksen, K. Engelbrecht, C.R.H. Bahl, R. Bjørk, K.K. Nielsen, A.R. Insinga, N. Pryds, Design and experimental tests of a rotary active magnetic regenerator prototype, *Int. J. Refrig.* 58 (2015) 14–21.

[48] C.R.H. Bahl, K. Engelbrecht, D. Eriksen, J.A. Lozano, R. Bjørk, J. Geyti, K.K. Nielsen, A. Smith, N. Pryds, Development and experimental results from a 1 kW prototype AMR, *Int. J. Refrig.* 37 (2014) 78–83.

[49] D. Eriksen, Active magnetic regenerator refrigeration with rotary multi-bed technology, *Technical University of Denmark*, 2016.

[50] D. Eriksen, K. Engelbrecht, C.R.H. Bahl, R. Bjørk, A.R. Insinga, S. Dall'Olio, N. Pryds, Experimental studies with an active magnetic regenerating refrigerator, in: *Int. Conf. Refrig.*, Yokohama, Japan, 2015.

[51] D. Eriksen, K. Engelbrecht, C.R.H. Bahl, R. Bjørk, K.K. Nielsen, Effects of flow balancing on

active magnetic regenerator performance, *Appl. Therm. Eng.* 103 (2016) 1–8.

[52]   D. Eriksen, K. Engelbrecht, C.R.H. Bahl, R. Bjørk, Exploring the efficiency potential for an active magnetic regenerator, *Sci. Technol. Built Environ.* 22 (2016) 527–533.

[53]   J.A. Lozano, M.S. Capovilla, P. V. Trevizoli, K. Engelbrecht, C.R.H. Bahl, J.R. Barbosa Jr., Development of a novel rotary magnetic refrigerator, *Int. J. Refrig.* 68 (2016) 187–197.

[54]   J.A. Lozano, Design of a rotary magnetic refrigerator, *Federal University of Santa Catarina*, 2015.

[55]   M.S. Capovilla, J.A. Lozano, P. V. Trevizoli, J.R. Barbosa Jr., Performance evaluation of a magnetic refrigeration system, *Sci. Technol. Built Environ.* 22 (2016) 534–543.

[56]   H. Johra, K. Filonenko, P. Heiselberg, C. Veje, T. Lei, S. Dall'Olio, Integration of a magnetocaloric heat pump in a low-energy residential building, *Build. Simul.* 11 (2018) 753–763.

[57]   S. Dall'Olio, D. Eriksen, K. Engelbrecht, A.R. Insinga, C.R.H. Bahl, Design, enhanced thermal and flow efficiency of a 2 kW active magnetic regenerator, in: *9th Worl Conf. Exp. Heat Transf. Fluid Mech. Thermodyn.*, Foz do Iguaçu, Brazil, 2017.

[58]   A.R. Insinga, R. Bjørk, A. Smith, C.R.H. Bahl, Optimally segmented permanent magnet structures, *IEEE Trans. Magn.* 52 (2016) 1–6.

[59]   S. Dall'Olio, T. Lei, K. Engelbrecht, C.R.H. Bahl, The effect of tapering on a magnetocaloric regenrator bed, *Int. J. Refrig.* 84 (2017) 300–308.

[60]   B.A. Monfared, Magnetic refrigeration for near room-temperature applications, *KTH Royal Institute of Technology*, 2018.

[61]   B.A. Monfared, Design and optimization of regenerators of a rotary magnetic refrigeration device using a detailed simulation model, *Int. J. Refrig.* 88 (2018) 260–274.

[62]   K. Engelbrecht, A numerical model of an active magnetic regenerator refrigerator with experimental validation, *University of Wisconsin-Madison*, 2008.

[63]   J. Li, T. Numazawa, K. Matsumoto, Y. Yanagisawa, H. Nakagome, A modeling study on the geometry of active magnetic regenerator, *AIP Conf. Proc.* 1434 (2012) 327–334.

[64]   J. Li, T. Numazawa, K.M. Matsumoto, Y. Yanagisawa, H. Nakagome, Comparison of different regenerator geometries for AMR system, 548 (2014) 548–554.

[65]   R.L. Webb, N.H. Kim, Principles of enhanced heat transfer, 2nd ed., Taylor and Francis CRC ebook account, Abingdon, Great Britain, 1994.

[66]   B. Rai, A. Chiney, V. Ganvir, Nanofluids for heat transfer applications, US 9937503 B2, 2018.

[67]   J. Bayat, A.H. Nikseresht, Investigation of the different base fluid effects on the nanofluids heat transfer and pressure drop, *Heat Mass Transf.* 47 (2011) 1089–1099.

[68]   A. Ahmad, K. Mansour, D. Masoud, An experimental comparison of water based alumina and silica nanofluids heat transfer in laminar flow regime, *J. Cent. South Univ.* 20 (2013) 3582–3588.

[69]   E. Ebrahimnia-Bajestan, M. Charjouei Moghadam, H. Niazmand, W. Daungthongsuk, S. Wongwises, Experimental and numerical investigation of nanofluids heat transfer characteristics for application in solar heat exchangers, *Int. J. Heat Mass Transf.* 92 (2016)

1041–1052.

[70] Y. Xuan, Q. Li, Investigation on convective heat transfer and flow features of nanofluids, *J. Heat Transfer*. 125 (2003) 151.

[71] S.D. Salman, A.A.H. Kadhum, M.S. Takriff, A.B. Mohamad, Heat transfer enhancement of laminar nanofluids flow in a circular tube fitted with parabolic-cut twisted tape inserts, *Sci. World J.* 2014 (2014).

[72] R.L. Webb, R. Narayanamurthy, P. Thors, Heat transfer and friction characteristics of internal helical-rib roughness, *J. Heat Transfer*. 122 (2000) 134.

[73] R. Karwa, S.C. Solanki, J.S. Saini, Heat transfer coefficient and friction factor correlations for the transitional flow regime in rib-roughened rectangular ducts, *Int. J. Heat Mass Transf.* 42 (1999) 1597–1615.

[74] J.Y. San, W.C. Huang, Heat transfer enhancement of transverse ribs in circular tubes with consideration of entrance effect, *Int. J. Heat Mass Transf.* 49 (2006) 2965–2971.

[75] D.L. Gee, R.L. Webb, Forced convection heat transfer in helically rib-roughened tubes, *Int. J. Heat Mass Transf.* 23 (1980) 1127–1136.

[76] S. Pourahmad, S.M. Pesteei, Effectiveness-NTU analyses in a double tube heat exchanger equipped with wavy strip considering various angles, *Energy Convers. Manag.* 123 (2016) 462–469.

[77] S.K. Saha, U.N. Gaitonde, A.W. Date, Heat transfer and pressure drop characteristics of laminar flow in a circular tube fitted with regulary spaced twisted-tape elements, *Exp. Therm. Fluid Sci.* (1989) 310–322.

[78] P. Sivashanmugam, S. Suresh, Experimental studies on heat transfer and friction factor characteristics of laminar flow through a circular tube fitted with helical screw-tape inserts, *Appl. Therm. Eng.* 26 (2006) 1990–1997.

[79] M.M.K. Bhuiya, M.S.U. Chowdhury, M. Shahabuddin, M. Saha, L.A. Memon, Thermal characteristics in a heat exchanger tube fitted with triple twisted tape inserts, *Int. Commun. Heat Mass Transf.* 48 (2013) 124–132.

[80] M.M.K. Bhuiya, A.K. Azad, M.S.U. Chowdhury, M. Saha, Heat transfer augmentation in a circular tube with perforated double counter twisted tape inserts, *Int. Commun. Heat Mass Transf.* 74 (2016) 18–26.

[81] V. Srinivasan, K. Vafai, R.N. Christensen, Analysis of heat transfer and fluid flow through a spirally fluted tube using a porus substrate approach, *J. Heat Transfer*. 116 (1994) 543–551.

[82] S. Garimella, R.N. Christensen, Heat transfer and pressure drop characteristics of spirally fluted annuli: part II--heat transfer, *J. Heat Transfer*. 117 (1995) 61–68.

[83] V. Srinivasan, R. Christensen, Experimental investigation of heat transfer and pressure drop characteristics of flow through spirally fluted tubes, *Exp. Therm. Fluid Sci.* 5 (1992) 820–827.

[84] S. Rainieri, G. Pagliarini, Convective heat transfer to orange juice in smooth and corrugated tubes, *Int. J. Heat Technol.* 15 (1997) 69–75.

[85] F.T. Akyildiz, D.A. Siginer, L. Khezzar, Energy losses and heat transfer enhancement in transversally corrugated pipes, *Int. J. Heat Mass Transf.* 54 (2011) 3801–3806.

[86] Z.S. Kareem, M.N. Mohd Jaafar, T.M. Lazim, S. Abdullah, A.F. Abdulwahid, Heat transfer

enhancement in two-start spirally corrugated tube, *Alexandria Eng. J.* 54 (2015) 415–422.

[87]   Z.S. Kareem, S. Abdullah, T.M. Lazim, M.N. Mohd Jaafar, A.F. Abdul Wahid, Heat transfer enhancement in three-start spirally corrugated tube: Experimental and numerical study, *Chem. Eng. Sci.* 134 (2015) 746–757.

[88]   T.M. Lazim, Z.S. Kareem, M.N.M. Jaafar, S. Abdullah, A.F. Abdulwahid, Heat transfer enhancement in spirally corrugated tube, *Int. Rev. Model. Simulations.* 547 (2014).

[89]   H.H. Balla, Enhancement of heat transfer in six-start spirally corrugated tubes, *Case Stud. Therm. Eng.* 9 (2017) 79–89.

[90]   S. Pethkool, S. Eiamsa-ard, S. Kwankaomeng, P. Promvonge, Turbulent heat transfer enhancement in a heat exchanger using helically corrugated tube, *Int. Commun. Heat Mass Transf.* 38 (2011) 340–347.

[91]   S. Laohalertdecha, S. Wongwises, The effects of corrugation pitch on the condensation heat transfer coefficient and pressure drop of R-134a inside horizontal corrugated tube, *Int. J. Heat Mass Transf.* 53 (2010) 2924–2931.

[92]   S. Mac Nelly, W. Nieratschker, M. Nadler, D. Raab, A. Delgado, Experimental and numerical investigation of the pressure drop and heat transfer coefficient in corrugated tubes, *Chem. Eng. Technol.* 38 (2015) 2279–2290.

[93]   V. Zimparov, Enhancement of heat transfer by a combination of three-start spirally corrugated tubes with a twisted tape, *Int. J. Heat Mass Transf.* 44 (2001) 551–574.

[94]   S.K. Saha, Thermohydraulics of laminar flow through rectangular and square ducts with axial corrugation roughness and twisted tapes with oblique teeth, *J. Heat Transfer.* 132 (2010).

[95]   P.K. Pal, S.K. Saha, Experimental investigation of laminar flow of viscous oil through a circular tube having integral spiral corrugation roughness and fitted with twisted tapes with oblique teeth, *Exp. Therm. Fluid Sci.* 57 (2014) 301–309.

[96]   S.K. Saha, Thermohydraulics of laminar flow through a circular tube having integral helical corrugations and fitted with helical screw-tape insert, *Chem. Eng. Commun.* 200 (2013) 418–436.

[97]   S.K. Saha, B.N. Swain, G.L. Dayanidhi, Friction and thermal characteristics of laminar flow of viscous oil through a circular tube having axial corrugations and fitted with helical screw-tape inserts, *J. Fluids Eng.* 134 (2012) 051210.

[98]   Y. Hong, J. Du, S. Wang, Experimental heat transfer and flow characteristics in a spiral grooved tube with overlapped large/small twin twisted tapes, *Int. J. Heat Mass Transf.* 106 (2017) 1178–1190.

[99]   S. Rainieri, F. Bozzoli, L. Cattani, G. Pagliarini, Compound convective heat transfer enhancement in helically coiled wall corrugated tubes, *Int. J. Heat Mass Transf.* 59 (2013) 353–362.

[100]   F. Bozzoli, L. Cattani, S. Rainieri, Effect of wall corrugation on local convective heat transfer in coiled tubes, *Int. J. Heat Mass Transf.* 101 (2016) 76–90.

[101]   Z.Y. Guo, D.Y. Li, B.X. Wang, A novel concept for convective heat transfer enhancement, *Int. J. Heat Mass Transf.* 41 (1998) 2221–2225.

[102]   J.A. Meng, X.G. Liang, Z.J. Chen, Z.X. Li, Experimental study on convective heat transfer in

alternating elliptical axis tubes, *Exp. Therm. Fluid Sci.* 29 (2005) 457–465.

[103] H.N. Khaboshan, H.R. Nazif, Investigation of heat transfer and pressure drop of turbulent flow in tubes with successive alternating wall deformation under constant wall temperature boundary conditions, *J. Brazilian Soc. Mech. Sci. Eng.* 40 (2018) 1–16.

[104] B. Li, B. Feng, Y.L. He, W.Q. Tao, Experimental study on friction factor and numerical simulation on flow and heat transfer in an alternating elliptical axis tube, *Appl. Therm. Eng.* 26 (2006) 2336–2344.

[105] G.F. Hewitt, J.S. Marshall, Particle focusing in a suspension flow through a corrugated tube, *J. Fluid Mech.* 660 (2010) 258–281.

[106] M. Penzel, M. Zinecker, A. Schubert, M. Hackert-Oschätzchen, A. Ludwig, A. Adamczewski, A. Schulz, M. Lausberg, Investigation of forced convection in pin structured cold plates for improved heat transfer and heat spreading, in: *9th World Conf. Exp. Heat Transf. Fluid Mech. Thermodyn.*, Foz do Iguaçu, Brazil, 2017.

[107] G. Fabbri, R. Rossi, Analysis of the heat transfer in the entrance region of optimised corrugated wall channel, *Int. Commun. Heat Mass Transf.* 32 (2005) 902–912.

[108] C.S. Fernandes, R.P. Dias, J.M. Nóbrega, J.M. Maia, Laminar flow in chevron-type plate heat exchangers: CFD analysis of tortuosity, shape factor and friction factor, *Chem. Eng. Process. Process Intensif.* 46 (2007) 825–833.

[109] P. Peukert, J. Hrub, Comparison of heat transfer in straight and corrugated minichannels with two-phase flow, *EPJ Web Conf. 67.* 93 (2014) 1–6.

[110] P. Forooghi, K. Hooman, Effect of buoyancy on turbulent convection heat transfer in corrugated channels - A numerical study, *Int. J. Heat Mass Transf.* 64 (2013) 850–862.

[111] Z. Grant Mills, T. Shah, A. Warey, S. Balestrino, A. Alexeev, Onset of unsteady flow in wavy walled channels at low Reynolds number, *Phys. Fluids.* 26 (2014).

[112] J.S. Shi, Q.Z. Zhang, A perturbation analysis of the fully developed convective heat transfer inside a longitudinal corrugation channel, *Adv. Mater. Res.* 588–589 (2012) 1858–1861.

[113] N. Tokgoz, M.M. Aksoy, B. Sahin, Investigation of flow characteristics and heat transfer enhancement of corrugated duct geometries, *Appl. Therm. Eng.* 118 (2017) 518–530.

[114] G.H. Yoon, Topological design of heat dissipating structure with forced convective heat transfer, *J. Mech. Sci. Technol.* 24 (2010) 1225–1233.

[115] J.H.K. Haertel, G.F. Nellis, A fully developed flow thermofluid model for topology optimization of 3D-printed air-cooled heat exchangers, *Appl. Therm. Eng.* 119 (2017) 10–24.

[116] J.H.K. Haertel, K. Engelbrecht, B.S. Lazarov, O. Sigmund, Topology optimization of thermal heat sinks, in: *Comsol Conf. 2015*, 2015.

[117] A. Pizzolato, A. Sharma, K. Maute, A. Sciacovelli, V. Verda, Topology optimization for heat transfer enhancement in latent heat thermal energy storage, *Int. J. Heat Mass Transf.* 113 (2017) 875–888.

[118] T. Lei, J. Alexandersen, B.S. Lazarov, F. Wang, J.H.K.K. Haertel, S. De Angelis, S. Sanna, O. Sigmund, K. Engelbrecht, Investment casting and experimental testing of heat sinks designed by topology optimization, *Int. J. Heat Mass Transf.* 127 (2018) 396–412.

[119] J.H.K.K. Haertel, K. Engelbrecht, B.S. Lazarov, O. Sigmund, Topology optimization of a

pseudo 3D thermofluid heat sink model, *Int. J. Heat Mass Transf.* 121 (2018) 1073–1088.

[120] Z. Huang, Y. Hwang, R. Radermacher, Review of nature inspired heat exchanger technology, *Int. J. Refrig.* 78 (2017) 1–17.

[121] K. Manjunath, S.C. Kaushik, Second law thermodynamic study of heat exchangers: A review, *Renew. Sustain. Energy Rev.* 40 (2014) 348–374.

[122] B. Bhushan, Biomimetics: lessons from nature-an overview, *Philos. Trans. R. Soc. A Math. Phys. Eng. Sci.* 367 (2009) 1445–1486.

[123] E. Jantsch, Tubular heat transfer aparatus, USA Patent 2663321, 1953.

[124] K. Johansen, C. Bech, Heat conservation during cold exposure in birds (vasomotor and respiratory implications), *Polar Res.* 1 (1983) 259–268.

[125] K.A. Dickson, J.B. Graham, Evolution and consequences of endothermy in fishes, *Physiol. Biochem. Zool.* 77 (2004) 998–1018.

[126] N.C. Wegner, O.E. Snodgrass, H. Dewar, J.R. Hyde, Whole-body endothermy in a mesopelagic fish, the opah, Lampris guttatus, *Science (80-.).* 348 (2015) 786–789.

[127] P. Börnert, D. Jensen, Coronary artery imaging at 0.5 T using segmented 3D echo planar imaging, *Magn. Reson. Med.* 34 (1995) 779–785.

[128] K. Navickaitė, A. Mocerino, L. Cattani, F. Bozzoli, K. Liltrop, X. Zhang, C.R.H. Bahl, K. Engelbrecht, Enhanced heat transfer in tubes based on vascular heat exchangers in fish: experimental investigation, *Int. J. Heat Mass Transf.* (*submitted*) 1–20.

[129] M.R. Spiegel, Mathematical handbook of formulas and tables, McGraw-Hill, inc., USA, 1995.

[130] S. Rainieri, A. Farina, G. Pagliarini, Experimental investigation of heat transfer and pressure drop augmentation for laminar flow in spirally enhanced tubes, *Proc. 2nd Eur. Therm. 14th UIT Natl. Heat Transf. Conf. Ed.* (1996) 203–209.

[131] B.R. Munson, D.F. Young, T.H. Okishi, Fundamentals of fluid mechanics, 4th ed., John Wiley&Sons, Iowa, USA, USA, 2002.

[132] S. V. Patankar, C.H. Liu, E.M. Sparrow, Fully Developed Flow and Heat Transfer in Ducts Having Streamwise-Periodic Variations of Cross-Sectional Area, *J. Heat Transfer.* 99 (1977) 180.

[133] J. Hærvig, K. Sørensen, T.J. Condra, On the fully-developed heat transfer enhancing flow field in sinusoidally, spirally corrugated tubes using computational fluid dynamics, *Int. J. Heat Mass Transf.* 106 (2017) 1051–1062.

[134] T.L. Bergman, A.S. Lavine, F.P. Incropera, D.P. Dewitt, Introduction to heat transfer, 6th ed, 2014.

[135] A. Zachár, Analysis of coiled-tube heat exchangers to improve heat transfer rate with spirally corrugated wall, *Int. J. Heat Mass Transf.* 53 (2010) 3928–3939.

[136] F.P. Incropera, D.P. DeWitt, T.L. Bergman, A.S. Lavine, Fundamentals of heat and mass transfer, 6th ed., John Wiley & Sons, Inc., United States of America, 2007.

[137] A.E. Bergles, A.R. Blumenkrantz, J. Taborek, Performance evaluation criteria for enhanced heat transfer surfaces, in: 5th *Int. Heat Transf. Conf.*, Tokyo, Japan, 1974.

[138] D. Martinez-Maradiaga, O. Mishin, K. Engelbrecht, Thermophysical properties of AlSi$_{10}$Mg

products obtained by metal additive manufacturing, (*in prep.*).

[139] D.S. Miller, Internal flow systems, 2nd ed., BHRA Information services, Cranfield, Bedford, UK, 1990.

[140] J. V. Beck, K.J. Arnold, Parameter estimation in engineering and science (probability & mathematical statistics), John Wiley & Sons Inc, New York, 1977.

[141] B. Efron, The jackknife, the bootstrap and other resampling plans, Society for Industrial and Applied Mathematics, 1982.

[142] B. Blackwell, J. V. Beck, A technique for uncertainty analysis for inverse heat conduction problems, *Int. J. Heat Mass Transf.* 53 (2010) 753–759.

[143] S.J. Kline, F.A. McClintok, Describing uncertainties in single-sample experiments, *Mech. Eng.* (1953).

[144] Y. Nakayama, R.F. Boucher, Introduction to fluid mechanics, Butterworth-Heinemann, Oxford, UK, 2000.

[145] D. Clamond, Efficient resolution of the colebrook equation, *Ind. Eng. Chem. Res.* 48 (2009) 3665–3671.

[146] J.R. Taylor, Introduction to error analysis, 2nd ed., Maple-Vail book manufacturing group, California, USA, USA, 1997.

[147] J. Tušek, A. Kitanovski, I. Prebil, A. Poredoš, Dynamic operation of an active magnetic regenerator (AMR): Numerical optimization of a packed-bed AMR, *Int. J. Refrig.* 34 (2011) 1507–1517.

[148] K.K. Nielsen, J. Tušek, K. Engelbrecht, S. Schopfer, A. Kitanovski, C.R.H. Bahl, A. Smith, N. Pryds, A. Poredoš, Review on numerical modeling of active magnetic regenerators for room temperature applications, *Int. J. Refrig.* 34 (2011) 603–616.

[149] C. Aprea, A. Greco, A. Maiorino, Modelling an active magnetic refrigeration system: A comparison with different models of incompressible flow through a packed bed, *Appl. Therm. Eng.* 36 (2012) 296–306.

[150] T. Lei, K. Engelbrecht, K.K. Nielsen, H. Neves Bez, C.R.H. Bahl, Study of multi-layer active magnetic regenerators using magnetocaloric materials with first and second order phase transition, *J. Phys. D. Appl. Phys.* 49 (2016) 345001.

[151] K.K. Nielsen, K. Engelbrecht, D. V. Christensen, J.B. Jensen, A. Smith, C.R.H. Bahl, Degradation of the performance of microchannel heat exchangers due to flow maldistribution, *Appl. Therm. Eng.* 40 (2012) 236–247.

[152] R. Bulatova, C.H.R. Bahl, K. Andersen, L.T. Kuhn, N. Pryds, Functionally graded ceramics fabricated with side-by-side tape casting for use in magnetic refrigeration, *Int. J. Appl. Ceram. Technol.* 12 (2015) 891–898.

[153] K. Engelbrecht, C.R.H. Bahl, K.K. Nielsen, Experimental results for a magnetic refrigerator using three different types of magnetocaloric material regenerators, *Int. J. Refrig.* 34 (2011) 1132–1140.

[154] K. Engelbrecht, B.J. Jesper, C.R.H. Bahl, Experiments on a modular magnetic refrigeration device, *Stroj. Vestnik/Journal Mech. Eng.* 58 (2012) 3–8.

[155] H. Neves Bez, Magnetocaloric materials and first order phase transitions, *Technical University*

of Denmark, 2016.

[156] S. Jacobs, Modeling and optimal design of a multilayer refrigeration system, in: *Proc. 3ʳᵈ Int. Conf. Magn. Refrig. Room Temp.*, Des Moines, Iowa, USA, 2009: pp. 267–273.

[157] R. Teyber, P. V. Trevizoli, T. V. Christiaanse, P. Govindappa, I. Niknia, A. Rowe, Performance evaluation of two-layer active magnetic regenerators with second-order magnetocaloric materials, *Appl. Therm. Eng.* 106 (2016) 405–414.

[158] B.A. Monfared, B. Palm, New magnetic refrigeration prototype with application in household and professional refrigerators, *7ᵗʰ Int. Conf. Caloric Cool.* (2016) 11–14.

Published or submitted papers

P.1. Enhanced heat transfer in tubes based on vascular heat exchangers in fish: experimental investigation

Enhanced heat transfer in tubes based on vascular heat exchangers in fish: experimental investigation

Kristina Navickaitė[1]*, Andrea Mocerino[2], Luca Cattani[3], Fabio Bozzoli[2,4], Christian Bahl[1], Klaus Liltrop[5], Xiaodan Zhang[5], Kurt Engelbrecht[1]

[1]Technical University of Denmark, Department of Energy Conversion and Storage, Frederiksborgvej 399, 4000 Roskilde, Denmark

[2]Department of Engineering and Architecture, University of Parma, Parco Area delle Scienze 181/A, 43121, Parma, Italy

[3]CIDEA, Interdepartmental Centre, University of Parma, Parco Area delle Scienze 181/A, I-43124 Parma, Italy

[4]SITEIA.PARMA Interdepartmental Centre, University of Parma, Parco Area delle Scienze 181/A, I-43124 Parma, Italy

[5]Technical University of Denmark, Department of Mechanical engineering, Nils Koppels Allé 404, 2800 Kgs. Lyngby, Denmark

*knav@dtu.dk

Abstract. A double corrugated tube geometry for improved heat transfer performance inspired by vascular heat exchangers found in fish such as the tuna and the opah is presented. The geometry features a cross section that varies continuously in the flow direction while maintaining a constant hydraulic diameter, which gives enhanced heat transfer at a relatively low increase in pressure drop. Five ellipse-based tubes with varying corrugation severity and period that emulate blood vessels of fish were produced in an aluminium alloy using additive manufacturing technology. Thermal performance of the novel tube design was experimentally investigated in a counter flow tube-in-shell heat exchanger in a range of Reynold numbers from 1000 to 2500. Correlations for the Nusselt number and friction factor for each tube are proposed and the experimental results show that Nusselt number increases up to 500 % in corrugated tubes compared to a straight tube. The global thermo-hydraulic performance, evaluated for the same pumping power, of the double corrugated tubes is up to 160 % higher than of a straight tube.

Keywords. Vascular heat exchanger, double corrugation, high performance heat transfer devices, biomimetic, modified Wilson plot, Nusselt number correlation

Nomenclature

Variables				
AR	Aspect ratio, [-]		*R*	Radius, [m]
A_c	Cross-section area, [m²]		*Re*	Reynolds number, [-]
A_s	Surface area, [m²]		R_w	Thermal wall resistance, [m²KW^{-1}]
C	Multiplicative constant, [-]		S_q	Root square mean surface roughness, [m]
c_p	Specific heat, [J(kg K)$^{-1}$]		*U*	Overall heat transfer coefficient, [W(m²K)$^{-1}$]
D	Diameter, [m]		*Y*	The twist ratio, [-]
f	Friction factor, [-]		*x, y, z*	Geometric coordinates, [m]
h	Convection coefficient, [W(m²K)$^{-1}$]		*w*	Fluid flow velocity, [m s^{-1}]
k	Thermal conductivity, [W(m K)$^{-1}$]		ΔT	Temperature difference, [K]
L	Length, [m]		ΔT_{lm}	Logarithmic mean temperature difference, [K]
N	Number of experiments, [-]		Δp	Pressure difference, [Pa]
Nu	Nusselt number, [-]		*Abbreviations*	
PEC	Performance evaluation criteria, [-]		AEA	Alternating elliptical axis
Pr	Prandtl number, [-]		HST	Helical screw-tape
p	Corrugation period, [m]		OD	Outer diameter, [m]
Q	Heat transfer, [W]		T	Thermocouple
			Greek letters	

α	Re exponent, [-]		exp	Experimental
β	Pr exponent, [-]		f	Fluid
δ	Wall thickness, [m]; standard error of estimate, [-]		h	Hydraulic
			i	Inner (tube side)
ζ	Vorticity, [-]		in	Inlet
μ	Dynamic viscosity, [Pa s]		m	Mean
ρ	Density, [kg m^{-3}]		o	Outer (shell side)
			out	Outlet
	Subscripts		s	Shell side
cal	Calculated		t	Tube side
est	Estimate		0	Straight (reference)

1

1. Introduction

Nature can be an excellent source of inspiration for advanced structures, designs and materials, and the approach is referred to as biomimetics [1]. According to Mattheck [2], as early as 1893, it was suggested by K. Metzger that trees grow in a way that results in an even stress distribution throughout their structure. For example, the concept of even stress flow in mechanical systems has resulted in numerical models that can explain how trees grow and adapt to their unique loading case, including how root systems grow. Flies, beetles, spiders and geckos have specialized attachment geometries on their skin that allow them to climb up smooth vertical surfaces [3], and sharks have small riblets on their skin that reduce drag [4]. In this article, we look to nature for examples of advanced heat exchanger designs, although there are relatively few examples of biological systems that require high heat transfer performance. Many examples of complex thermal insulation techniques can be found in nature, but cases where high heat transfer is required are less common. Examples of insulation techniques include the fur of arctic animals or the insulating blubber layer found on seals and whales [5]. Some examples of high heat transfer performance in nature include the feet of some birds that have a counter-flow heat exchanger composed of blood vessels entering and exiting the feet [6]. This heat exchanger allows the feet to operate at a lower temperature than the rest of the bird's body and thus eliminates the need for insulation, in the form of feathers, on the feet. The counter-flow vascular heat exchanger at the core of several fish species, such as lamnid sharks and tuna [7] and opahs [8] also represents a compact, high performance heat exchanger. This heat exchanger recovers heat generated in the fish's muscles that is carried in the blood before it is pumped to the gills where the heat is rejected to the surroundings, giving these fish the unique ability to maintain a body temperature that is significantly higher than their surroundings. This heat recovery technique allows them to hunt in waters with lower temperatures than fish without the regenerative heat exchanger. Vascular heat exchangers in fish are fascinating and often complex. For example, the heat exchanger section of a 1.9 kg skipjack tuna was found to have over 250,000 blood flow passages with two distinct diameters of approximately 0.036 mm and 0.084 mm [9]. A photo of blood vessels that comprise part of the counter-flow heat exchanger of an opah is shown in Figure 1(a), and a photo of a skipjack tuna heat recovery vascular system from ref. [9] shows a similar geometry. In Figure 1(a), it can be seen that some blood vessels are nearly circular, others resemble ellipses, and others are irregular. Cross-sections such as shown in Figure 1(a) only show the geometry at one plane in the heat exchangers, and it is not known how the cross section of these blood vessels behaves along the flow direction. To get an idea of how these blood vessels might behave in 3D, we can look at imaging of larger blood vessels. Börnert and Jensen, [10] present a 3D image of coronary arteries shown in Figure 1(b) using magnetic resonance imaging. In the 3D reconstruction, the shape of the arteries seems to fluctuate along the flow path but we assume that the area for flow stays nearly constant to prevent any high flow resistance areas, which would cause stress on the heart.

<div align="center">(a)   (b)</div>
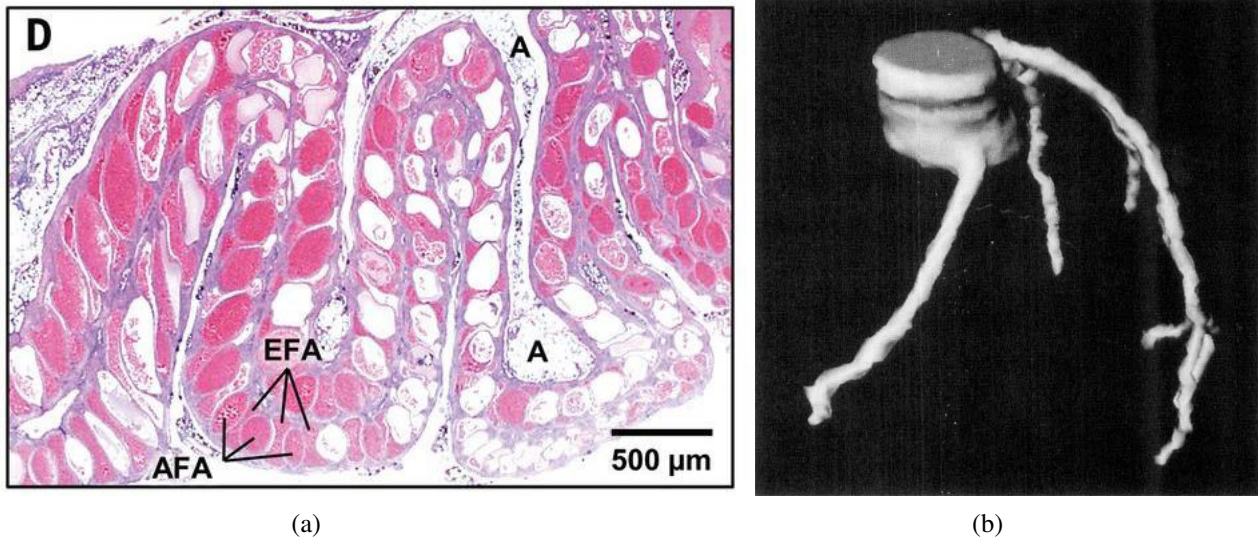
Figure 1. Photo of blood vessels in the rete mirabile (a), which is located in the gill of the opah. Reproduced with the permission from ref. [8]. MRI image of coronary arteries, reproduced with the permission from ref. [10]

Based on the images in Figure 1 and using fish such as the tuna and opah as inspiration, we suggest a double corrugated tube geometry for enhanced heat transfer at a relatively low increase in pressure drop. The proposed flow cross-section is elliptical and constantly changes aspect along the flow path in order to continuously break up the thermal boundary layer that attempts to form in the fluid flow while maintaining a constant hydraulic diameter. A similar concept was proposed by Jantsch, [11] where a proposed tube was deformed to change the cross sectional shape while maintaining a constant flow area. Jantsch, [11] claimed that the geometry gave "an effective kneading of the fluid in the column" that improved contact between the tube wall and fluid. However, no evidence that Jantsch's invention was demonstrated or tested could be found.

While nature shows quite rare examples where enhanced heat transfer is necessary, the request for such techniques is huge in industry. With growing energy consumptions, the appeal for more efficient techniques to use the available energy is increasing constantly. The food industry, aerospace, paint production, naval, chemical engineering, and paper manufacturing are only few examples where enhanced heat transfer is in high demand [12–18]. In most applications, laminar flow or viscous fluids are required and that reduces the thermal efficiency of such processes or apparatuses.

Many attempts using different techniques to enhance the heat transfer have been reported in literature. Webb and Kim, [15] suggested to classify the methods into active, passive and combined techniques. Active heat transfer enhancement techniques use an external mechanical aid or electrostatic field, fluid vibration or injections, to promote the thermal performance. Passive techniques involve various inserts in a flow, artificial surface roughness and enhanced surfaces such as fins and various types of corrugation. Combined technique couples both passive and active techniques. Due to the flexibility and low maintenance cost, the passive heat transfer enhancement techniques were most widely implemented into engineering applications.

Experimental investigation of the thermo-hydraulic performance of spirally or transversally corrugated tubes, inserts that induce secondary flow inside a tube were reported by many authors for different flow regimes and fluids. Zimparov, [19] demonstrated that three start spirally corrugated tubes combined with five twisted tape inserts show superior performance to a straight tube as well as to cases when twisted tapes and spirally corrugated tubes are used separately. Meng *et al.*, [13] experimentally proved that heat transfer in alternating ellipse axis (AEA) tubes increases up to 500% with a penalty in pressure being up to 350% when compared with a straight tube. Laohalertdecha and Wongwises, [20] compared experimental results obtained for three helically corrugated tubes with a straight tube for two-phase R-134a flow. The Authors found that the heat transfer and the pressure drop in the corrugated tubes increase with the average fluid quality. The reported increase in heat transfer and pressure drop were 50% and 70%, respectively. Pal and Saha, [21] found that a combination of integral spiral corrugation in a circular duct and twisted tape with oblique teeth

provides up to 85% increased heat transfer at fixed pumping power in a laminar flow of viscous oil compared to a circular duct. Moreover, combining both techniques is more efficient than each heat transfer enhancement method separately. Rainieri and Pagliarini, [12] investigated thermal performance of spirally corrugated tubes for fruit juice with a different sucrose concentration. The Authors showed that corrugation has negligible effect on heat transfer when juice with sucrose concentration of 65 °Bx is used while 14.7 times higher heat transfer was observed for juice with 12 °Bx. In another study performed by Rainieri *et al*., [22], it was found that for Reynold numbers (*Re*) higher than 1000, the thermal performance of the helically coiled corrugated tubes increases up to 25 times with a pressure drop increase up to 3 times. The Authors also concluded that the combination of the two heat transfer techniques is more effective than each of them separately. Mac Nelly *et al*., [23] investigated single spirally corrugated and cross spirally corrugated tubes using laboratory air in the *Re* range 4000 to 20000 with a Prandlt number (*Pr*) lower than 1. The Authors concluded that Nusselt number (*Nu*) increases up to 1.88 times in cross-spirally corrugated tubes with increasing *Re* when compared with a straight one. However, single spirally corrugated tubes showed 1.66 times higher *Nu* value regardless of *Re*. Moreover, increase in pressure drop, as concluded in [23], depends on the corrugation angle in single spirally corrugated tubes while in cross-spirally corrugated tubes pressure drop rose significantly regardless of the corrugation angle. Pethkool *et al*., [17] reported up to 300 % higher *Nu* values for helically corrugated tubes with the increase in friction factor by 1.93 when compared with a smooth tube. It is interesting to note that the Authors found that *Nu* increases with an increase in the ratio between corrugation period (pitch), *p*, and hydraulic diameter, D_h. Pethkool *et al*., [17] also concluded that the thermal performance of the corrugated tubes is higher when *Re* is lower. Harleß *et al*., [24] investigated helically corrugated tubes in the *Re* range from 5000 to 23000. It was concluded that smaller corrugation angles lead to higher *Nu* when tubes with identical *p* and corrugation height are considered. Moreover, in the same study it was concluded that the dimensionless severity index, ϕ, used for quantifying the corrugation geometry is not sufficient to determine the heat transfer and friction characteristics. This finding also agrees with the conclusions derived by Rainieri *et al*., [25] and later study by Harleß *et al*., [26].

Modelling of the thermal performance of these tubes has been previously reported [27] for a flow with constant pressure drop and fluid properties. The modelling considered both ellipse-based and super ellipse-based geometries and the ellipse-based tubes were found to give the best performance. Based on the modelling results, five double corrugated tubes that emulate blood vessels of the opah and an equivalent straight tube were manufactured in an aluminium alloy using selective laser melting (SLM). The tubes were tested in a counter-flow tube-in-shell heat exchanger setup. The concept of the double corrugation is similar to AEA tubes. However, the transition in the cross-section along the flow path is smoother for the double corrugated tubes, which should lead to a lower pressure drop. The double corrugated tubes have an elliptical cross section and D_h is held constant along the flow direction. The experimental results are obtained for *Re* number from 1000 to 2500. The obtained thermal and hydraulic performance results are presented as *Nu* and *f* correlations.

2. Experimental methodology

2.1. Design and construction of the tubes

The double corrugated tubes, previously described in [27], and an equivalent straight tube were manufactured using selective laser melting technique in $AlSi_{10}Mg$ powders. The relative density of the alloy after SLM process was 99.5 %. The external surface of all the tested tubes was manually polished using fine sand paper.

The double corrugated tubes are based on an elliptical cross section that changes aspect ratio (*AR*) of *x* and *y* in the flow direction while maintaining a constant D_h along the *z*-axis. The geometry of the investigated tubes is defined by Eq. (1). The cross section of the tube at any point in the flow direction is defined as an ellipse with one axis equal to *x* and the other equal to *y*, that periodically become equal, forcing the cross-section to be a circle.

$$\begin{cases} x = \frac{R}{2} AR^{\left(sin\left(\frac{2\pi}{p}z\right)\right)} + \frac{R}{2} \\ y = \frac{R}{2} AR^{\left(-sin\left(\frac{2\pi}{p}z\right)\right)} + \frac{R}{2} \end{cases} \tag{1}$$

Where R is the radius of an equivalent straight tube and p is the corrugation period. The geometries for additive manufacturing process were drawn using the *Parametric equation* tool and *Lofted Boss/Base* feature build in CAD software, which approximated Eq. (1) for D_h with a maximum inaccuracy of ± 3.6 %. The manufacturing process adds additional geometrical uncertainty, but it has not been characterized. It is noticeable that the inaccuracy decreases with decreasing AR or increasing p. For the further discussion, it is assumed that D_h is constant across the flow channel and equivalent to the straight tube. The geometrical data and the inaccuracy in D_h of the tested tubes are given in Table 1.

Table 1. The geometrical data of the experimentally investigated tubes.

Tube name	AR	p, mm	L, mm	$A_{s,i}$, mm²	$A_{s,o}$, mm²	D_h, mm	δ, mm	Inaccuracy in D_h, %
AR1.6 p=7.5	1.6	7.5	250	4195.4	5873.3	5	1	±0.4
AR2.0 p=7.5	2.0	7.5	250	4525.2	6349.8	5	1	±2.8
AR1.6 p=20	1.6	20.0	250	4087.5	5526.9	5	1	±1.8
AR2.0 p=20	2.0	20.0	250	4280.2	5893.9	5	1	±2.9
AR2.2 p=20	2.2	20.0	250	4396.8	6028.2	5	1	±3.6
Straight	-	-	250	3925.0	5495.0	5	1	-

Figure 2 shows three of the tubes that were tested in a counter flow tube-in-shell heat exchanger. 3D models of all of the experimentally investigated tubes are available as supplementary material of this article. The double corrugated tube geometry varies in AR and p. The manufacturing process of the tubes may result in higher inner surface roughness of the tubes. Therefore, surface roughness analysis was carried out using a LEXT OLS4100 3D Measuring Laser Microscope made by Olympus Corporation. A sample for the surface roughness analysis was cut along the flow direction of the straight tube. The surface root square mean roughness, S_q, of a rectangular area 0.62×6.56 mm was directly measured according the standard ISO 4287 and found to be 0.013 mm with the maximum difference between the highest and the lowest measured points of 145.6 ± 13 μm.
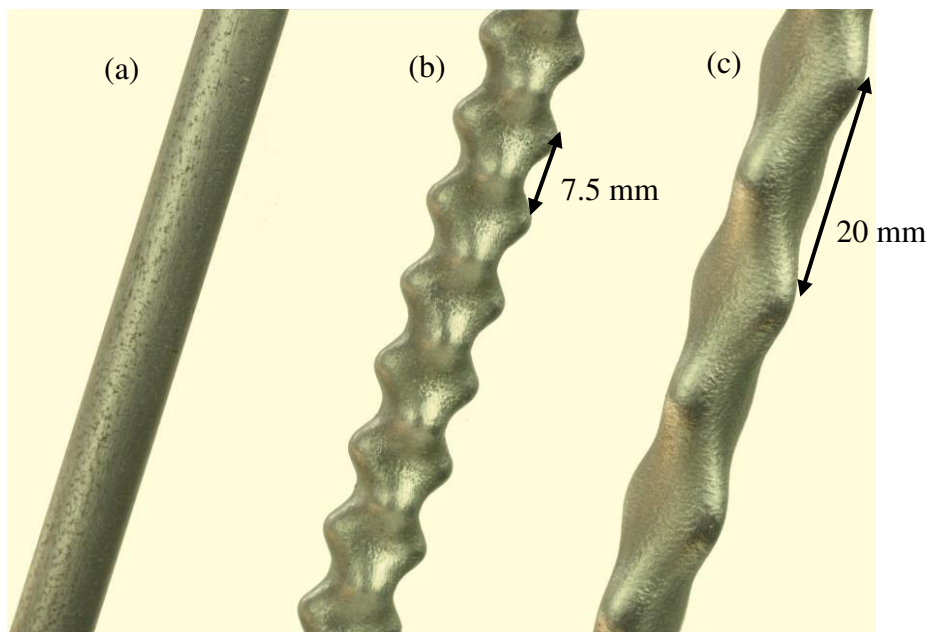
Figure 2. The 3D printed tubes (a) the straight reference tube, (b) double corrugated tube with $AR = 2.0$ and $p = 7.5$ mm, (c) double corrugated tube with $AR = 2.2$ and $p = 20.0$ mm.

The geometry of the double corrugated tubes constantly impinges the fluid flow and prevents the development of boundary layers. Modelling showed that the changing wall profile effectively

alters the velocity profile near the wall and improves heat transfer along the entire length of the tube [27]. Figure 3 demonstrates how the thermal boundary layers are disturbed in the double corrugated tube with *AR*=2.0 and *p*=7.5 mm and the corresponding straight tube in CFD modelling.
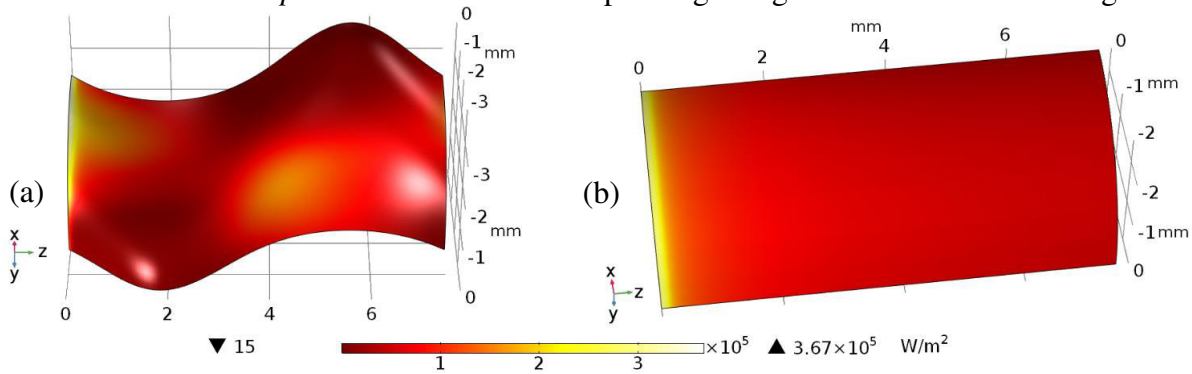
Figure 3. The heat flux in a double corrugated tube (flow rate 0.002 m³ h^{-1}) (a) and a straight (flow rate 0.004 m³ h^{-1}) tube (b) at the same pressure drop Δp = 1.843 Pa.

One can see that the heat exchange in the double corrugated tube continues all over the length, while the straight tube experiences the maximum heat flux only in the inlet region. The full description of the modelling procedure and the obtained results are presented in Ref. [27]. For the sake of clarity in this article, it has to be noted that fully hydraulically developed fluid flow with a constant wall temperature condition and a constant pressure difference condition were modelled while the experiments were conducted at developing flow conditions and the wall temperature cannot be considered constant. Finally, a single period of each double corrugated tube with different geometrical characteristics was considered in the model. Experiments, on the other hand, were carried out on tubes with constant length. Note that number of corrugation periods per length of the examined tubes is an integer.

2.2. The test setup

Figure 4 shows the tube-in-shell counter-flow heat exchanger that all the tubes were tested in. The connectors (3) shown in Figure 4 (b) of the heat exchanger were machined out of nylon and have a conical shape to ensure sealing between the tube and the shell sides. Figure 5 shows the schematic of the full experimental setup.
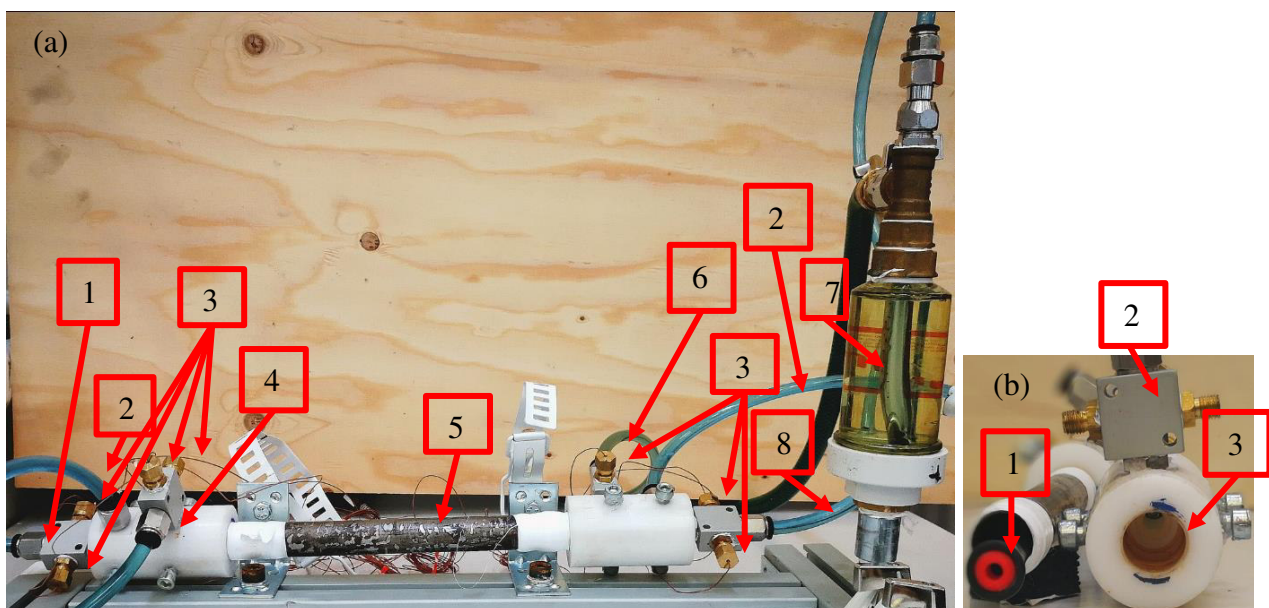
Figure 4. (a) A photograph of the experimental tube-in-shell setup. 1 – tube side outlet; 2 – blocked connections for pressure measurements; 3 – thermocouples; 4 – shell side inlet; 5 – shell (OD 20 mm); 6 – shell side outlet; 7 – air

separator; 8 – tube side inlet. (b) 1 – 3D printed connector with an O-ring for sealing the tube side in the shell; 2 – manifold for mounting thermocouples; 3 – a nylon connector.
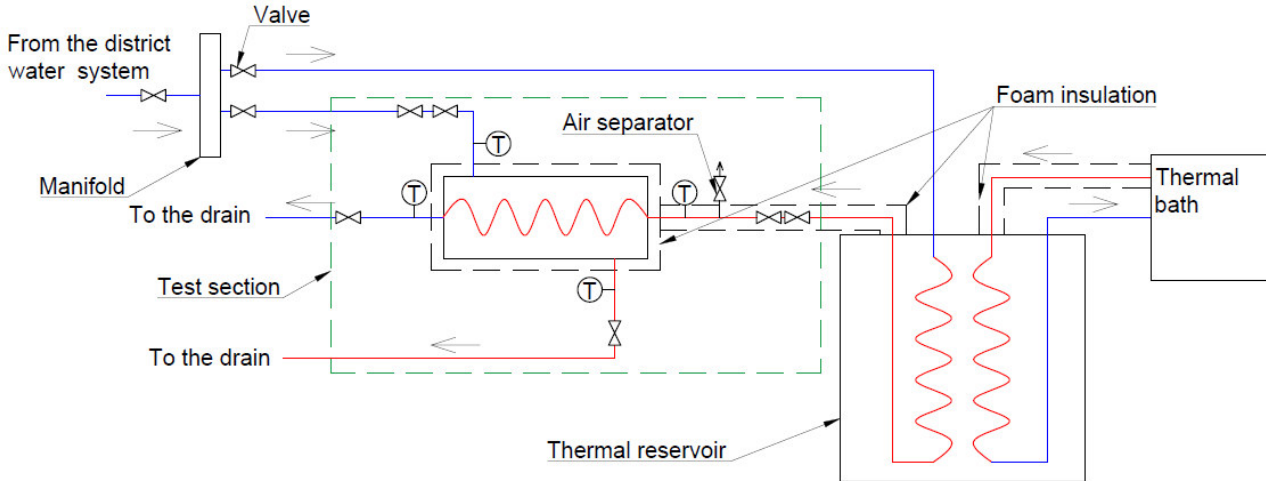
Figure 5. Schematic of the experimental setup for convective heat transfer measurements.

The water for the test rig was supplied from the district water supply system. The water flow was separated into two streams by a manifold with the possibility to regulate/close both flows using valves. A cold-water stream was directly connected to the shell side. Two valves were used to regulate the flow rate. The hot-water side was connected through a thermal reservoir with a copper coil heat exchanger. The water temperature at the thermal reservoir was maintained using a thermal bath. The heated water ($T_{hot} \approx 60$ °C) was pushed to the air separator and then to the test section. The flow rate was regulated using two valves at the inlet to the tube and one valve at the outlet of the tube. This flow regulation technique ensured bubble-free water flow with no temperature stratification at low flow rates. The temperatures at the inlet and the outlet of the tube and shell sides were measured by two T-type thermocouples at each point. The thermocouples were connected to an NI Ice point reference and the results were logged using LabView. The experimental uncertainty was ±0.1 °C. The pressure drop was measured at isothermal conditions using a differential manometer. The uncertainty of the differential manometer was ± 10 Pa.

2.3. Data Processing

The main goal of the present experimental work is to characterize the behaviour of the tested double corrugated tubes. The heat transfer performance and the pressure drop penalty were quantified by means of the Nusselt number (*Nu*) distribution and friction factor (*f*) respectively. In the data reduction, D_h was used as the characteristic length.

2.3.1. Heat transfer: parameter estimation approach

For any parallel flow heat exchanger, the average overall heat transfer coefficient, *U*, referred to the outer heat transfer surface area A_o can be obtained from Eq. (2).

$$U = \frac{Q}{A_o \Delta T_{lm}} \qquad (2)$$

Where ΔT_{ml} is the logarithmic mean temperature difference and *Q* is the heat flow rate. The heat flow rate *Q* from Eq. (2), can be suitably determined by the energy balance, Eq. (3), for the fluid stream on the tube side.

$$Q = m_i c_{p,i} \left(T_{i,in} - T_{i,out} \right) \qquad (3)$$

Where $T_{i,in}$ and $T_{i,out}$ express the tube-side fluid bulk temperatures evaluated at the inlet and outlet sections, respectively.

The energy balance can also be evaluated on the shell stream (Eq. (4)) but, in this case, some care is needed to measure the bulk temperature, as the temperature difference between the inlet and the outlet is quite small.

$$Q = m_o c_{p,o} (T_{o,out} - T_{o,in}) \tag{4}$$

The overall heat transfer coefficient is related to the tube side and shell side fluid convective heat transfer coefficients by Eq. (5).

$$\frac{1}{U\,A_o} = \frac{1}{h_i\,A_i} + R_w + \frac{1}{h_o\,A_o} \tag{5}$$

Where h_i is the convective heat transfer coefficient of the water flowing in the tube and h_o is the convective heat transfer coefficient of the water stream flowing on the shell side, A_i and A_o are the inner and outer heat transfer surface areas and R_w is the thermal resistance of the wall that separates the two fluids, expressed by Eq. (6) for circular tubes.

$$R_w = \frac{\ln(D_0/D_i)}{2\pi L k_w} \tag{6}$$

Where L the heat exchanger's length, k_w is the thermal conductivity of the wall material, which is approximately $k_w = 150$ Wm^{-1}K^{-1} [28].

The wall thermal resistance, R_w, can be assumed known and constant for a given heat exchanger and under a given operating condition. By using the internal D_h of the tested tubes as the characteristic length for the tube section, the internal side Nusselt number is expressed by Eq. (7).

$$Nu_i = \frac{h_i D_h}{k_f} \tag{7}$$

Where k_f is thermal conductivity of water inside the tube.

It is not easy to predict which is the dominating thermal resistance in Eq. (5) in this case because the internal-side and shell-side heat transfer coefficient are of the same order of magnitude.

In Eq. (5) both h_i and h_o are generally unknown and they can be suitably determined by adopting a parameter estimation technique under an inverse data processing methodology [29].

The tube and shell side heat transfer coefficients can be correlated in terms of the Nusselt number using Colburn's analogy expressed as in Ref. [30].

$$Nu_i = C_i Re^{\alpha_i} Pr^{\beta_i} \tag{8}$$

$$Nu_o = C_o Re^{\alpha_o} Pr^{\beta_o} \tag{9}$$

It follows that the characterization of the studied heat exchangers can be described by assuming that in Eq. (5) the unknown variables are C_i, α_i, β_i, C_o, α_o, β_o. In the present case water is the only working fluid. Thus, the Prandtl number does not vary significantly during the tests. Therefore, the value of the coefficients $\beta_{i,o}$ has been assumed equal to a classical value of 0.33 present in many of the Nusselt number correlations that characterized the fluid flow inside straight tube [30]. Both h_i and h_o could be concurrently estimated under the parameter estimation approach by minimizing the squared errors of the prediction with respect to the experimentally measured values for U [29]. This implies to minimize, under the usual least square approach, the following function:

$$S(C_i, \alpha_i, C_o, \alpha_o) = \sum_{j=1}^{N} \left[(U)_{exp,j} - (U)_{calc,j} \right]^2 \tag{10}$$

Where N is the number of measurements which are performed by varying fluid mass flow rate for both the tube and shell side with the resulting and U_{calc} is expressed as follows:

$$U_{calc} = \frac{1}{A_o}\left(\frac{D_{h,i}}{k_f A_i} \cdot \frac{1}{C_i Re^{\alpha_i} Pr^{0.33}} + R_w + \frac{D_{h,o}}{k_f A_o} \cdot \frac{1}{C_o Re^{\alpha_o} Pr^{0.33}}\right)^{-1} \tag{11}$$

Then, the parameter estimation procedure applied to the heat transfer characterisation of the studied heat exchanger is represented by the minimisation of the objective function S expressed by Eq. (10) by considering Re as the independent variable and C_i, α_i, C_o and α_o as the unknown variables, and all the other properties and geometrical quantities to be known.

2.3.2. Friction factor

Regarding the pressure drop, the average Darcy-Weisbach friction factor was calculated as given by Eq. (12).

$$f = 2\frac{\Delta p D_h}{\rho w^2 L} \tag{12}$$

Where w is the mean fluid axial velocity and Δp is the pressure drop along the tested section of length L. Due to the experimental setup configuration, a concentrated pressure drop is present and originates from strong cross sectional area variations that occur in the connectors. Therefore, the full pressure drop, Δp, in the test region is expressed by Eq. (13).

$$\Delta p = f\frac{\rho w^2}{2D_h}L + \xi\frac{\rho w^2}{2} \tag{13}$$

The first term on the right hand side of Eq. (13) expresses frictional pressure drop losses, while the second term expresses the concentrated pressure drop. Here ξ is the vorticity [31].

Since the concentrated pressure drop is caused by the experimental setup, it must be the same for all the investigated tubes. It is important to separate the frictional and concentrated pressure drop in order to enable fair comparison of the friction factor in double corrugated tubes and the equivalent straight tube. This can be done if the ξ value, which is unique for every flow regime regardless of the geometry of the tested tubes, is determined. For this reason, the experimental data obtained for the straight tube were analysed. Two well-known correlations were used to calculate friction factor f causing the frictional pressure drop. Namely, the Darcy friction factor, given by Eq. (14), and Colebrook correlations, given by Eq. (15), used for the laminar and turbulent flow regimes [32], respectively.

$$f_{laminar} = \frac{64}{Re} \tag{14}$$

$$\frac{1}{\sqrt{f_{turbulent}}} = -2.0\log\left(\frac{S_q/D}{3.7} + \frac{2.51}{Re\sqrt{f_{turbulent}}}\right) \tag{15}$$

Where the relative roughness $S_q/D = 0.0026$ was used for solving the Colebrook equation for f by using MATLAB routine, presented by Clamond [33]. The experimentally obtained pressure measurement data for the straight tube were sorted into laminar $Re \leq 2000$ [32] and turbulent $Re > 3500$ regimes, the range in between them was considered to be transitional.

Once the frictional and concentrated pressure drop were separated, the ξ values were determined for laminar and turbulent flow regimes using a least square fit method. Friction factor for experimentally the investigated tubes was determined from frictional pressure loss component that was obtained by subtracting concentrated pressure drop form the full pressure drop. The obtained f values for all the tubes were fitted to the form given in Eq. (16) [25] using the nonlinear regression approach.

$$f = KRe^\gamma \tag{16}$$

The uncertainty of the predicted friction factor values is expressed in terms of standard error of estimate, σ_{est}, as defined by Taylor [34].

$$\sigma_{est} = \sqrt{\frac{\Sigma(f_{exp} - f_{est})^2}{N-2}} \tag{17}$$

2.3.3. Performance evaluation criteria

The global performance evaluation criteria (*PEC*) at constant pumping power is the most commonly used approach to evaluate the overall performance of any enhanced geometry. The *PEC* is calculated as in Ref. [15].

$$PEC = \frac{Nu/Nu_0}{\left(f/f_0\right)^{1/3}} \tag{18}$$

To enable a straightforward comparison of the double corrugated tubes when designing heat exchangers, the presented *Nu* correlations are obtained using geometrical data such as surface area, A_s, cross-section area, A_c and hydraulic diameter, D_h, of an equivalent straight. Using this approach, the benefits of the enhanced surface area are already included in the comparison. Moreover, Bergles *et al.*, [35] pointed out that it is more convenient to use a nominal geometry for identifying heat transfer augmentation especially if the enhanced tube is used as a direct replacement of an existing straight tube. It must be mentioned that the maximum enhancement of the surface area in the investigated double corrugated tube was less than 16 %, thus it is of less importance. The penalty for the enhanced surface is evaluated via the friction factor, which is obtained from pressure drop measurements.

3. Results and discussion

The obtained experimental results for the tube side are presented in terms of correlations of *Nu*, *f* and *PEC*. The experimental results presented in this study are compared with other state-of-the-art enhanced geometries. It must be acknowledged that most of experimental studies, published on enhanced heat transfer in laminar flow regime, were conducted under uniform heat flux conditions [18,36–38]. This implies that, considering a straight tube, the *Nu* is generally higher due to the experimental boundary conditions [30]. Thus, more appropriate comparison of the thermal effectiveness of different kinds of enhanced surfaces could be done only by evaluating ratios of enhanced *Nu*. The experimental studies on AEA tubes and tubes fitted with helical screw-tape reported in Ref. [13,18] are chosen for the comparison because of the most suitable interval of *Re*. The *Nu* correlation for an AEA tube (Nu_{AEA}) is given by Eq. (19) as in Ref. [13] and for a helical screw-tape (Nu_{HST}) by Eq. (20) as in Ref. [18].

$$Nu_{AEA} = 0.0615 Re^{0.76} Pr_f^{1/3} \left(\frac{Pr_f}{Pr_w}\right)^{0.11} \tag{19}$$

$$Nu_{HST} = 0.017 Re^{0.996} Pr \, Y^{-0.5437} \tag{20}$$

Where *Y* is the twist ratio (length of one twist/diameter of the twist). According to the Ref. [18], the best performing helical screw-tape had *Y* = 1.95. Thus, this value was used for comparison. The *Nu* correlation reported in Ref. [13] is obtained for the AEA tube with $p/D_o = 2$ and *AR* = 1.6. The correlation is valid for a *Re* range from 500 to 50000. The p/D_o ratio of the double corrugated tubes reported in this study is from 1.1 to 2.9.

Correlations for *f* for the corresponding AEA tube (f_{AEA}) were given by Eq. (21) as in Ref. [13] and for the corresponding helical screw-tape (f_{HST}) by Eq. (22) as in Ref. [18].

$$f_{AEA} = 1.54 Re^{-0.32} \tag{21}$$

$$f_{HST} = 10.7564 Re^{-0.387} Y^{-1.054} \tag{22}$$

However, neither of the selected studies report correlations for *Nu* and *f* of their reference geometries. Moreover, the precise *Pr* number of the working fluid and the fluid layer close to the wall are not reported either. Thus, experimental data obtained in this study were correlated using the Eqs. (19 – 22) with the awareness of increasing uncertainty when comparing results. The ratio of *Pr* number of the fluid and the fluid layer at the wall in Eq. (19) is assumed to be 1. Due to above mentioned reasons the *PEC* of double corrugated tubes is not compared with the *PEC* of AEA tube and helical screw-tape.

A qualitative comparison of the experimental and numerical results is also provided in the discussion. The Reader is asked to remember that the modelling boundary conditions in Ref. [27] and the experimental conditions were different, thus quantitative analysis is not possible. Modelling showed that heat transfer performance increased with increasing *AR* and decreasing corrugation period.

3.1. Heat transfer results

The experimental heat transfer results for the straight tube were compared to both the Hausen (Eq. (23)) and the Sieder–Tate (Eq. (24)) correlations for the thermal entry region [39] in the laminar flow regime.

$$Nu_{Hausen} = 3.66 + \frac{0.0668\left(\left(D_h/L\right)Re\,Pr\right)}{1 + 0.04\left(\left(D_h/L\right)Re\,Pr\right)^{2/3}} \tag{23}$$

$$Nu_{Sieder-Tate} = 1.86 \left(\frac{Re\,Pr}{L/D_h}\right)^{1/3} \left(\frac{\mu}{\mu_w}\right)^{0.14} \tag{24}$$

Where μ is dynamic viscosity of water. The term evaluating the ratio of dynamic viscosities is considered to be one, since the measured temperature difference measured in a straight tube is approximately 10 °C and the change in viscosity is minor.

Figure 6 shows that the obtained results agree very well with the Hausen correlation, with a confidence of 85 %, and with the Sieder–Tate correlation, with a confidence of 95%. This is a good indication that the test setup and the method of data analysis are reliable. The entire estimation procedure was repeated for all the double corrugated tubes: the experimental conditions are reported the *Data in Brief* article and representative results are shown in Figure 7.
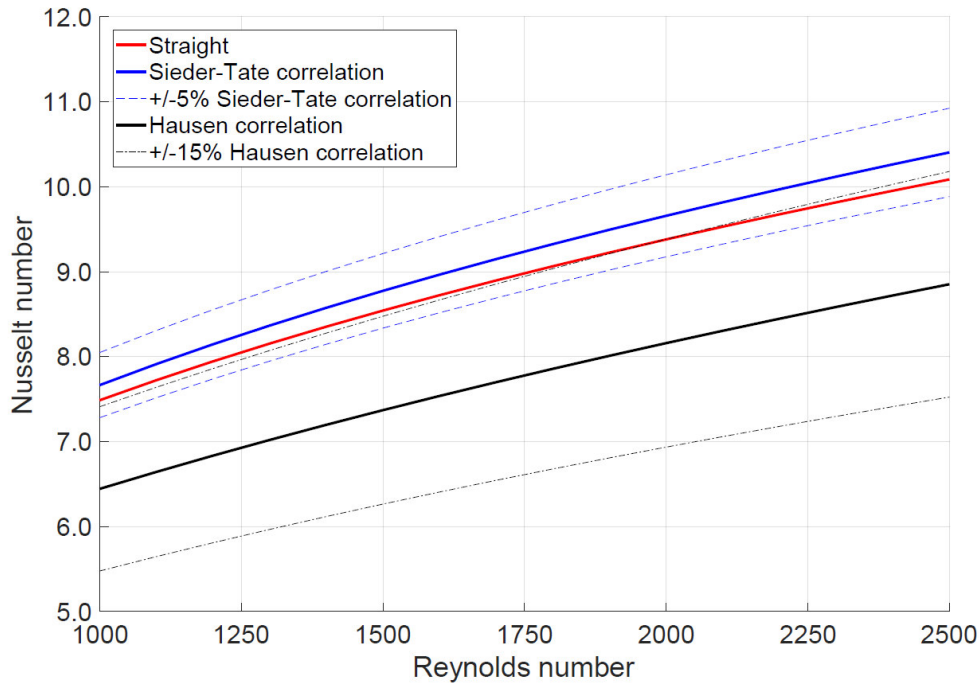
Figure 6. Comparison of *Nu* correlation obtained from experimental data for a straight tube and the Hausen and the Sieder–Tate correlations as a function of *Re*.

The accuracy associated with the estimated values was assigned by the parametric bootstrap method [40,41]. In this procedure, the term U_{exp} has been substituted by the distribution:

$$U_{exp} = U_{calc} \cdot (1 + \varepsilon) \tag{25}$$

Where U_{calc} was obtained from Eq. (11) adopting the heat transfer coefficients found by Eqs. (8-9). In order to find the heat transfer correlations, the *C* and α values estimated from the procedure described above. Moreover, ε represents a uniformly distributed random noise with zero mean and variance σ. The variance σ has been considered equal to the uncertainty related to the measured quantity $\Delta T = T_{i,in} - T_{i,out}$. Considering the overall heat transfer coefficient U_{exp} re-sampled from its probability distribution, as the starting value, the unknowns are calculated by the estimation procedure explained above; this process is repeated many times, and the results are processed using standard statistical techniques for evaluating 95 % confidence intervals (Figure 7). It also represents the uncertainty of the estimation procedure: in order to evaluate the overall uncertainty of the Nusselt number the usual propagation of errors procedure was used [42] considering, in addition to the error of the estimation technique, the uncertainty of temperature measurements, fluid properties and mass flow rate: they were assumed to be 2.5 %, 2 % and 5 % respectively). The obtained correlation coefficients and the uncertainty on *Nu* are given in Table 2.

Table 2. Experimentally obtained correlation coefficients for calculating *Nu* inside the tubes and *Nu* uncertainty.

Tube name	C_i	α_i	ε_{Nu}
AR1.6 p=7.5	0.039	0.88	±8.0 %
AR2.0 p=7.5	0.16	0.77	±8.5 %
AR1.6 p=20	0.056	0.75	±9.0 %
AR2.0 p=20	0.037	0.76	±11.0 %
AR2.2 p=20	0.016	0.91	±9.0 %
Straight	0.52	0.33	±14.0 %

Figure 7 shows that the higher *Nu* values are obtained for double corrugated tubes with shorter corrugation periods. One can see that thermal performance of the double corrugated tubes strongly depends on *p* while *AR* is a less significant factor. Generally double corrugated tubes with *p* = 7.5 mm show up to 35 % higher *Nu* than double corrugated tubes with *p* = 20 mm. Figure 7 shows that the double corrugated tube with the *AR* = 1.6 and *p* = 7.5 mm outperforms the double corrugated tube

with the $AR = 2.0$ and $p = 7.5$ mm once Re is above 2200. This signifies that more intense corrugations are more thermally efficient at lower Re. This is in agreement with previous modelling results.
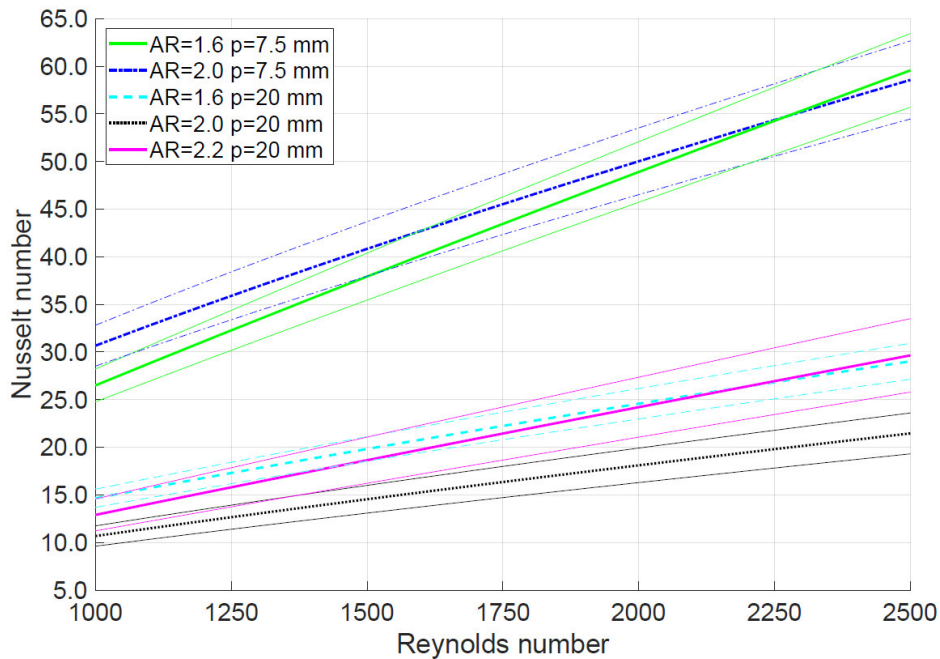
Figure 7. Nusselt number distribution for the tube side and corresponding uncertainty. The Prandtl number used here is $Pr = 3.5$.

However, the double corrugated tubes with $p = 20$ mm, show that higher thermal performance is obtained for tubes with lower aspect ratios. Namely the double corrugated tubes with $AR = 1.6$ shows the highest Nu until Re exceeds 2000, then the double corrugated tube with the $AR = 2.2$ outperforms it. It is noticeable that the double corrugated tube with $AR = 2.0$ shows somewhat lower thermal performance than tubes with $AR = 1.6$ and $AR = 2.2$. Numerical modelling predicted that performance of the $AR = 2.0$ tube should lie between $AR = 1.6$ and $AR = 2.2$. Several effects could be considered to explain the later findings. One of the contributing factors could be inaccuracy from manufacturing process, especially geometrical variations on the inner surface. It is hard to manipulate the results since the quality of the inner surface of this tube is unknown. Another explanation could be effects related to transition to turbulent flow, which was not considered in the modelling. Flow visualization tests should be done in order to fully understand and finalize the findings in Figure 7.

The ratio of Nu for the double corrugated tubes to the straight tube are shown in Figure 8, which demonstrates that the double corrugated tubes have up to a 500 % increase in Nu when $p = 7.5$ mm and up to a 200 % increase when $p = 20$ mm compared to an equivalent straight tube. It is also noticeable that the Nu ratio increases with increasing Re. Figure 8 shows more clearly that the thermal efficiency of the double corrugated tubes with $p = 7.5$ mm is generally 100% higher than the double corrugated tubes with $p = 20$ mm. The performance of an AEA tube and a helical screw-tape are also plotted on Figure 8.
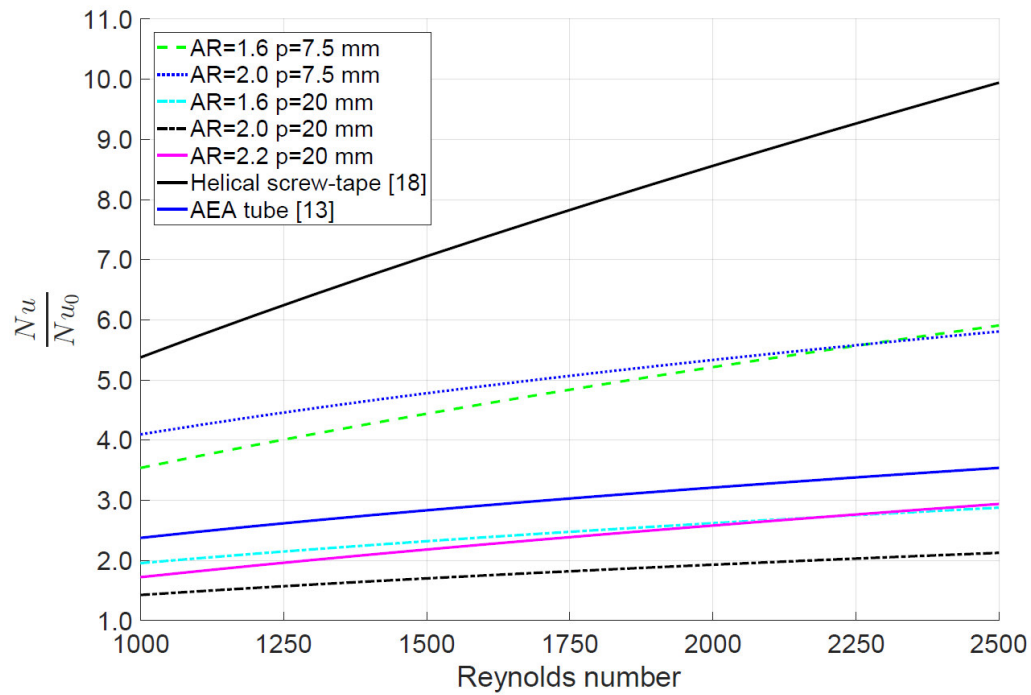
Figure 8. Nu/Nu_0 as a function of *Re*.

Comparing experimental results of this study with the AEA tube correlation reported in ref. [13], it is seen that the double corrugated tubes with *p* = 7.5 mm show significantly higher thermal performance than the AEA tube. On the other hand, double corrugated tubes with *p* = 20 mm show similar, however, somewhat lower thermal performance.

Figure 8 shows that the *Nu* ratio for the double corrugated tubes is lower than for the helical screw-tape [18]. However, it is worth noting that the *Nu* correlation for the tube with helical screw-tape was obtained at a constant heat flux condition while the correlation for Nu_0 was obtained in the tube-in-shell heat exchanger with water-water system because no equivalent straight tube correlation was given by Ref. [18]. Thus, the thermal efficiency for the helical screw-tape is to some extent over predicted.

The agreements between experimental data and the correlation were checked in terms of the overall heat transfer coefficient, *U*. Figure 9 shows a comparison between experimental and correlated *U* values for the double corrugated tube with *AR* = 2.0 and *p* = 7.5 mm inside the tube (a) and inside the shell (b) and experimental values against correlated ones (c). It is found that experimental data and values derived from the correlations are in a very good agreement.
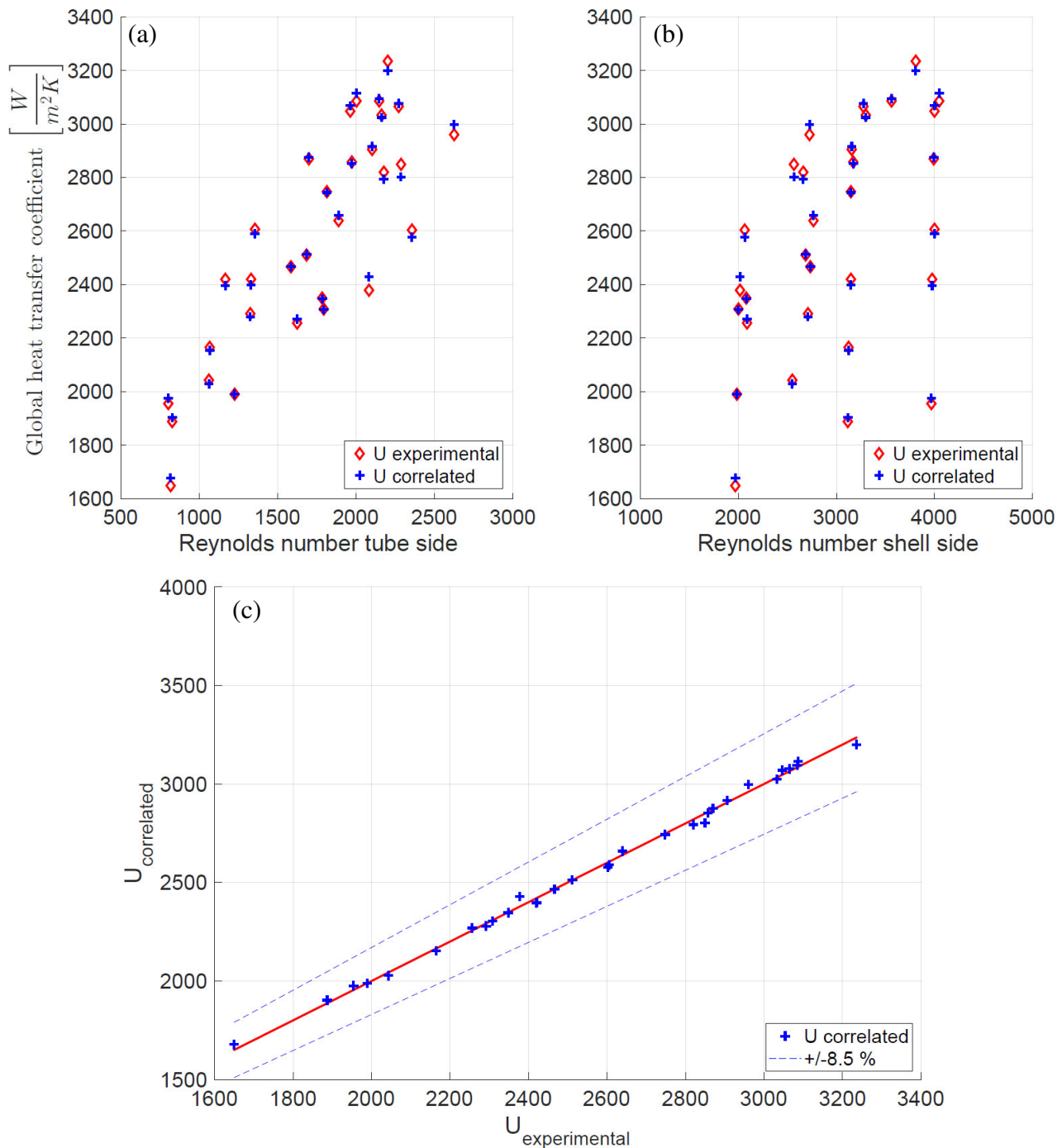
Figure 9. Global heat transfer coefficient *U* for the double corrugated tube with *AR* = 2.0 *p* = 7.5 mm measured experimentally and calculated using the obtained correlations as a function of *Re* in the tube side (a) and in the shell side (b). Comparison of the measured and predicted *U* values for the same double corrugated tube (c).

3.2. Pressure measurement results

Figure 10 shows a comparison of experimentally measured friction factors for the straight tube when the ξ value is subtracted from the measured values. The corrected experimental data for the straight tube were also compared with Petukhov's correlation as given in Ref. [30], which is valid in a range of $3000 \lesssim Re \lesssim 5 \cdot 10^6$.

$$f_{Petukhov} = (0.790 \ln Re - 1.64)^{-2} \qquad (24)$$

Figure 10 shows an excellent agreement between the corrected experimental data and classical theoretical correlations. The determined values are $\xi = 1.3$ for the turbulent regime and $\xi = 2.9$ for the laminar regime in a straight tube. The *Re* range from 200 to 3500 is considered the transition region

for the straight tube and a spline curve is used to represent f in this region for plotting purposes when comparing friction factor in the straight tube to corrugated ones. The obtained ξ values agrees well with the data presented by Nakayama and Boucher [31]. It was pointed out by several authors that flow transition in corrugated tubes occurs much earlier than in a straight tube [13,25], finding that the *Re* transition value varies from 500 to 800 depending on corrugation intensity [25]. The experimental data presented in this study are in *Re* interval from 1000 to 2500, thus the flow in double corrugated tubes is considered turbulent and a single value of $\xi = 1.3$ was used to normalize the friction factor for the double corrugates tubes.
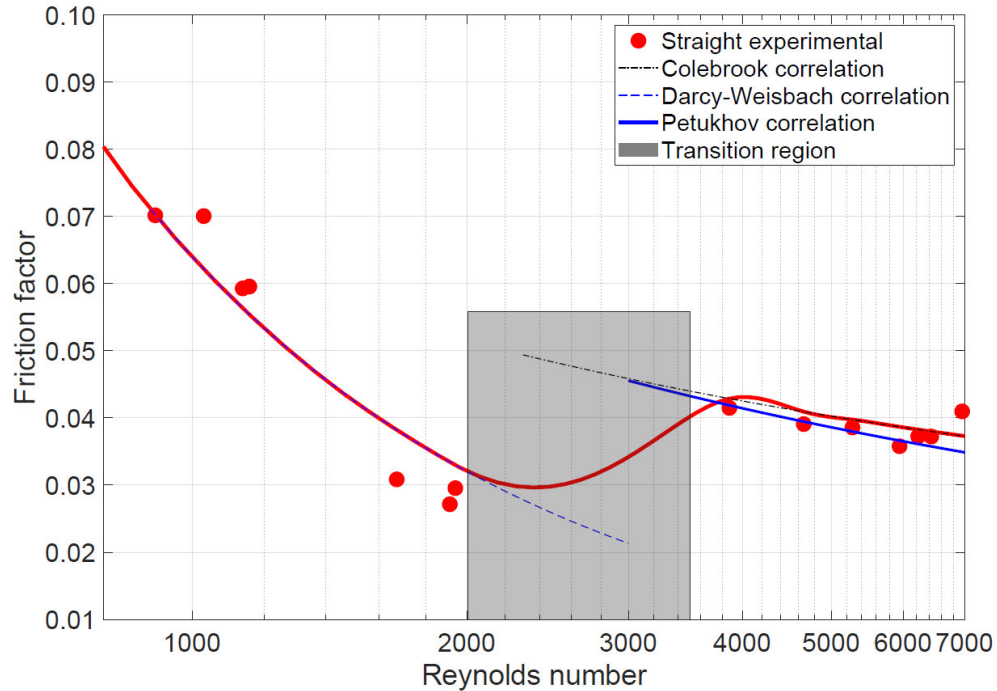
Figure 10. Comparison of the corrected experimental friction factor with Darcy-Weisbach and Colebrook correlations for laminar and turbulent flow regimes, respectively.

The pressure measurements were conducted at isothermal flow conditions on a dedicated rig. Figure 11 shows the corrected experimental f as a function of *Re*. The obtained coefficients of data fit and standard error of estimate are given in Table 3.

Table 3. Data fit coefficients for friction factor and standard error of estimate.

Tube name	K	γ	σ_{est}
AR1.6 p=7.5	1.22	-0.17	±1.97 %
AR2.0 p=7.5	1.17	-0.12	±2.24 %
AR1.6 p=20	10.0	-0.57	±0.35 %
AR2.0 p=20	7.66	-0.54	±0.94 %
AR2.2 p=20	5.94	-0.52	±0.73 %
Straight (700≤*Re* <2000)	581	-1.31	±0.81 %
Straight (3000<*Re*≤6400)	0.21	-0.20	±0.10 %

Figure 11 shows the corrected experimental f for the double corrugated tubes and the results of nonlinear regression analysis. From Figure 12 it is clear that the highest f values are obtained for the most corrugated tubes. It can be seen that similar values of f are obtained for all the tubes with $p = 20$ mm regardless of *AR*. However, Figure 12 shows that, for the double corrugated tubes with $p = 7.5$ mm, an increase in *AR* leads to greater f values. Figure 12 shows that for the most corrugated tube with $AR = 2.0$ and $p = 7.5$ mm, f increases up to 17 times at laminar-transition *Re* region, while for all the tubes with $p = 20$ mm, f increases up to 4 times at the same *Re*.
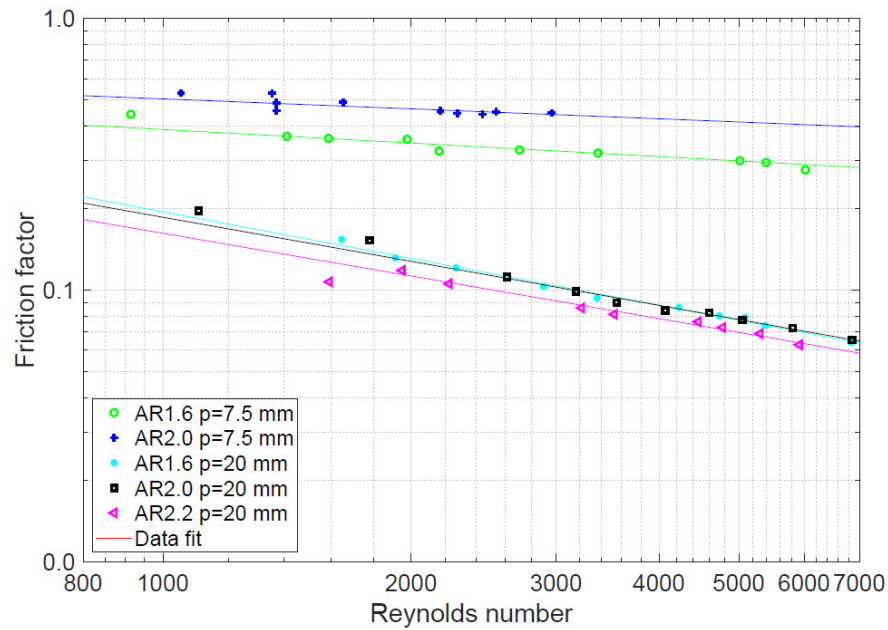
Figure 11. The friction factor, *f*, as a function of *Re* for double corrugated tubes.
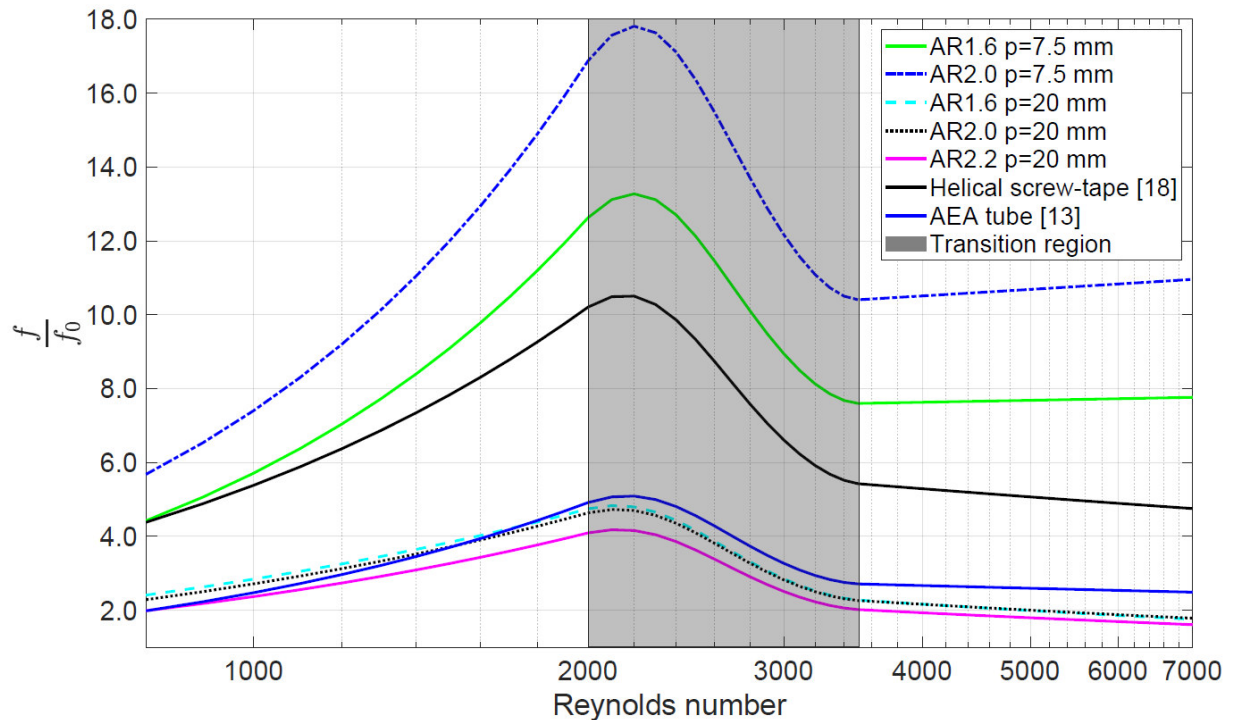
Figure 12. The ratio of *f/f₀* as a function of *Re*. Note that the transition *Re* is considered to be 2000 for the straight tube.

The ratio of *f* for the double corrugated tubes is compared to other state-of-the-art geometries. Figure 12 demonstrates that the *f* ratio for double corrugated tubes with *p* = 20 mm and the AEA tube is similar, however, somewhat lower in the turbulent flow region. Moreover, with increasing *Re*, *f* decreases faster for the double corrugated tubes with *p* = 20 mm, than for the AEA tube. This finding shows that the smoother geometrical transition between ellipse-based flow cross-section leads to lower *f* in comparison with the geometry of the AEA tubes. It is noticeable that the experimental results were sorrelated with single expression in a range of *Re* from 800 to 7000 for the double corrugated tubes. This was also found by in Ref. [13] for AEA tubes.

The ratio of *f* for a tube fitted with the helical screw-tape [18] is somewhat similar, however lower when compared to the double corrugated tubes with *p* = 7.5 mm. This is especially noticeable in the turbulent flow region.

The simulations, described in Ref. [27], were performed at constant Δp, thus the hydraulic performance of the double corrugated tubes was analysed in terms of volumetric flow reduction. Generally, the predicted flow resistance of double corrugated tubes increases for higher AR and smaller p.

3.3. Evaluation of the global performance

The overall performance of the double corrugated tubes was evaluated at constant pumping power using PEC. Figure 13 demonstrates that the overall performance of the double corrugated tubes is up to 160 % higher than the straight tube. It is noticeable that the double corrugated tubes with shorter period demonstrate higher PEC values than tubes with a longer period. Comparison of Figure 8,Figure 12 and Figure 13 suggests that the thermal performance of the double corrugated tubes is more significant than the friction factor when evaluating PEC of the double corrugated tubes with $p = 20$ mm. However, for the double corrugated tubes with $p = 7.5$ mm the friction factor compromises the PEC the most.
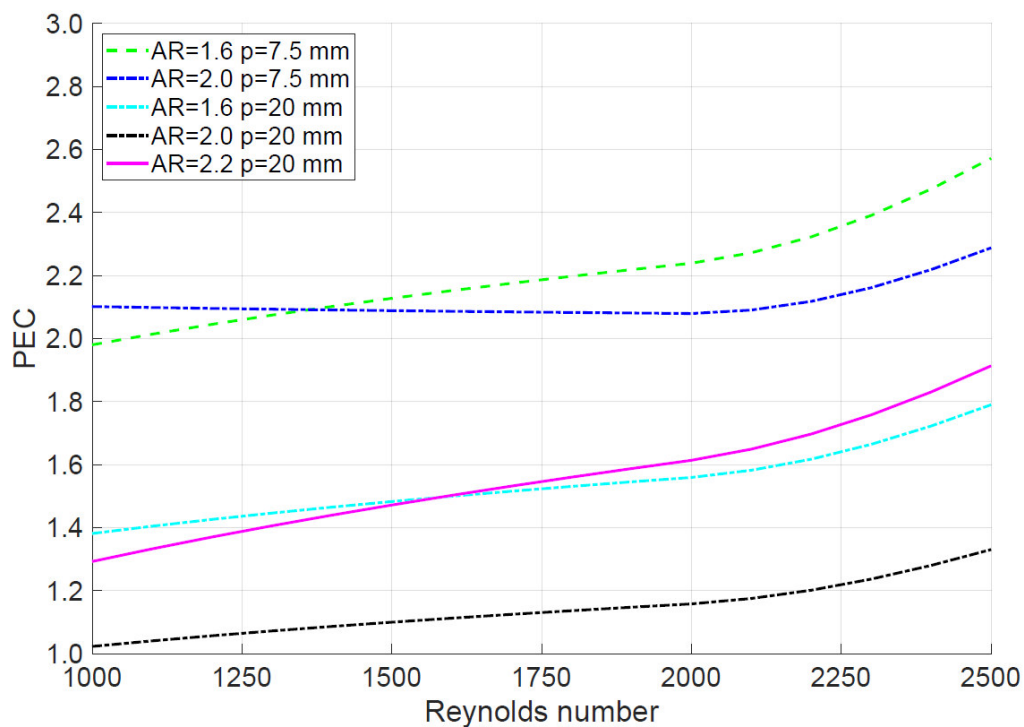
Figure 13. *PEC* as a function of *Re*.

Finally it is worth to mention that the predictions of numerical simulations reported in Ref. [27] generally agree with the experimental PEC results. Both experimental results and numerical predictions agree that PEC is the highest for the double corrugated tubes with $AR = 1.6$ when $p = 7.5$ mm and $AR = 2.2$ when $p = 20$ mm. However, PEC values predicted by CFD modelling are lower than obtained experimentally. This is due to different boundary conditions of the model and experiment.

4. Conclusions

Five double corrugated tubes, whose geometry is inspired by vascular heat exchangers found in fish such as the opah, were experimentally investigated in a tube-in-shell heat exchanger at low Re and compared to other state-of-the-art enhanced heat transfer geometries. The double corrugated tubes, presented in this study, demonstrate superior thermal and global thermo-hydraulic efficiency compared to AEA tubes, however thermal performance of the previous tubes is lower when compared to a tube fitted with a helical screw-tape.

Experimental results demonstrate that the double corrugated tubes significantly outperform the equivalent straight tube in the tested *Re* region. The thermal performance of the double corrugated tubes is up to 500 % higher than a straight tube. The heat transfer benefit comes at a cost of increased pressure drop, but the global thermo-hydraulic performance is up to 160 % higher than an equivalent straight tube, indicating that the overall thermal performance is enhanced.

Tubes with shorter corrugation period are shown to be generally more efficient. For the tubes tested, the corrugation period has a higher impact on the thermal and overall performance than the aspect ratio. The novel geometry of the double corrugated tubes demonstrates superior thermal performance in comparison with the AEA tubes, although somewhat lower than spirally corrugated tubes with twisted tape inserts. However, most of the reported experimental results on performance of enhanced surfaces were obtained in higher *Re* flow regimes, where data does not exist for the double corrugated tubes. In order to conduct comprehensible comparison of the performance of double corrugated tubes and other enhanced surfaces, deeper experimental investigation is required. Importantly, the first experimental results, obtained for double corrugated tubes, encourage future research efforts and provides the possibility of more detailed comparisons with other enhanced surfaces. Future studies on fouling behaviour, additional fluids, and two-phase flow could give a better characterization of the double corrugated tubes.

Experiments show that the double corrugated tubes are a promising geometry for enhanced heat transfer. Although the geometry presented here is based on tubes, the concept of holding the hydraulic diameter of the flow cross section constant while varying the geometry can be applied to plate heat exchangers, porous media and other heat transfer applications. Further improvements in performance may be realized by optimization of the corrugation pattern or by using non-elliptical cross sections.

5. Acknowledgement

6. References

[1]   B. Bhushan, Biomimetics: lessons from nature-an overview, Philos. Trans. R. Soc. A Math. Phys. Eng. Sci. 367 (2009) 1445–1486.

[2]   C. Mattheck, K. Bethge, J. Schäfer, Safety factors in trees, J. Theor. Biol. 165 (1993) 185–189.

[3]   E. Arzt, S. Gorb, R. Spolenak, From micro to nano contacts in biological attachment devices, Proc. Natl. Acad. Sci. 100 (2003) 10603–10606.

[4]   B. Dean, B. Bhushan, Shark-skin surfaces for fluid-drag reduction in turbulent flow: A review, Philos. Trans. R. Soc. A Math. Phys. Eng. Sci. 368 (2010) 4775–4806.

[5]   P.F. Scholander, V. Walters, R. Hock, L. Irving, Body insulation of some arctic and tropical mammals and birds, Biol. Bull. 99 (1950) 225–236.

[6]   K. Johansen, C. Bech, Heat conservation during cold exposure in birds (vasomotor and respiratory implications), Polar Res. 1 (1983) 259–268.

[7]   K.A. Dickson, J.B. Graham, Evolution and consequences of endothermy in fishes, Physiol. Biochem. Zool. 77 (2004) 998–1018.

[8]   N.C. Wegner, O.E. Snodgrass, H. Dewar, J.R. Hyde, Whole-body endothermy in a mesopelagic fish, the opah, Lampris guttatus, Science (80-.). 348 (2015) 786–789.

[9]   E.D. Stevens, H.M. Lam, J. Kendall, Vascular anatomy of the counter-current heat exchanger of skipjack tuna, J. Exp. Biol. 61 (1974) 145–153.

[10]   P. Börnert, D. Jensen, Coronary artery imaging at 0.5 T using segmented 3D echo planar imaging, Magn. Reson. Med. 34 (1995) 779–785.

[11]   E. Jantsch, Tubular heat transfer aparatus, 2663321, 1953.

[12] S. Rainieri, G. Pagliarini, Convective heat transfer to orange juice in smooth and corrugated tubes, Int. J. Heat Technol. 15 (1997) 69–75.

[13] J.A. Meng, X.G. Liang, Z.J. Chen, Z.X. Li, Experimental study on convective heat transfer in alternating elliptical axis tubes, Exp. Therm. Fluid Sci. 29 (2005) 457–465.

[14] J.F. Fan, W.K. Ding, J.F. Zhang, Y.L. He, W.Q. Tao, A performance evaluation plot of enhanced heat transfer techniques oriented for energy-saving, Int. J. Heat Mass Transf. 52 (2009) 33–44.

[15] R.L. Webb, Principles of enhanced heat transfer, 2nd ed., Taylor and Francis CRC ebook account, Abingdon, Great Britain, 1994.

[16] Y. Dong, L. Huixiong, C. Tingkuan, Pressure drop, heat transfer and performance of single-phase turbulent flow in spirally corrugated tubes, Exp. Therm. Fluid Sci. 24 (2001) 131–138.

[17] S. Pethkool, S. Eiamsa-ard, S. Kwankaomeng, P. Promvonge, Turbulent heat transfer enhancement in a heat exchanger using helically corrugated tube, Int. Commun. Heat Mass Transf. 38 (2011) 340–347.

[18] P. Sivashanmugam, S. Suresh, Experimental studies on heat transfer and friction factor characteristics of laminar flow through a circular tube fitted with helical screw-tape inserts, Appl. Therm. Eng. 26 (2006) 1990–1997.

[19] V. Zimparov, Enhancement of heat transfer by a combination of three-start spirally corrugated tubes with a twisted tape, Int. J. Heat Mass Transf. 44 (2001) 551–574.

[20] S. Laohalertdecha, S. Wongwises, The effects of corrugation pitch on the condensation heat transfer coefficient and pressure drop of R-134a inside horizontal corrugated tube, Int. J. Heat Mass Transf. 53 (2010) 2924–2931.

[21] S. Pal, S.K. Saha, Experimental investigation of laminar flow of viscous oil through a circular tube having integral axial corrugation roughness and fitted with twisted tapes with oblique teeth, Heat Mass Transf. Und Stoffuebertragung. 51 (2015) 1189–1201.

[22] S. Rainieri, F. Bozzoli, L. Cattani, G. Pagliarini, Compound convective heat transfer enhancement in helically coiled wall corrugated tubes, Int. J. Heat Mass Transf. 59 (2013) 353–362.

[23] S. Mac Nelly, W. Nieratschker, M. Nadler, D. Raab, A. Delgado, Experimental and numerical investigation of the pressure drop and heat transfer coefficient in corrugated tubes, Chem. Eng. Technol. 38 (2015) 2279–2290.

[24] A. Harleß, E. Franz, M. Breuer, Experimental investigation of heat transfer and friction characteristic of fully developed gas flow in single-start and three-start corrugated tubes, Int. J. Heat Mass Transf. 103 (2016) 538–547.

[25] S. Rainieri, A. Farina, G. Pagliarini, Experimental investigation of heat transfer and pressure drop augmentation for laminar flow in spirally enhanced tubes, Proc. 2nd Eur. Therm. 14th UIT Natl. Heat Transf. Conf. Ed. (1996) 203–209.

[26] A. Harleß, E. Franz, M. Breuer, Heat transfer and friction characteristics of fully developed gas flow in cross-corrugated tubes, Int. J. Heat Mass Transf. 107 (2017) 1076–1084.

[27] K. Navickaitė, L. Cattani, C. Bahl, K. Engelbrecht, Elliptical double corrugated tubes for enhanced heat transfer, Int. J. Heat Mass Transf. 128 (2019) 363–377.

[28] D. Martinez-Maradiaga, O. Mishin, K.L. Engelbrecht, Thermophysical properties of $AlSi_{10}Mg$ products obtained by metal additive manufacturing, (in prep.).

[29] J. V. Beck, K.J. Arnold, Parameter estimation in engineering and science (probability & mathematical statistics), John Wiley & Sons Inc, New York, 1977.

[30] T.L. Bergman, A.S. Lavine, F.P. Incropera, D.P. Dewitt, Introduction to heat transfer, 6th ed, 2014.

[31] Y. Nakayama, R.F. Boucher, Introduction to fluid mechanics, Butterworth-Heinemann, Oxford, UK, 2000.

[32] B.R. Munson, D.F. Young, T.H. Okiishi, Fundamentals of fluid mechanics, 4th ed., John Wiley&Sons, Iowa, USA, USA, 2002.

[33] D. Clamond, Efficient resolution of the colebrook equation, Ind. Eng. Chem. Res. 48 (2009)

3665–3671.

[34] J.R. Taylor, Introduction to error analysis, 2nd ed., Maple-Vail book manufacturing group, California, USA, USA, 1997.

[35] A.E. Bergles, A.R. Blumenkrantz, J. Taborek, Performance evaluation criteria for enhanced heat transfer surfaces, in: Proc. Fifth Int. Heat Transf. Conf., Tokyo, Japan, 1974.

[36] Z.S. Kareem, S. Abdullah, T.M. Lazim, M.N. Mohd Jaafar, A.F. Abdul Wahid, Heat transfer enhancement in three-start spirally corrugated tube: Experimental and numerical study, Chem. Eng. Sci. 134 (2015) 746–757.

[37] K.S. Saha, U.N. Gaitonde, A.W. Date, Heat transfer and pressure drop characteristics of laminar flow in a circular tube fitted with regulary spaced twisted-tape elements, Exp. Therm. Fluid Sci. (1989) 310–322.

[38] S.K. Saha, B.N. Swain, G.L. Dayanidhi, Friction and thermal characteristics of laminar flow of viscous oil through a circular tube having axial corrugations and fitted with helical screw-tape inserts, J. Fluids Eng. 134 (2012) 051210.

[39] F.P. Incropera, D.P. DeWitt, T.L. Bergman, A.S. Lavine, Fundamentals of heat and mass transfer, 6th ed., John Wiley & Sons, Inc., United States of America, 2007.

[40] B. Efron, The jackknife, the bootstrap and other resampling plans, Society for Industrial and Applied Mathematics, 1982.

[41] B. Blackwell, J. V. Beck, A technique for uncertainty analysis for inverse heat conduction problems, Int. J. Heat Mass Transf. 53 (2010) 753–759.

[42] S.J. Kline, F.A. McClintok, Describing uncertainties in single-sample experiments, Mech. Eng. (1953).

P.2. Elliptical double corrugated tubes for enhanced heat transfer

Elliptical double corrugated tubes for enhanced heat transfer

Kristina Navickaitė [a,*], Luca Cattani [b], Christian R.H. Bahl [a], Kurt Engelbrecht [a]

[a] Department of Energy Conversion and Storage, Technical University of Denmark, Frederiksborgvej 399, 4000 Roskilde, Denmark
[b] CIDEA, Interdepartmental Centre, University of Parma, Parco Area delle Scienze 181/A, I-43124 Parma, Italy

ABSTRACT

The thermal performance at constant pumping power conditions was numerically investigated in ellipse and super ellipse-based double corrugated tubes. A significant increase in thermal efficiency in double corrugated tubes is accompanied with a reasonable penalty in flow reduction for the cases modelled. An ellipse and a super ellipse-based double corrugated tubes were modelled at laminar fully hydraulically developed incompressible flow. Each base geometry was analysed holding either hydraulic diameter constant or the cross-sectional area constant. The pressure drop was normalized to the length of each modelled tube in order to maintain the pumping power. Thermal analysis was conducted under constant wall temperature boundary condition. The governing equations for non-isothermal flow were solved using the finite element method, and the results of the simulations were normalized to an equivalent straight tube. Numerical results predict a thermal efficiency enhanced by 400% maintaining 4.2 times lower volumetric flow rate in double corrugated tubes at the same pressure drop. The global performance evaluation criterion increases up to 14% for the double corrugated tubes with an ellipse-base and up to 11% for the tubes with super ellipse-base.

© 2018 Elsevier Ltd. All rights reserved.

1. Introduction

Enhanced heat transfer techniques are of interest for many different industrial fields, from the food industry all the way to aerospace engineering [1–5]. These techniques are particularly interesting for industrial applications in which the thermal processing of medium and high viscosity fluids is required. Moreover, in many cases, the fluid flow is necessarily laminar and therefore the efficiency of the heat transfer apparatuses in which fluids are conveyed is inevitably penalized. Techniques producing enhanced heat transfer accompanied by reduced pumping power are in high demand in these industries. Improved heat transfer allows thermodynamic cycles to operate at conditions that are more efficient and opens new opportunities for alternative cycles and sustainable energy technologies.

Heat transfer enhancement techniques essentially reduce the thermal resistance by increasing the heat transfer coefficients with or without an increase of the heat transfer surface area. The benefits that can be derived are, for instance, the reduction of the size of the heat exchangers which can reduce cost, and the decrease of the temperature difference at which the working fluids operate which increases thermal performance or efficiency. The

literature suggests to classify the techniques of enhanced heat transfer into active techniques that require a mechanical aid or electrostatic fields, passive techniques that do not require an external power and compound techniques that represent the combination of two or more different techniques [1]. Passive techniques are based on changes induced on the fluid flow through geometrical disruptions or modification of the surface, such as curvature of the walls or surfaces roughness or corrugation or through the insertion of devices in the main flow directly or by means of additives [1,6]. Since these techniques do not require any external power input, they are of great interest for industrial applications. Moreover, in the case of renovation or modification of an existing heat exchanger, the passive techniques offer much faster and easier solutions compared to active techniques. In addition, manufacturing process of realization of insertion or particular shape modifications of a tube wall is quite simple and nowadays it is a mature technology.

For all those reasons, the passive techniques became the most frequently employed for engineering applications, such as rippled and spirally corrugated tubes in systems for domestic hot water preparation using solar energy, finned tube geometries, treated surfaces, rough surfaces, displaced enhancement devices, swirl-flow devices, surface-tension devices, coiled tubes, or flow additives [1]. One of the most widely adopted passive technique is wall corrugation: the enhancement effect associated with wall corruga-

---

* Corresponding author.
  E-mail address: knav@dtu.dk (K. Navickaitė).

Nomenclature

Variables

A_s	surface area, m^2
A_c	cross-section area, m^2
AR	aspect ratio
a, b	semi-major and semi-minor axes of an ellipse, m
C	heat capacity rate, W K^{-1}
c_p	specific heat, J(kg K)$^{-1}$
D	diameter, m
f	friction factor, –
$\bar{h}$	average local convection coefficient, W(m^2 K)$^{-1}$
k	thermal conductivity of water, W(m K)$^{-1}$
$\dot{m}$	mass flow rate, kg s^{-1}
n	ellipse shape factor, –; unit normal to the surface
NTU	number of transfer units, –
Nu	Nusselt number, –
P	perimeter, m
Pr	Prandtl number, –
p	corrugation period, m
PEC	performance evaluation criteria, -
q	heat transfer, W
R	radius, m
Re	Reynolds number, –
$\bar{U}$	average overall heat transfer coefficient, W(m^2 K)$^{-1}$
U, u	fluid velocity in x direction, m s^{-1}
x, y, z	geometric coordinates, m
$\dot{V}$	flow rate, m^3 s^{-1}
ΔT	temperature difference, K
ΔT_{lm}	logarithmic mean temperature difference, K
Δp	pressure difference, Pa

Abbreviations

AEA	alternating elliptical axis
BC	boundary conditions
BL	boundary layers
CFD	computational fluid dynamics
err	error

Greek letters

ε	effectiveness, –
γ	geometric surface equation
Θ	temperature difference, K
μ	dynamic viscosity, Pa s
ρ	density, kg m^{-3}

Subscripts

c	coarse
conv	convective
f	fine, fluid
h	hydraulic
i	inlet
m	mean
max	maximum
min	minimum
s	surface
o	outlet
0	straight (reference)

tion is due to the periodic interruption of the development of both the thermal and hydraulic boundary layers, an increase in heat transfer area, generation of swirling and/or secondary flows and the promotion of flow transition to an unsteady regime. They are employed in a high number of industrial applications. It has also been emphasized that corrugated tubes give an advantage for more rapid thermal food processing which is important for retaining natural and organic properties of food [7].

The main research efforts over the last five years have been focused on investigating spirally or transversally corrugated tubes and channels, fins or inserts of wavy strip tapes, and other techniques that allow disturbance of thermal boundary layers [8–16]. A concept of fluted tubes was investigated by Srinivasan et al. [12]. The definition of the shape of the cross-section of the fluted tubes was given by bore and envelope diameters, flute depth, pitch and the helix angle, which depends on the number of flute starts. Most of the investigated corrugated tubes have a non-circular cross-section, e.g. a triangle shaped cross-section or a star shaped cross-section.

Another method to increase heat transfer was presented by Guo et al. [17], who suggested that convection can be enhanced by increasing the included angle between the fluid velocity and the temperature gradient. In other words, the thermal gradient in the radial direction must be forced to be more perpendicular to the velocity profile in the flow direction. This means that the mixing of the flow should be ensured in the radial direction. This can be done by changing the boundaries of the fluid channel, and an implementation of the principles suggested by Guo et al. [17] is an alternating elliptical axis geometry (AEA) tube where the flow geometry transitions from an elliptical cross section at a specific angle to an elliptical cross section at another angle. Li et al. [18] demonstrated that AEA tubes give at least an 84% increase in heat

transfer compared to a straight tube. Khaboshan and Nazif [13] performed modelling of AEA tubes for turbulent flow and showed that the tubes have an enhanced heat transfer performance at a performance evaluation criterion that is above 1 for some flow ranges. Meng et al. [19] proved experimentally that the heat transfer is 100–500% enhanced in AEA tubes for the Reynolds number (Re) region from 500 to 2300 with a 100–350% increase in flow resistance. Moreover, the Authors proposed uniform correlations for Nusselt number (Nu) and friction factor (f) in a range of Re from 500 to 50,000 for AEA tubes that have period and diameter ratio of $p/D = 2$. The uniform correlation of Nu shows that the AEA tubes exhibits early transition from laminar to turbulent flow regime.

Generally, the geometries presented in literature show an increase in Nu with increasing Re within the laminar flow regime. Research on more intensive ways to disrupt the thermal boundary layer has also been carried out. These methods include artificially increased wall roughness and different types of inserts or turbulators [20]. All the approaches discussed above increase the surface area for the heat transfer, the convection coefficient, and the pressure drop. The major attention of experimental and numerical work has been directed toward spirally corrugated tubes. Very few studies have reported results of global performance obtained using tubes, shaped in a sinusoidal manner [3,21,22]. Moreover, fewer results of experimental and modelling studies were obtained at low Re [22–28]. Generally, it was found that a significant increase in heat transfer in a corrugated tube of a given geometry is obtained in a certain range of Re number and further raising Re does not influence heat transfer as much. Hærvig et al. [3] reported that increasing the corrugation length in spirally corrugated tubes increases Nu. The same study also showed that at intense corrugations, the flow is radically different, which results in a slight increase in heat transfer, while pressure loss increases significantly.

In this paper, a novel geometry of a tube that is corrugated in both the transverse and annular directions, such that the hydraulic diameter (D_h) or cross-sectional area (A_c) at any point in the flow direction is constant is presented. Double corrugated tubes with either an ellipse-based or a super ellipse-based cross-section were analysed. The concept is similar in principle to AEA tubes, but the transition between cross sectional profiles occurs continuously along the flow direction, which can give a lower pressure drop while maintaining an enhanced heat transfer performance. The variation of channel aspect causes the tube walls to constantly impinge and disturb the thermal boundary layer and enhance heat transfer.

The approach of maintaining a constant cross-sectional area was suggested by, for example, Jantsch [29]. In the case of a constant cross-section area, the average fluid velocity is constant while the pressure drop profile can vary along the flow direction. When the hydraulic diameter is held constant, the effective flow opening remains constant but the flow area can change along the flow direction, thus the average fluid velocity varies in the flow direction. CFD (*Computational fluid dynamics*) simulations are extensively used to predict thermohydraulic performance of enhanced geometries. Numerous studies have been published discussing performance of enhanced geometries in different flow regimes or thermal boundary conditions. In this study, CFD is used as a tool to predict the thermo-hydraulic performance of the double corrugated tubes in a laminar flow regime with temperature at the inner wall of the tube and the pressure drop held constant. Many engineering applications exchange energy with a low temperature heat source, such as a heat pump. Thus, a low inlet temperature (T_h) was selected as an input parameter. In order to predict thermal performance and reduction in flow rate study based on CFD modelling was conducted. The results are presented for double corrugated tubes that are ellipse or super ellipse-based, and each for constant cross-sectional area and constant hydraulic diameter. All simulations were run for an equivalent tube diameter of 5 mm, with varying corrugation periods and aspect ratio of the flow area. All simulations were conducted in the laminar flow regime. A straight tube was modelled for comparison. Note that the fluid flow regime was determined and the *Re* number was calculated for a straight tube if not stated otherwise.

2. Corrugation geometry

The double corrugated tubes were designed in SolidWorks using the *Parametric equation* tool to define the longitudinal surface of the analysed geometries. The *Lofted Boss/Base* feature was used to create a solid body where the parametric equation defined the two axes of a double corrugated tube. The analysed tubes are based on an ellipse or super ellipse-based cross-section that

changes aspect in the flow direction while maintaining either a constant D_h or constant A_c along the z-axis. The double corrugated tubes with the constant D_h and an elliptical cross-section were reported previously in [30]. The cross-section of the corrugated tubes at any point in the flow direction is defined as an ellipse or a super ellipse with one axis equal to x and the other equal to y. Note, that the x and y axes periodically become equal, forcing the cross-section to be either a circle (ellipse-based), or an absolutely symmetrical super ellipse (super ellipse-based). Eq. (1) gives the general canonical expression of the cross section in Cartesian coordinates. The parametric version of this equation was used for constructing the tubes in SolidWorks.

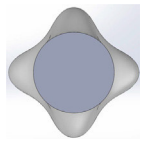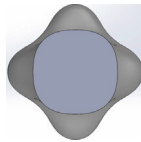$$\left|\frac{x}{a}\right|^n + \left|\frac{y}{b}\right|^n = 1 \tag{1}$$

Here a and b are the semi-major and semi-minor axes of the ellipse respectively. n is an ellipse shape factor. When $n = 2$, the shape becomes an ordinary ellipse, when $n > 2$, the shape becomes a super ellipse. In this work, $n = 2.5$ is chosen as it gives a good representation of the concept of a super ellipse.

The *Lofted Boss/Base* feature creates a solid body for *Guide curves* (surface equations (Table 1)) only if *Profile* (the start and end shapes) is given. Note, that an option to draw an ordinary ellipse already exists in SolidWorks. Thus, a modified Eq. (1) is used only for drawing a super ellipse as a *Profile* of the tubes with a super ellipse-base. Here, Eq. (1) is multiplied by $\gamma = 0.963$ in order to obtain values of D_h and A_c closer to the circle that has an equivalent R.

The equations used to approximate the surfaces of double corrugated tubes are given in Table 1. They define the geometry of a tube along the flow direction, z, corrugated in the x and y directions. The given equations approximate the surface of double corrugated tubes with a maximum of ±4% deviation from the assumption of constant hydraulic diameter or cross-sectional area. However, SolidWorks approximates the given surface equations within a certain accuracy as well. The measured maximum deviation from the target D_h and A_c values is ±4% and ±5%, respectively for the most corrugated tubes. The inaccuracy decreases with an increase in period (p) or decrease in aspect ratio (AR). Therefore, the tubes modelled here only approximate the desired geometry, but are considered to do so within an acceptable limit.

In the above reported equations, R is the radius of an equivalent straight tube. The constant $\gamma = 0.963$ is used to ensure the same cross-section and hydraulic diameter of the ellipse and super ellipse tubes based on the same value of R. The cross-sectional area of a super ellipse-based tube is a quadratic function of γ, while the perimeter, of super ellipse-based tubes is a linear function of γ. Thus, the hydraulic diameter becomes a linear function of γ. Therefore, a single γ coefficient is used to generate the eometry of super ellipse-based tubes for both constant D_h and constant A_c.

Table 1
The equation set for different analysed double corrugated tubes configuration.

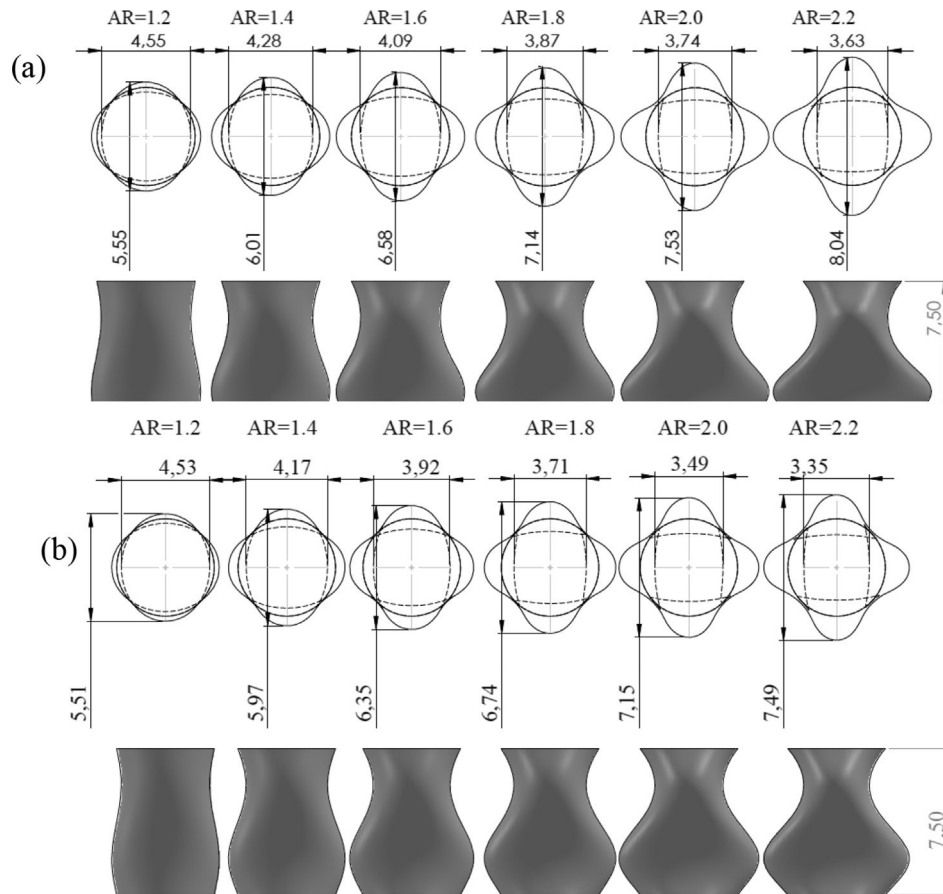| Type	Starting shape	Constant hydraulic diameter	Constant cross-sectional area
Ellipse-base		$\begin{cases} x = \frac{R}{2}AR^{\left(\sin\left(\frac{2\pi}{p}z\right)\right)} + \frac{R}{2} \\ y = \frac{R}{2}AR^{\left(-\sin\left(\frac{2\pi}{p}z\right)\right)} + \frac{R}{2} \end{cases}$ (2)	$\begin{cases} x = R\left(AR^{\left(\sin\left(\frac{2\pi}{p}z\right)\right)}\right) \\ y = R\left(AR^{\left(-\sin\left(\frac{2\pi}{p}z\right)\right)}\right) \end{cases}$ (3)
Super ellipse- base		$\begin{cases} x = \left(\frac{R}{2}AR^{\left(\sin\left(\frac{2\pi}{p}z\right)\right)} + \frac{R}{2}\right)\gamma \\ y = \left(\frac{R}{2}AR^{\left(-\sin\left(\frac{2\pi}{p}z\right)\right)} + \frac{R}{2}\right)\gamma \end{cases}$ (4)	$\begin{cases} x = \left(R\left(AR^{\left(\sin\left(\frac{2\pi}{p}z\right)\right)}\right)\right)\gamma \\ y = \left(R\left(AR^{\left(-\sin\left(\frac{2\pi}{p}z\right)\right)}\right)\right)\gamma \end{cases}$ (5)

Fig. 1. The ellipse-based double corrugated tubes with the hydraulic diameter (D_h) held constant (a) the constant cross-sectional area (A_c) (b). Dimensions are given in mm.

Fig. 1(a) shows changes in the aspect ratio of ellipse-based double corrugated tubes with D_h held constant and p = 7.5 mm. Fig. 1(b) shows the changes in aspect ratio of ellipse-based double corrugated tubes with A_c held constant and p = 7.5 mm.

Comparing Fig. 1(a) and (b), one can see that the double corrugated tubes with the constant D_h are more hydraulically rough than tubes with the constant A_c. This is because tubes with the constant A_c have smoother surface transition between the extreme points.

3. Model validation and the method of analysis

3.1. Mathematical formulation

Fully hydraulically developed incompressible laminar flow with constant fluid properties was assumed for all modelled cases. A constant surface temperature at the inner wall of the tube and a constant pressure drop in the flow direction were implemented into the COMSOL Multiphysics environment. The double corrugated geometries were compared with the straight tube holding the length of the tubes constant rather than the surface area. Note, that the corrugations increase the surface area.

Patankar et al. [31] and Hærvig et al. [3] showed that one period of the geometry of interest is sufficient for numerical investigation of heat transfer enhancement when fully thermally and hydraulically developed flow is analysed. However, the flow analysed in this study is only hydraulically fully developed and periodic boundary conditions (BCs) could be applied only for the velocity field. In order to confirm that one period of a double corrugated tube is sufficient for thermal analysis of 1, 3, 4 and 6 periods of

ellipse-based tube with D_h constant, AR = 1.6 and p = 7.5 mm were modelled as well as several different lengths of a straight tube. The obtained results were analysed as explained in 3.3. Method of analysis. Knowing the average local convection heat transfer coefficient ($\bar{h}$) at the outlets of the double corrugated tube with 6 periods and the straight tube with a length of 50 mm, the outlet temperatures (T_o) for fewer periods or shorter straight tubes were calculated by integrating from the tube inlets to a point of interest l within the tube length. Fig. 2 shows the comparison of calculated and modelled values for the double corrugated tube with D_h constant, AR = 1.6 and p = 7.5 mm and the straight tube at different number of periods (length). Generally, calculated and modelled values show a good agreement. Note that higher calculated temperature differences Θ for smaller lengths were obtained due to the nature of the heat transfer problem. The temperature in thermal entrance region decays exponentially with distance. Also the values of $\bar{h}$ are much higher at the tube inlets than at the outlets, thus the theoretical calculations could provide only a general overview. Since the generally good agreement between calculated values and modelling results was obtained for the corrugated and the straight tubes, it is proved that one period of a double corrugated tube or a corresponding length of a straight tube is sufficient to use for numerical analysis.

In order to make the simulations less computationally expensive, a quarter of the fluid volume of one period of each tube was modelled. Therefore, the symmetry boundary condition was applied on the grey sections shown in Fig. 3. The inlet (T_i) is marked green and the tube wall is marked blue (T_s), the outlet of the tube is an opposite wall to the inlet (yellow). The pressure drop was normalized by corrugation length. Boundary conditions and
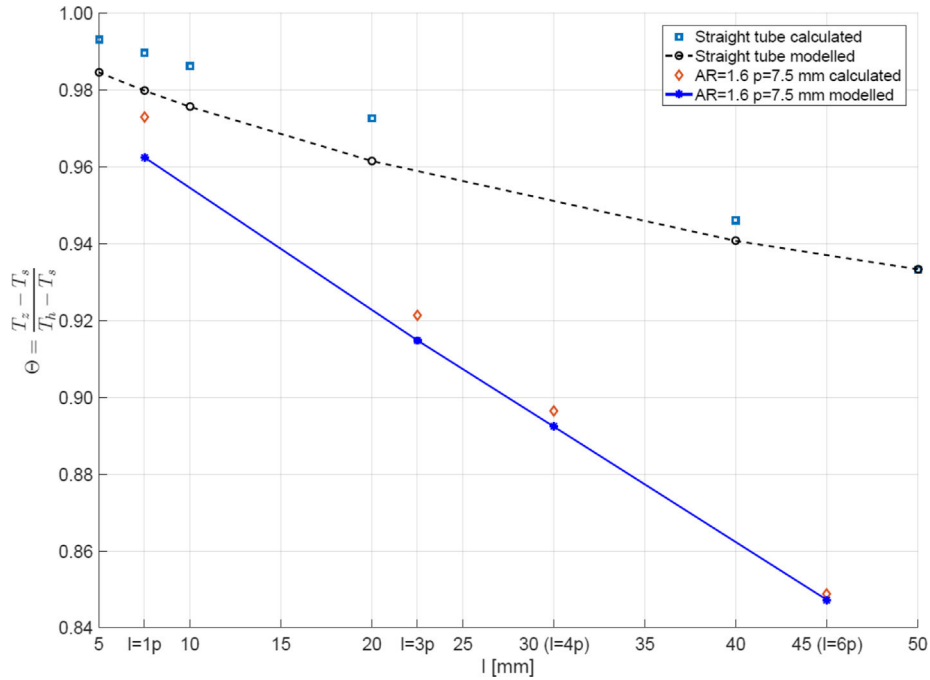
Fig. 2. Temperature difference at the outlet of an ellipse-base double corrugated tube with D_h constant, $AR = 1.6$ and $p = 7.5$ mm and a straight tube at different modelled number of periods or lengths.
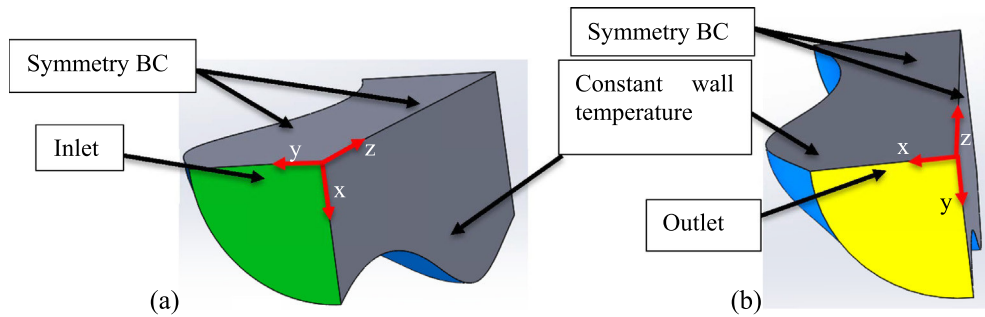
Fig. 3. Visualization of the boundary conditions applied on the modelled geometries. The inlet water temperature is marked in green, constant surface temperature is marked in blue. The symmetry boundary conditions are applied on the walls marked in grey. The outlet is opposite to the green boundary. Pressure gradient condition is applied on the inlet (green (a)) and outlet (yellow (b)). (For interpretation of the references to colour in this figure legend, the reader is referred to the web version of this article.)

thermo-physical properties of the modelled fluid are given in Table 2.

3.2. Mesh selection and model validation

All the modelled tubes were meshed using a swept mesh with tetrahedral elements and two boundary layers (BL). The Nusselt number Nu is selected as a control quantity for the mesh evaluation. It is well known that BLs are necessary to model fluid flow more precisely and obtain more accurate values of a velocity gradient near the wall. Thus, the simulation results of a straight tube model with two, five, seven and ten BLs were analysed to find out whether two BLs are sufficient. Also, four different sizes of meshes for each type of geometry with the element density from 1206 to 4030 elements/mm³ were analysed. The element density was used as a consistent comparison method of meshes of all the studied tubes since the volume of the tubes varies with corrugation height and length. Relative errors (err) of the control quantities were calculated as described in Eq. (6) [28].

$$err = 100\left|\frac{Nu_c - Nu_f}{Nu_f}\right| \qquad (6)$$

where: subscripts c and f denote the coarsest (fewest BLs) and the finest (most BLs) meshes, respectively.

Table 2
Fluid properties and flow conditions used in the modelling.

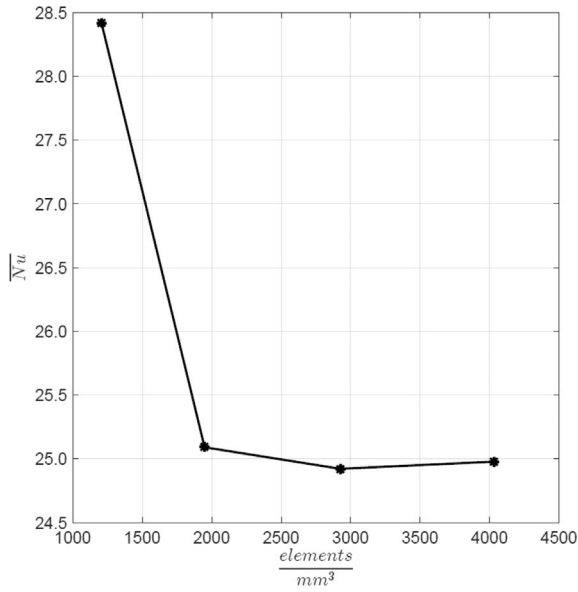| R, [mm]	ρ, [kg m^{-3}]	$\Delta p/l$, [Pa m^{-1}]	T_i, [K]	T_s [K]
2.5	1000	[246; 164; 82; 16]	303	281
c_p, [J(kg K)$^{-1}$]	v, [m^2 s^{-1}]	μ, [Pa s]	k, [W(m K)$^{-1}$]	Pr, [-]
4183	8 e−7	8 e−4	0.603	5.5

Fig. 4. The results of the study of mesh independency.

Increasing the number of BLs above two did not show a significant difference in the simulations results, the *err* was 0.006%, only the computational time had increased, showing that two BLs were sufficient. The relative errors in using the finest and the selected mesh were less than 0.5% suggesting that the accuracy of numerical models, when the selected mesh used, is acceptable. Note that mesh independency studies were carried out for all four types of double corrugated tubes separately and only the summarized conclusion is given. Moreover, Fig. 4 shows that the result of the mesh independency study follow asymptotical behaviour, thus it was concluded that the study is mesh independent when a mesh finer than 2000 elements per mm^{-3} was used. Additionally, numerical results of a straight tube agree with the analytical solution [30]. Thus, the model was proved to be valid. Fig. 5 shows the isometric view of a quarter of a cross-section of a double corrugated tube after being meshed in COMSOL.

Finally, the inaccuracy of the mass and energy balances for each model was less than 0.16% showing that all the models were adequately accurate. Note that the mass and energy balances were calculated for each modelled tube and only the largest value is reported.
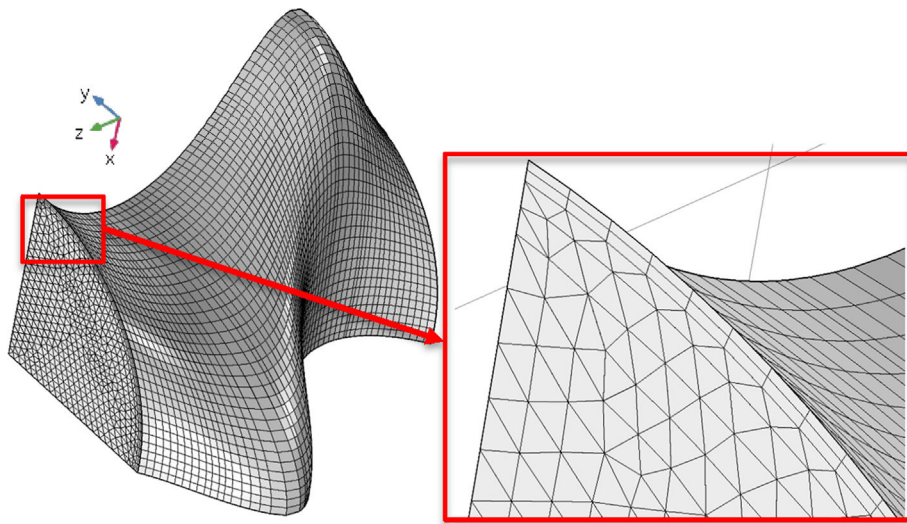
Fig. 5. The isometric view of the modelled geometry of a double corrugated tube after being meshed in COMSOL. The boundary layers are shown in the zoomed in view.
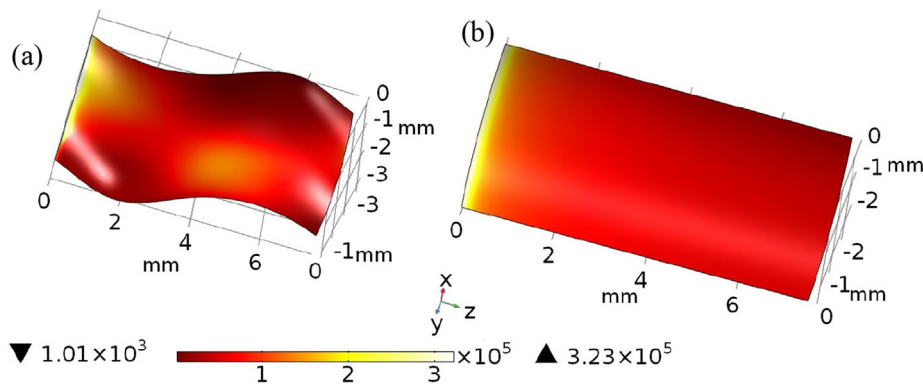
Fig. 6. The heat flux in a double corrugated (flow rate 0.002 m^3 h^{-1}) (a) tube and a straight (flow rate 0.004 m^3 h^{-1}) (b) tube at the same pressure drop Δp = 1.843 Pa. The ellipse-based double corrugated tube has following geometrical characteristics: AR = 1.6, p = 7.5 mm.

3.3. Governing equations and boundary conditions

The governing equations were formulated in Cartesian coordinates. The SIMPLE algorithm was used to couple steady-state equations for non-isothermal flow of incompressible fluid with constant properties. Laminar, pressure driven, fully developed internal flow was modelled. Thus, the continuity equation is formulated as given by Eq. (7).

$$\nabla \cdot \boldsymbol{u} = 0 \tag{7}$$

where $\boldsymbol{u}$ is the fluid velocity vector.

The momentum conservation equation is given by Eq. (8).

$$-\rho(\boldsymbol{u} \cdot \nabla \boldsymbol{u}) = \nabla p - \mu \nabla^2 \boldsymbol{u} \tag{8}$$

Here p is the pressure field. The heat transport equation, neglecting pressure work and viscous dissipation, is given by Eq. (9).

$$\rho c_p \boldsymbol{u} \nabla T = \nabla \cdot (k \nabla T) \tag{9}$$

To ensure that the flow is fully developed, a periodic boundary condition was applied in the form of a pressure gradient. No-slip boundary conditions were applied on the solid wall. A solid wall is treated as a streamline by imposing no-slip BC as can be seen from Eq. (10).

$$\boldsymbol{u} \cdot \boldsymbol{n} = \boldsymbol{U} \cdot \boldsymbol{n} \tag{10}$$

where U is the velocity vector of the solid body and n is the unit normal to the surface of the solid body. All the geometries were modelled for the same pressure drop.

The governing equations were solved using the finite element method in Comsol. P2 + P1 fluid discretization was used, which provides quadratic interpolation of the velocity field and linear interpolation of the pressure field. The stationary PARDISO solver with relative tolerance of 10^{-6} was used for all the modelled geometries.

3.4. Method of analysis

The main outputs of the thermal model are the fluid flow rate for the specified pressure drop and the resulting temperature profile. The thermal performance and hydraulic characteristics of the analysed double corrugated tubes were evaluated using average Nusselt number $\overline{Nu}$, the number of transfer units (NTU) method, and comparing the volumetric flow rate ($\dot{V}$) and performance evaluation criteria (PEC).

Eq. (11) defines the net rate of outflow of thermal energy, q, for an incompressible fluid.

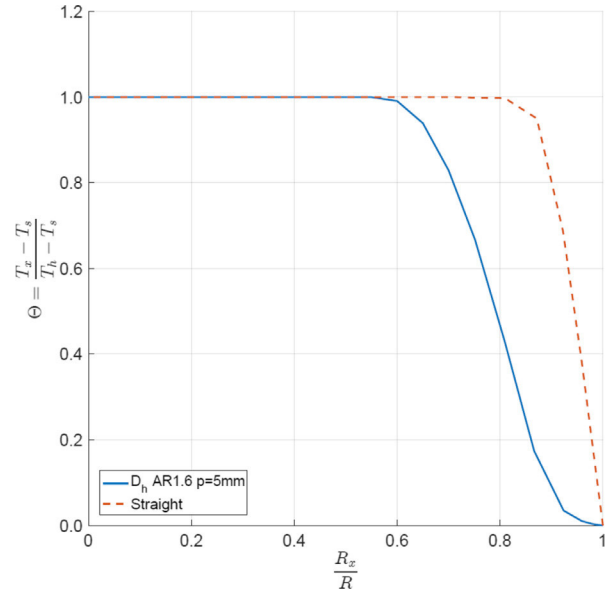**Fig. 8.** The flow temperature profile in the double corrugated tube, presented in Fig. 6, and straight tube at the outlet of geometries.
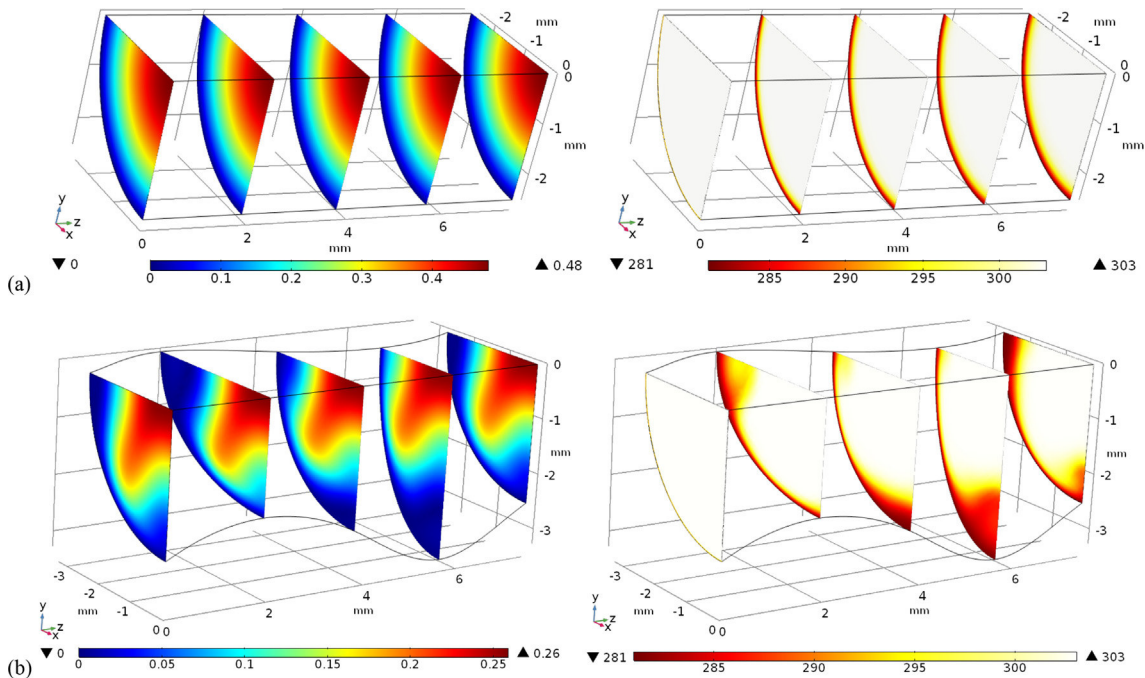

Fig. 7. Three-dimensional temperature (left side, scale bar in K) and velocity (right side, scale bar in m/s) fields at $\Delta p/l = 246$ Pa/m. (a) a straight tube, $l = 7.5$ mm. (b) the double corrugated tube with $AR = 1.6$, $p = 7.5$ mm, $l = 7.5$ mm.

$$q = \dot{m}c_p(T_i - T_o) \tag{11}$$

where T is the bulk temperature at the inlet i and outlet o of a modelled tube, respectively. Then the average convective heat transfer coefficient, $\bar{h}$, is calculated using Eq. (12).

$$\bar{h} = \frac{q}{A_s \Delta T_{lm}} \tag{12}$$

where A_s is a surface area and ΔT_{lm} is the log mean temperature difference, which is defined by Eq. (13).

$$\Delta T_{lm} = \frac{\Delta T_o - \Delta T_i}{\ln\left(\frac{\Delta T_o}{\Delta T_i}\right)} \tag{13}$$
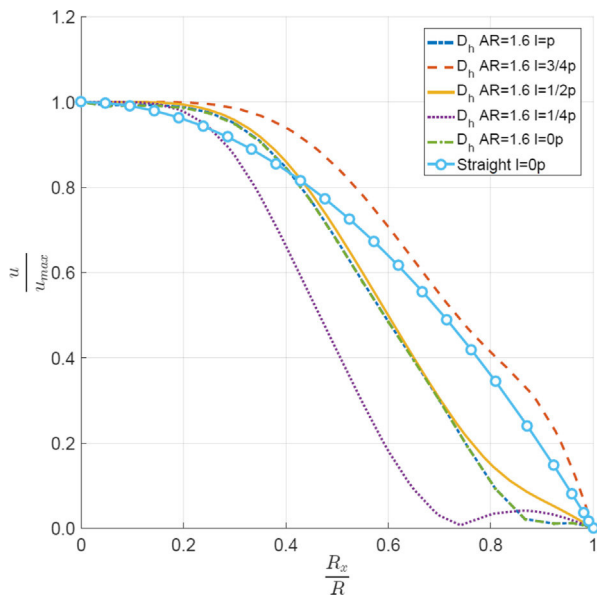
Fig. 9. The flow velocity profile in the double corrugated, presented in Fig. 6, and the straight tube at Δp = 1.84 Pa at different distances from the inlet.

where $\Delta T_{o,i}$ is temperature difference between temperature of a tube wall, T_s, and the bulk temperature, T. Then average Nusselt number, $\overline{Nu}$, is calculated using Eq. (14).

$$\overline{Nu} = \frac{\bar{h}D_h}{k} \tag{14}$$

where D_h is hydraulic diameter and k is thermal conductivity of water.

The friction factor f is calculated from Eq. (15) using the simulation results for mean velocity, u_m, and specified pressure drop, Δp.

$$f = \frac{2\Delta p D_h}{\rho u_m^2 L} \tag{15}$$

where l is the tube length. The global performance of the double corrugated tubes was analysed using the most commonly adopted performance evaluation criterion *PEC*, which is defined by Eq. (16) [1,13].

$$PEC = \frac{\overline{Nu}/\overline{Nu_0}}{(f/f_0)^{1/3}} \tag{16}$$

where f_0 is the Darcy-Weisbach friction factor for a straight tube given in Eq. (17) and $\overline{Nu_0}$ is the Nusselt number of a straight tube based on simulation results and calculated using Eqs. (11)–(14).

$$f_0 = \frac{64}{Re} \tag{17}$$

NTU is calculated as defined by Eq. (19).

$$NTU = -\ln(1 - \varepsilon) \tag{19}$$

where ε, is efficiency of a heat exchanger defined by Eq. (20).

$$\varepsilon = \frac{q}{q_{max}} \tag{20}$$

where q_{max} is maximum possible heat transfer that is calculated using Eq. (21).

$$q_{max} = \dot{m}c_p(T_i - T_s) \tag{21}$$

Fig. 10. Normalized annular flow velocity $\bar{u}$ as a function of relative tube length in the ellipse-based double corrugated tubes and a straight tube.

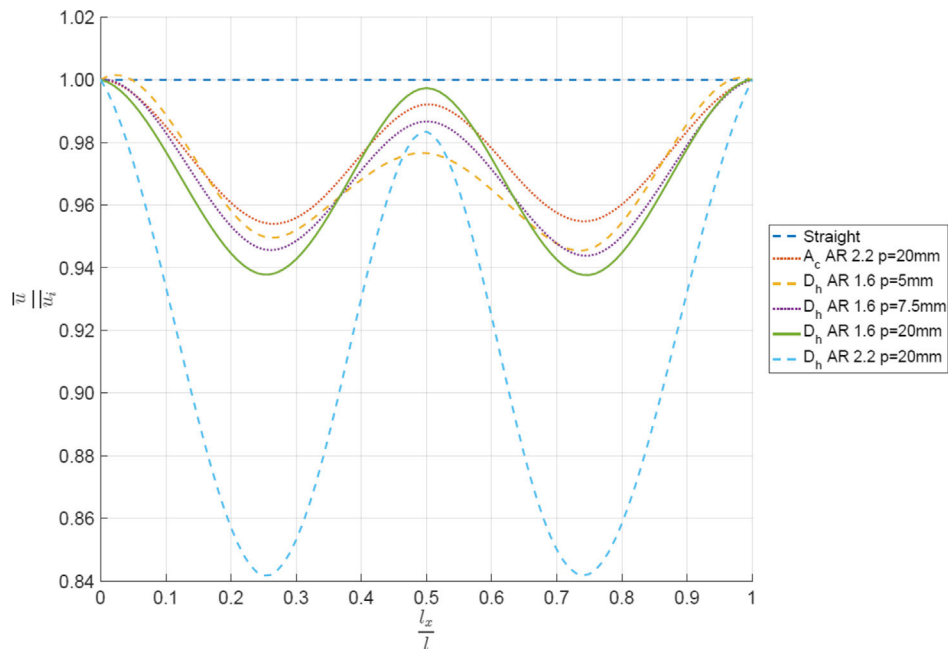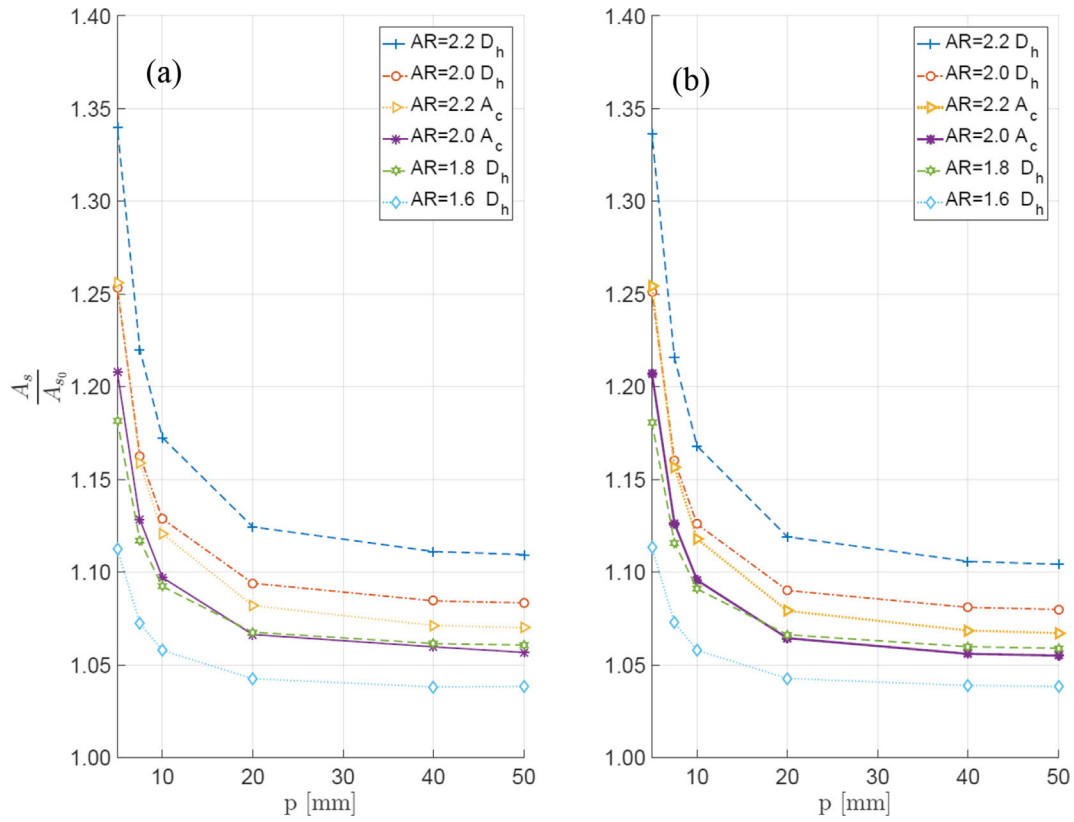**Fig. 11.** Increase in the inner surface area of double corrugated tubes with respect to a corresponding straight tube. The plots show double corrugated tubes with an ellipse-based holding (a) a super ellipse-base holding (b).
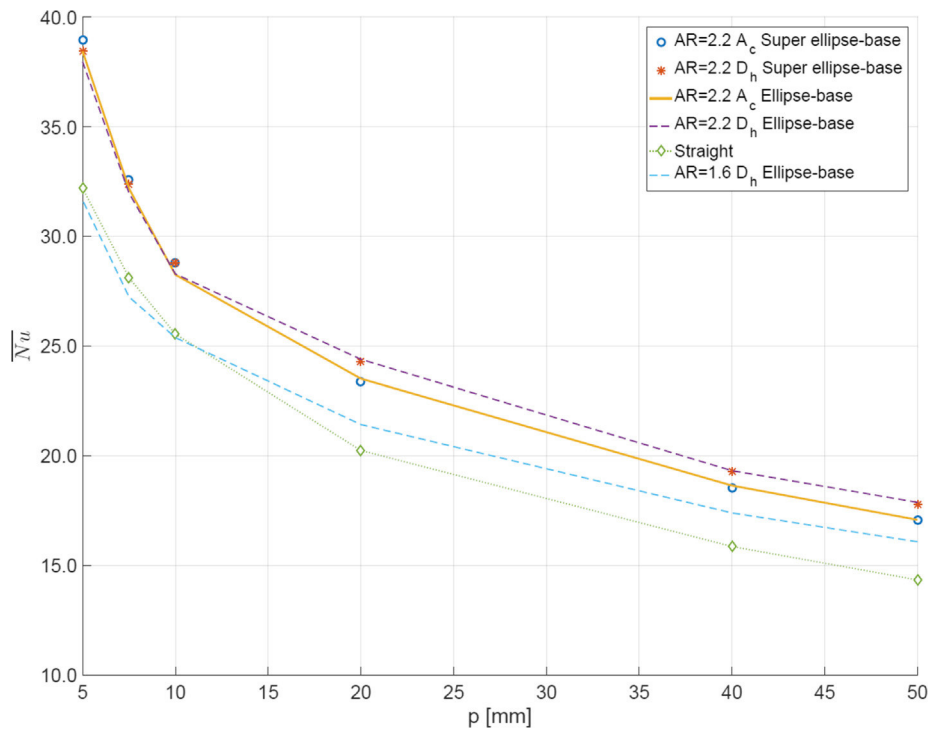
Fig. 12. The $\overline{Nu}$ in ellipse-based and in super ellipse-based double corrugated tubes as a function of the period at constant Δp.

4. Results and discussion

As it was discussed above, the purpose of enhanced geometries is to disturb thermal boundary layers and enhance the heat transfer. The wall of a double corrugated tube periodically impinges a flow and thus, prevents thermal development of the flow. A detail explanation of the changes in flow and temperature profiles is given for a double corrugated tube with an ellipse base and D_h constant. The geometrical characteristics of the presented tube are $AR = 1.6$ and $p = 7.5$ mm. The analysis is presented in comparison with a corresponding straight tube. By holding the pressure drop across the tubes constant, the corrugated tubes reduce flow rate, but the tubes could be directly substituted for straight tubes without requiring a different pump or pipes/fittings. Fig. 6 presents the comparison of a heat flux through the wall of a double corrugated tube (a) and a straight tube (b). One can see that a high heat transfer rate takes place over the entire length of the double corrugated tube because the thermal boundary layers are interrupted by the tube geometry, while the straight tube exhibits high heat transfer rates at the tube inlet that gradually diminish in the flow direction.

Fig. 13. Ratio of *NTU* in ellipse-based (a) and in super ellipse-based (b) double corrugated tubes as a function of the period at constant Δp.

It can be seen that the highest heat transfer rates occur in the regions where one of the axis of ellipses are smallest. Note that the flow rate in the straight tube is twice that of the double corrugated tube under the same pressure drop.
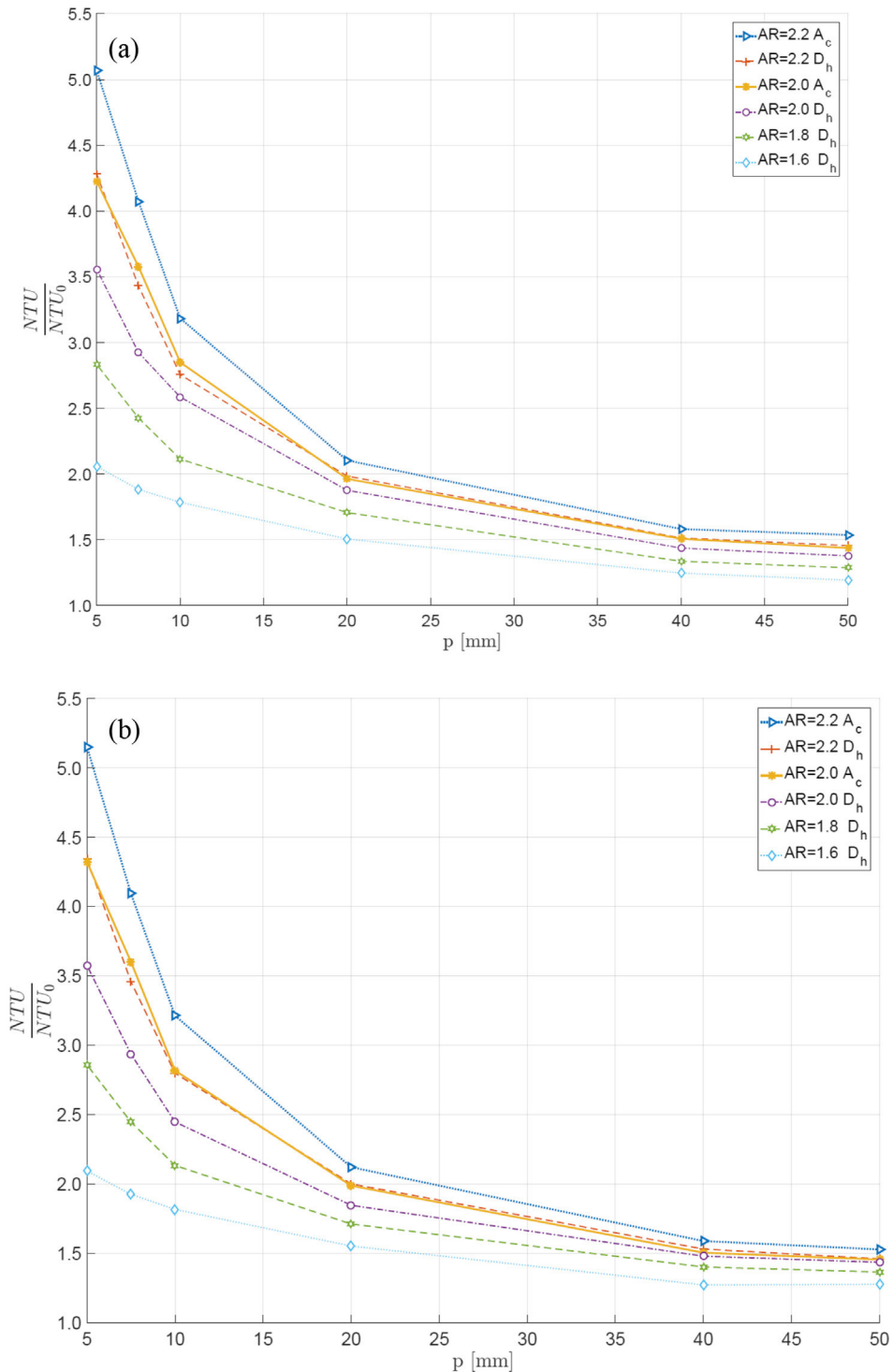
Fig. 7 shows the flow velocity and the temperature field of the straight and a corrugated tube with $AR = 1.6$ and $p = 7.5$ mm. As expected, the velocity field does not change along the flow direction in the straight tube at laminar fully hydraulically developed conditions. Moreover, one can see from Fig. 7(a) that the temperature boundary layers develop rather quickly along the flow direction. On the other hand, the flow is contorted in the radial axis and the walls of the double corrugated tubes have a periodic contact to the faster moving fluid along the tube on both x and y axis in the double corrugated tubes, as it is seen in Fig. 7(b). In this way, warmer fluid is periodically pushed closer to the tube wall and thus thermal gradients in the radial direction are increased as shown in Fig. 8.

Fig. 8 shows the normalized temperature profiles at the outlet of the above presented double corrugated and straight tubes under cooling conditions. One can see that the temperature gradient in the radial axis of the double corrugated tube is greater than in the straight tube. This indicates that there is a larger portion of the fluid that takes part in the heat transfer process in the double corrugated geometry compared to the straight tube.

Further comparison of the changes of a flow in a double corrugated and a straight tube showed that the velocity profile in an annular face is also tweaked. Fig. 9 shows the corrugation effect on the velocity profile in an ellipse-based double corrugated tube and a straight tube of the same length at $[0; 1/4; 1/2; 3/4; 1]$ of a period. The geometry of a double corrugated tube interrupts the flow profile significantly and especially close to the tube walls. This signifies that the boundary layers are strongly disturbed, which increases heat transfer and pressure drop.

By analysing Fig. 9, one can raise a question how then the mean velocity in an annular face $\bar{u}$ is changing along the double corrugated tubes. Based on fundamental knowledge of the fluid dynamics, one can expect the mean flow velocity remain constant in tube with A_c held constant since the mass conservation law must be satisfied. On the other hand, the concept of D_h yields that due to maintained effective opening of a flow channel, the conservation of momentum must be maintained. Therefore, $\bar{u}$ should vary along the tubes with D_h held constant. This can be seen in Fig. 10, where the normalized $\bar{u}$ in an annular face is shown along ellipse-based double corrugated tubes. One can see that the double corrugation approach with D_h held constant significantly induces throttling of the mean flow velocity along the tube. It is also clear that the AR has bigger impact on the throttling effect than p. The fluctuation of $\bar{u}$ in a double corrugated tube with A_c constant occurred due to geometrical inaccuracies reported in Section 2.

The double corrugation not only tweaks the flow, but also enhances the surface area of the tubes. Fig. 11 shows how much the inner surface area A_s of the double corrugated tubes increases compared to a straight tube. Since A_s for $p \geq 50$ mm approaches the value of a straight tube and the ratio of the surface area follows an asymptotic behaviour, the tubes with $p \geq 50$ mm are not presented in this figure to avoid clutter. One can see that the tubes with constant D_h, regardless of their base geometry, generally have higher increase in A_s than the tubes with the constant A_c. The inner surface area increases with increasing AR and with decreasing p. The biggest increase in the inner surface area A_s is for tubes with $AR = 2.2$ at $p = 5$ mm and it is up to 34%, 26%, 25% for the tubes with the constant D_h of both types, and constant A_c for ellipse-based and
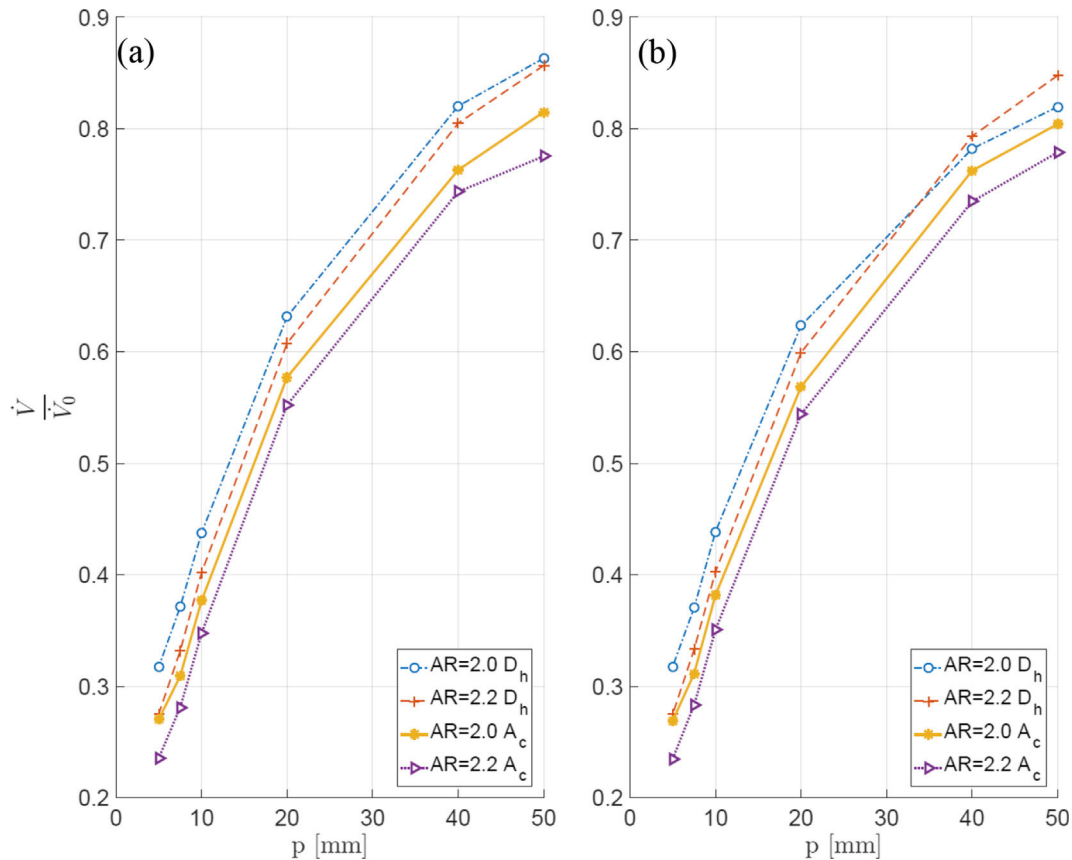
Fig. 14. The ratio of the volumetric flow rate $\dot{V}$ in ellipse-based (a) and super ellipse based (b) double corrugated tubes as a function of the period of the tubes at the constant Δp.

super ellipse-based, respectively. In the next figures, only selected modelling results will be presented due to space limitations.

Fig. 12 shows that $\overline{Nu}$ increases in double corrugated tubes even though Δp is maintained constant rather than Re. One can see that $\overline{Nu}$ increases up to 20% in double corrugated tubes compared to a straight tube. The double corrugated tubes with the greater AR show higher increase in $\overline{Nu}$. It is noticeable that for both ellipse-based and super ellipse-based tubes the $\overline{Nu}$ increases in the same manner. In addition, once the p exceeds value of 10 mm, double

corrugated tubes with constant D_h show slightly higher values in $\overline{Nu}$ than tubes with constant A_c. However, NTU analysis suggest that double corrugated tubes with A_c held constant are more efficient than tubes with constant D_h (Fig. 13).

Fig. 13 shows the NTU ratio in double corrugated tubes with respect to corresponding straight tubes. One can see that the NTU ratio decreases significantly with decreasing either AR or p. The double corrugated tubes with A_c constant at the most intense corrugation show more than 400% increase in NTU ratio for both
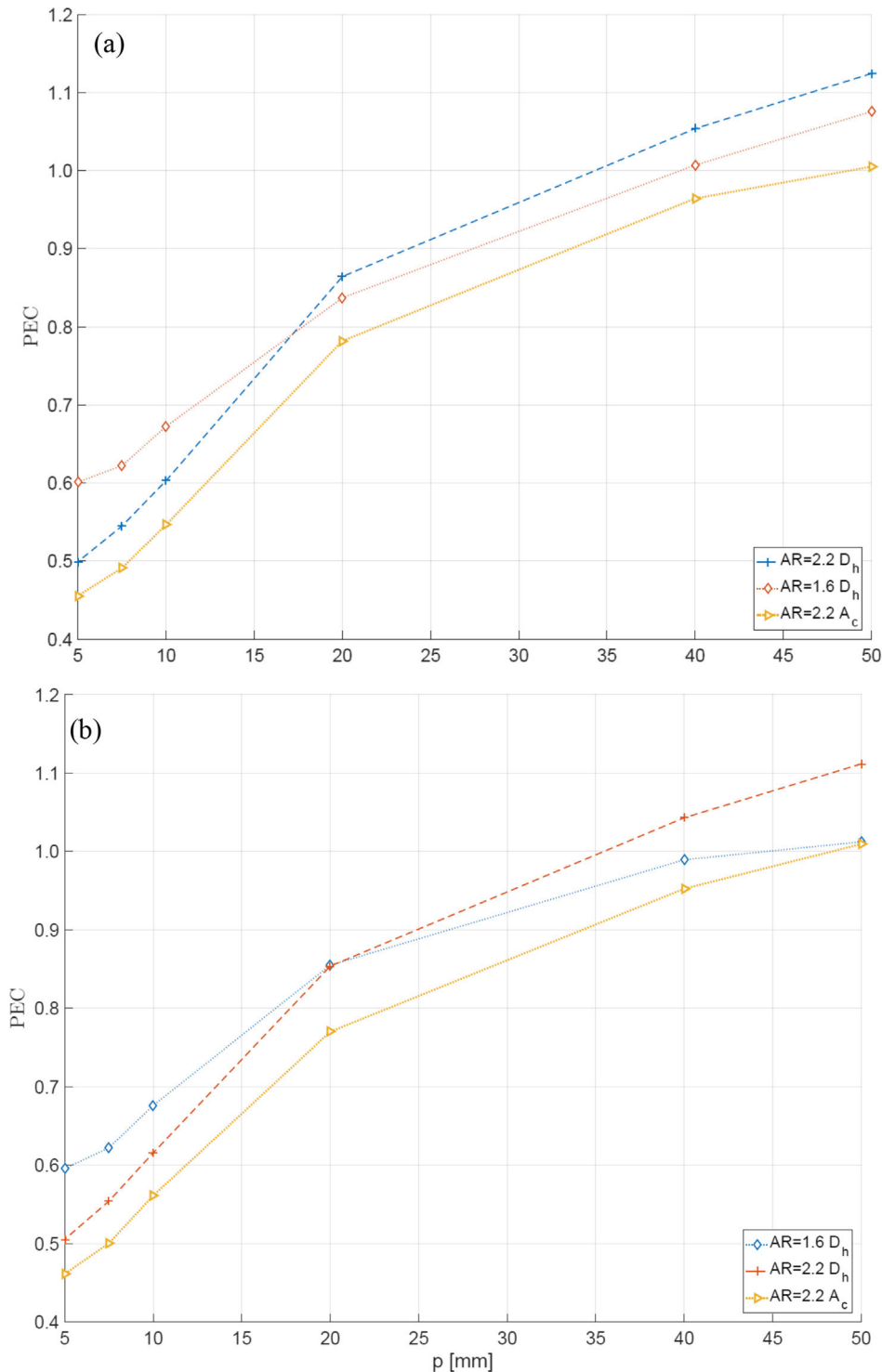

Fig. 15. The *PEC* of ellipse-based (a) and super ellipse-based (b) double corrugated tubes as a function of a period at the constant Δp.

ellipse-base and super-ellipse base cases. The *NTU* ratio for tubes with the D_h constant exceeds 330% for both ellipse-base and super-ellipse base cases. The *NTU* drops drastically as the period increases above 10 mm and eventually approaches values of straight tubes at high values of *p*. It should be noted that since the pressure drop is held constant, the flow rate is lower for the corrugated tubes than the straight tube (Fig. 14). Since the double corrugated tubes with ellipse-base and super ellipse-base shows similar *NTU* behaviour, however somewhat lower flow resistance is observed for the previous case, several cases of ellipse-based double corrugated tubes were selected for the study varying *Re*.

Fig. 14 shows the ratio of the flow rates in the double corrugated tubes and corresponding straight tubes for the same pressure drop. One can see that the flow resistance is lower in the double corrugated tubes with the D_h held constant rather than A_c held constant. The volumetric flow rate ratio is 3.6 and 4.2 times lower in double corrugated tubes with constant D_h and constant A_c, respectively, than in a straight tube. The double corrugated tubes with an ellipse-base showed 5% lower flow resistance than the tubes with a super ellipse-base. The very sharp decrease of $\dot{V}$ in the region of intense corrugation indicates a significant flow resistance that compromises overall performance (Fig. 15). The simulation results show that flow at the high *Re* is insensitive to a high corrugation with a short *p*. In other words, flow at high *Re* passes the intense corrugation as if only a diameter of a tube would be reduced. Thus, it is more efficient to use corrugated tubes with longer corrugation period for a flow at high *Re* [26,32].

The *PEC* analysis showed that ellipse-based double corrugated tubes achieve 14% higher efficiency than straight tubes, while supper ellipse-based double corrugated tubes demonstrate 11% better performance than straight tubes when $p \leq 50$ mm (Fig. 15). From Fig. 15(a), one can noticed that ellipse-based double corrugated tubes with A_c constant show global performance equivalent to a straight tube (*PEC* = 1) once *p* = 50 mm. This means that the same the same or even higher efficiency provided by double corrugated tubes is obtained using geometry that is more compact. Moreover,

up to 10% higher *PEC* is achieved in ellipse-based double corrugated tubes at lower *Re* (Fig. 16). From Fig. 16, one can see that at lower *Re*, the *PEC* is less dependent on *AR* than on *p*. It is noticeable that double corrugated tubes with shorter *p* are more efficient at lower *Re*. However, the overall performance decreases significantly when the corrugation period exceed a certain value. At that point, the thermal performance of the double corrugated tubes approaches a straight tube, while the flow rate is still significantly lower.

Performance of the double corrugated tubes was compared to the AEA tubes reported by Khaboshan and Nazif, [13]. The latter tubes were modelled in the turbulent flow regime with constant temperature of the tube wall. The AEA tubes showed up to 10% higher efficiency than an equivalent straight tube in terms of *PEC* with at lower *Re*. The double corrugated tubes presented in this study demonstrate somewhat higher efficiency than AEA tubes, which is mostly due to the smoother geometrical transitions that reduce pressure losses in the former tubes.

Finally, the analysis of the thermo-hydraulic performance of the presented double corrugated tubes was performed using same approach as for the straight tube including the numerical model. The simulation results show that the double corrugated geometry has potential to enhance the heat transfer with acceptable penalty in pressure drop. However, experimental investigation is necessary in order to understand the thermo-hydraulic behaviour and find out a real potential of the presented double corrugated tubes.

5. Conclusions

In this paper, a numerical comparison of heat transfer performance of double corrugated tubes and straight tubes for laminar flow conditions was presented. Constant pressure drop and wall temperature conditions were analysed. Two types of double corrugated tubes with constant hydraulic diameter and constant cross-section area were analysed for tubes with either ellipse-based or super ellipse-based cross-sections. The efficiency and global
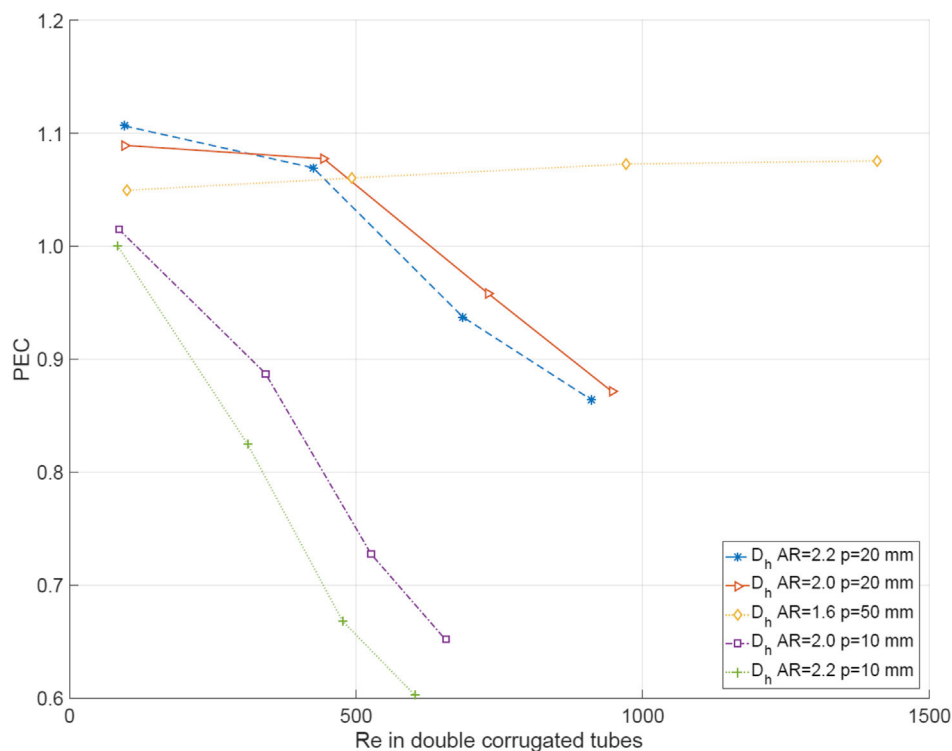

Fig. 16. The *PEC* in ellipse-based tubes as a function of *Re*.

thermo-hydraulic performance of the tubes were characterized in terms of the number of transfer units (*NTU*), average Nusselt number ($\overline{Nu}$) and performance evaluation criterion (*PEC*), which evaluates performance at the same pumping power.

The simulation results showed that the novel geometry of double corrugated tubes affects the fluid flow by disturbing thermal boundary layers and modifying the flow profile compared to a straight tube as well as by increasing the surface area of the inner surface of the tube. These result in enhanced heat transfer and a reduced fluid flow rate for a constant pressure drop. *Nu* increases up to 20% for intensively corrugated tubes with ellipse and super ellipse-based cross sections. However, the flow rate reduction in super ellipse-based double corrugated tubes is 5% higher than in ellipse-based tubes. The double corrugated tubes with constant D_h show lower flow rate reduction than tubes with constant A_c, when comparing the ratio of volumetric flow rate with a straight tube. It is 3.6 and 4.2 times lower in double corrugated tubes with constant D_h and constant A_c, respectively.

The thermal performance in terms of *NTU* for double corrugated tubes with A_c constant is more than 400% greater when compared to a straight tube. The double corrugated tubes with constant D_h showed lower *NTU* than tubes with constant A_c. However, it is still more than 330% greater than for a straight tube. It was also shown that the *NTU* ratio for double corrugated tubes with a super ellipse-based cross-section is slightly higher than for tubes with an ellipse-based cross-section.

Numerical results show that the ellipse-based tubes with constant hydraulic diameter are more than 14% more effective than equivalent straight tubes when the pressure drop per length of tube is held constant. Even though the super ellipse-based tubes show slightly higher thermal performance than ellipse-based tubes, they show lower *PEC* values due to a somewhat higher flow rate reduction. The study results of varying *Re* revealed that the double corrugated tubes are 10% more efficient than corresponding straight tubes at lower *Re*. It was also concluded that corrugations with shorter periods are more efficient at lower *Re*. Moreover, an ellipse-based double corrugated tube with *AR* = 2.2 and constant A_c showed *PE*C values equivalent to a straight tube for *p* = 50 mm. It is worth mentioning that in this case the double corrugated tubes are as efficient as a straight tube while being more compact.

Moreover, the study shows that fluid at high *Re* passes peaks in corrugation, when the corrugation period is short, with a minor disturbance in the flow path. For these reasons, mentioned above, the recommendation is to use double corrugated tubes with the short corrugation periods at lower *Re*, and tubes with the longer periods in applications where faster flow is required.

Additionally, ellipse-based tubes have an additional advantage of having a circular inlet and outlet. This feature enables fast and easy mounting to a new or existing application without any additional modifications. Moreover, the double corrugated tube geometry allows for stacking of tube bundles, further increasing compactness of a heat exchanger. However, one should select accurately the type of the double corrugated tubes to meet requirements of a specific application the best.

Conflict of interest

The authors declare that there is no conflict of interest.

Acknowledgments

Appendix A. Supplementary material

Supplementary data associated with this article can be found, in the online version, at https://doi.org/10.1016/j.ijheatmasstransfer.2018.09.003.

References

[1] R.L. Webb, N.-H. Kim, Principles of Enhanced Heat Transfer, second ed., Taylor & Francis, Abingdon, Great Britain, 2005.

[2] S. Rainieri, G. Pagliarini, Convective heat transfer to orange juice in smooth and corrugated tubes, Int. J. Heat Technol. 15 (1997) 69–75.

[3] J. Hærvig, K. Sørensen, T.J. Condra, On the fully-developed heat transfer enhancing flow field in sinusoidally, spirally corrugated tubes using computational fluid dynamics, Int. J. Heat Mass Transf. 106 (2017) 1051–1062.

[4] A. Harleß, E. Franz, M. Breuer, Heat transfer and friction characteristics of fully developed gas flow in cross-corrugated tubes, Int. J. Heat Mass Transf. 107 (2017) 1076–1084.

[5] J.F. Fan, W.K. Ding, J.F. Zhang, Y.L. He, W.Q. Tao, A performance evaluation plot of enhanced heat transfer techniques oriented for energy-saving, Int. J. Heat Mass Transf. 52 (2009) 33–44.

[6] M.W. Rohsenow, P.J. Hartnett, I.Y. Cho, Handbook of Heat Transfer Calculations, third ed., 1998.

[7] A. Barba, S. Rainieri, M. Spiga, Heat transfer enhancement in a corrugated tube, Int. Commun. Heat Mass Transf. 29 (2002) 313–322.

[8] Z.S. Kareem, S. Abdullah, T.M. Lazim, M.N. Mohd Jaafar, A.F. Abdul Wahid, Heat transfer enhancement in three-start spirally corrugated tube: experimental and numerical study, Chem. Eng. Sci. 134 (2015) 746–757.

[9] S. Rainieri, F. Bozzoli, L. Cattani, Passive techniques for the enhancement of convective heat transfer in single phase duct flow, J. Phys. Conf. Ser. 547 (2014).

[10] Y. Dong, L. Huixiong, C. Tingkuan, Pressure drop, heat transfer and performance of single-phase turbulent flow in spirally corrugated tubes, Exp. Therm. Fluid Sci. 24 (2001) 131–138.

[11] F.T. Akyildiz, D.A. Siginer, L. Khezzar, Energy losses and heat transfer enhancement in transversally corrugated pipes, Int. J. Heat Mass Transf. 54 (2011) 3801–3806.

[12] V. Srinivasan, K. Vafai, R.N. Christensen, Analysis of heat transfer and fluid flow through a spirally fluted tube using a porus substrate approach, J. Heat Transfer. 116 (1994) 543–551.

[13] H. Najafi Khaboshan, H.R. Nazif, Investigation of heat transfer and pressure drop of turbulent flow in tubes with successive alternating wall deformation under constant wall temperature boundary conditions, J. Brazilian Soc. Mech. Sci. Eng. 40 (2018) 1–16.

[14] T.M. Lazim, Z.S. Kareem, M.N.M. Jaafar, S. Abdullah, A.F. Abdulwahid, Heat transfer enhancement in spirally corrugated tube, Int. Rev. Model. Simulations. 547 (2014).

[15] P. Forooghi, K. Hooman, Effect of buoyancy on turbulent convection heat transfer in corrugated channels - a numerical study, Int. J. Heat Mass Transf. 64 (2013) 850–862.

[16] N. Tokgoz, M.M. Aksoy, B. Sahin, Investigation of flow characteristics and heat transfer enhancement of corrugated duct geometries, Appl. Therm. Eng. 118 (2017) 518–530.

[17] Z.Y. Guo, D.Y. Li, B.X. Wang, A novel concept for convective heat transfer enhancement, Int. J. Heat Mass Transf. 41 (1998) 2221–2225.

[18] B. Li, B. Feng, Y.L. He, W.Q. Tao, Experimental study on friction factor and numerical simulation on flow and heat transfer in an alternating elliptical axis tube, Appl. Therm. Eng. 26 (2006) 2336–2344.

[19] J.A. Meng, X.G. Liang, Z.J. Chen, Z.X. Li, Experimental study on convective heat transfer in alternating elliptical axis tubes, Exp. Therm. Fluid Sci. 29 (2005) 457–465.

[20] S.K. Saha, Thermohydraulics of turbulent flow through rectangular and square ducts with axial corrugation roughness and twisted-tapes with and without oblique teeth, Exp. Therm. Fluid Sci. 34 (2010) 744–752.

[21] N. Phan-Thien, M.M.K. Khan, Flow of an oldroyd-type fluid through a sinusoidally corrugated tube, J. Nonnewton. Fluid Mech. 24 (1987) 203–220.

[22] S. Mahmud, A.K.M. Sadrul Islam, C.M. Feroz, Flow and heat transfer characteristics inside a wavy tube, Heat Mass Transf. Und Stoffuebertragung. 39 (2003) 387–393.

[23] Z. Cao, J. Xu, D. Sun, J. Xie, F. Xing, Q. Chen, X. Wang, Numerical simulation of modulated heat transfer tube in laminar flow regime, Int. J. Therm. Sci. 75 (2014) 171–183.

[24] W.G. Osley, P. Droegemueller, P. Ellerby, CFD investigation of heat transfer and flow patterns in tube side laminar flow and the potential for enhancement, Chem. Eng. Trans. 35 (2013) 997–1002.

[25] S.K. Saha, Thermohydraulics of laminar flow through a circular tube having integral helical corrugations and fitted with helical screw-tape insert, Chem. Eng. Commun. 200 (2013) 418–436.

[26] Z. Grant Mills, T. Shah, A. Warey, S. Balestrino, A. Alexeev, Onset of unsteady flow in wavy walled channels at low Reynolds number, Phys. Fluids 26 (2014).

[27] P.G. Vicente, A. García, A. Viedma, Mixed convection heat transfer and isothermal pressure drop in corrugated tubes for laminar and transition flow, Int. Commun. Heat Mass Transf. 31 (2004) 651–662.

[28] A. Zachár, Analysis of coiled-tube heat exchangers to improve heat transfer rate with spirally corrugated wall, Int. J. Heat Mass Transf. 53 (2010) 3928–3939.

[29] E. Jantsch, Tubular heat transfer aparatus, 2663321, 1953.

[30] K. Navickaite, D. Noel, K. Engelbrecht, C. Bahl, Passive heat transfer enhancement in 3D corrugated tube, in: 9th World Conf. Exp. Heat Transf. Fluid Mech. Thermodyn., Foz do Iguaçu, Brazil, 2017, pp. 3–5.

[31] S.V. Patankar, C.H. Liu, E.M. Sparrow, Fully developed flow and heat transfer in ducts having streamwise-periodic variations of cross-sectional area, J. Heat Transf. 99 (1977) 180.

[32] J. Hærvig, T. Condra, K. Sørensen, Numerical investigation of single-phase fully developed heat transfer and pressure loss in spirally corrugated tubes, in: 56th SIMS, 2015, pp. 391–397.

P.3. Experimental and numerical comparison of multi-layered La(Fe,Si,Mn)$_{13}$H$_y$ active magnetic regenerators

Experimental and numerical comparison of multi-layered La(Fe,Si,Mn)$_{13}$H$_y$ active magnetic regenerators

Kristina Navickaitė [a,*], Henrique Neves Bez [b], Tian Lei [a], Alexander Barcza [c], Hugo Vieyra [c], Christian R.H. Bahl [a], Kurt Engelbrecht [a]

[a] Department of Energy Conversion and Storage, Technical University of Denmark, 4000 Roskilde, Denmark
[b] The Ames Laboratory of the US DOE, Iowa State University, Ames, IA 50011-3020, USA
[c] Vacuumschmelze GmbH & Co. KG, 63450 Hanau, Germany

ARTICLE INFO

ABSTRACT

We present an experimental and numerical comparison of epoxy bonded multi-layered La(Fe,Si,Mn)$_{13}$H$_y$ active magnetic regenerators. First, no-load tests were performed on four regenerators with two layers of material and varying amounts of epoxy (from 1 wt% to 4 wt%) in order to find the amount of epoxy necessary to maintain the mechanical integrity of the regenerators. As the second part of the study, experimental results of two regenerators with five and nine layers are compared to predictions from the one-dimensional numerical model. A maximum temperature span, ΔT_{span}, over 20 K was measured and it is effectively equal for both regenerators. The numerical modelling was generally in good agreement with experimental results.

1. Introduction

Magnetic refrigeration (MR) is a promising alternative to conventional vapour compression technology, and an active research topic for magnetocaloric materials and system performance. It is an appealing technology since the theoretical energy efficiency of a well-designed system is equal or even larger than that of conventional refrigeration (Gschneidner and Pecharsky, 2008). Moreover, MR uses no greenhouse or ozone-depleting gases (Jacobs et al., 2014), as solid magnetocaloric materials (MCM) are used as the refrigerant. MCMs exhibit changes in temperature and entropy upon a change in external magnetic field.

According to the phase transition, MCMs can either undergo a first order phase transition (FOPT) or a second order phase transition (SOPT). A SOPT between the non-magnetic and magnetic phase results in a continuous entropy change across a broad temperature range. A first order phase transition (FOPT) results in a very narrow and sharp entropy change as a function of temperature. Although most FOPT materials exhibit a large magnetocaloric effect, other challenges to implementing them in a high performance MR system accompany them. In addition to the magne-

tocaloric effect being large over only a narrow temperature range, they often exhibit thermal and magnetic hysteresis. Furthermore, FOPT materials are accompanied by a change either in the crystal volume or crystal structure, which can lead to cracking and mechanical instability (Bez Neves et al., 2016; Brück et al., 2004).

The La(Fe,Mn,Si)$_{13}$H$_y$ intermetallic material family has attracted significant attention as a FOPT material and is the subject of this study. The Curie temperature, T_C, of this compound can be tuned by substituting Fe with Mn. The T_C of an La(Fe,Mn,Si)$_{13}$H$_y$ material decreases monotonically with increased Mn concentration (Basso et al., 2015; Bratko et al., 2016). At a certain concentration of Mn, the phase transition becomes second order with no hysteresis. Thus, it was suggested that by using Mn it is possible to prepare weakly first order materials, which would provide high magnetocaloric properties without hysteresis even at a low magnetic field of about 0.5 T (Basso et al., 2015).

La(Fe,Mn,Si)$_{13}$H$_y$ exhibits changes in volume during the phase transition, causing brittleness when the material is cycled magnetically. Thus, porosity was introduced as a tool to avoid cracking of the material over the (de)magnetization cycles, as suggested by Lyubina et al. (2010). The porosity, which was obtained by crushing and re-pressing dense bricks of the material, leads to the removal of grain boundaries. Subsequently the volume expansion that appears at the phase transition can take place more freely without damaging the material. However, induced porosity did not prevent

---

* Corresponding author.
E-mail address: knav@dtu.dk (K. Navickaitė).

Nomenclature

Abbreviations

AMR	active magnetic regenerator
COP	coefficient of performance
FOPT	first order phase transition
Fe	iron
Gd	gadolinium
HEX	hot heat exchanger
MCE	magnetocaloric effect
MCM	magnetocaloric material
Mn	manganese
MR	magnetic refrigeration
SOPT	second order phase transition
VSM	vibration sample magnetometer

Variables

a_c	cross section area
a	specific area
c	specific heat
d_h	hydraulic diameter
H	magnetic field
k	thermal conductivity
m	Mass
$\dot{m}$	mass flow rate
Nu	Nusselt number
P	pressure drop
S	specific entropy
ΔS	entropy change
T	temperature
T_C	Curie temperature
ΔT_{ad}	adiabatic temperature change
ΔT_{span}	temperature span
t	time
U	utilisation
V_h	total volume of the housing
v	Velocity
x	axial position

Greek letters

ε	porosity
ρ	density

Subscripts

e	epoxy
disp	dispersion
f	fluid
H	magnetic field
reg	regenerator
s	solid
stat	static

the material from disintegrating during extended operation in an active magnetic regenerator (AMR). A compound of MCM and thermoplastic (epoxy) was tested as a further possible solution in order to prevent regenerators from fragmenting and at the same time to shape the material (Lanzarini et al., 2015). Once the MCM and the epoxy are cured together, there is no chemical interaction between them. Thus, the epoxy itself does not change the magnetocaloric properties or T_C of the MCE.

One of the major challenges to deal with for FOPT materials is the narrow temperature range over which a significant MCE appears. Literature shows that it might be solved by constructing regenerators with successive layers each with a different T_C (Richard et al., 2004; Zimm et al., 2005). The T_C of each layer is chosen according to the temperature gradient desired in the regenerator.

Modelling results show the effect of layering MCM with different T_C and how important the accuracy of the T_C distribution is along a regenerator (Lei et al., 2015). Here the authors showed that the optimal temperature span between two neighbouring layers is around 2.5 K for materials such as La(Fe,Mn,Si)$_{13}$H$_y$. This spacing produces 90% of the cooling power that would be obtained in an infinitely layered bed. It is also shown that an uneven distribution of T_C along the regenerator may lead to at least a 17% performance reduction when the standard deviation of T_C is 0.6 K. Moreover, Monfared and Palm (2015) emphasized the difference in T_C selection for each layer when a regenerator is designed either for maximum temperature span and/or seeking to maximise the Carnot efficiency.

Although the majority of AMR devices in the literature use SOPT materials (Kitanovski et al., 2015), some experimental studies using FOPT materials have been reported. Regenerators based on La(Fe,Si)$_{13}$H$_y$ or MnFePAs have been tested in both reciprocating and rotary devices (Bahl et al., 2017; Bez Neves et al., 2016; Govindappa et al., 2017; Jacobs et al., 2014; Lei et al., 2018). Notably a large-scale rotary device developed by Astronautics Corporation of America (Jacobs et al., 2014) used six layers of FOPT La(Fe,Si)$_{13}$H$_y$ spheres with T_C ranging from 303.6 to 316.2 K. With a total mass of the MCM 1.52 kg the device provided 2.5 kW cooling power at a temperature span of 11 K and coefficient of performance (COP) of 1.9. The operating frequency of the machine was 4 Hz.

In this paper, we present a comparison between experimental and numerical results of the performance of multi-layered La(Fe,Si,Mn)$_{13}$H$_y$ regenerators having two, five and nine layers. The model has been presented previously and verified against SOPT experimental results (Lei et al., 2017). AMR modelling is an active research topic and many models have been reported in the literature. Models using a 1D porous approach have been widely reported, including Plaznik et al. (2013), Vuarnoz and Kawanami (2013), Trevizoli et al. (2016), and Mugica Guerrero et al. (2017). 2D AMR models have been presented using a porous construction Liu and Yu (2010), by directly modelling a regenerator geometry that emulates spheres (Aprea et al., 2015) and by directly modelling flow between MCM plates (Tura et al., 2012). A detailed 3D model that directly models the regenerator geometry has also been reported by Bouchard et al. (2009). The vast majority of model results, especially those that are compared directly to experiments, have been generated for SOPT materials, and those are almost exclusively based on Gd and its alloys. Jacobs et al. (2014) presented good agreement between a 1D porous model and FOPT LaFeSiH materials. In this paper, the porous 1D model is used as a check of experimental results that the behaviour is as expected and there are no large discrepancies between expected results and experiments.

All investigated regenerators were made of epoxy bonded irregular particles. The total height of all the tested regenerators was the same, resulting in varying layer thicknesses. We also investigated the optimal amount of epoxy necessary to maintain the mechanical integrity of the regenerators. The results of no-load experiments showed that the temperature spans reported in this paper are the largest ever obtained in this small-scale test machine, emphasising the potential of La(Fe,Mn,Si)$_{13}$H$_y$ materials.

2. Experimental procedure

Vacuumschmelze GmbH provided six regenerators made of La(Fe,Si,Mn)$_{13}$H$_y$ irregularly shaped particles with a particle size between 250 µm and 500 µm. The particles were bonded into plastic housings having a height of 40 mm and an inner diameter of 30 mm and 34 mm for the two-layered beds and for five- and nine-layer beds, respectively, using epoxy (Fig. 1). Four of the tested regenerators were constructed in two layers (Fig. 2) and each of the
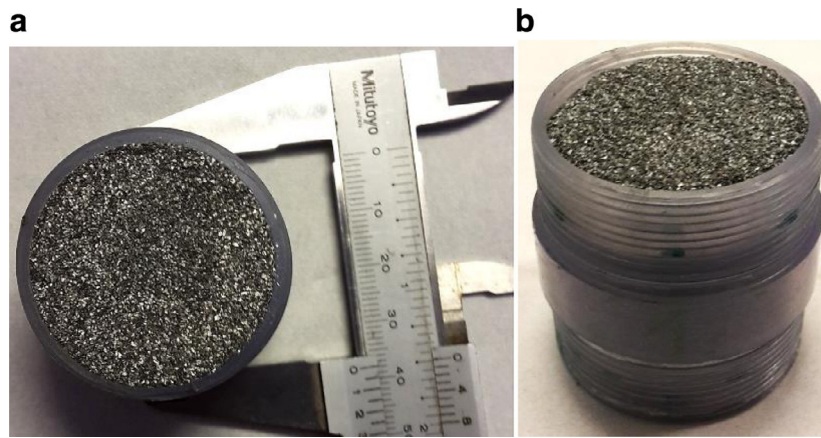
Fig. 1. The regenerators tested in the versatile machine: a) the sample with five layers of MCM before the tests (the housing is fully filled with the MCM until the top) and b) the sample with five layers of MCM after the no-load tests. The small gap on the top of the regenerator shows significant losses of MCM during the experiments.

Table 1
The properties of the tested regenerators.

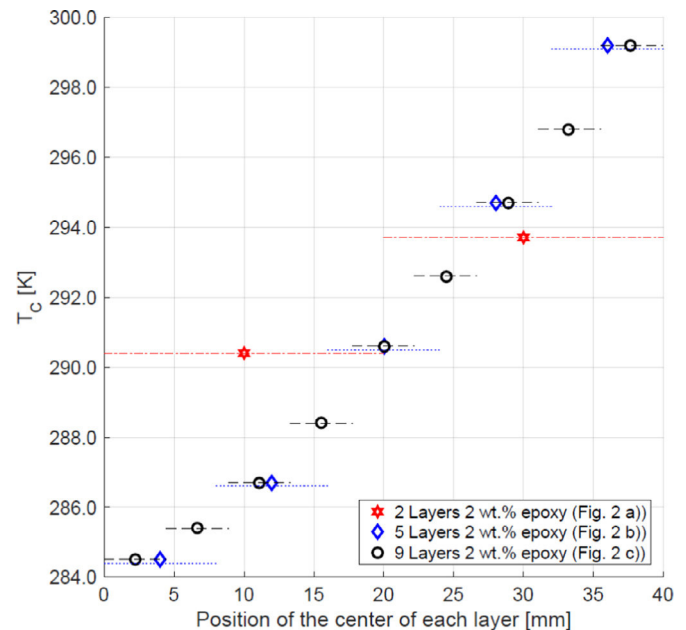|	Inner dimensions, (diameter x height) (mm)	Overall mass of MCM (g)	Porosity (vol%)	Mass fraction of epoxy (wt%)
Regenerators with two layers	30 × 40	94.1	50	1
		93.1	48	2
		93.0	45	3
		91.2	43	4
Regenerators with five layers	34 × 40	122.9	47	2
Regenerators with nine layers		126.0	45	
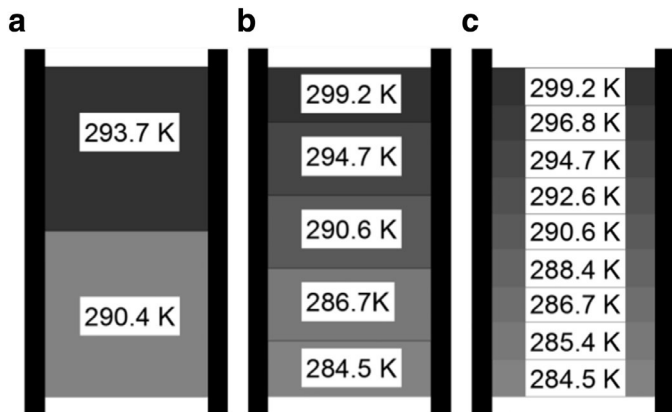
Fig. 2. Schematic drawings of a) two-layered, b) five-layered and c) nine-layered regenerator with T_c of each layer.

Fig. 3. T_C distribution over a regenerator bed. The colour guidelines represent layer thickness in each bed.

regenerators had a different amount of epoxy varying from 1 wt% to 4 wt%. Two other regenerators were fabricated after the experimental investigation to determine the necessary amount of epoxy was conducted. They were constructed with the same amount of epoxy as the best performing two-layer regenerator, but with more layers (Fig. 2). The T_C distribution along the regenerators is presented in Figs. 2 and 3. The T_C of each material was measured in a Lake Shore 7407 Vibrating Sample Magnetometer (VSM) using a sample mass of each material of approximately 10 mg. The applied field for the measurements was 10 mT and the Curie temperature was defined as an inflection point of the magnetisation in that field. The Curie temperature defined in this way will be lower than the temperature at which ΔS or ΔT_{ad} have their maximum (Smith et al., 2012).

The regenerators are described in more detail elsewhere (Bez Neves et al., 2016). The porosity ε was estimated for each regenerator using Eq. (1) and is shown in Table 1.

$$\varepsilon = 1 - \frac{\frac{m_s}{\rho_s} + \frac{m_e}{\rho_e}}{V_h} \tag{1}$$

where V_h is the total inner volume of the housing, m_s and m_e are the masses of the solid and epoxy, respectively, and ρ_s and ρ_e are the densities of the solid and epoxy, respectively. The values for ρ_s and ρ_e are 7000 kg m^{-3} and 1250 kg m^{-3}, respectively.

Hot HEX
Magnet
Regenerator
Magnet
El. heater
Displacer
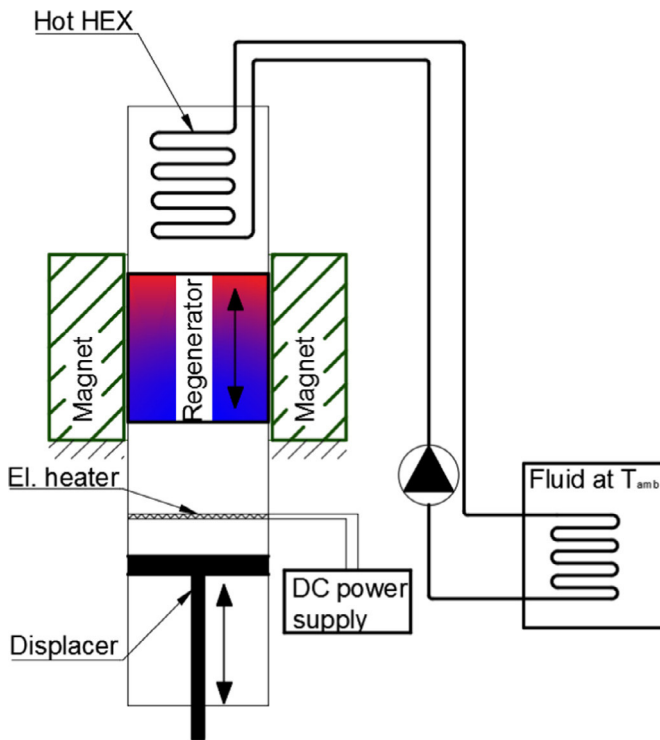DC power supply
Fluid at T_{amb}

Fig. 4. The schematic drawing of the testing device.

The regenerators were tested in a versatile small-scale reciprocating device described previously in Bahl et al. (2008). Fig. 4 shows the schematic drawing of the test machine, which is placed inside a commercial refrigerator with a temperature-control system. The test machine consists of a Halbach array permanent magnet that is placed at a fixed position. The average generated magnetic field inside the magnet bore (ø 40 mm) is 1.1 T. A regenerator is moved in and out of the magnetic field by a stepper motor, and a displacer, placed at the cold side of the regenerator, provides reciprocating flow of the heat transfer fluid timed to the changes in magnetic field. The design of the device enables testing of a relatively small amount of MCM for varying operational parameters, such as the cycle frequency, utilisation and hot side temperature. A wire heater (Fig. 4) is used as a heating load at the cold side of the regenerator. The applied heating power is controlled via an Aim TTi EL302P power supply varying voltage and registering current. The stated power accuracy is $\pm 0.9\%$. Temperatures are measured by calibrated E-type thermocouples placed at the hot and cold sides of the test setup and inside the temperature controlling cabinet. The measurement error is ± 0.5 K.

The temperature at the hot side of the setup is maintained by a forced convection heat exchanger, which is placed in the cabinet. Note that the heat transfer fluid, which is in thermal connection with the solid, is hydraulically independent from the fluid circulating in the heat exchanger loop. Thus, we control the hot end temperature when controlling ambient temperature. The flow characteristics such as velocity and flow rate are changed by modifying the speed and the amplitude of the displacer movement, respectively. One of the most important parameters for testing regenerators is utilisation. It is a dimensionless parameter describing the ratio between the thermal mass of the fluid pushed through the regenerator per one cycle and the thermal mass of the solid. The utilisation U is defined here as:

$$U = \frac{m_f c_f}{m_{reg} c_s} \tag{2}$$

where m_f is the mass of the fluid pushed through the regenerator in one direction, c_f the specific heat of the fluid, m_{reg} the mass of the regenerator and c_s is the specific heat of the regenerator material (Kitanovski et al., 2015). The values used for c_f and c_s are 4210 J kg^{-1} K^{-1} and 501 J kg^{-1} K^{-1} (Basso et al., 2015), respectively. Note that the utilisation is defined using the background value of c_s rather than the peak value.

3. Numerical modelling

Numerical modelling is a powerful tool to study the AMR performance. In this paper, a 1D numerical model is used to investigate and predict the theoretical performance of the presented regenerators. The model was developed and presented elsewhere (Lei et al., 2015), and has previously been validated against SOPT materials. However, it has not been verified against multi-material FOPT materials and here it is used to check that model predictions are in general agreement with experimental results. The modelling is used to verify that the regenerators are constructed properly and that the MCM is behaving as expected. The model is based on two energy equations for the solid refrigerant and fluid (Lei et al., 2015), as shown in Eqs. (3) and (4). It is assumed that the fluid is incompressible and the regenerator housing is adiabatic.

$$\frac{\partial}{\partial x}\left(k_{stat} A_c \frac{\partial T_s}{\partial x}\right) + \frac{Nu k_f}{d_h} a_s A_c (T_f - T_s)$$
$$= A_c (1 - \varepsilon) \rho_s \left[c_H \frac{\partial T_s}{\partial t} + T_s \left(\frac{\partial s_s}{\partial H}\right)_{T_s} \frac{\partial H}{\partial t} \right] \tag{3}$$

$$\frac{\partial}{\partial x}\left(k_{disp} A_c \frac{\partial T_f}{\partial x}\right) - \dot{m}_f c_f \frac{\partial T_f}{\partial x} - \frac{Nu k_f}{d_h} a_s A_c (T_f - T_s) + \left| \frac{\partial P}{\partial x} \frac{\dot{m}_f}{\rho_f} \right|$$
$$= A_c \varepsilon \rho_f c_f \frac{\partial T_f}{\partial t} \tag{4}$$

where: k, T, ρ, c, and s are the thermal conductivity, temperature, density, specific heat, and specific entropy; A_c, d_h, a_s, and ε are the cross section area, hydraulic diameter, specific area, and porosity, which reflect the geometry characteristics of a regenerator; x, t, $\dot{m}$, and H are the axial position, time, mass flow rate, and internal magnetic field. The subscripts f and s represents fluid and solid refrigerant, respectively, $\frac{\partial P}{\partial x}$ is pressure drop, and Nu is Nusselt number.

The two terms on the left hand side of Eq. (3) represent the thermal conduction through the regenerator bed and the heat transfer between the fluid and MCM. The term on the right hand side determines the energy storage and magnetic work of the solid. From the left hand side the thermal conduction (the first term), enthalpy flow (the second term), heat transfer with the solid (the third term), viscous dissipation (the fourth term) and energy storage for the fluid (the right hand side) are described by Eq. (4). Nielsen and Engelbrecht (2012) gives explicit explanation for the static thermal conductivity and due to the fluid dispersion, Nusselt number and pressure drop. One can note that both equations are coupled by the heat transfer term, and they are solved numerically by discretising in time and spatial domains. More details about the model and related expressions of each term are given in Lei et al. (2016).

It should be noted that the effect of epoxy was not included in the model. This is because the mass of epoxy is small in comparison to the mass of fluid and solid. In the results section below, it is shown that there is a noticeable effect due to the presence of epoxy, but the difference is similar to the expected level of uncertainty in the modelling due to uncertainties in the geometry and material properties.
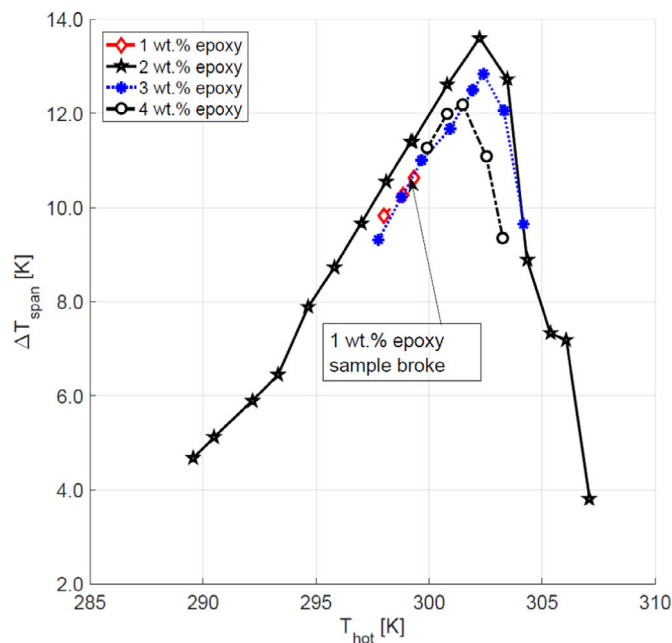
Fig. 5. The steady state temperature span between the hot and the cold side as a function of hot side temperature at different epoxy ratios in the tested two-layer regenerators.

Fig. 6. The steady state temperature span between the hot and the cold side as a function of the utilisation at no-load at hot side temperature 30 °C and best-case flow velocity.

4. Results and discussion

A water-based solution with 2 wt% of the corrosion inhibitor Entek FNE was used as the heat transfer fluid. Even though the MCM is epoxy bonded into regenerators, it is susceptible to corrosion in aquatic systems because parts of the MCM are directly exposed to the fluid. Firstly, the best operational point for the regenerators was determined by a series of experiments at constant hot end temperature. The optimal fluid velocity, v_f, was found while holding the utilisation constant. The optimal utilisation was found while holding the fluid velocity constant at the optimum and varying the fluid displacement. Note that the cycling speed changed when the utilisation or fluid velocity was changed. The optimal operational point at which the performance of the two-layer regenerators at no-load experiments were tested was $U = 0.45$ and $v_f = 8.2$ mm s^{-1}. The cycling speed at the operational point was approximately 0.15 Hz.

The two-layer regenerators were tested to determine the effects of varying epoxy amounts. Fig. 5 gives the no-load temperature span across each regenerator for a range of hot side temperatures. One can see that the maximum temperature spans are $\Delta T_{span} = 13.6$ K, 12.8 K and 12.2 K for the samples with 2 wt%, 3 wt% and 4 wt% of epoxy, respectively. The regenerator with 1 wt% epoxy could not withstand the forces during the test and disintegrated before adequate results could be obtained. Thus, the test could not be finished.

The first series of experiments showed that the epoxy itself does affect the performance of the regenerators negatively when the amount is increased. This is because the epoxy is a passive material, which is also a poor thermal conductor. The larger mass fraction of epoxy leads to a reduction in both the mass fraction of active material and the heat transfer in the bed. Summarising the first series of experiments, it is concluded that 2 wt% of epoxy is the optimum for the two-layer regenerators. Based on these results, two more regenerators with more layers were constructed with 2 wt% epoxy (Figs. 1 and 2).

The two, five and nine-layer regenerators with 2 wt% epoxy were then tested at no-load conditions varying the utilisation. The
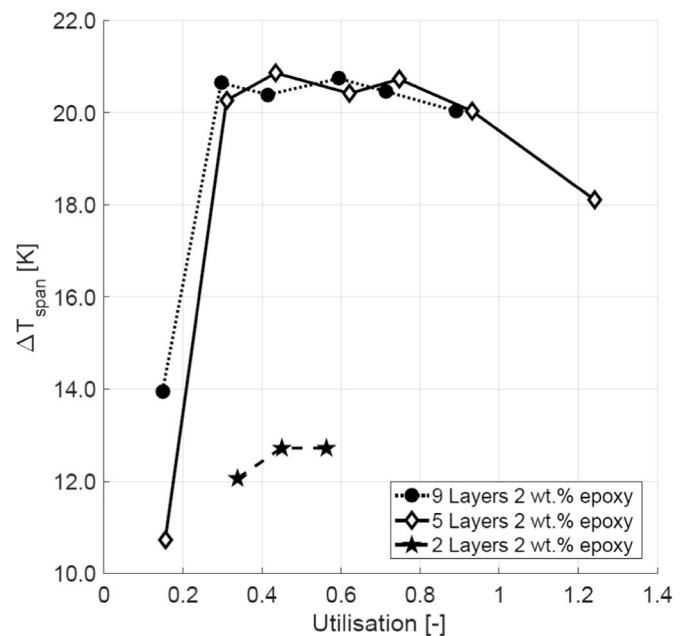
optimal operational flow velocity v_f for five and nine-layer beds were 21.7 mm s^{-1} and 22.7 mm s^{-1}, respectively. The no-load temperature span of each bed at the reported optimal flow velocity as a function of utilisation is shown in Fig. 6. One can see that even at similar utilisations of 0.45, 0.43 and 0.42 for two, five and nine layer regenerators, respectively, the temperature is more than 8 K higher for the five- and nine-layer regenerators than for the two-layer regenerator. It is noticeable from Fig. 6 that utilisation does not have a strong influence on the no-load performance of regenerators with five and nine layers in a range from 0.3 to 0.9, but at relatively low or high values of the utilisation performance decreases drastically. This weak dependence of the temperature span on utilisation was also reported by Bez Neves et al. (2016) for similar regenerators with one and two layers. In comparison, a Gd-based single layer AMR showed stronger dependency of performance on utilisation (Engelbrecht et al., 2013; Tušek et al., 2014).

Later, the regenerators were characterised varying the hot side temperature. As it is shown in Fig. 7, the maximum temperature span established by a two-layer regenerator is much lower than the maximum temperature of five and nine-layer regenerators. This is a consequence of the five- and nine-layer regenerators having a larger range of Curie temperatures than the regenerator with two layers (Fig. 2).

One could note that the utilisation of the five-layer regenerator is approximately two times bigger than of two- and nine-layer regenerators. This is due to initially chosen operational temperature point. Firstly the five- and nine-layer regenerator were tested at 305.5 K hot side temperature to define the optimal utilisation. Obtained results (not presented in this paper) showed that the optimal utilisations for five- and nine-layer regenerators are 0.93 and 0.42, respectively. Further experiments showed that the optimal working temperature for both regenerators is approximately 303 K. Therefore, we can conclude the more layers a regenerator has the more sensible it is to any changes in operational point, especially hot side temperature changes.

Numerical studies predict that the more layers a regenerator has, the better the performance is and a higher specific cooling power is obtained, although there is a diminishing gain in
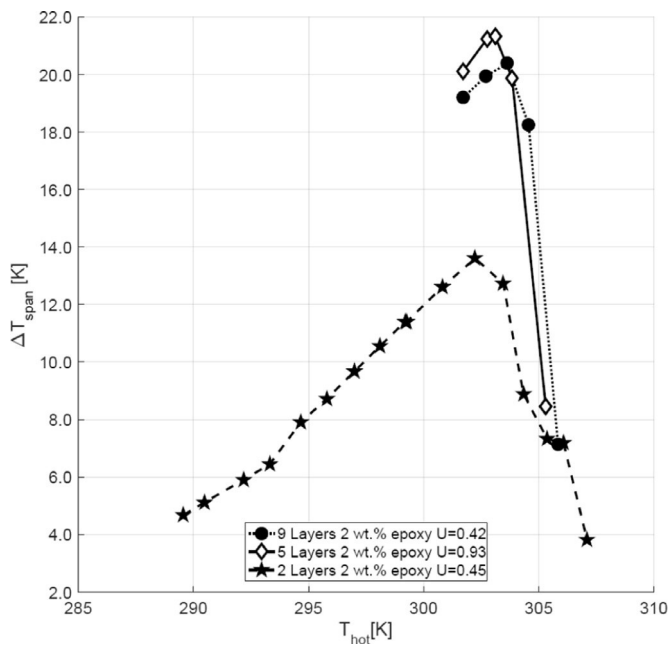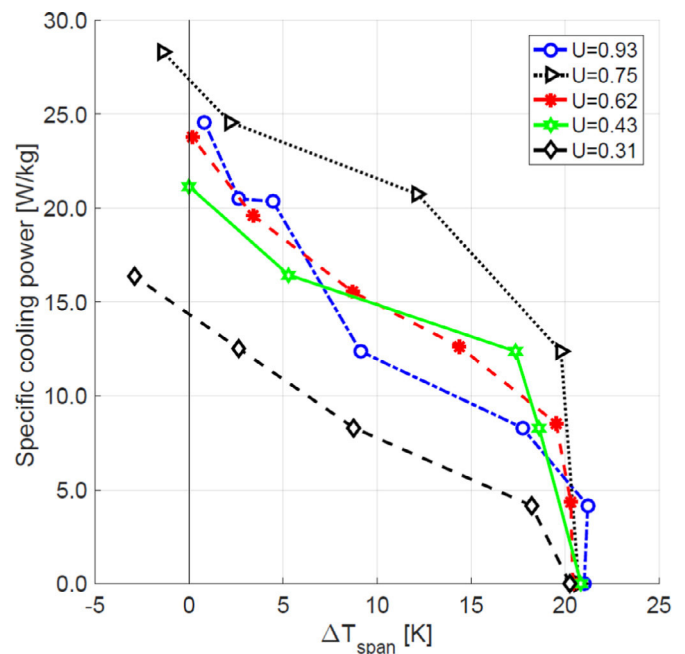
Fig. 7. The steady state no-load temperature span between the hot and the cold side as a function of hot side temperature for two-, five- and nine-layer regenerators.

Fig. 8. The cooling power of the material with five layers as a function of temperature span obtained at several different utilisations at the constant hot side temperature of 303 K. The maximum applied cooling power for this regenerator was 3.5 W.

Fig. 9. The cooling power of the material with nine layers as a function of temperature span obtained at several different utilisations at the constant hot side temperature of 303 K. The maximum applied cooling power for this regenerator was 3.5 W.
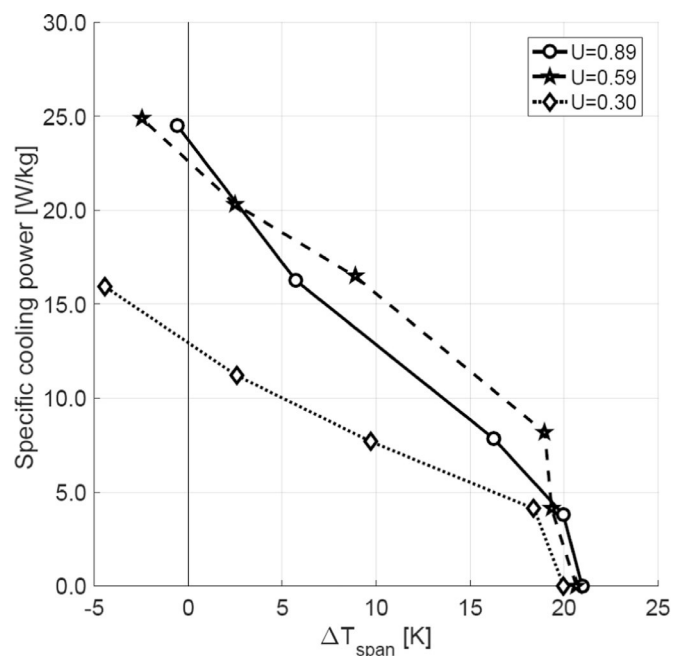
performance as the number of layers increases above a certain level (Lei et al., 2015). The same study concludes that in order to get 90% of cooling power at maximum field of 1.2 T the temperature gap between two neighbouring layers should be around 2.5 K. It is noticeable that FOPT materials require 4–6 times more layers than SOPT to achieve the maximum temperature span (Lei et al., 2016). From Fig. 3 it is evident that the distribution in T_C of the tested regenerators is close to but not completely even. This may be the reason that the nine-layer regenerator did not perform better than the five-layer one. Another possible explanation is that the layer thickness of the nine-layer regenerator was too small. Therefore, it cannot successfully establish larger temperature span than the five-layer regenerator (Govindappa et al., 2017).

Cooling load tests were performed at different utilisations for both the five-layer and nine-layer regenerators (see Figs. 8 and 9). Both regenerators showed similar results and established a temperature span up to $\Delta T = 18$ K under a specific heat load of 5 W kg^{-1}. Note that the blown fluid mass through both regenerators was the same for all the corresponding experiments. The slight difference in utilisation and the applied specific power is due to a slight difference in the regenerator mass, used for calculations. Jacobs (2009, 2013) and Tušek et al. (2014) reported that the cooling power drops drastically as soon as the span exceeds the range of Curie temperatures in the bed, as is also observed in Figs. 8 and 9. Teyber et al. (2016) showed that cooling power of SOPT material two-layer regenerators highly depends on the transitional temperature between layers. We found that the highest cooling capacity is achieved at utilisations of around 0.75. This effect is a combination of magnetocaloric and heat transfer properties of the beds. Therefore, at this utilisation point, enough fluid was pushed through to maintain a high cooling power and it was small enough not to destroy the temperature span. In other words, the operational temperature of each layer was close enough to its transitional temperature.

The temperature of the thermal reservoir at HEX was set to be constant for all the experiments. However, the measured value of the hot side temperature increased from 303.5 K to 304.4 K for the five-layer regenerator and from 303.3 K to 303.9 K for the nine-

layer regenerator when the specific cooling power was increased. This change in the hot side temperature is a combination of several processes behind the tests. The first reason is that the sensitivity of the temperature-control cabinet is ±0.5 K. Secondly, the fluid flow rate in the HEX was slightly too low to effectively remove the generated heat from the hot side during the cooling load tests. This began to be a concern only at tests with the specific cooling power above 10 W kg^{-1} when the utilisation factor was above 0.6. It means that the flow rate of the fluid in the HEX circuit was too
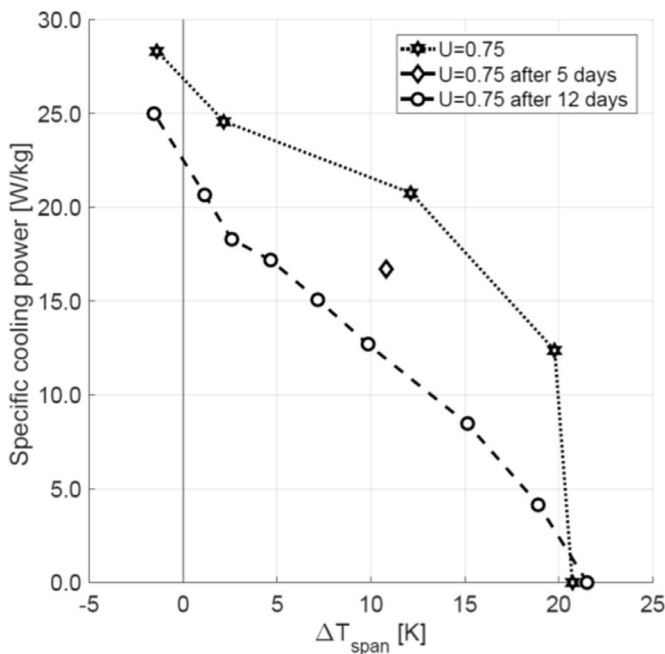
Fig. 10. Comparison of initial and repeated cooling power tests at $U = 0.75$ with five-layer regenerator at the constant hot side temperature of 303 K. The maximum applied cooling power for this regenerator was 3.5 W.
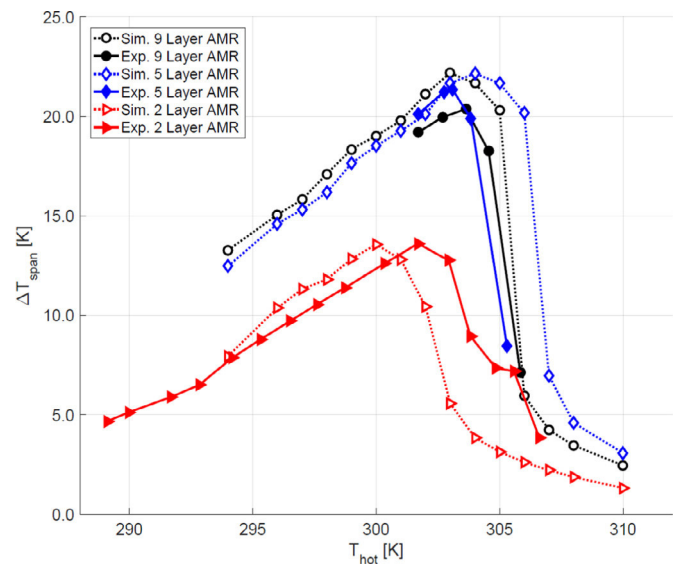

Fig. 11. The experimental steady state no-load temperature span between the hot and the cold side as a function of a constant hot side temperature and the modelling results.

low and could not remove the generated heat effectively at higher mass flow rates through the regenerator and higher applied cooling power.

Fig. 10 shows that the performance of the five-layer regenerator decreased after the initial test at utilisation of 0.75. In order to analyse the phenomenon, the cooling load test was repeated at $U = 0.75$ twice in the period of two weeks (Fig. 10). One can observe that the system performance at the latest test was the lowest. One month later, we found that the regenerator could not establish the initial temperature span at no-load tests and the system could not be drained. The blockage of the flow paths was possibly caused by mechanical breakdown of particles inside the bed. Thus, it was concluded that the regenerator disintegrated. The test on the nine-layer regenerator was also conducted in order to investigate its disintegration after three months. The regenerator could not reach steady state conditions and system could not be drained as well as the five-layer regenerator. However, a similar five-layer regenerator made of the La(Fe,Si,Mn)$_{13}$H$_y$ spherical particles, which was used for another study, showed no signs of mechanical degradation after a long term experiment (Lei et al., 2018). The regenerators were periodically tested for six months. Each time they were dried and stored at room temperature after a set of experiment was finished. One could note from Fig. 10 that the cooling power decreases while the temperature difference nearly does not change. This phenomenon could happen due to reduction of the utilisation during the cycle. The blockage of the flow paths caused maldistribution or reduction of the fluid mass flow, even though it was set to be the same.

We also investigated the possibility that regenerators lost their magnetocaloric properties after long-term experiments. VSM measurements were conducted for this purpose. No changes of magnetocaloric properties were found.

One also can observe that the decrease in performance is rather systematic. Figs. 8 and 10 show that five-layer regenerator performance after 12 days of testing at utilisation of 0.75 has similar trend as the initial performance at utilisation of 0.31. The mechanical breakdown of particles caused unfavourable changes in actual utilisation of the cycle.

It is evident from Fig. 1, that the five-layer regenerator lost a significant amount of mass from its top layer during the tests, as it was filled to the top of the housing before testing. This also happened to the nine-layer bed. Both regenerators were weighed after drying with pressurised air in the direction from the hot to cold side. The reason of this was to ensure that the regenerators were always dried in the same direction as well as secure that particles would not be removed from top layer by pressurised airflow. Note that all the regenerators were constructed from the cold side to the hot side allowing gravitational epoxy distribution. The five- and nine-layer regenerators lost 3.4% and 1.7% of their mass, respectively after testing. It is meaningful to emphasise that the temperature span in the regenerators are different for the beds with two layers and ones with five and nine layers. This is also linked to the increased magnetic forces due to increased mass of the used MCM and a larger T_C span over the beds. Thus, increasing the amount of epoxy in regenerators where the MCM must withstand larger magnetic forces should be considered.

Fig. 11 shows the modelling results compared with the experimental data set at no-load conditions. In general, good agreement is observed for all of the regenerators.

Even though the simulation results predicted an approximately 5 K broader working temperature range for both the five- and nine-layer regenerators, the overall prediction follows the trend and the maximum temperature span is well captured. From Fig. 11 it is evident that the model slightly under predicts the working temperature range for the regenerators with two layers. The maximum temperature span and the shape of the simulation curve fit the experimental data well, though. The slight shift in the performance curve might occur due to imperfections of the tested beds. It is widely discussed that the FOPT materials are very susceptible to variation in temperature range, Curie temperature distribution, or unevenness of the magnetocaloric properties in the MCM, etc. (Barcza et al., 2011; Lei et al., 2016, 2015; Lyubina et al., 2010). Numerical models are limited in predicting possible imperfections of a physical regenerator, such as uneven epoxy distribution, actual MCM particle size deviation, etc.

In this study, we showed that effectively using the layering technique, the FOPT materials could establish high performance under both no-load and cooling load conditions performance. Moreover, we presented the FOPT material, which established

the highest temperature span at no-load experiments and demonstrated the highest specific cooling power ever obtained using this small-scale testing device.

5. Conclusions

Six irregular particle La(Fe,Mn,Si)$_{13}$H$_y$ regenerators were tested in order to investigate the optimal amount of epoxy necessary to bond the MCM particles without compromising the performance and the effect of having multi-layered MCM regenerators. Firstly, four regenerators with two layers of MCM and a varying amount of epoxy were tested. It was concluded that 2 wt% gave the best trade-off between mechanical integrity and MCM/heat transfer performance. However, the regenerators with five and nine layers with 2 wt% of epoxy showed some mechanical degradation.

In this study, we show that layering the MCM does increase the performance of regenerators with FOPT materials. The two-layer regenerator showed a no-load temperature span of $\Delta T_{span} = 12.7$ K, while the five- and nine-layer regenerators showed no-load temperature spans of $\Delta T_{span} = 20.9$ K and $\Delta T_{span} = 20.7$ K, respectively. However, regenerators must be layered accurately and precisely in order to achieve the full benefits of the concept.

Experiments presented here show that La(Fe,Mn,Si)$_{13}$H$_y$ is a promising material for magnetic refrigeration. The material used in this study shows the highest temperature span of $\Delta T_{span} = 20.9$ K for no-load tests in comparison with other materials used in this small-scale device and also it exhibits the highest temperature span for a given cooling load $\Delta T_{span} = 19.8$ K at a heat load of 12.4 W kg^{-1}. This shows the significant potential for La(Fe,Mn,Si)$_{13}$H$_y$ to be used as regenerative material. However, the functional problems still exist when the material is used for long-term experiments. It is crucially important to overcome these problems in order to make La(Fe,Mn,Si)$_{13}$H$_y$ applicable in commercial devices.

Finally, the modelling results showed a good agreement with the experimental data with a slight offset in the range of working temperatures. The uncertainties between the experimental and modelling results are mainly due to inaccuracies in physical regenerators that the model cannot capture. However, generally good agreement between modelling and experimental data indicates that the regenerators generally functioned as expected and encourages using modelling as a beforehand tool to predict performance of materials.

Acknowledgements

References

Aprea, C., Cardillo, G., Greco, A., Maiorino, A., Masselli, C., 2015. A comparison between experimental and 2D numerical results of a packed-bed active magnetic regenerator. Appl. Thermal Eng. 90, 376–383. doi:10.1016/j.applthermaleng.2015.07.020.

Bahl, C.R.H., Navickaitė, K., Neves Bez, H., Lei, T., Engelbrecht, K., Bjørk, R., Li, K., Li, Z., Shen, J., Dai, W., Jia, J., Wu, Y., Long, Y., Hu, F., Shen, B., 2017. Operational test of bonded magnetocaloric plates. Int. J. Refrigeration 76, 245–251. doi:10.1016/j.ijrefrig.2017.02.016.

Bahl, C.R.H., Petersen, T.F., Pryds, N., Smith, A., 2008. A versatile magnetic refrigeration test device. Rev. Sci. Instrum. 79. doi:10.1063/1.2981692.

Barcza, A., Katter, M., Zellmann, V., Russek, S., Jacobs, S., Zimm, C., 2011. Stability and magnetocaloric properties of sintered La(Fe,Mn,Si)$_{13}$H$_z$ alloys. IEEE Trans. Magn. 47, 3391–3394. doi:10.1109/TMAG.2011.2147774.

Basso, V., Küpferling, M., Curcio, C., Bennati, C., Barzca, A., Katter, M., Bratko, M., Lovell, E., Turcaud, J., Cohen, L.F., 2015. Specific heat and entropy change at the first order phase transition of La(FeMnSi)$_{13}$H compounds. J. Appl. Phys. 118, 53907. doi:10.1063/1.4928086.

Bez Neves, H., Navickaitė, K., Lei, T., Engelbrecht, K., Barcza, A., Bahl, R., H., C., 2016. Epoxy-bonded La(Fe,Mn,Si)13Hz as a multi layered active magnetic regenerator. doi:10.18462/iir.thermag.2016.0147

Bouchard, J., Nesreddine, H., Galanis, N., 2009. Model of a porous regenerator used for magnetic refrigeration at room temperature. Int. J. Heat Mass Transf. doi:10.1016/j.ijheatmasstransfer.2008.08.031.

Bratko, M., Lovell, E., Caplin, A.D., Basso, V., Barcza, A., Katter, M., Cohen, L.F., 2016. Determining the First Order Character of La(Fe,Mn,Si)13.

Brück, E., Tegus, O., Zhang, L., Li, X.W., De Boer, F.R., Buschow, K.H.J., 2004. Magnetic refrigeration near room temperature with Fe$_2$P-based compounds. J. Alloys Compd. 383, 32–36. doi:10.1016/j.jallcom.2004.04.042.

Engelbrecht, K., Nielsen, K.K., Bahl, C.R.H., Carroll, C.P., van Asten, D., 2013. Material properties and modeling characteristics for MnFeP$_{1-x}$As$_x$ materials for application in magnetic refrigeration. J. Appl. Phys. doi:10.1063/1.4803495.

Govindappa, P., Trevizoli, P.V, Campbell, O., Niknia, I., Christiaanse, T.V, Teyber, R., Misra, S., Schwind, M.A., van Asten, D., Zhang, L., Rowe, A., 2017. Experimental investigation of MnFeP$_{1-x}$As$_x$ multilayer active magnetic regenerators. J. Phys. D: Appl. Phys. 50, 315001. doi:10.1088/1361-6463/aa7a33.

Gschneidner, K.A., Pecharsky, V.K., 2008. Thirty years of near room temperature magnetic cooling: where we are today and future prospects. Int. J. Refrigeration 31, 945–961. doi:10.1016/j.ijrefrig.2008.01.004.

Jacobs, S., 2009. Modeling and optimal design of a multilayer active magnetic refrigeration system. In: Proceedings of 3rd International Conference on Magnetic Refrigeration at Room Temperature, pp. 267–273.

Jacobs, S., Russek, S., Auringer, J., Boeder, A., Chell, J., Komorowski, L., Leonard, J., Zimm, C., 2013. The Performance of Rotary Magnetic Refrigerators with Layered Beds of LaFeSiH 2, 21–27.

Jacobs, S., Auringer, J., Boeder, A., Chell, J., Komorowski, L., Leonard, J., Russek, S., Zimm, C., 2014. The performance of a large-scale rotary magnetic refrigerator. Int. J. Refrigeration 37, 84–91. doi:10.1016/j.ijrefrig.2013.09.025.

Kitanovski, A., Tušek, J., Tomc, U., Plaznik, U., Ožbolt, M., Poredoš, A., 2015. Magnetocaloric Energy Conversion. Springer, London doi:10.1007/978-3-319-08741-2.

Lanzarini, J., Barriere, T., Sahli, M., Gelin, J.C., Dubrez, A., Mayer, C., Pierronnet, M., Vikner, P., 2015. Thermoplastic filled with magnetocaloric powder. Mater. Des. 87, 1022–1029. doi:10.1016/j.matdes.2015.08.057.

Lei, T., Engelbrecht, K., Nielsen, K.K., Neves Bez, H., Bahl, C.R.H., 2016. Study of multilayer active magnetic regenerators using magnetocaloric materials with first and second order phase transition. J. Phys. D: Appl. Phys. 49, 345001. doi:10.1088/0022-3727/49/34/345001.

Lei, T., Engelbrecht, K., Nielsen, K.K., Veje, C.T., 2017. Study of geometries of active magnetic regenerators for room temperature magnetocaloric refrigeration. Appl. Thermal Eng. 111, 1232–1243. doi:10.1016/j.applthermaleng.2015.11.113.

Lei, T., Navickaite, K., Engelbrecht, K., Barcza, A., Vieyra, H., Nielsen, K., Bahl, C.. H., 2018. Passive Characterization and Active Testing of Epoxy Bonded Regenerators for Room Temperature Magnetic Refrigeration. doi:10.1016/j.applthermaleng.2017.08.152

Lei, T., Nielsen, K.K., Engelbrecht, K., Bahl, C.R.H., Neves Bez, H., Veje, C.T., 2015. Sensitivity study of multi-layer active magnetic regenerators using first order magnetocaloric material La(Fe,Mn,Si)$_{13}$H$_y$. J. Appl. Phys. 118, 0–8. doi:10.1063/1.4923356.

Liu, M., Yu, B., 2010. Numerical investigations on internal temperature distribution and refrigeration performance of reciprocating active magnetic regenerator of room temperature magnetic refrigeration 'riques sur la distribution de la tempe´rature Etudes nume´ne´rateur. Int. J. Refrigeration 34, 617–627. doi:10.1016/j.ijrefrig.2010.12.003.

Lyubina, J., Schäfer, R., Martin, N., Schultz, L., Gutfleisch, O., 2010. Novel design of La(Fe,Si)$_{13}$ alloys towards high magnetic refrigeration performance. Adv. Mater. 22, 3735–3739. doi:10.1002/adma.201000177.

Monfared, B., Palm, B., 2015. Optimization of layered regenerator of a magnetic refrigeration device. Int. J. Refrigeration 57, 103–111. doi:10.1016/j.ijrefrig.2015.04.019.

Mugica Guerrero, I., Poncet, S., Bouchard, J., Mugica Guerrero, I., Poncet, S., Bouchard, J., 2017. Entropy generation in a parallel-plate active magnetic regenerator with insulator layers. J. Appl. Phys. 74901. doi:10.1063/1.4975818.

Nielsen, K.K., Engelbrecht, K., 2012. The influence of the solid thermal conductivity on active magnetic regenerators. J. Phys. D: Appl. Phys. doi:10.1088/0022-3727/45/14/145001.

Plaznik, U., Tušek, J., Kitanovski, A., Poredoš, A., Tu, J., Kitanovski, A., Poredo, A., 2013. Numerical and experimental analyses of different magnetic thermodynamic cycles with an active magnetic regenerator. Appl. Thermal Eng. 59, 52–59. doi:10.1016/j.applthermaleng.2013.05.019.

Richard, M.A., Rowe, A.M., Chahine, R., 2004. Magnetic refrigeration: Single and multimaterial active magnetic regenerator experiments. J. Appl. Phys. 95, 2146–2150. doi:10.1063/1.1643200.

Smith, A., Bahl, C.R.H., Bjork, R., Engelbrecht, K., Nielsen, K.K., Pryds, N., 2012. Materials challenges for high performance magnetocaloric refrigeration devices. Adv. Energy Mater. 2, 1288–1318. doi:10.1002/aenm.201200167.

Teyber, R., Trevizoli, P.V., Christiaanse, T.V., Govindappa, P., Niknia, I., Rowe, A., 2016. Performance evaluation of two-layer active magnetic regenerators with second-order magnetocaloric materials. Appl. Thermal Eng. 106, 405–414. doi:10.1016/j.applthermaleng.2016.06.029.

Trevizoli, P.V, Nakashima, A.T., Barbosa Jr., J.R., 2016. Performance evaluation of an active magnetic regenerator for cooling applications – part II: mathematical modeling and thermal losses Évaluation de la performance d'un régénérateur magnétique actif pour les applications de refroidissement – Partie II. Int. J. Refrigeration 72, 206–217. doi:10.1016/j.ijrefrig.2016.07.010.

Tura, A., Nielsen, K.K., Rowe, A., 2012. Experimental and modeling results of a parallel plate-based active magnetic regenerator. Int. J. Refrigeration. doi:10.1016/j.ijrefrig.2012.04.016.

Tušek, J., Kitanovski, A., Tomc, U., Favero, C., Poredoš, A., 2014. Experimental comparison of multi-layered La–Fe–Co–Si and single-layered Gd active magnetic regenerators for use in a room-temperature magnetic refrigerator. Int. J. Refrigeration 37, 117–126. doi:10.1016/j.ijrefrig.2013.09.003.

Vuarnoz, D., Kawanami, T., 2013. Experimental validation of a coupled magneto-thermal model for a fl at-parallel-plate active magnetic regenerator. Appl. Thermal Eng. 54, 433–439. doi:10.1016/j.applthermaleng.2013.01.007.

Zimm, C., Boeder, A., Chell, J., Sternberg, A., Fujita, A., Fujieda, S., Fukamichi, K., 2005. Design and performance of a permanent magnet rotary refrigerator. In: Proceedings of the 1st International Conference on Magnetic Refrigeration at Room Temperature, pp. 367–373.

P.4. Passive characterisation and active testing of epoxy bonded regenerators from room temperature magnetic refrigeration
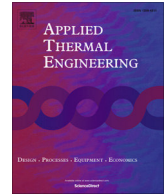
Research Paper

Passive characterization and active testing of epoxy bonded regenerators for room temperature magnetic refrigeration

Tian Lei [a],*, Kristina Navickaitė [a], Kurt Engelbrecht [a], Alexander Barcza [b], Hugo Vieyra [b], Kaspar K. Nielsen [a], Christian R.H. Bahl [a]

[a] Department of Energy Conversion and Storage, Technical University of Denmark, 4000 Roskilde, Denmark
[b] Vacuumschmelze GmbH & Co. KG, 63450 Hanau, Germany

HIGHLIGHTS

- Two epoxy bonded regenerators are characterized in an oscillating flow test.
- The friction factor and overall Nusselt number are presented and compared.
- A five-layer AMR achieves a no-load temperature span of 16.8 °C.
- A series of active tests with cooling loads is done and analyzed.
- 1D AMR model is validated against the test results, exhibiting a good prediction.

ARTICLE INFO

ABSTRACT

Epoxy bonded regenerators of both spherical and irregular La(Fe,Mn,Si)$_{13}$H$_y$ particles have been developed aiming at increasing the mechanical strength of active magnetic regenerators (AMR) loaded with brittle magnetocaloric materials and improving the flexibility of shaping the regenerator geometry. Although the magnetocaloric properties of these materials are well studied, the flow and heat transfer characteristics of the epoxy bonded regenerators have seldom been investigated. This paper presents a test apparatus that passively characterizes regenerators using a liquid heat transfer fluid with an oscillating flow at low Reynolds numbers, simulating the hydraulic working conditions in AMRs. Dimensionless parameters, including friction factor, effectiveness and overall Nusselt number, are presented for the epoxy bonded La(Fe,Mn,Si)$_{13}$H$_y$ regenerators and reference packed particle beds. Moreover, a five-layer AMR based on spherical particles is tested actively in a small reciprocating magnetic refrigerator, achieving a no-load temperature span of 16.8 °C using about 143 g of epoxy-bonded La(Fe,Mn,Si)$_{13}$H$_y$ materials. Simulations based on a one-dimensional (1D) AMR model are also implemented to validate and analyze the results from the active test.

© 2017 Elsevier Ltd. All rights reserved.

1. Introduction

Magnetic refrigeration, which exhibits advantages such as the avoidance of volatile, harmful gases and potentially high efficiency [1], is an alternative to the traditional vapor compression technology. Recently, emerging prototypes that approach the performance of vapor-compression based systems have been reported and they presented high cooling capacity on the order of kilowatts [2,3] and improved efficiency up to 18% of the Carnot efficiency [4]. An active magnetic regenerator (AMR) is a porous matrix consisting of magnetocaloric materials (MCMs), in which the fluid exchanges heat with the solid matrix during a periodical reciprocating flow coupled to a varying magnetic field. The refrigeration cycle of an AMR consists of four steps [5,6]: the magnetization process associated with the temperature increase in the MCM; the cold-to-hot blow that cools the porous matrix by rejecting heat to the ambient; the demagnetization process resulting in a further temperature decrease; the hot-to-cold blow where the fluid absorbs a cooling load and the MCM returns to its original temperature. During the two blows, the inlet fluid temperatures at the hot and cold ends are kept constant as T_h and T_c, the hot and cold reservoir temperatures, respectively. After several cycles, a temperature span $\Delta T = T_h - T_c$ is built up along the regenerator and the system reaches a periodic steady state. The enthalpy differences at the cold and hot ends are the cooling capacity and the heat dissipation,

respectively. The concept of heat regeneration allows materials arranged along the temperature gradient to operate at their own thermodynamic cycles, which realizes a temperature span several times larger than the adiabatic temperature change, ΔT_{ad}, of the MCMs.

In order to improve the cooling performance, much effort has been devoted to developing magnetocaloric materials and shaping these into regenerators with suitable porous geometries. The derivatives of La(Fe,Si)$_{13}$ [7], including LaFeCoSi [8] and La(Fe,Mn, Si)$_{13}$H$_y$ [9,10], are promising MCMs with a first order phase transition (FOPT), which exhibit a large peak in isothermal entropy change, moderate adiabatic temperature change and tunable Curie temperatures. Both experimental and theoretical studies [3,11] show that proper layering of La(Fe,Si)$_{13}$ materials in AMRs could realize an outstanding cooling performance. However, many of these materials are brittle and can break during the cycling of the magnetic field, which may lead to problems such as mechanical instability and possible degradation of the magnetocaloric effect [12]. The possible reason of the cracking lies in the significant volume change up to 1% associated with the phase transition [13] and the magneto-structural transitions. Therefore, epoxy bonded regenerators have been developed to increase the overall mechanical strength of the porous media [3,14,15] and to facilitate building a monolithic MCM regenerator [16].

Richard et al. [16] bonded Gd and GdTb flakes with a thin coating of epoxy to form monolithic layers in an AMR, which realized a no-load temperature span near to 20 °C. Jacobs et al. [3] introduced the epoxy-connection process to fabricate six-layer LaFeSiH regenerators and tested them in a rotary magnetic refrigeration device. This refrigerator realized a cooling power of around 2500 W over a span of 11 °C with a coefficient of performance (COP) of approximately 2. Pulko et al. [14] constructed epoxy-bonded LaFeCoSi plates, which maintained the mechanical integrity after 90,000 cycles of applying magnetic field. A no-load temperature span of about 10 °C was achieved in a magnetic refrigerator using these plates. Neves Bez et al. [15] tested epoxy bonded AMRs using 1 and 2 layers of La(Fe,Mn,Si)$_{13}$H$_y$, which achieved a maximum no-load temperature span of 13 °C. Note that a technique of compositing magnetocaloric and metal by hot pressing also has the function of increasing the mechanical stability potentially [17]. However, most of the studies focus on active testing of the epoxy bonded regenerators, and the investigation of the flow and heat transfer characteristics of such regenerators is seldom done. Besides, the particles used in these epoxy bonded regenerators were usually irregular and testing of spherical particles has not yet been reported. Therefore, a passive characterization of the epoxy bonded regenerators is presented in the first part of this article, followed by an active test of a five-layer AMR using spherical particles as the second part. Herein, "passive" means that no magnetic field is applied and in contrast "active" represents testing the cooling performance of AMRs with the magnet assembly.

A quantitative study based on the technique of entropy production minimization [18] has shown that viscous dissipation and imperfect heat transfer are the two mechanisms that present the largest irreversibility inside AMRs. The viscous dissipation is associated with the large pump power and high pressure drop, which reduce efficiency and require thicker housing walls, wasting more magnetized volume. In addition, perfect heat transfer is impossible and there is always a certain temperature difference between the fluid and the solid bed. Enhancing the heat transfer and decreasing the flow resistance simultaneously is always challenging. Therefore, the dimensionless parameters such as the friction factor f_F and the Nusselt number Nu are of essential interest, as they are tightly connected to both irreversible effects. In the passive test, the friction factor could be calculated from the measured pressure

drop over the regenerator in either unidirectional or oscillating flow. Moreover, the heat transfer coefficient h_f and Nu in the convective flow through the porous regenerator could be estimated using different methods, including the unidirectional flow test with constant wall temperature/heat flux, single blow test [19], and the oscillating flow test [20,21]. In the single blow test, a fluid with constant temperature is blown through the regenerator that starts at a uniform temperature different from the inlet fluid and the response of the outflow temperature is recorded for deducing the heat transfer coefficient. Engelbrecht [22] and Frischmann et al. [23] presented experimental results for packed sphere beds in the single blow test. Under oscillating flow condition, Schopfer [20] studied the thermal-hydraulic properties of the liquid-saturated regenerators. The friction factor and the Nusselt number in the regenerators with microchannels and packed beds were estimated in experiments based on a harmonic approximation technique. Trevizoli et al. [21] constructed a laboratory apparatus and presented the pressure drop, the pumping power and the effectiveness of passive regenerators. The effectiveness is the heat transfer efficiency of a regenerator and is defined as the ratio of the amount of heat that transferred during a blow process to the maximum possible amount of heat transfer.

In this study, two groups of regenerators, including epoxy bonded regenerators using irregular or spherical La(Fe,Mn,Si)$_{13}$H$_y$ particles, as well as reference regenerators packed with stainless steel (SS) particles, are characterized in a passive test apparatus. The experiments are run with an oscillating flow in the low Reynolds number region. The dimensionless group consisting of the friction factor f_F, the effectiveness η, and the overall Nusselt number Nu$_o$ is deduced and presented, based on the measured pressure drop and the temperature profiles. Furthermore, an AMR using five layers of spherical La(Fe,Mn,Si)$_{13}$H$_y$ particles is tested actively and the experimental results are validated with the simulations based on an established 1D AMR model.

2. Passive characterization of epoxy bonded regenerators

2.1. Test apparatus and methodology

The passive regenerator test apparatus is composed of four main sections: the regenerator test section, the oscillating flow generator, the cold heat exchanger with a cold reservoir and the hot heat exchanger with an electric heater. The schematic diagram and a photograph of the test apparatus are shown in Fig. 1 (a) and (b), respectively. In detail, the regenerator test section includes a porous regenerator bed (REG), four check valves (CV), thermocouples (T) and two piezoelectric pressure gauges (P). The oscillating flow generator is a motor-crank system (MT) connected to two cylinders (CYL 1 and 2). The displacement of the cylinders is measured by a linear encoder. The cold heat exchanger (CHX) is a double-pipe type. The cold water with a constant temperature is circulating from the cold reservoir to cool down the thermal liquid in the inner tube. The hot heat exchanger (HHX) for heating up the fluid is made by inserting and sealing an electrical cartridge heater in a small insulated chamber.

The reciprocating movement of the two cylinders generates the oscillating flow through the porous regenerator. During the cold-to-hot blow, the fluid is pushed from CYL1, cooled down by CHX, blown through CV1-REG-CV4, and then stored in CYL2. A similar flow pattern is seen in the hot-to-cold blow, and the fluid is heated up by the electric heater in the HHX. On each side of the regenerator, two check valves are set to separate the inflow and outflow, ensuring unidirectional flows in both heat exchangers. By using the check valve system, the dead volume is reduced to 4% of the
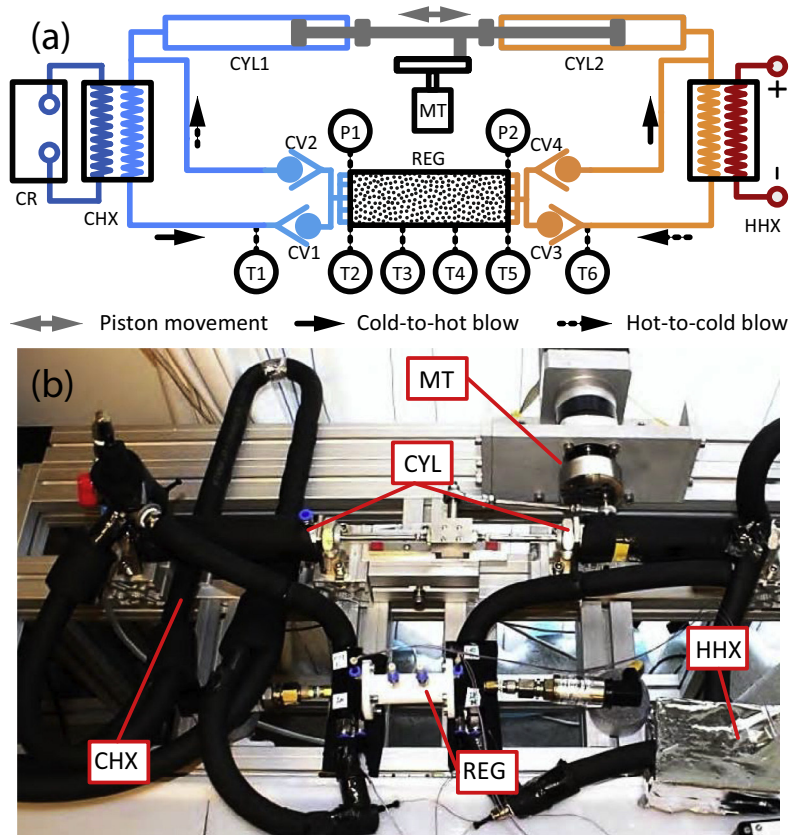
Fig. 1. (a) Schematic diagram and (b) photograph of the passive regenerator test apparatus. The labels represent: CHX cold heat exchanger; CR cold reservoir with circulating pump; CV check valve; CYL cylinder; HHX hot heat exchanger; MT motor and crank; P pressure gauge; REG regenerator; T thermocouple. The solid and dashed arrows show the flow direction during two blows, respectively.

regenerator volume. The dead volume is an empty space where the fluid mixes freely without the contact with the solid, and it causes the irreversible loss. After several cycles, the oscillating flow system will reach a periodic steady state with a stable temperature span for a certain heating power. For each steady state, the temperature profiles along the regenerator, the heating power and the pressure drop are recorded for further analysis. E-type thermocouples, installed as shown in Fig. 1, are calibrated in a water bath before installation. The measurement error is ±0.3 °C and the response time is estimated to be less than 0.15 s, which is the time required to reach 63% of an instantaneous temperature change. The temperature data are recorded by a NI (National Instruments) 9213 thermocouple module and a NI cDAQ 9174 acquisition device. The calibrated pressure gauges at both ends have an accuracy of 0.25% of the full scale and the signal is acquired by a NI 9203 current module. The response time of the pressure gauges is 0.5 ms. The power supply for the heater has meter accuracies of 0.1% in voltage and 0.3% in current. To reduce the heat loss to the ambient, all the components are thermally insulated by foam insulation tubes.

Fig. 2 shows an example of the pressure drop data as a function of time, as well as the piston velocity calculated from the measured piston displacement. The fluid and regenerator temperatures are held about 21 °C during the pressure drop test. Both curves behave similarly to the sinusoidal wave according to the crank design. The piston velocity is approximately $v_p = 0.5 S_p \omega \sin \omega t$ and the mass flow rate is $\dot{m}_f = 0.5 \rho_f A_p S_p \omega \sin \omega t$. A_p and S_p are the cross sectional area and the stroke of the piston; ω is the angular speed; ρ_f is the fluid density. There is a certain phase difference (about 0.1 s) between the piston velocity and the pressure drop over the regenerator. It may be because the measurements with the
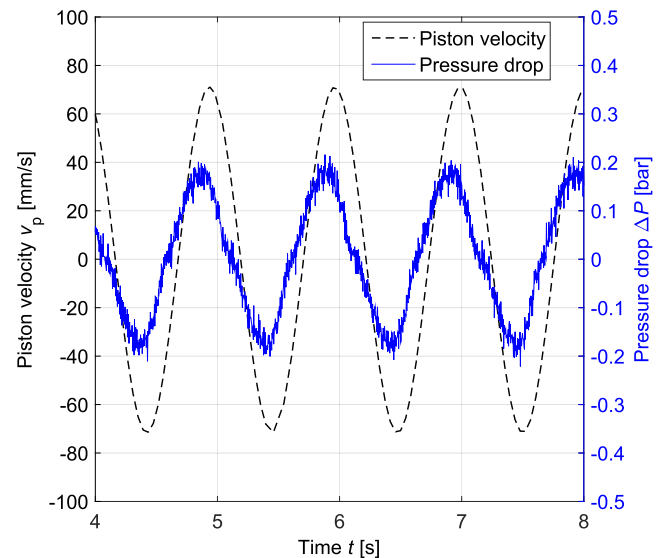
Fig. 2. Example of pressure drop and piston velocity during a typical passive experiment.

encoder and pressure gauges are performed with different acquisition components that were not strictly synchronized. Besides, there are some bubbles taking an estimated volume fraction less than 2% trapped in the system, which can also influence the phase difference. The maximum pressure drop and the maximum

superficial velocity v_s, are used to calculate the friction factor f_F and the Reynolds number Re_h by:

$$v_s = \frac{\dot{m}_f}{\rho_f A_c} \tag{1}$$

$$f_F = \frac{\Delta P}{L} \frac{2D_h}{\rho_f v_s^2} \tag{2}$$

$$Re_h = \frac{\rho_f v_s D_h}{\mu_f} \tag{3}$$

where A_c, D_h, μ_f, and L are the cross sectional area, hydraulic diameter, dynamic viscosity and regenerator length, respectively. Note that Re_h is based on the hydraulic diameter D_h and the superficial velocity v_s. Note that the superficial velocity is based on the cross sectional area, which is different from the real flow velocity in the interval between the particles, so-called interstitial velocity.

Dynamic temperature profiles over the regenerator with an oscillating flow are illustrated in Fig. 3, where T1-T6 represent the positions from the cold to hot end as shown in Fig. 1(a). The temperature information is used to estimate the effectiveness, as mentioned above. Assuming that the specific heat capacity of the fluid is temperature independent and the flows are balanced, the effectiveness η in each blow period is [21]:

$$\eta_c = \frac{2/\tau \int_0^{\tau/2} T_{f,h} dt - T_c}{T_h - T_c} \tag{4}$$

$$\eta_h = \frac{T_h - 2/\tau \int_{\tau/2}^{\tau} T_{f,c} dt}{T_h - T_c} \tag{5}$$

where $T_{f,h}$, $T_{f,c}$, T_h, T_c, and τ are the outflow temperatures at hot and cold ends, the inflow temperatures at both ends and the cycle period. It is assumed that the cold-to-hot blows takes place from $t = 0$ to $\tau/2$. In Fig. 3, T_c, $T_{f,c}$, $T_{f,h}$, and T_h are T1, T2, T5, and T6, respectively. An ideal regenerator with infinite solid mass gives an effectiveness of 1, while real regenerators give η less than 1, as the outflow is always lower than the end (reservoir) temperature.

Another dimensionless index is the utilization ratio U, which is the ratio between the thermal mass of fluid moving through the regenerator to the total thermal mass of the regenerator. In the

gas-saturated regenerator, only the thermal mass of the solid $m_s c_s$ is considered for counting the total thermal mass, that is, $U = 0.5\dot{m}_f c_f \tau/m_s c_s$. Due to the large heat capacity of the aqueous domain, the heat mass of the entrained liquid inside the regenerator is also taken into account. Thus the definition of the utilization ratio is modified to:

$$U = \frac{\rho_f c_f A_p S_p}{m_s c_s + \rho_f V_r \varepsilon c_f} \tag{6}$$

where c_f, c_s, m_s and V_r are the specific heat capacity of the fluid, specific heat capacity of the solid, solid mass and regenerator volume, respectively.

The effectiveness is a function of the utilization ratio and number of transfer units (NTU), that is, $\eta = f(U, \text{NTU})$. NTU describes the ratio of the amount of heat transferred between the solid and the fluid to the thermal mass of the fluid moved:

$$\text{NTU} = \frac{h_f a_s V_r}{\dot{m}_f c_f} \tag{7}$$

where h_f and a_s are the convective heat transfer coefficient and the specific surface area, respectively. In general, high effectiveness is obtained with high NTU and low utilization ratio. High NTU means more heat is transferred and low utilization ratio indicates that less fluid is blown through the regenerator bed. Both effects lead to an outflow temperature closer to the reservoir temperature, resulting in an effectiveness closer to 1. Many studies investigate the effectiveness of a regenerator by either numerical modeling [24] or simplified deduction. In this study, we use a 1 D numerical model to obtain the relation $\eta = f(U, \text{NTU})$. By turning off the magnetocaloric effect and assuming a constant NTU in a 1D AMR model [22,25], the two energy equations of the solid and the fluid in the passive regenerator become:

$$\frac{\partial}{\partial x}\left(k_{stat} A_c \frac{\partial T_s}{\partial x}\right) + \frac{\text{NTU}\dot{m}_f c_f}{L}(T_f - T_s) = A_c(1-\varepsilon)\rho_s c_s \frac{\partial T_s}{\partial t} \tag{8}$$

$$\frac{\partial}{\partial x}\left(k_{disp} A_c \frac{\partial T_f}{\partial x}\right) - \dot{m}_f c_f \frac{\partial T_f}{\partial x} - \frac{\text{NTU}\dot{m}_f c_f}{L}(T_f - T_s) + \left|\frac{\partial P}{\partial x}\frac{\dot{m}_f}{\rho_f}\right|$$
$$= A_c \varepsilon \rho_f c_f \frac{\partial T_f}{\partial t} \tag{9}$$

where T_s, T_f, x, A_c, L, k_{stat}, k_{disp} and $\partial P/\partial x$ are the solid temperature, fluid temperature, axial position, cross sectional area, regenerator length, static thermal conductivity, thermal conductivity due to fluid dispersion, and pressure drop per unit length. Solving the two equations numerically gives the dynamic temperature profiles, which can be used to calculate the effectiveness. With this relation, the overall number of transfer units NTU_o can be back-calculated from the measured effectiveness directly. This index describes the overall heat transfer performance of the regenerator, as the fluid velocity varies in the oscillating flow. Substituting $\text{Nu} = h_f D_h/k_f$ into Eq. (7) gives the overall Nusselt number Nu_o:

$$\text{Nu}_o = \frac{\text{NTU}_o \overline{\dot{m}}_f c_f D_h}{k_f a_s V_r} \tag{10}$$

where k_f is the hydraulic diameter and $\overline{\dot{m}}_f$ is the average mass flow rate.

2.2. Particle characterization and epoxy bonded regenerators

As revealed in the literature, the cooling performance of the bonded AMRs degraded with an increasing amount of epoxy [15], which is due to the decreasing MCM volume and the possible reduction in the overall heat transfer performance. By improving the formulation of the Amerlock epoxy, the mass can be reduced to as little as 1 wt.%, while maintaining the required mechanical
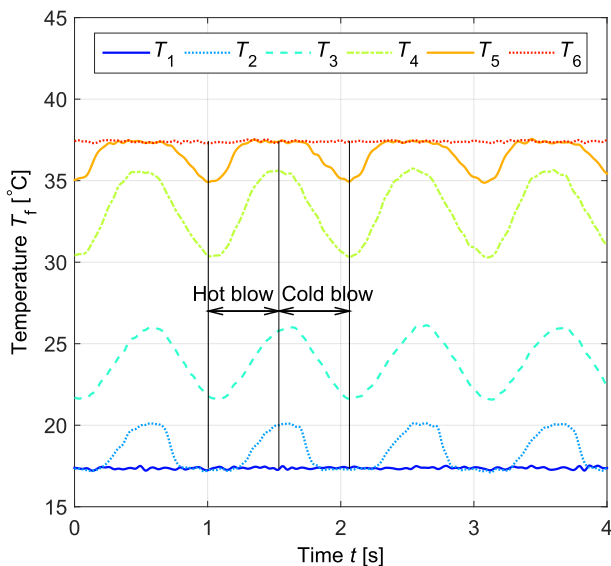
Fig. 3. Example of temperature profiles along a regenerator packed with particles in a passive test.

strength. Therefore, 1 wt.% epoxy is applied in the regenerators for the passive test. For future applications, 1–2 wt.% could be the optimal mass fraction considering the trade-off between the mechanical stability and the cooling performance, as the magnetic field in a real "active" device will challenge the mechanical strength more.

Two groups of La(Fe,Mn,Si)$_{13}$H$_y$ particles, irregular and spherical, as shown in Fig. 4(a) and (b), were bonded with 1 wt.% epoxy in regenerator housings for the passive test. The micrographs of the particles are taken by a Hitachi TM3000 Scanning Electron Microscope (SEM) and the insets show photographs of the regenerators. The two epoxy bonded regenerators were provided by Vacuumschmelze GmbH & Co. KG. Most particles in Fig. 4(a) have a high degree of irregularity. A particle distribution analysis was done using the image analysis software ImageJ and the equivalent diameter was found from the measured area of about 470 and 530 particles, respectively. The size of irregular particles ranges from 0.2 to 1.0 mm. For La(Fe,Mn,Si)$_{13}$H$_y$, only irregular particles have been tested before and there is a lack of investigation on the spherical particles. For the spherical particles in Fig. 4(b), the particle size is about 0.3–0.9 mm and most of the particles are in the diameter range around 0.5–0.8 mm. By fitting the Gaussian distribution, the average particle sizes for both groups are estimated as 0.56 mm with a standard deviation of 0.21 mm and 0.58 mm with a standard deviation of 0.14 mm, respectively. Both materials have Curie temperatures around 20 °C and densities of about 6900 kg/m^3. In the first regenerator VAC-A, about 79 g of La(Fe,Mn,Si)$_{13}$H$_y$ irregular particles with 1 wt.% epoxy is loaded into the 3 D-printed nylon housing, while about 73 g of spherical particles are packed in the second regenerator VAC-B. The housings have a length of 72 mm, an inner diameter of 20 mm, and are printed by the Sinterstation 2500 Plus Selective Laser Sintering (SLS) printer. The housings are further treated with epoxy to be watertight. Due to a low packing density, the regenerators VAC-A and VAC-B have porosities $\varepsilon = 1 - V_s/V_r$ around 0.46 and 0.48, respectively, where V_s is the total solid volume including the MCM and the epoxy. Furthermore,

the specific surface area for each group is estimated by $a_s = \sum A_s/V'_r$, where $\sum A_s$ is the total surface area of about 500 particles and V'_r is the corresponding regenerator volume. Since most of the groups are spherical particles, $\sum A_s$ can be calculated from the profiles and the equivalent diameters mentioned above. Here the specific surface areas are estimated as 4640 and 5030 m^{-1} for the two regenerators respectively, assuming the contacted points between the particles are very small and the epoxy are coated thinly end evenly.

As the baseline experiments, four different SS particles are also tested, which are 0.4–0.5, 0.5–0.7 mm and 0.8–1.0 mm spherical particles, as well as 1.0 mm precise balls. The average particles sizes are about 0.45, 0.6, 0.9 and 1.0 mm, and the standard deviations are estimated to be 0.05, 0.06, 0.05, and <0.01 mm for each group respectively, using probability distribution fitting. The particle sizes of the first three groups are controlled by sieving. In general, the size deviation is much smaller compared to the La(Fe,Mn,Si)$_{13}$H$_y$ particles according to the particle analysis. For these four regenerators, SS particles are loaded randomly into the same housing and stopped by one piece of thin mesh at each end. About 113–116 g SS particles are packed into the regenerators, giving porosities around 0.35–0.37 although the particle size varies. For the packed particle bed, the hydraulic diameter is calculated by:

$$D_{\mathrm{h}} = \frac{2\varepsilon}{3(1-\varepsilon)} D_{\mathrm{p}} \tag{11}$$

where D_{p} is the average particle diameter.

The specific surface area a_s of a porous media can be expressed as [26]:

$$a_{\mathrm{s}} = \frac{4\varepsilon}{D_{\mathrm{h}}} \tag{12}$$

Eq. (12) in return can be used to calculate the hydraulic diameter of a porous medium from the porosity and the specific surface area,
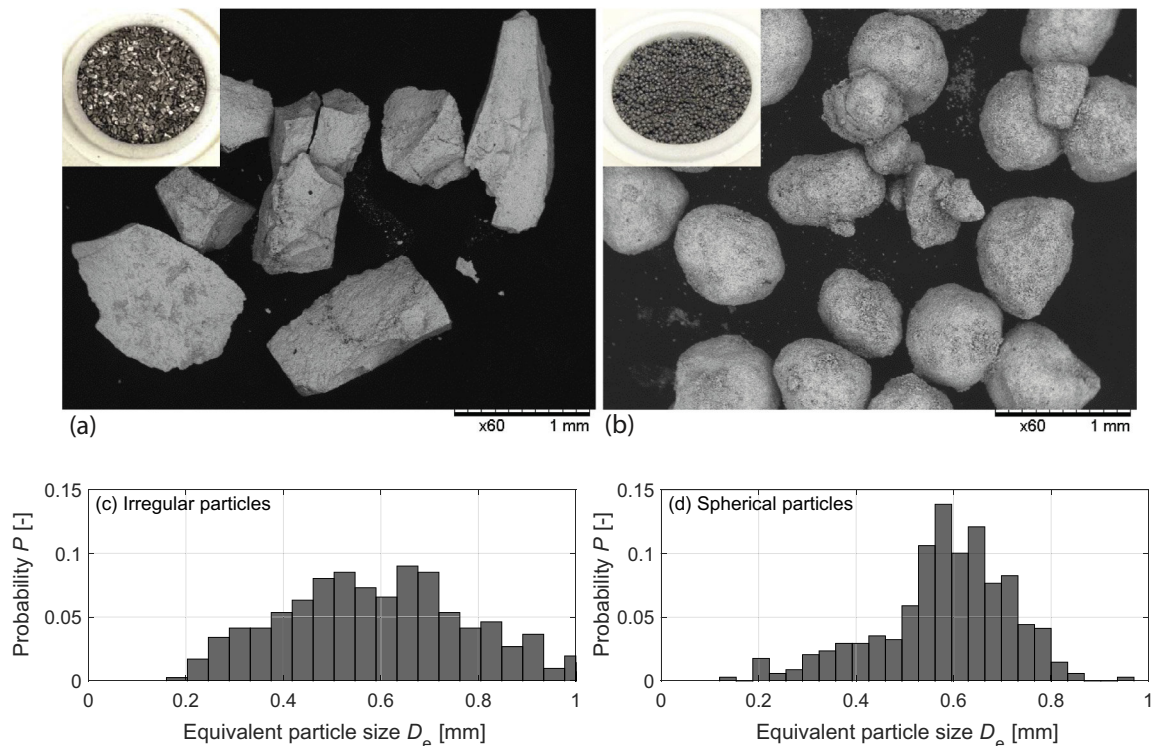

Fig. 4. Photographs and size distribution of the La(Fe,Mn,Si)$_{13}$H$_y$ particles used in the passive regenerators.

which are 0.41 mm and 0.38 mm for VAC-A and VAC-B, respectively.

2.3. Experimental results

In the test, the heat transfer fluid is an aqueous solution with 20 v/v% ethylene glycol (EG). Measured on a viscometer (Anton Paar Lovis 2000 M/ME), the heat transfer fluid has a density of 1031 kg/m^3 and a dynamic viscosity of 1.77 mPa·s. The piston stroke S_p is changed from 10 to 45 mm by adjusting the crank distance and the operating frequency is controlled from 0.5 to 1.25 Hz by increasing the motor rotation speed. The superficial velocity in the regenerator is strongly related to both the stroke and the frequency, while the utilization ratio mainly depends on the stroke according to the definition in Eq. (6). In addition, the temperature span is controlled by applying power to the heater.

2.3.1. Friction factor

Fig. 5 gives the friction factor calculated from the maximum pressure drop data for different regenerators based on Eqs. (2) and (3). During the measurements, the stroke is adjusted from 15 to 40 mm and the frequencies vary from 0.50 to 1.25 Hz with a step of 0.25 Hz. The pressure drop ΔP is velocity dependent, so the measured ΔP increases with both the stroke and the frequency. The results of the friction factors are compared with the Ergun equation [27] for spherical particles and the modified Ergun equation [28] for irregular particles, which are widely used correlations for calculating the pressure drop over packed beds. Fig. 5 shows that the friction factor of the regenerators packed with SS particles fits the Ergun equation quite well, and the average deviation is less than 12%. The friction factor of the epoxy bonded regenerators are also presented and compared with the Ergun equation, which could be extended to the porosity up to 0.46. The comparison shows that the friction factors of the epoxy bonded regenerators are much higher than those predicted by the Ergun equation. Compared to irregular particles, the spherical ones have relatively lower friction factors, which is preferable for reducing the pump loss and the pressure drop. The La(Fe,Mn,Si)$_{13}$H$_y$ particles in VAC-A are highly irregular and the particle size is distributed widely for both epoxy bonded regenerators. Furthermore, the epoxy occupies about 4% of the regenerator volume and it may also
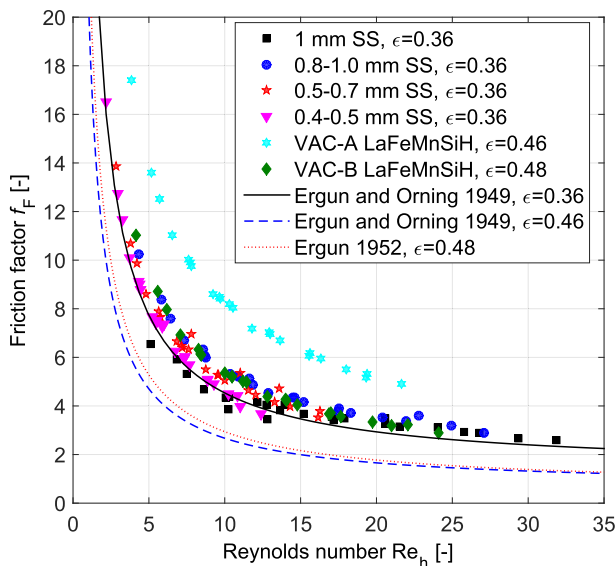
block the channels and decrease the overall channel sizes. These effects may introduce a considerable increase in the friction factors of the two epoxy bonded regenerators.

2.3.2. Heat transfer performance

Based on Eqs. (4)–(6), the effectiveness and utilization ratio for different regenerators are calculated and presented in Fig. 6. The temperature span ranges from 22 to 42 °C and the operating frequency is about 1 Hz. In order to estimate the utilization ratio, the specific heat capacity of the fluid from the commercial software EES (Engineering Equation Solver) [29] is used. For La(Fe, Mn,Si)$_{13}$H$_y$, the temperature dependence of the specific heat capacity c_s (as seen in Ref. [25]) is also considered and the average c_s is about 540 J/(kg K) for a temperature span of 20 °C. In Fig. 6, smaller particles always exhibit higher effectiveness with the same utilization ratio for the packed SS particle beds. This is attributed to the larger specific surface area and the higher overall heat transfer coefficient, and then the higher NTU. A high NTU regenerator is always preferable for the AMR design. However, it requires smaller channel sizes in return, which raises the pressure drop. Thus the trade-off between the flow and heat transfer performance becomes important to the system design. For the two epoxy bonded regenerators, although the regenerator mass is lower, the utilization ratios, U, are still similar to those for the packed SS particle beds. This is because both solid and fluid thermal masses are included in the calculation of U based on Eq. (6). VAC-A packed with irregular particles exhibits slightly higher effectiveness than VAC-B with spherical particles, while presenting significantly higher pressure drop during the test. For the spherical particles, the effectiveness can potentially be improved without increasing the pressure drop much by decreasing the particle size and adjusting the size distribution. Therefore, we present the active test of an AMR using the spherical La(Fe,Mn,Si)$_{13}$H$_y$ particles to demonstrate the material's active performance. In the experiments, the heating power applied on the hot side of the regenerators is inversely proportional to the effectiveness, as it in fact represents the total enthalpy difference at the hot end and the degree to which the outflow temperature is close to T_h.

Fig. 7 gives the relation $\eta = f(U, \text{NTU})$ theoretically based on the 1D numerical model introduced in Section 2.1. Here the packed SS particle beds are simulated. With smaller utilization ratio and higher NTU, the effectiveness increases. By interpolating the
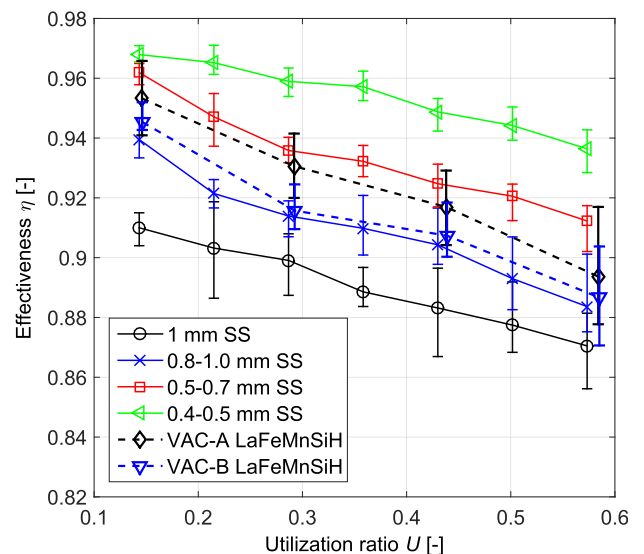

Fig. 5. Friction factor as a function of the Reynolds number for different regenerators compared with the Ergun equation.

Fig. 6. Effectiveness as a function of the utilization ratio for different regenerators.
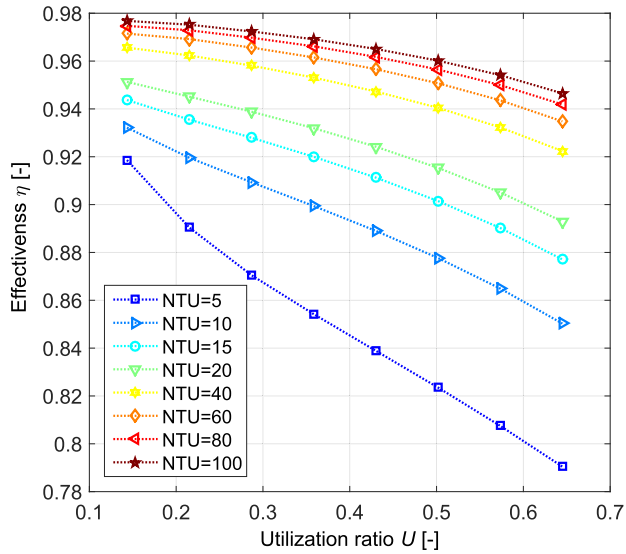
Fig. 7. Simulated effectiveness as a function of NTU and the utilization ratio for regenerators using packed SS particles.

measured effectiveness in Fig. 6, the intermediate index NTU_o can be calculated. For the four regenerators packed with SS particles, average NTU_o are 8.5, 11.5, 21.3 and 41.4 respectively, increasing with smaller particles. Then VAC-A and VAC-B hold average NTU_o of 17.8 and 13.0, within the range for SS particles. Furthermore, the overall Nusselt number Nu_o found from Eq. (10) is calculated and presented in Fig. 8. The same procedure is done in order to obtain Nu_o for the epoxy bonded regenerators. Herein, the average superficial velocity $\bar{v}_s$ is used to calculate the mean Reynolds number $Re_{h,m} = \rho_f \bar{v}_s D_h / \mu_f$. As seen in Fig. 8, Nu_o increases with higher mean Reynolds number for all the regenerators. Higher Nu_o is observed with smaller particles and VAC-A in the two groups of regenerators. The data of Nu_o are also compared to Wakao et al.'s [30] and Engelbrecht's [22] correlations in Fig. 8. Wakao et al. [30] did a comprehensive review and proposed a general correlation extending to the low Reynolds number region. For comparison, the Reynolds number based on the particle dimension is
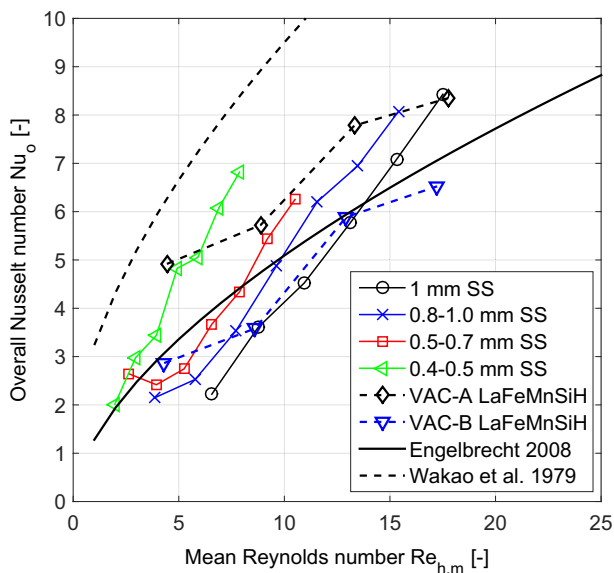
modified to that based on the hydraulic diameter here. Engelbrecht [22] presented the heat transfer correlation for a packed bed by the single blow test, which is $Nu = 0.7 \, Pr^{0.23} \, Re_h^{0.6}$. The plots in Fig. 8 show that the experimental curves in this study follow the trend of both correlations from literature, and the data are closer to the latter. Note that Wakao et al. proposed the correlation based on literature data with $Re_p > 100$, equivalent to $Re_h > 38$, and the correlation was extended to the region with $Re_h < 38$ for comparison here.

3. Active test of epoxy bonded regenerators

3.1. Test apparatus and 1D numerical AMR model

An epoxy bonded regenerator using five layers of La(Fe,Mn, Si)$_{13}$H$_y$ spherical particles was tested actively in a small-scale reciprocating magnetic refrigerator. This test apparatus was developed at the Technical University of Denmark (DTU) for verifying different AMR concepts [31]. As seen in Fig. 9, the whole setup consists of six main components. A Halbach cylinder permanent magnet, which generates an average magnetic flux density around 1.0 T in the magnetized area, is fixed. A heater at the cold end simulates the cooling load and a hot heat exchanger serves to maintain the hot end temperature. To generate a periodically changing applied magnetic field, the whole regenerator is moved reciprocally into and out of the magnetized area of the magnet by the motor with a linear guide. Synchronized with the applied magnetic field, the moving piston generates an oscillating flow through the regenerator with a certain phase difference, which forms a four-step refrigeration cycle as seen in Fig. 10. The cycle period is about 6–8 s, depending on the timing of the different parts of the cycle. Note that it is the magnetic field applied in the middle of the regenerator which is shown in Fig. 10. In fact, the applied magnetic field varies in the perpendicular direction, as the field strength is lower at the edge of the magnetized area than that in the centre. The whole apparatus is installed in a temperature controlled cabinet and the hot heat exchanger is in thermal contact with the air inside. Thus the hot end temperature is controlled by adjusting the cabinet temperature. The temperature span is recorded by E-type thermocouples with a measurement error of ±0.3 °C. The current and the voltage applied to the resistance heater are also measured to calculate the cooling load.

Simulations of this AMR are implemented based on a 1D numerical model developed at DTU [11,25]. The AMR model [22,25] is built up based on Eqs. (8) and (9) by using the empirical
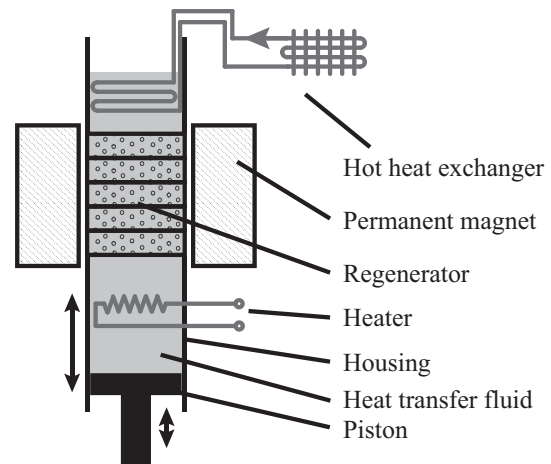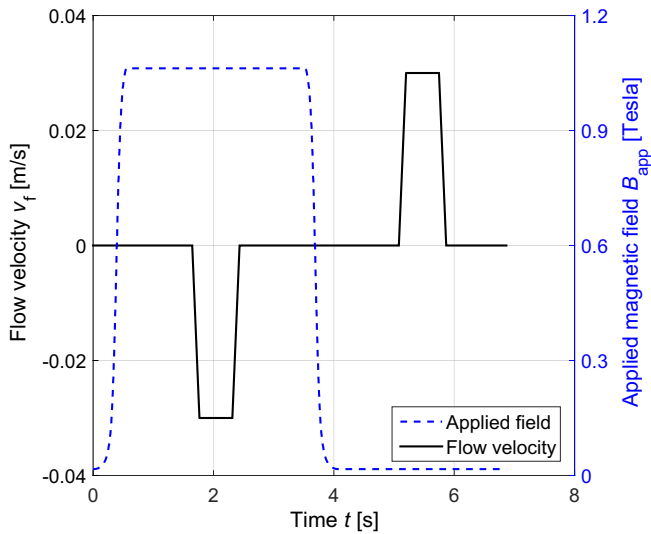

Fig. 8. Overall Nusselt number as a function of the mean Reynolds number for different regenerators.

Fig. 9. Schematic diagram of the small-scale reciprocating magnetic refrigerator.

Fig. 10. Flow and magnetic field profiles of the small-scale reciprocating magnetic refrigerator.

Fig. 11. Impact of the hot end temperature on the no-load temperature span of the epoxy bonded AMR.

correlation of the heat transfer coefficient instead of constant NTU and adding a term representing the magnetocaloric transition. This transient model discretizes and solves these two modified energy equations in order to predict the dynamic temperature profiles along the AMR. After reaching steady state within a numerical tolerance, the performance indices, such as the cooling power and COP, can be calculated from the temperature information in the last cycle. The properties of materials and the operating parameters could be modified according to the active test, making this model flexible to study the AMR performance. Based on an observation that ΔS_{iso} of La(Fe,Mn,Si)$_{13}$H$_y$ with different T_{Curie} are similar for the temperature range studied here, an approach of shifting one group of experimental data according to designed T_{Curie} [25] is used in simulation to determine the magnetocaloric properties of each material. More details of this 1D AMR model are given in Ref. [22,25]. In the simulation, the demagnetization factor is estimated to be about 0.36 according to the method presented in Ref. [32].

3.2. Experimental results and validation using 1D AMR model

In total, about 143 g of material was loaded into the regenerator housing made of a Perspex tube, which has an inner diameter of 32 mm and a length of 40 cm. The dimensions of this 5-layer AMR are not the same as VAC-B due to different connection interfaces in two apparatuses and test purposes. About 2 wt.% epoxy is used inside the AMR, corresponding to an estimated volume fraction of about 8%. The Curie temperature of the materials and their volume fractions are summarized in Table 1. A sample of each material (approximately 10 mg) was characterized on a Lake Shore 7407 Vibrating Sample Magnetometer (VSM). The Curie temperature was defined as the inflection point of the magnetisation, measured in a 10 mT applied field. Note that for first order phase transition materials, the Curie temperatures determined in this way will be lower than those where the peaks of ΔS_{iso} or ΔT_{ad} appear. The average spacing of the Curie temperature is about
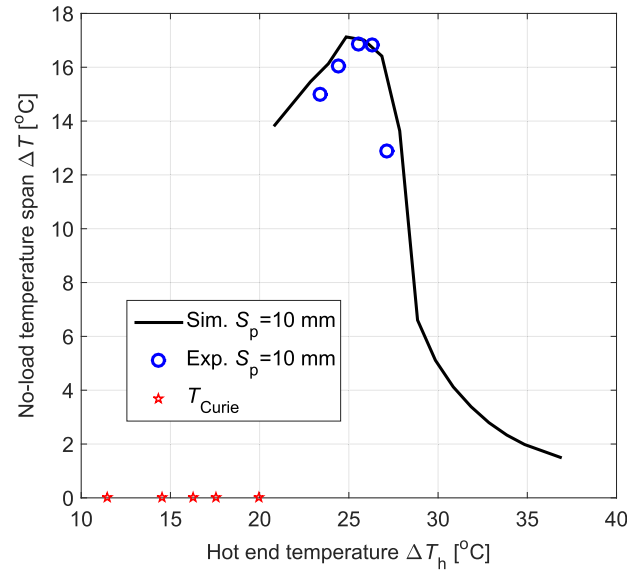
2.0 °C. The heat transfer fluid is 2 v/v% of the commercial anti-corrosion additive ENTEK FNE in an aqueous solution [33]. A low concentration such as 1–2 v/v% has proven sufficient to protect the magnetocaloric materials well in a four-month static corrosion test at DTU. The stroke S_p, the hot end temperature T_h and the cooling load $\dot{Q}_c$ are adjusted to investigate the cooling performance of this five-layer AMR. In both passive and active tests, the epoxy bonded regenerators are quite stable and maintain mechanical integrity well after testing for two months. Due to the first order characteristics of the materials, the specific heat is strongly dependent on the temperature. This makes the utilization always change for different temperature spans. Therefore the piston stroke is presented mainly instead of the utilization. The roughly estimated utilization varies from 0.4 to 0.8 with the piston stroke from 7 to 15 mm.

Fig. 11 presents the no-load temperature span ΔT over the epoxy bonded regenerator as a function of the hot end temperature as well as the simulation results. This 5-layer regenerator achieves a maximum no-load temperature span of 16.8 °C when the hot end temperature is about 25 °C, which is larger than that of 13.5 °C for a two-layer regenerator using similar materials [15]. The span obtained here is also larger than 8.9 °C for Gd and 8.5 °C for 2-layer La(Fe,Co,Si)$_{13}$ tested in the same apparatus [31]. Note there are no check valves to separate the flows in both ends, and the dead volume is larger than that in the passive test setup. The simulation results are slightly higher than the experimental data and fit the trends quite well. Both experiments and simulations show that the no-load temperature span is quite sensitive to the hot end temperature as discussed and analyzed in Ref. [25]. This is attributed to the strong temperature dependence of the magnetocaloric effect and the narrow working temperature region for the FOPT MCMs. The materials in some layers may not be fully "activated" when the working temperature deviates from the best region.

Table 1
Curie temperatures of the materials and volume fraction in each layer.

Layer sequence	1	2	3	4	5
Curie temperature [°C]	11.4	14.5	16.2	17.5	19.9
Volume fraction [%]	12.6	22.4	21.3	22.2	21.5

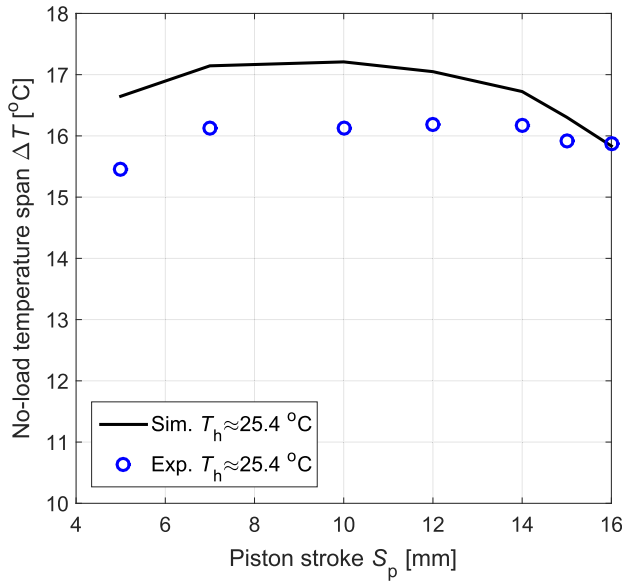**Fig. 12.** Impact of the piston stroke on the no-load temperature span of the epoxy bonded AMR.

Fig. 13. Impact of the working temperature on the cooling load curves of the epoxy bonded AMR.

Fig. 12 shows that the impact of the piston stroke S_p on the no-load temperature span ΔT is quite small in this case. ΔT only slightly increases when S_p < 10 mm and reaches the maximum at a stroke around 7 mm. The average deviation between simulations and experiments is less than 0.8 °C. Simulations also show that no-load temperature spans did not change much in regard to the piston stroke.

Fig. 13 presents the results from applying a cooling load when the piston stroke is 10 mm. The hot end temperature in experiments (black dot line) varies slightly for different points and the average value is around 25.4 °C. The regenerator provides 2.8 W cooling power with $\Delta T = 2$ °C and realizes a no-load temperature span of 16 °C. In addition, a batch of simulations is implemented and presented assuming T_h ranges from 20.8 to 27.8 °C. Similar to the results in Fig. 11, the simulated load curves vary largely even with a small change in T_h. In the low ΔT region with lower T_h, higher $\dot{Q}_c$ is obtained and the slope becomes significantly larger. The experimental data fit the curve with $T_h = 24.8$ °C better, rather than the one with $T_h = 25.4$ °C. The reason may lie in the facts that
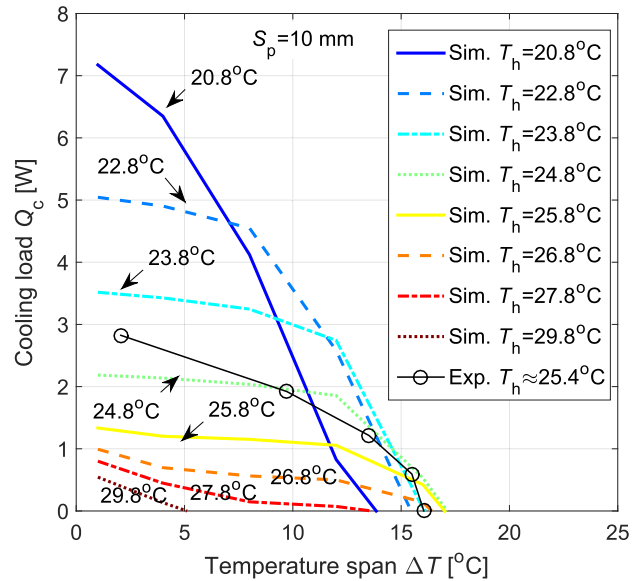
the hot end temperature is fluctuating during each cycle and the real hot end temperature (the reservoir temperature in simulations) is lower than the measured average value.

More cooling load curves are presented in Fig. 14(a) and (b). In Fig. 14(a), the maximum temperature span is about 16 °C for different piston strokes, and the temperature span decreases when more cooling load is applied. Compared to experimental results, the simulations deviates from the cooling load but still reflect the trends. As discussed previously, the load curve is so sensitive to T_h that any small change in hot end temperature would lead to a considerable change in the device performance, which could be the reason of the deviation. Compared with Fig. 14(a), the experiments in Fig. 14(b) are run with lower T_h, realizing higher $\dot{Q}_c$ at the small ΔT region but smaller no-load temperature span around 13.6 °C. This effect is also reflected in the simulations, reading the curves with $T_h = 23.8$ and 25.8 °C shown in Fig. 13. The overall absolute deviations between simulations and experiments in Fig. 14(a) and (b) are about 0.42 and 0.74 W respectively. The small regenerator achieves a considerable cooling power of 5.7 W at $\Delta T = 9.5$ °C with $S_p = 14$ mm, as a typical working point.
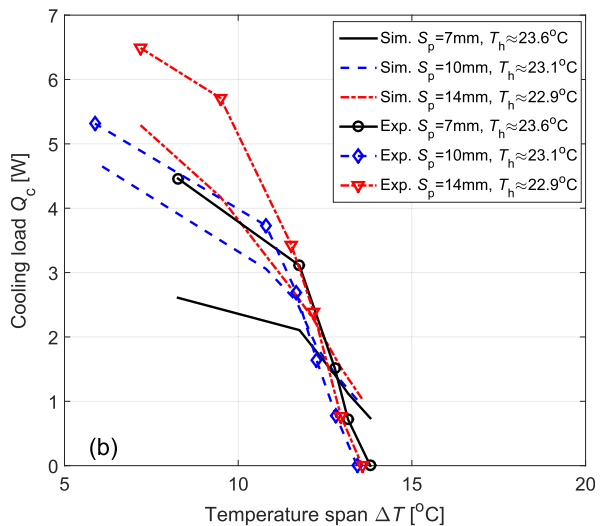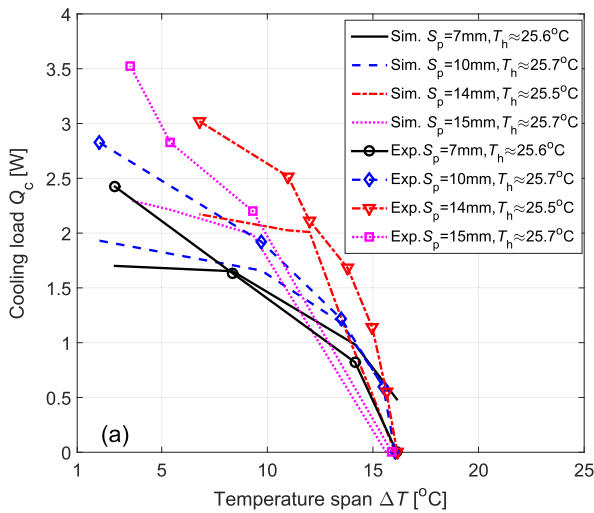

Fig. 14. Cooling load as a function of the temperature span of the epoxy bonded AMR.

4. Conclusions

The passive characterization and active testing of epoxy-bonded regenerators are presented in this study. The epoxy-bonding technique serves to increase the mechanical strength of regenerators using brittle materials and to build monolithic regenerators. The particle size analysis showed that the La(Fe,Mn,Si)$_{13}$H$_y$ particles in the first group were quite irregular and had a broader distribution in the particle size compared to the second group of spherical particles. Two epoxy bonded regenerators based on these particles and four reference packed beds loaded with SS particles were tested passively. The friction factors of the SS packed beds fit the classic Ergun equation quite well, while the epoxy bonded regenerator showed a significantly higher f_F than the prediction, especially for the irregular particles. This was due to the high irregularity, the broad distribution in the particle size and the introduction of epoxy. Moreover, the results show that the regenerator loaded with smaller SS particles always yields a higher effectiveness. The epoxy bonded regenerator with the irregular particles exhibited slightly higher effectiveness than that with spherical particles, while the pressure drop over the former was higher. New spherical particles with a smaller diameter of 0.2–0.3 mm could be interesting for future studies and applications, which has also been investigated theoretically [18]. In addition, the overall Nusselt number of both groups of regenerators fit the trends of Wakao et al.'s and Engelbrecht's correlations and the results in this study fit the latter better. It is noted that the epoxy bonded regenerators show good stability and no failure is observed in a 2-month discontinuous test. Only tiny dusts escape from the regenerator and they are stopped by the screen meshes at each end of the regenerator.

A five-layer epoxy bonded AMR using spherical La(Fe,Mn,Si)$_{13}$H$_y$ particles was also tested actively in a small reciprocating magnetic refrigerator. This regenerator realized a maximum no-load temperature span up to 16.8 °C and provided 5.7 W of cooling power at a temperature span of 9.5 °C, showing the spherical particles realize a good performance. In addition, the experimental results verify that the AMR using MCMs with a first order phase transition is quite sensitive to the working temperature [25]. To realize the full potential of a layered AMR, all the layers should be activated properly by adjusting the temperature distribution along the regenerator. The 1D numerical model was validated with the experiments, showing the simulations can predict the trends of the AMR performance well.

Acknowledgements

References

[1] A. Kitanovski, J. Tušek, U. Tomc, U. Plaznik, M. Ožbolt, A. Poredoš, Magnetocaloric Energy Conversion, Springer, 2015, http://dx.doi.org/10.1007/978-3-319-08741-2.

[2] K. Engelbrecht, D. Eriksen, C.R.H. Bahl, R. Bjørk, J. Geyti, J.A. Lozano, K.K. Nielsen, F. Saxild, A. Smith, N. Pryds, Experimental results for a novel rotary active magnetic regenerator, Int. J. Refrig. 35 (6) (2012) 1498–1505, http://dx.doi.org/10.1016/j.ijrefrig.2012.05.003.

[3] S. Jacobs, J. Auringer, A. Boeder, J. Chell, L. Komorowski, J. Leonard, S. Russek, C. Zimm, The performance of a large-scale rotary magnetic refrigerator, Int. J. Refrig. 37 (2014) 84–91, http://dx.doi.org/10.1016/j.ijrefrig.2013.09.025.

[4] D. Eriksen, K. Engelbrecht, C.R.H. Bahl, R. Bjørk, K.K. Nielsen, A.R. Insinga, N. Pryds, Design and experimental tests of a rotary active magnetic regenerator prototype, Int. J. Refrig. 58 (2015) 14–21, http://dx.doi.org/10.1016/j.ijrefrig.2015.05.004.

[5] J.A. Barclay, S. Sarangi, Selection of regenerator geometry for magnetic refrigerator applications, Technical report, Los Alamos National Laboratory U.S., 1984.

[6] A. Rowe, Thermodynamics of active magnetic regenerators: Part I, Cryogenics 52 (2012) 111–118, http://dx.doi.org/10.1016/j.cryogenics.2011.09.005.

[7] A. Fujita, S. Fujieda, Y. Hasegawa, K. Fukamichi, Itinerant-electron metamagnetic transition and large magnetocaloric effects in La(Fe$_x$Si$_{1-x}$)$_{13}$ compounds and their hydrides, Phys. Rev. B 67 (2003) 104416, http://dx.doi.org/10.1103/PhysRevB.67.104416.

[8] J. Tušek, A. Kitanovski, U. Tomc, C. Favero, Experimental comparison of multilayered La-Fe-Co-Si and single-layered Gd active magnetic regenerators for use in a room temperature magnetic refrigerator, Int. J. Refrig. 37 (2014) 117–126, http://dx.doi.org/10.1016/j.ijrefrig.2013.09.003.

[9] A. Barcza, M. Katter, V. Zellmann, S. Russek, S. Jacobs, C. Zimm, Stability and magnetocaloric properties of sintered La(Fe, Mn, Si)H alloys, IEEE Trans. Magn. 47 (2011) 3391–3394, http://dx.doi.org/10.1109/TMAG.2011.2147774.

[10] V. Basso, M. Küpferling, C. Curcio, C. Bennati, A. Barzca, M. Katter, M. Bratko, E. Lovell, J. Turcaud, L.F. Cohen, Specific heat and entropy change at the first order phase transition of La(Fe-Mn-Si)$_{13}$-H compounds, J. Appl. Phys. 118 (2015) 053907, http://dx.doi.org/10.1063/1.4928086.

[11] T. Lei, K. Engelbrecht, K.K. Nielsen, H. Neves Bez, C.R.H. Bahl, Study of multi-layer active magnetic regenerators using magnetocaloric materials with a first and second order phase transition, J. Phys. D: Appl. Phys. 49 (2016) 345001, http://dx.doi.org/10.1088/0022-3727/49/34/345001.

[12] J. Liu, J.D. Moore, K.P. Skokov, M. Krautz, K. Löwe, A. Barcza, M. Katter, O. Gutfleisch, Exploring La(Fe, Si)$_{13}$-based magnetic refrigerants towards application, Scr. Mater. 67 (2012) 584–589, http://dx.doi.org/10.1016/j.scriptamat.2012.05.039.

[13] S. Fujieda, A. Fujita, K. Fukamichi, Y. Yamazaki, Y. Iijima, Giant isotropic magnetostriction of itinerant-electron metamagnetic La(Fe$_{0.88}$Si$_{0.12}$)$_{13}$H$_y$ compounds, Appl. Phys. Lett. 79 (5) (2001) 653, http://dx.doi.org/10.1063/1.1388157.

[14] B. Pulko, J. Tušek, J.D. Moore, B. Weise, K. Skokov, Epoxy-bonded La–Fe–Co–Si magnetocaloric plates, J. Magn. Magn. Mater. 375 (2015) 65–73, http://dx.doi.org/10.1016/j.jmmm.2014.08.074.

[15] H. Neves Bez, K. Navickaité, T. Lei, K. Engelbrecht, A. Barcza, C.R.H. Bahl, Epoxy bonded La(Fe,Mn,Si)$_{13}$H$_z$ as a multi-layered active magnetic regenerator, in: Proceedings of the 7th IIF-IIR International Conference on Magnetic Refrigeration at Room Temperature, 2016.

[16] M.A. Richard, A.M. Rowe, R. Chahine, Magnetic refrigeration: single and multimaterial active magnetic regenerator experiments, J. Appl. Phys. 95 (4) (2004) 2146–2150, http://dx.doi.org/10.1063/1.1643200.

[17] M. Krautz, A. Funk, K.P. Skokov, T. Gottschall, J. Eckert, A new type of La(Fe, Si)$_{13}$-based magnetocaloric composite with amorphous metallic matrix, Scr. Mater. 95 (2015) 50–53, http://dx.doi.org/10.1016/j.scriptamat.2014.10.002.

[18] T. Lei, K. Engelbrecht, K.K. Nielsen, C.T. Veje, Study of geometries of active magnetic regenerators for room temperature magnetocaloric refrigeration, Appl. Therm. Eng. 111 (2017) 1232–1243, http://dx.doi.org/10.1016/j.applthermaleng.2015.11.113.

[19] T.E.W. Schumann, Heat transfer: a liquid flowing through a porous prism, J. Franklin Inst. 208 (3) (1929) 405–416, http://dx.doi.org/10.1016/S0016-0032(29)91186-8.

[20] S. Schopfer, Experimental and Numerical Determination of Thermohydraulic Properties of Regenerators Subjected to Oscillating Flow, Ph.D. thesis, University of Victoria, 2011.

[21] P. Trevizoli, Y. Liu, A. Tura, A. Rowe, J. Barbosa, Experimental assessment of the thermal-hydraulic performance of packed-sphere oscillating-flow regenerators using water, Exp. Therm. Fluid Sci. 57 (2014) 324–334, http://dx.doi.org/10.1016/j.expthermflusci.2014.06.001.

[22] K. Engelbrecht, A Numerical Model of an Active Magnetic Regenerator Refrigerator with Experimental Validation, Ph.D. Thesis, University of Wisconsin-Madison, 2008.

[23] M. Frischmann, K. Engelbrecht, G. Nellis, S. Klein. Heat transfer coefficient in a packed sphere regenerator for use in active magnetic regenerative refrigeration, in: Proceedings of the 2008 International Refrigeration and Air Conditioning Conference, 2008.

[24] B.S. Baclic, G.D. Dragutinovic, Operation of Counterflow Regenerators, WIT Press, 1998.

[25] T. Lei, K.K. Nielsen, K. Engelbrecht, C.R.H. Bahl, H. Neves Bez, C.T. Veje, Sensitivity study of multi-layer active magnetic regenerators using first order magnetocaloric material La(Fe, Mn, Si)$_{13}$H$_y$, J. Appl. Phys. 118 (2015) 014903, http://dx.doi.org/10.1063/1.4923356.

[26] C. Shin, Tortuosity correction of Kozeny's hydraulic diameter of a porous medium, Phys. Fluids 29 (2017) 023104, http://dx.doi.org/10.1063/1.4976550.

[27] S. Ergun, A.A. Orning, Fluid flow through randomly packed columns and fluidized beds, Ind. Eng. Chem. 41 (6) (1949) 1179–1184, http://dx.doi.org/10.1021/ie50474a011.

[28] S. Ergun, Fluid flow through packed columns, Chem. Eng. Prog. 48 (2) (1952) 89–94.

[29] EES, Engineering equation solver, Technical report, F-Chart Software LLC, 2016.

[30] N. Wakao, S. Kaguei, T. Funazkri, Effect of fluid dispersion coefficients on particle to fluid heat transfer coefficients in packed beds: correlation of Nusselt numbers, Chem. Eng. Sci. 34 (3) (1979) 325–336, http://dx.doi.org/10.1016/0009-2509(79)85064-2.

[31] K. Engelbrecht, C.R.H. Bahl, K.K. Nielsen, Experimental results for a magnetic refrigerator using three different types of magnetocaloric material regenerators, Int. J. Refrig. 34 (4) (2011) 1132–1140, http://dx.doi.org/10.1016/j.ijrefrig.2010.11.014.

[32] R.I. Joseph, Ballistic demagnetizing factor in uniformly magnetized cylinders, J. Appl. Phys. 37 (1966) 4639, http://dx.doi.org/10.1063/1.1708110.

[33] D. Velazquez, M. Castro, nd E. Palacios, Practical properties of LaFeCoSi materials to be used in magnetic cooling regenerators, in: Proceedings of 6th IIF-IIR International Conference on Magnetic Refrigeration at Room Temperature, 2014.

P.5. Operational test of bonded magnetocaloric plates

Operational test of bonded magnetocaloric plates

Christian R.H. Bahl [a,*], *Kristina Navickaitė* [a], *Henrique Neves Bez* [a],
Tian Lei [a], *Kurt Engelbrecht* [a], *Rasmus Bjørk* [a], *Ke Li* [b], *Zhenxing Li* [b],
Jun Shen [b], *Wei Dai* [b], *Jichen Jia* [c], *Yuanyuan Wu* [c], *Yi Long* [c],
Fengxia Hu [d], *Baogen Shen* [d]

[a] *Department of Energy Conversion and Storage, Technical University of Denmark, Frederiksborgvej 399, Roskilde DK-4000, Denmark*
[b] *Technical Institute of Physics and Chemistry, Chinese Academy of Sciences, Beijing 100190, China*
[c] *University of Science and Technology Beijing, Beijing 100083, China*
[d] *Institute of Physics, Chinese Academy of Sciences, Beijing 100190, China*

ARTICLE INFO

ABSTRACT

Bonded plates made by hot pressing $La_{0.85}Ce_{0.15}Fe_{11.25}Mn_{0.25}Si_{1.5}H_y$ particles and resin have been tested as active magnetic regenerators in a small scale magnetocaloric device. Firstly, the plates were carefully characterised magnetically and thermally. The plates were prepared with 5 wt% resin, and from density measurements it was found that the volume ratio of the magnetocaloric material in the plates was 0.53, due to the resin and porosity. The best operating conditions for the plate regenerator were determined at which a temperature span of 6.4 K was measured along the plates.

© 2017 Elsevier Ltd and IIR. All rights reserved.

Test opérationnel de plaques magnétocaloriques liées

1. Introduction

For the past decade significant progress has been made in bringing magnetic refrigeration towards commercialisation. New magnetocaloric materials have been developed and magnetocaloric demonstration devices become ever more powerful and efficient (Kitanovski et al., 2015). Most of these devices have employed the so called active magnetic regenerator (AMR) cycle as a method of utilising the magnetocaloric effect in a device. Here the temperature of a porous regenerator structure is increased and decreased by applying and removing a

---

magnetic field, while a heat transfer fluid is reciprocated back and forth in order to build up a temperature gradient. Keys to utilising the AMR concept are firstly to have a magnetocaloric material, or a cascade of such, with high magnetocaloric effect, and secondly, to shape this material in a way that there is good thermal contact between solid and fluid, allowing an effective heat transfer as, e.g., discussed in Ferreira et al. (2014).

Many magnetocaloric materials have been studied and considered for application in devices (Smith et al., 2012). Recently a lot of research has been done on materials that undergo a first order magnetic phase transition, so-called first order materials, as they have a very high magnetic entropy change ΔS_M around the phase transition. An important example of this class of materials is the intermetallic $La(Fe,Si)_{13}H_y$, which has been studied with a number of different elements doped into the Fe and Si sites (Zhang et al., 2013). In general this material series has a high magnetocaloric effect, a tunable Curie temperature and only a small amount of undesirable thermal hysteresis. The disadvantage of these materials is the lack of structural stability due to the volume change at the phase transition (Lyubina et al., 2010).

Recently, different strategies for shaping these and similar magnetocaloric materials into the desired shapes have been proposed and tested. Polymer bonding and pressing to plates has been demonstrated for first order materials (Radulov et al., 2015; Skokov et al., 2014) and second order materials of the same type (Pulko et al., 2015). Other methods of producing structures have also been presented, such as injection moulding (Lanzarini et al., 2015), hot pressing with Cu (Liu et al., 2015) and extrusion into monoliths (Pryds et al., 2011). Actual AMR performance in a test device has only been reported for the second order bonded plates (Pulko et al., 2015). However, porous particle based regenerators where the particles are bonded for stability have been presented, most notably by Jacobs et al. (2014) using $La(Fe,Si)_{13}H_y$.

Here we demonstrate in a small versatile AMR device the performance of plates of first order materials bonded with resin and cured during pressing.

2.   Experimental

A $La_{0.85}Ce_{0.15}Fe_{11.25}Mn_{0.25}Si_{1.5}$ ingot was prepared in an induction furnace. The purity of the raw materials was at least 99.9 wt%. The annealed ingots were crushed into particles less than 0.35 mm in size for the hydrogenation process. These were annealed in a high purity hydrogen atmosphere until saturation. The structure of the hydrides was confirmed by x-ray powder diffraction. The hydrogen concentration y of $La_{0.85}Ce_{0.15}Fe_{11.25}Mn_{0.25}Si_{1.5}H_y$ (referred to as LaFeSiH in the following) was estimated to be 0.2 wt% by the inert gas pulse infrared absorption method. When vacuum annealing under 350 °C for 2 hours a sharp decrease of the Curie temperature was observed due to the escape of H.

2.1.   Processing the plates

The resulting powder was mixed with a phenolic resin system in a mass ratio of 20:1. The mixed powders were pressed into plate shape under pressure of 20 MPa and then solidified at 150 °C for 10 minutes, as shown in Fig. 1. The plates were prepared in the size 25 mm by 40 mm, in order to fit into the regenerator test device, with a thickness of 0.5 mm. Measuring the specific heat shows that the Curie temperature does not change during the resin curing process, indicating that the LaFeSiH is unaffected by this treatment.

2.2.   Characterisation of the plates

Thermal conductivity was measured at 300 K using a Thermal Transport Option (TTO) on a Quantum Design physical property measurement system (PPMS). The density of the plates was measured using an AccuPyc 1340 helium pycnometer repeating each measurement 10 times, and the density of the resin was measured with a Pentapyc5200e Auto Density Analyzer. The magnetic properties were analysed in a LakeShore 7407 vibrating sample magnetometer (VSM). The sample was measured in the temperature range 270 K–306 K at applied fields up to 1.5 T. The specific heat of the sample was measured using a custom built differential scanning calorimeter (DSC), allowing the applied field to be varied in the range 0–1.5 T at a fixed orientation relative to the sample (Jeppesen et al., 2008). A scanning electron microscope (SEM), Hitachi TM3000, equipped with a Bruker Quantax Energy-dispersive X-ray spectroscopy detector (EDS) was used to analyse the microstructure of a piece of one of the plates.
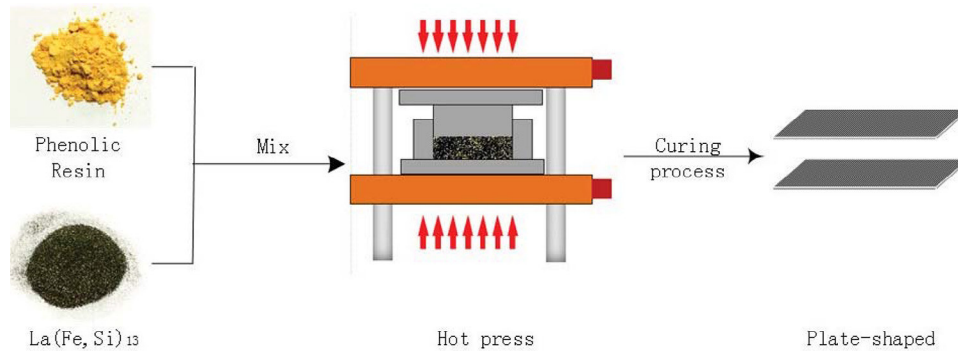
Fig. 1 – Illustration of the fabrication process, showing the mixing of powder with resin, hot pressing and the final plates.

3. Results

3.1. *Physical properties of the plates*

Fig. 2 shows the structure of a plate. It consists of irregular particles of LaFeSiH with a broad size range. There is a significant porosity between the particles. Using EDS mapping we can probe the presence of the resin by isolating the carbon signal, as this will be unique to the resin. As shown in Fig. 3 the resin covers large areas binding together the particles, but there are still significant volumes of porosity between particles. So the system can be considered to consist of three distinct volumes, LaFeSiH, resin and pores.

An average density value of 5721 kg m^{-3} was measured based on pieces of plates weighing in total 2.3947 g. The mass fraction of magnetocaloric material is 0.95 and the mass fraction of resin is 0.05. Based on the structural symmetry and lattice parameters the density of the LaFeSiH, ρ_{LaFeSiH}, is 7207 kg m^{-3} and the density of the resin, ρ_{resin}, is 1166 kg m^{-3} found by crushing down a sample of pure resin into a powder and measuring the density. Assuming that there are no pores closed to helium penetration, the weighted average density of the LaFeSiH and the resin is 5724 kg m^{-3}, very close to the measured value.
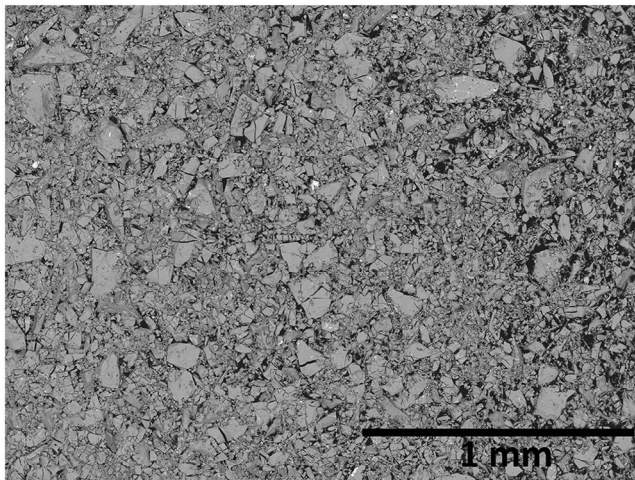
Geometrically measuring and weighing a plate gave a density of approximately 4000 kg m^{-3}, which includes all pores. From this we can calculate the porosity of the plates as 0.30. Thus the volume fractions of LaFeSiH, resin and pores are approximately 0.53, 0.17 and 0.30, respectively.

Based on the mass fractions of LaFeSiH and resin the reduction in effective adiabatic temperature change due to the presence of resin is quite limited. The actual temperature change $\Delta T_{\text{effective}}$ will be given by:

$$\Delta T_{\text{effective}} = \frac{\Delta T_{\text{ad}} c_{\text{H,MCM}}}{0.95 c_{\text{H,MCM}} + 0.05 c_{\text{H,resin}}} \approx 0.94 \Delta T_{\text{ad}}, \tag{1}$$

where $c_{\text{H,MCM}}$ and $c_{\text{H,resin}}$ are the specific heats of LaFeSiH (500 J kg^{-1} K^{-1}) and resin (1200 J kg^{-1} K^{-1}), respectively. As the peak of specific heat in LaFeSiH is very narrow and field dependent we use the background value away from the peak. Closer to the peak $\Delta T_{\text{effective}}$ will be even closer to ΔT_{ad}.

Magnetisation measurements were used to calculate the magnetic entropy change, ΔS_M, in the conventional way described by Pecharsky and Gschneidner (1999b). A piece of one of the plates was used with a mass of 11.76 mg and approximate dimensions 2.8 mm × 1.75 mm × 0.6 mm, keeping the field along the longest direction. This piece seemed free of resin,

Fig. 2 – Backscattered SEM image of an area of a plate. The image shows the surface of the plate as prepared.
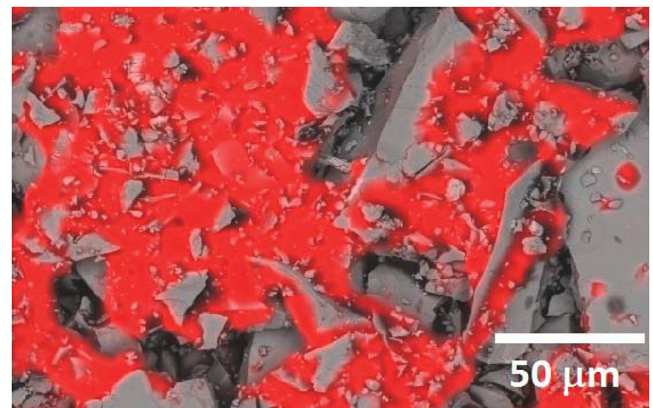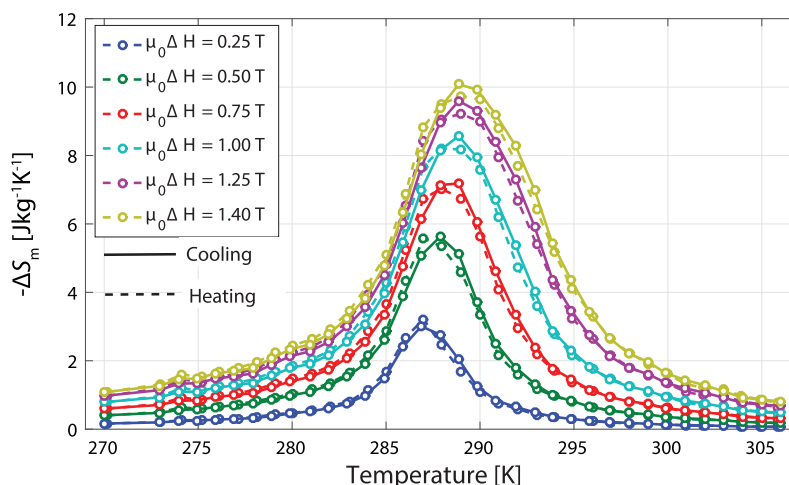

Fig. 3 – EDS filtered to show carbon. The resin is observed to bind together the particles, but there is also a significant porosity (the darker areas) remaining as discussed in the text.

Fig. 4 – Measured entropy change of a sample of one of the plates. Both the heating and cooling curves are shown, and the hysteresis is observed to be small. The legend indicates the internal field values.

but there may be a little resin included. As the data are mass normalised any small amount of resin would only slightly change the level reached by the peak, but not the profile shape. The data were corrected for demagnetisation approximating the slightly irregular sample to a prism and using the expression by Aharoni (1998).

To probe for the presence of hysteresis the magnetic entropy was measured both during cooling and during heating. Between each measurement the sample was "reset" at an equilibrium temperature far above or below the measurement range, for cooling and heating, respectively (Caron et al., 2009). The ΔS_M values are consistent with those found in literature (Zhang et al., 2013). Fig. 4 shows that the hysteresis at the phase transition is very low. In order to further probe the presence of hysteresis the specific heat of the sample was measured during heating and cooling at different temperature ramp rates in the range 1 K min^{-1} to 5 K min^{-1}. By applying a linear regression of the peak temperatures with respect to the temperature rates, the hysteresis is found to be 0.4 ± 0.2 K, consistent with the magnetisation data, as shown in Fig. 5.

When applying a magnetic field the temperature of the peak of the specific heat increases at a rate of about 4.3 K T^{-1}. Also, the peak goes from being very sharp to becoming more broad, as shown in Fig. 6, which was measured at a rate of 1 K min^{-1}. This is consistent with the results reported by Basso et al. (2015). Due to the very low value of the hysteresis and the errors on the lines fitted to the peak temperatures, determining the critical field at which the hysteresis vanishes cannot be done with confidence.

3.2. Regenerator testing

A stack of 25 plates was tested as an AMR in a small scale test device at the Technical University of Denmark. The stack was prepared as described in Engelbrecht et al. (2011) by layering the plates with ø0.25 mm metal wire as spacers. The sides were then sealed with epoxy before removing the metal wire. This resulted in a 20.5 mm tall stack, 25 mm wide and 40 mm long, which was then mounted in a cylindrical regenerator housing

using silicone around the border of the stack. The mass of each plate was approximately 2 g, so the mass of the regenerator was 50 g.

The glued stack, before being mounted in the regenerator housing, is shown in Fig. 7. The channels between the plates are clearly seen, but close inspection reveals that with the chosen plate spacing the unevenness of the plates becomes significant. Thus the actual channel height varies significantly across the regenerator. The effect of this will be discussed later.
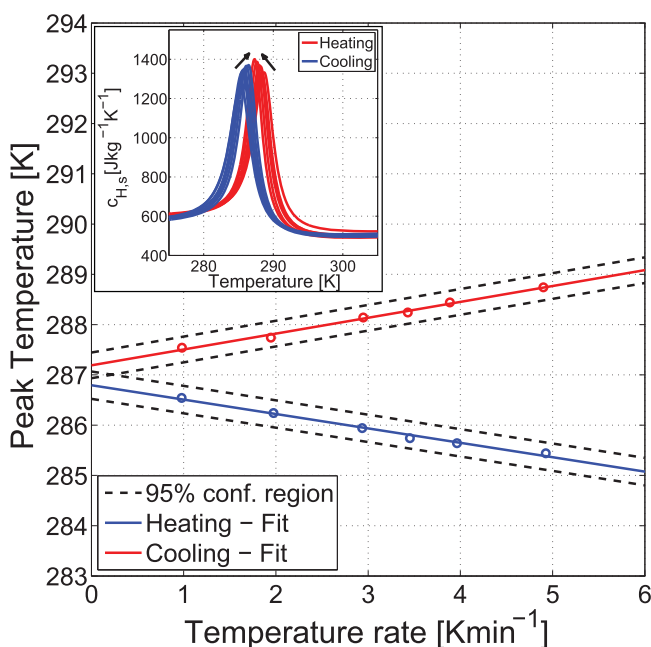

Fig. 5 – The peak temperature of the specific heat measured at different ramp rates in the DSC. Both the heating peak and the cooling peak have been measured, as shown in the inset. Extrapolating to zero ramp rate gives a measure of the hysteresis.
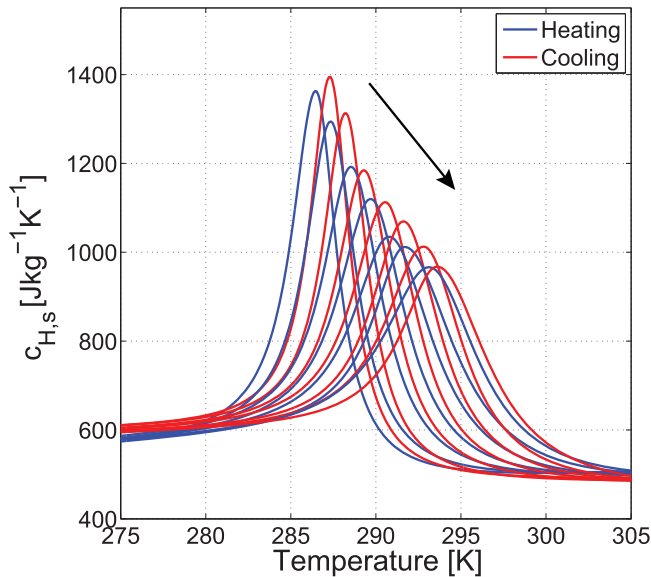
Fig. 6 – Field dependence of the peak in specific heat, for cooling and heating. Applied fields of 0, 0.25, 0.50, 0.75, 1.00, 1.25 and 1.50 T are shown, with the peak moving up in temperature and broadening as the field increases. The arrow indicates the direction of increasing field.

Testing of the regenerator was done in the versatile test device described previously (Bahl et al., 2008; Engelbrecht et al., 2011). Here the cylindrical regenerator housing moves in and out of the bore of a 1.1 T permanent magnet Halbach cylinder. A ø18 mm reciprocating piston forces the heat transfer fluid through the regenerator to perform the well known four steps of the AMR cycle (Pecharsky and Gschneidner, 1999a). Demineralised water, mixed with 2 vol% of ENTEK FNE corrosion inhibitor, as recommended for a similar material by Velazquez et al. (2014), was used as the heat transfer fluid.

Three parameters were varied in the testing of the regenerator, the fluid velocity, the length the piston is moved, and the ambient temperature. A heat exchanger at the hot end of the regenerator keeps the temperature of this close to that of the temperature controlled cabinet, in which the device is mounted. The length the piston moves is conventionally expressed as the utilisation, ϕ, defined as (Bahl et al., 2012)
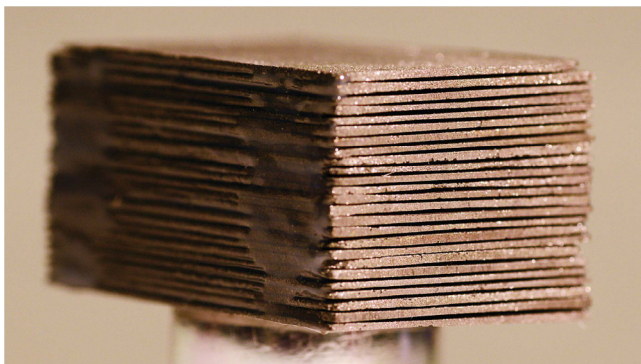
Fig. 7 – The stack of plates used in the regenerator before being mounted in the cylindrical regenerator housing.
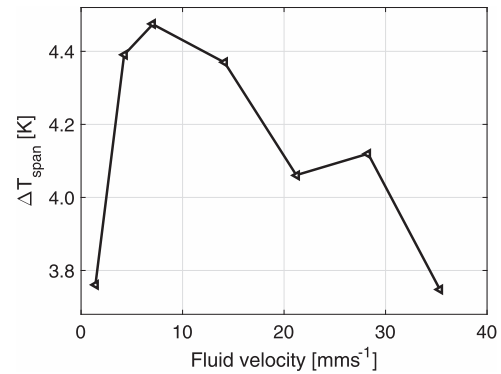
Fig. 8 – The steady state temperature span between the hot and the cold end as a function of the velocity of the fluid being pushed between the plates. The data are obtained at an ambient temperature of 290 K and a utilisation of 0.23.

$$\phi = \frac{m_f c_f}{m_s c_{H,s}} \qquad (2)$$

where m_f is the mass of the fluid pushed through the regenerator in one blow, c_f is the specific heat of the fluid, m_s is the mass of the solid regenerator and $c_{H,s}$ is the specific heat of the bonded plates. m_f is found from the movement of the ø18 mm piston, c_f is set as the textbook value of 4200 J kg^{-1} K^{-1}, ignoring the small amount of corrosion inhibitor, m_s is 50 g and for $c_{H,s}$ the background value of 600 J kg^{-1} K^{-1} is used, as found from Fig. 6, including the resin.

Starting at an ambient temperature of 290 K and a utilisation of 0.23, the AMR cycle was repeated until the temperature difference between the cold end and the hot end, known as the temperature span, ΔT_{span}, reached a constant value. Different values of the fluid velocity were tested recording the achieved ΔT_{span}, as shown in Fig. 8. Note that the fluid velocity reported is the average velocity in the channels based on the movement of the piston and cross-sections of the channels and tube. It is observed that the highest values of the span are found in a broad optimum around about 7 mm s^{-1}, which is consistent with that previously found for plates of a similar material (Engelbrecht et al., 2011). The plates in Engelbrecht et al. (2011) were somewhat thicker and cut from blocks made of different La(Fe,Co,Si)$_{13}$ compounds, all with a second order phase transition. Using this fluid velocity of 7 mm s^{-1} and staying at an ambient temperature of 290 K the utilisation was varied to find the best performance, as shown in Fig. 9. Again a broad peak of ΔT_{span} is observed, the utilisation giving the highest values being about 0.23, similar to Engelbrecht et al. (2011); Bahl et al. (2012). Due to the change in the distance and velocity of the piston movement the cycle time varies in the range of 5 to 24 s in Fig. 8 and in the range 5.5–12 s in Fig. 9.

The magnetocaloric effect in materials with a first order magnetic phase transition occurs over a narrow range of temperatures, as shown in Fig. 4. Thus it is very important when utilising these materials in a device that the span of the device is across the peak in magnetocaloric effect. Fig. 10 shows the achieved span of the device as the hot end temperature is changed, while keeping a utilisation of 0.23 and a fluid velocity of 7 mm s^{-1}. The cycle time remains constant at about 9 s.
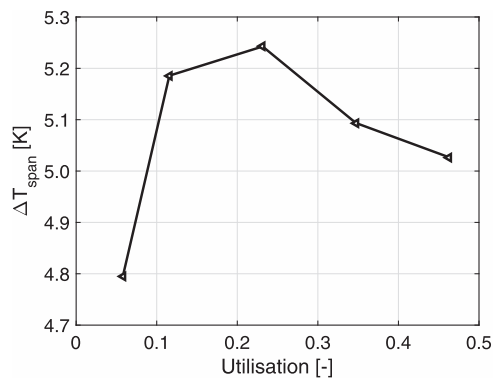
Fig. 9 – The steady state temperature span between the hot and the cold end as a function of the utilisation. The data are obtained at an ambient temperature of 290 K and a fluid velocity of 7 mm s⁻¹.

We observe a relatively narrow peak that drops off sharply at 293 K, which is a few degrees above the peak temperature of ΔS_M in a 1 T field. The maximum ΔT_{span} was 6.4 K, which is around double the maximum adiabatic temperature change of such a material in this applied field, see e.g. Basso et al. (2015), demonstrating the AMR cycle in the regenerator. The maximum span is lower than the 10.2 K span achieved using plates of the benchmark material Gd (Engelbrecht et al., 2011), but comparable to the spans achieved using plates of a single second order LaFeCoSi material or the single perovskite type material La$_{0.67}$Ca$_{0.26}$Sr$_{0.07}$Mn$_{1.05}$O$_3$ (Engelbrecht et al., 2011; Pulko et al., 2015). When grading the regenerator to two similar materials with Curie temperatures close to each other the span can be significantly increased for both the LaFeCoSi type materials (Engelbrecht et al., 2011) and the perovskite type materials (Bahl et al., 2012). Layering materials is key to the success of first order materials, due to the narrow peaks of the magnetocaloric effect, so it is clearly expected that if a regenerator were constructed with a number of different Curie temperatures along the flow direction significantly higher performance could be reached. However, as shown recently it is extremely important to have the correct spacing of the Curie temperatures, as
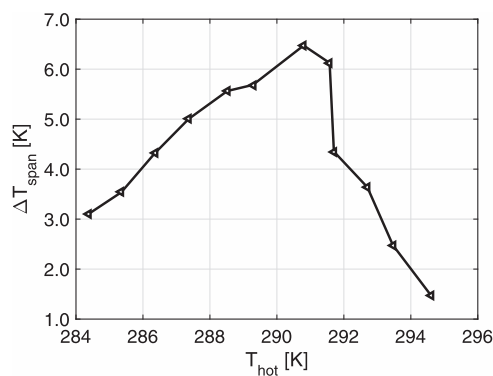
Fig. 10 – The steady state temperature span between the hot and the cold end as a function of the constant hot end temperature. The data are obtained at a utilisation of 0.23 and a fluid velocity of 7 mm s⁻¹.

the performance can easily be significantly reduced if this is not the case (Lei et al., 2015).

4.   Discussion

The measured maximum temperature span of 6.4 K is relatively low compared to other reported spans from this and similar devices. But when using just a single first order material, there is a natural limit to the achievable span, due to the very narrow ΔS_M peak. This span may be expanded by layering materials with slightly different Curie temperatures, as done by Jacobs et al. (2014). Previously it has been shown how thin plates consisting of a number of magnetocaloric materials have been produced by tape casting (Bulatova et al., 2015). A similar production technique could be imagined for hot-pressing single plates consisting of multiple materials.

Regenerator performance is heavily influenced by the morphology of the regenerator. In the present study flat parallel plates were chosen, giving a regenerator with a significantly reduced pressure drop compared to an equivalent packed bed one. Lower pressure drop leads to higher efficiency, although this is not measured in the device used here. The disadvantage of plates is the demand for thin very parallel plates with small plate spacing, which is often hard to realise. The increase of the Biot number for thicker plates will result in a slower heat transfer to the surrounding fluid, preventing fast operation and high performance. A higher thermal conductivity will allow for the use of thicker plates. The thermal conductivity of the plates tested here has been measured to be 3.13 W m⁻¹ K⁻¹, reduced from the generally accepted value of about 9 W m⁻¹ K⁻¹ for this type of material (Fujieda et al., 2004), due to porosity and the presence of resin in the plates. In order to realise the full potential of plates with this relatively low thermal conductivity the thickness would have to be significantly reduced, and the channel thicknesses be reduced accordingly.

In addition to the challenges of producing significantly thinner plates the flatness requirement of such plates will also become more critical. The reduction in regenerator performance due to a maldistribution of the plate spacings has been shown both by modelling and experimentally (Engelbrecht et al., 2013; Nielsen et al., 2012). Even seemingly insignificant variation in the channel thicknesses can have a large impact. With sub-millimeter plates a requirement of less than 10% variation in spacing, in accordance with the general recommendation in Nielsen et al. (2012), will necessitate very accurate production techniques.

Although the addition of the low mass fraction resin hardly influences ΔS_M per unit mass, the volumetric ΔS_M decreases from about 70 mJ cm⁻³ K⁻¹ to about 40 mJ cm⁻³ K⁻¹ due to the porous structure of the bonded material under a changing magnetic field of 1.4 T. From a practical point of view, the volumetric ΔS_M is of more importance (Gschneidner et al., 2005), since the magnetic system is the most expensive part and the magnetic field volume is thus limited. This is a challenge when making bonded plates and reducing the amount of resin to the minimum amount that will still maintain the structural integrity of the plates should be considered. Also, the 0.30 volume fraction of

pores could possibly be reduced by improving the processing route.

5. Conclusion

We have shown that it is possible to use resin bonded plates of the magnetocaloric material $La_{0.85}Ce_{0.15}Fe_{11.25}Mn_{0.25}Si_{1.5}H_y$ as regenerators in a small scale magnetocaloric testing device. The plates were characterised thermally and magnetically to determine the magnetic entropy change, the heat capacity and the hysteresis. The maximum achieved temperature span was 6.4 K. Increasing this span may be achieved by layering materials, reducing the amount of resin and pores or by manufacturing thinner and flatter plates.

Acknowledgments

REFERENCES

Aharoni, A., 1998. Demagnetizing factors for rectangular ferromagnetic prisms. J. Appl. Phys. 83, 3432.

Bahl, C.R.H., Petersen, T.F., Pryds, N., Smith, A., 2008. A versatile magnetic refrigeration test device. Rev. Sci. Instrum. 79, 093906.

Bahl, C.R.H., Velazquez, D., Nielsen, K., Engelbrecht, K., Andersen, K., Bulatova, R., et al., 2012. High performance magnetocaloric perovskites for magnetic refrigeration. Appl. Phys. Lett. 100, 121905.

Basso, V., Küpferling, M., Curcio, C., Bennati, C., Barzca, A., Katter, M., et al., 2015. Specific heat and entropy change at the first order phase transition of La(Fe-Mn-Si)₁₃-H compounds. J. Appl. Phys. 118, 053907.

Bulatova, R., Bahl, C.R.H., Andersen, K.B., Theil Kuhn, L., Pryds, N., 2015. Functionally graded ceramics fabricated with side-by-side tape casting for use in magnetic refrigeration. Int. J. Appl. Ceram. Tech. 12, 891898.

Caron, L., Ou, Z., Nguyen, T., Thanh, D.C., Tegus, O., Brück, E., 2009. On the determination of the magnetic entropy change in materials with first order transitions. J. Magn. Magn. Mater. 321, 35593566.

Engelbrecht, K., Bahl, C., Nielsen, K., 2011. Experimental results for a magnetic refrigerator using three different types of magnetocaloric material regenerators. Int. J. Refrigeration 34, 1132–1140.

Engelbrecht, K., Tusek, J., Nielsen, K., Kitanovski, A., Bahl, C., Poredos, A., 2013. Improved modelling of a parallel plate active magnetic regenerator. J. Phys. D Appl. Phys. 46, 255002.

Ferreira, L.D.R., Bessa, C.V.X., da Silva, I., Gama, S., 2014. A heat transfer study aiming optimization of magnetic heat exchangers of thermomagnetic motors. Int. J. Refrigeration 37, 209–214.

Fujieda, S., Hasegawa, Y., Fujita, A., 2004. Thermal transport properties of magnetic refrigerants La(FeₓSi₁₋ₓ)₁₃ and their hydrides, and Gd₅Si₂Ge2 and MnAs. J. Appl. Phys. 95, 24292431.

Gschneidner, K.A., Jr., Pecharsky, V.K., Tsokol, A.O., 2005. Recent developments in magnetocaloric materials. Rep. Prog. Phys. 68, 1479.

Jacobs, S., Auringer, J., Boeder, A., Chell, J., Komorowski, L., Leonard, J., et al., 2014. The performance of a large-scale rotary magnetic refrigerator. Int. J. Refrigeration 37, 84–91.

Jeppesen, S., Linderoth, S., Pryds, N., Kuhn, L.T., Jensen, J.B., 2008. Indirect measurement of the magnetocaloric effect using a novel differential scanning calorimeter with magnetic field. Rev. Sci. Instrum. 79 (8), 083901.

Kitanovski, A., Tusek, J., Tomc, U., Plaznik, U., Ozbolt, M., Poredos, A., 2015. Magnetocaloric Energy Conversion: From Theory to Applications. Springer International Publishing, New York.

Lanzarini, J., Barriere, T., Sahli, M., Gelin, J., Dubrez, A., Mayer, C., et al., 2015. Thermoplastic filled with magnetocaloric powder. Mater. Des. 87, 1022–1029.

Lei, T., Nielsen, K., Engelbrecht, K., Bahl, C., Bez, H.N., Veje, C., 2015. Sensitivity study of multi-layer active magnetic regenerators using first order magnetocaloric material La(Fe,Mn,Si)₁₃Hᵧ. J. Appl. Phys. 118, 014903.

Liu, J., Zhang, M., Shao, Y., Yan, A., 2015. LaFe₁₁.₆ Si₁.₄/Cu magnetocaloric composites prepared by hot pressing. IEEE Trans. Magn. 51, 2501502.

Lyubina, J., Schäfer, R., Martin, N., Schultz, L., Gutfleisch, O., 2010. Novel design of La(Fe,Si)₁₃ alloys towards high magnetic refrigeration performance. Adv. Mater. 22, 3735–3739.

Nielsen, K., Engelbrecht, K., Christensen, D., Jensen, J., Smith, A., Bahl, C., 2012. Degradation of the performance of microchannel heat exchangers due to flow maldistribution. Appl. Therm. Eng. 40, 236.

Pecharsky, V.K., Gschneidner, K.A., Jr., 1999a. Magnetocaloric affect and magnetic refrigeration. J. Magn. Magn. Mater. 200, 44.

Pecharsky, V.K., Gschneidner, K.A., Jr., 1999b. Magnetocaloric effect from indirect measurements: magnetization and heat capacity. J. Appl. Phys. 86, 565–575.

Pryds, N., Clemens, F., Menon, M., Nielsen, P.H., Brodersen, K., Bjørk, R., et al., 2011. A monolithic perovskite structure for use as a magnetic regenerator. J. Am. Ceram. Soc. 94, 2549–2555.

Pulko, B., Tusekek, J., Moore, J.D., Weise, B., Skokov, K., Mityashkin, O., et al., 2015. Epoxy-bonded lafecosi magnetocaloric plates. J. Magn. Magn. Mater. 375, 65–73.

Radulov, I., Skokov, K., Nad, T., Braun, D.K., Gutfleisch, O., 2015. Polymer-bonded La(Fe,Mn,Si)₁₃Hₓ plates for heat exchangers. IEEE Trans. Magn. 51, 2501204.

Skokov, K.P., Karpenkov, D., Kuzmin, M.D., Radulov, I., Gottschall, T., Kaeswurm, B., et al., 2014. Heat exchangers made of polymer-bonded La(Fe,Si)₁₃. J. Appl. Phys. 115, 17A941.

Smith, A., Bahl, C., Bjørk, R., Engelbrecht, K., Nielsen, K., Pryds, N., 2012. Materials challenges for high performance magnetocaloric refrigeration devices. Adv. Energy Mater. 2, 1288–1318.

Velazquez, D., Castro, M., Palacios, E., Burriel, R., 2014. Practical properties of lafecosi materials to be used in magnetic cooling regerators. In: Proceedings 6th IIF-IIR International Conference on Magnetic Refrigeration, 7–10 September 2014. Victoria, BC.

Zhang, H., Hu, F., Sun, J., Shen, B., 2013. Effects of interstitial H and/or C atoms on the magnetic and magnetocaloric properties of La(Fe, Si)₁₃-based compounds. Sci. China Phys. Mech. Astron. 56, 2302–2311.

P.6. From a magnet to a heat pump

73

From a Magnet to a Heat Pump

Kristina Navickaitė*, Henrique Neves Bez, Kurt Engelbrecht, Christian R. H. Bahl

Technical University of Denmark, Department of Energy Conversion and Storage
Frederiksborgvej 399, 4000 Roskilde, Denmark

*Corresponding author: **knav@dtu.dk**

http://dx.doi.org/10.5755/j01.sace.14.1.15927

The magnetocaloric effect (MCE) is the thermal response of a magnetic material to an applied magnetic field. Magnetic cooling is a promising alternative to conventional vapor compression technology in near room temperature applications and has experienced significant developments over the last five years. Although further improvements are necessary before the technology can be commercialized. Researchers were mainly focused on the development of materials and optimization of a flow system in order to increase the efficiency of magnetic heat pumps. The project, presented in this paper, is devoted to the improvement of heat pump and cooling technologies through simple tests of prospective regenerator designs. A brief literature review and expected results are presented in the paper. It is mainly focused on MCE technologies and provides a brief introduction to the magnetic cooling as an alternative for conventional vapor compression technology.

KEYWORDS: heat pump, heat transfer, magnetic refrigeration, magnetocaloric effect, test device modelling.

The magnetocaloric effect (MCE) was discovered by French and Swiss physicists Weiss and Piccard (Smith et al. 2012). In the mid-1920s Debye and Giauque proposed a method of adiabatic demagnetization to reach very low temperatures (Smith et al. 2012). The discovery of magnetocaloric materials (MCM) with Curie temperatures (T_C) near room temperature (RT) has opened an opportunity for magnetic refrigeration (MR) to become an alternative to conventional vapor compression devices. Furthermore, MR technology is environmentally friendly since it has zero vapor pressure, no Ozone Depletion Potential (ODP), no direct Global Warming Potential (GWP), it has potential to be more compact layout since the working material is solid, and has the potential to work more silently than conventional compressors (Bahl et al. 2008, Barbosa et al. 2014, Engelbrecht et al. 2011, Eriksen et al. 2015, Lei et al. 2016, Smith et al. 2012).

The MC cooling technique is based on the thermal response of a magnetic material when magnetized/demagnetized, such as a temperature increases when the field is increased and vice versa. The isothermal entropy change is negative upon magnetization and positive upon demagnetization, see **Fig. 1**. This scenario is valid when an ordinary MCE takes place and is analogous to the negative change in entropy associated with the isothermal compression of a gas.

MR near RT is a desirable, but at the same time technically challenging idea. Challenges are related to device engineering. Barclay et al. (1981) patented the active magnetocaloric regenerator (AMR) with its own 'distributed refrigeration' cycle which can provide refrigeration over a temperature span that is much larger than the adiabatic temperature change of the material. Nevertheless, an efficient AMR device requires a large magnetic field. Rowe et al. (2006) concluded that

Introduction

ktu
1922

Fig. 1

An MR material with randomly oriented spins is magnetized – the temperature of a material increases adiabatically (a) and then entropy decreases under isothermal conditions (b)
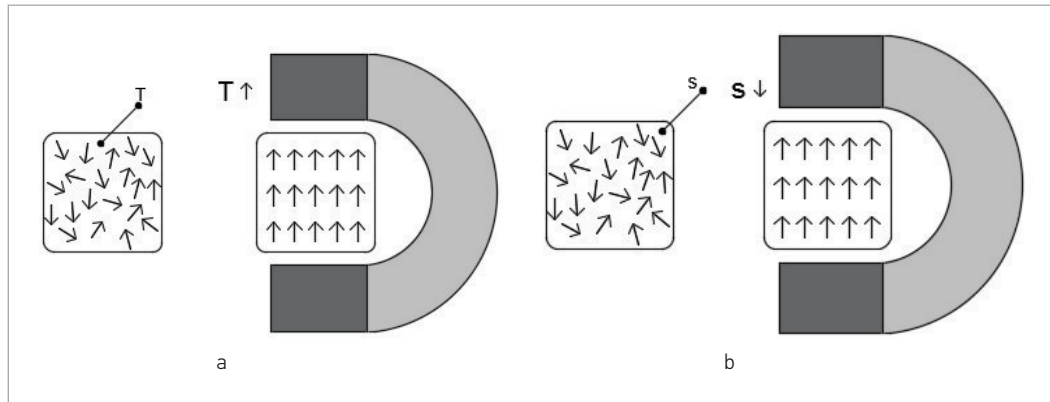
the lower magnetic field might be compensated by increasing the operating frequency. However, Nielsen and Engelbrecht (2012) showed that in case of a long AMR (200 mm) the importance of the thermal conductivity increases when a device is operated at a high frequency – the higher the operating frequency, the higher the thermal conductivity is necessary.

Seeking to optimize the configuration of machines, attention is mainly paid to the performance of it. There are several ways to increase the efficiency of an MR such as optimizing the flow system, optimizing the magnet assembly, improving regenerator geometry, and investigating new MCMs, etc. Nevertheless, the main attention of other researchers is paid on the investigation of materials such as changing their composition (Kaštil et al. 2013).

On the other hand, to build an MR with a high COP, an efficient heat exchanger is required. Since the adiabatic temperature span in the MCE (in the magnetic field up to 1.5 T) is limited to a maximum 5.8 K per one layer of MCM, conventional heat exchangers are not sufficient to be directly implemented in this application. The temperature span is required to be at least 30 K for conventional devices (Kitanovski et al. 2015). This suggests considering a novel concept of heat exchanger. It has long been a goal to design a heat exchanger with a high heat transfer rate and low pressure drop, but now it turned to be crucially important for the successful implementation of novel cooling technologies.

Methods

Discovered compositions are available in a variety of shapes and packing of new materials should be tested before applying them in larger and more complex prototypes. The properties of a series of such MCMs are tested in a vertically oriented versatile device – the test machine, see **Fig. 2**. It is designed in a way to allow the variation and control of many experimental parameters. A brief introduction to the main parts and operation of the test machine are given in this paper, more detailed description of the device and operational conditions are given in Bahl et al. (2008) and Engelbrecht et al. (2012). The device is built in a temperature controlled cabinet. The hot reservoir (1) is placed above the regenerator (2) and is linked to the forced convection heat exchanger (HEX) (3) and the cold reservoir (4) (below the regenerator) is covered by thermal insulation (not shown). A Halbach cylinder permanent magnet is used as a magnetic field source, with an average flux density in the bore of 1.03 T. The temperature of the hot end (T_{hot}) is controlled via the ambient (air inside the cabinet) temperature.

During operation a regenerator is moved vertically by a stepper motor while the magnet is kept in a stationary position (see **Fig. 3**). Magnetization and demagnetization of the MCM is achieved in this way and a temperature span across the thermal reservoirs is built up. The heat transfer fluid is moved through the regenerator by mean of a displacer in the cold end. The entire device is in thermal contact with the same ambient air i.e. hot end is thermally linked to the ambient via a forced convection heat exchanger while the cold end is thermally insulated using foam tubing.

The test machine can be operated in different combinations of various parameters, such as a different piston (displacer) stroke (amplitude) and velocity. The heat transfer fluid flow is provided by pushing the piston backwards and forwards. In this manner the fluid velocity and volume of the flow can be controlled. The velocity of the fluid directly affects utilization, which represents the ratio of the thermal capacity of the fluid that moves into regenerator to the thermal capacity of the solid regenerator material. The expression to define utilization (ϕ) is given below:

$$\phi = \frac{\dot{m}_f c_f}{m_s c_s} \quad (1)$$

where:

$\dot{m}_f$ – mass of the fluid pushed through the regenerator in one direction;

c_f and c_s – specific heat of the fluid and the solid, respectively;

m_s – mass of the solid regenerator (Neves Bez et al. 2016).

To find the optimal working point of the MCM, T_{hot} is set slightly above the T_C of the working material and series of tests are run under the following conditions:

1   At different piston amplitudes, when the utilization (Eq. 1) of a regenerator is known. The sample is tested at the same temperature (slightly above the T_C) and piston velocity conditions. The point where the temperature span is the highest is selected to be the optimal piston amplitude for the remaining tests of the same regenerator.

2   At different piston velocities, when the optimal piston amplitude is known. The sample is tested at the same temperature (same as at the first step) and piston amplitude conditions. The point where the temperature span is at the peak is selected to be the optimal piston velocity for the remaining tests of the same regenerator.

3   At the different temperature range, when the piston amplitude and velocity is constant. When working point is known, a test against temperature change is made in order to find the peak of the temperature span of the tested sample.

Two types of regenerators have been tested in the test machine. The parallel plate regenerator is shown in the **Fig. 4. a)**. The irregular particle regenerator is shown in **Fig. 4 b)** and **c)**. The MCM and their characteristics are not discussed further in this paper. More information about the both types of the regenerators might be found in Bahl et al. (2016) and Neves Bez et al. (2016), respectively.

The results for three regenerators, in the form of irregular particles (see **Fig. 4 b** and **c**) are presented in this paper. All of the presented regenerators were bonded with a small amount of epoxy
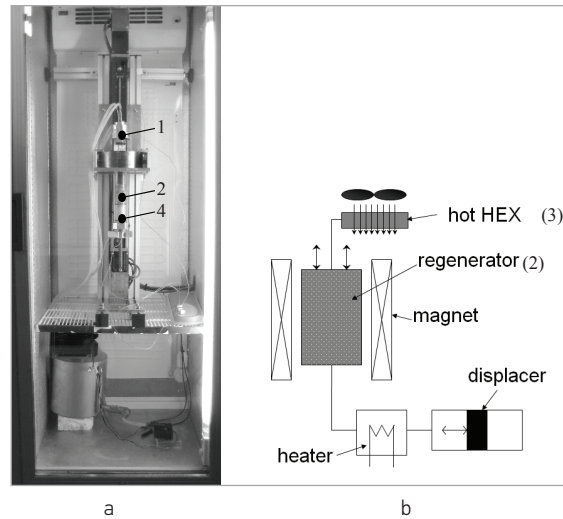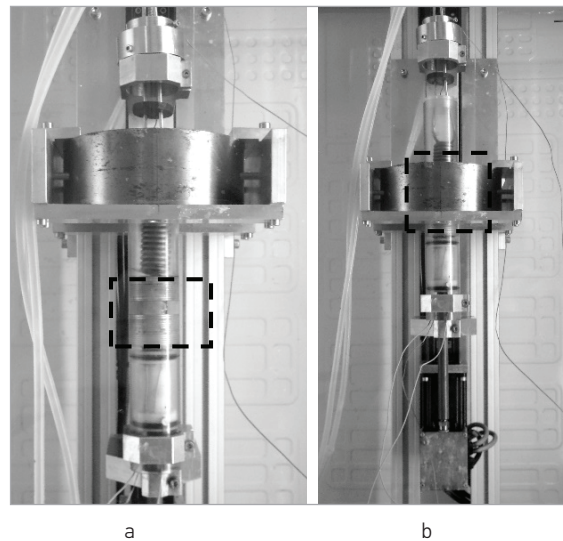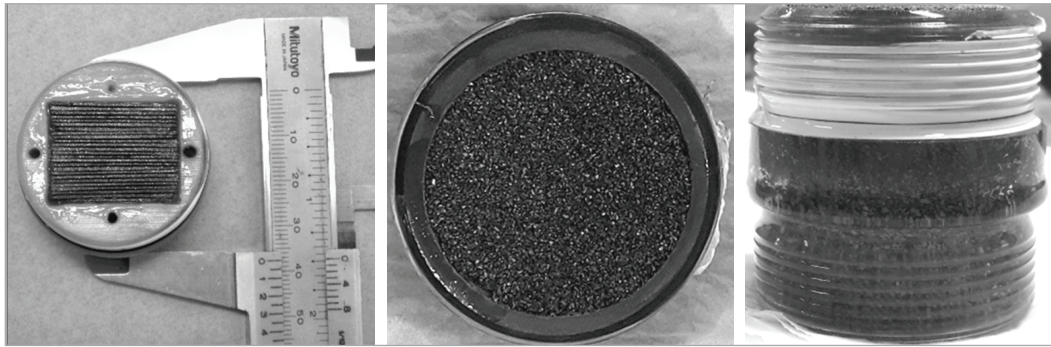
which is meant to maintain the mechanical integrity of the regenerator. A water based solution (2 wt%) of anti-corrosion inhibitor ENTEK FNE was used as a heat transfer liquid. All the samples have the same mass (95 g), and average specific heat (500 J/kgK) (the difference in the specific heat of the samples might be neglected) (Neves Bez et al. 2016). The bonding epoxy has poorer thermal properties than pure MCM, nevertheless it is necessary for structural integrity of the regenerator. Thus it is important to measure the MCE characteristics of the regenerators before applying the material on a larger prototypes or magnetic heat pumps. Particularly this material is will be used in the ENOVHEAT (*Efficient Novel Magnetocaloric Heat Pumps*) prototype, which is under design at DTU Energy. More information can be found at the project's home page http://www.enovheat.dk/.

Set-up for measurements

In order to measure and log the temperature of the ambient, cold and hot end, the type E thermocouples and Pico TC-08 thermocouple data logger (Pico logger) were used.

The measurable temperature range for E type thermocouple is -270 +870 °C. Standard accuracy is +/- 1.7°C or +/- 0.5%.

A Pico logger has 8 channels for thermocouples and the cold junction compensation (CJC) measuring ambient temperature is used in this work. The features of the device are as follow:

_ measureable temperature range is -270 +1820 °C;

_ temperature accuracy sum of +/- 0.2% of reading and +/- 0.5 °C;

_ voltage accuracy sum of +/- 0.2% of reading and +/-10mV;

_ conversion time 100 ms per thermocouple channel;

_ sampling rate is up to 10 samples per second;

_ resolution 20 bits.

Results and discussion
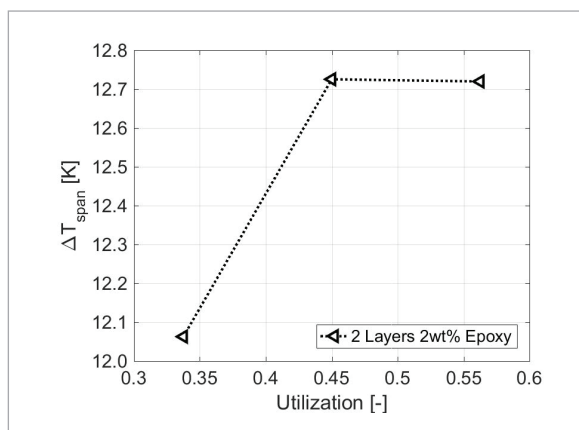
The optimal working point of the tested regenerators was at a piston amplitude of 20 mm and piston velocity 15 mm/s ($\phi = 0.45$), see **Fig. 5** and **Fig. 6**. The working point was tested only for the sample of 2 wt.% epoxy. All of the presented samples kept their mechanical integrity during the tests, indicating that 2 wt % epoxy is adequate from a mechanical standpoint. The volume of the epoxy bonding the MCM particles was varied in order to find the minimum necessary amount to maintain the mechanical integrity of the regenerators.

The regenerators with 3 wt% and 4 wt% of epoxy were tested at the same working point. As it was expected, the regenerator with 2 wt% of epoxy showed the best performance: ΔT_{span} = 13.6 K at T_{hot} = 301 K (28 ºC). The peaks of the samples with 3 wt% and 4 wt% were ΔT_{span} = 12.8 K (at T_{hot} = 301 K (28 ºC)) and ΔT_{span} = 12.2 K (at T_{hot} = 300 K (27 ºC)), respectively.

The obtained results agree with the previously published knowledge and suggest that increasing the number of layers in the regenerator in the form of powders may lead to a broader temperature span (Eriksen 2016, Neves Bez et. al 2016). However, a more powerful and more efficient machine is necessary to allow us to perform a full test of multilayered regenerators. Thus, it is planned to build an advanced testing device with higher operating frequency and an adjustable magnetic field. The main purpose of the machine would be kept the same – to test and optimize active magnetic regenerators on a small scale before implementing them in larger, more complex prototypes, such as the rotary prototypes, built

Fig. 6

No-load temperature span as a function of fluid velocity for a two layers regenerator

Fig. 7

No-load temperature span as a function of the temperature of the hot end for a two layers regenerator.

at DTU Energy (Bahl2013, Eriksen 2016). The design and arrangement of the machine is not well discussed yet, though. It is clear that the new device should be designed to be very flexible with regards to materials, regenerator geometry and operating conditions. Also, the available literature suggests that the temperature of a heat-sink must be decided a priori if a new device is going to be designed.

Finally, the efficiency and coefficient of performance (COP) of magnetocaloric prototypes has been significantly increased over the past three years – Okuamura and Hirano (2013) presented a device with a COP of 2.5 at a ΔT_{span} of 5 K of their previous prototype, later Jacobs et al. (2014) published results about a prototype, operating at a COP above 2 at a ΔT_{span} of 10 K. The latest published prototype with a COP of 3.6 at a ΔT_{span} of 15.5 K and efficiency of 18% was developed at DTU Energy, it is described in Eriksen et al. (2016).

Conclusions

A brief introduction to the MCE as an alternative to the conventional vapor compression device has been given in the present paper. The existing test machine, built at DTU Energy, has been described. Additionally, the interested reader might find more information about the rotary prototype of the magnetic cooling technology in Eriksen (2016).

No-load temperature spans have been presented for the regenerators with varying amounts of bonding epoxy. It is seen that the smaller amount of epoxy in the volume of the regenerator, the better is the performance. The minimal amount of epoxy should be incorporated in order to sustain the mechanical integrity of the regenerator, though. As it is presented in the results section, the utilisation for all of the tested regenerators was ϕ = 0.45, which corresponded to a
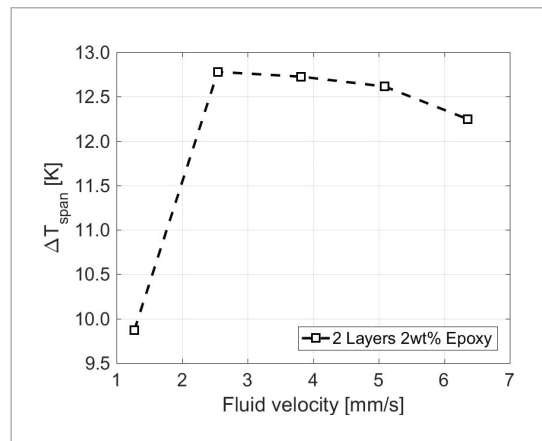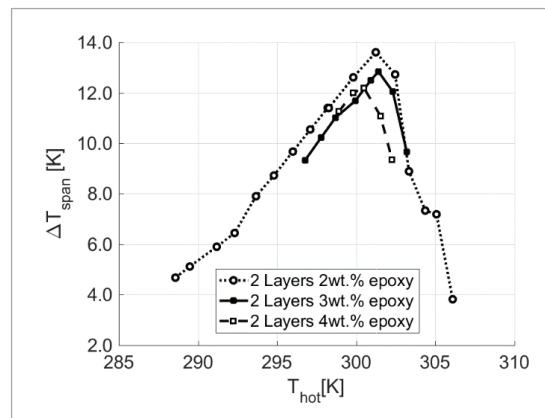
piston amplitude 20 mm. The sample with the least amount of epoxy showed the best perform and temperature span ΔT_{span}=13.6°C, while the sample with 4% of epoxy showed the lowest temperature span ΔT_{span}=12.2°C. The regenerator with 3% of epoxy showed the temperature span of ΔT_{span}=12.8°C.

The experiments on the same MCM with the 2% of epoxy will be continued in order to find the best configuration of the particles geometry and number of the layers in a regenerator.

Acknow-ledgment

References

Bahl C. R. H. *et al.*, Bonded LaFeSiH plates tested in a magnetocaloric device. International journal of refrigeration. 2016. In preparation.

Bahl C.R.H., Engelbrecht K., Eriksen D., Lozano J.A., Bjørk R., Geyti J., Nielsen K.K., Smith A., Pryds N. Development and experimental results from a 1 kW prototype AMR, Int. J. Refrigeration, 2013, 37:78. http://dx.doi.org/10.1016/j.ijrefrig.2013.09.001

Bahl C. R. H., Petersen T. F., Pryds N., Smith A. A versatile magnetic refrigeration test device. Review of scientific instruments, 2008, 79, 093906. http://dx.doi.org/10.1063/1.2981692

Barbosa J,. Lozano J., Trevizoli P. Magnetocaloric refrigeration research at the INCT in cooling and thermophysics. 15th Brazilian congress of thermal science and engineering, 2014. Conference proceedings.

Barclay J. A., Steyert W. A. Active magnetic regenerator. United States Patent. 1981. Application No. 228,836.

Engelbrecht K., Bahl C. R. H., Nielsen K. K. Experimental results for a magnetic refrigerator using three different types of magnetocaloric material regenerators. International journal of refrigeration, 2011, 34: 1132-1140. http://dx.doi.org/10.1016/j.ijrefrig.2010.11.014

Engelbrecht K., Jensen J. B., Bahl C. R. H. Experiments on a modular magnetic refrigeration device. Journal of mechanical engineering 58, 2012, 1: 3-8.

Eriksen D. Active magnetic regenerator refrigeration with rotary multi-bed technology. PhD thesis submitted to DTU. 2016.

Eriksen D., Engelbrecht K., Bahl C. R. H. Bjørk R. Exploring the efficiency potential for an active magnetic regenerator. Science and technology for the built environment, 2016, 0:1-7.

Eriksen D., Engelbrecht K., Bahl C. R. H., Bjørk R., Nielsen K. K., Insinga A. R., Pryds N. Design and experimental test of a rotary active magnetic regenerator prototype. International journal of refrigeration, 2015, 58: 14-21. http://dx.doi.org/10.1016/j.ijrefrig.2015.05.004

Jacobs S., Auringer J., Boeder A., Chell J., Komorowski L., Leonard J., Russek S., Zimm C. The performance o a large-scale rotary magnetic refrigerator. International journal of refrigeration, 2014, 37: 84-91. http://dx.doi.org/10.1016/j.ijrefrig.2013.09.025

Kaštil J., Tětek J., Tuček A. Experimental investigation of small-scale magnetocaloric refrigeration. Acta Physica Polonica A, 2013, 4 (124): 740-744. http://dx.doi.org/10.12693/APhysPolA.124.740

Kitanovski A., Tušek J., Tomc U., Plaznik U., Ožbolt M., Poredoš A. Magnetocaloric energy conversion from theory to application. Switzerland: Springer International publishing; 2015.

Lei Z., Haberstroh Ch., Odenbach S., Eckert K. Heat transfer enhancement in magnetic cooling by means of magnetohydrodynamic convection. International journal of refrigeration, 2016, 62: 166-176. http://dx.doi.org/10.1016/j.ijrefrig.2015.10.002

Neves Bez H., Navickaitė K., Lei T., Engelbrecht K., Barcza A., Bahl C. R. H. Epoxy-bonded La(Fe,Mn,Si)$_{13}$H$_z$ as a multi layered active magnetic regenerator. Seventh IIF-IIR international conference on magnetic refrigeration at room temperature, ThermagVII, 2016. Submitted.

Nielsen K. K., Engelbrecht K. The influence of the solid thermal conductivity on active magnetgic regenerators. J Phys D Appl Phys, 2012, 45:145001. http://dx.doi.org/10.1088/0022-3727/45/14/145001

Okamura T., Hirano N. Improvement of the performance of room temperature magnetic refrigerator using Gd-alloy. Journal of the Japan society of applied electromagnetics and mechanics, 2013, 21 (1):10-4. http://dx.doi.org/10.14243/jsaem.21.10

Rowe A., Tura A. Experimental investigation of a three-material layered active magnetic regenerator. International journal of refrigeration, 2006, 29: 1286-1293. http://dx.doi.org/10.1016/j.ijrefrig.2006.07.012

Smith A., Bahl C. R. H., Bjørk R., Engelbrecht K., Nielsen K. K., Pryds N. Materials challenges for high performance magnetocaloric refrigeration device. Advance energy materials, 2012, 1-31.

About the authors

KRISTINA NAVICKAITE

PhD student

Technical University of Denmark, Department of Energy Conversion and Storage, Section of Electrofunctional materials

Main research area

Heat transfer, renewable energy, fluid dynamic

Address

DTU Risø Campus, Frederiksborgvej 399, B 779, R15, 4000 Roskilde, Denmark
Tel: +45 93 51 15 91
E-mail: knav@dtu.dk

HENRIQUE NEVES BEZ

PhD student

Technical University of Denmark, Department of Energy Conversion and Storage, Section of Electrofunctional materials

Main research area

Material science, renewable energy

Address

DTU Risø Campus, Frederiksborgvej 399, B 778, R19, 4000 Roskilde, Denmark
Tel: +45 51 30 83 87
E-mail: hnbe@dtu.dk

KURT ENGELBRECHT

Senior Researcher

Technical University of Denmark, Department of Energy Conversion and Storage, Section of Electrofunctional materials

Main research area

Heat transfer, renewable energy, fluid dynamic, energy conversion

Address

DTU Risø Campus, Frederiksborgvej 399, B 779, R26, 4000 Roskilde, Denmark
Tel: +45 46 77 56 49
E-mail: kuen@dtu.dk

CHRISTIAN R. H. BAHL

Senior Researcher

Technical University of Denmark, Department of Energy Conversion and Storage, Section of Electrofunctional materials

Main research area

Heat transfer, renewable energy, fluid dynamic, energy conversion, material science

Address

DTU Risø Campus, Frederiksborgvej 399, B 779, R26, 4000 Roskilde, Denmark
Tel: +45 46 77 56 49
E-mail: chrb@dtu.dk

C.1. Experimental investigation of fifteen-layer epoxy-bonded La(Fe,Mn,Si)$_{13}$H$_z$ active magnetic regenerator

Experimental investigation of fifteen-layer epoxy-bonded La(Fe,Mn,Si)$_{13}$H$_y$ active magnetic regenerator

Kristina Navickaitė[(a,b)1], **Behzad Monfared**[(b)1], **David Martinez**[(a)], **Björn Palm**[(b)],

Christian Bahl[(a)], **Kurt Engelbrecht**[(a)]

[(a)]Department of Energy Conversion and Storage – Technical University of Denmark, Frederiksborgvej 399, Roskilde 4000, Denmark, knav@dtu.dk, davm@dtu.dk, chrb@dtu.dk, kuen@dtu.dk

[(b)]KTH Royal Institute of Technology, School of Industrial Engineering and Management, Department of Energy Technology, Brinellvägen 68, Stockholm SE-100 44, Sweden, behzadam@ktu.se, Bjorn.Palm@enrgy.kth.se

ABSTRACT

We present the experimental results compared with numerical simulations of a fifteen-layer epoxy bonded regenerator with the first order phase transition material La(Fe,Mn,Si)$_{13}$H$_y$. The maximum temperature span established at zero-load conditions was ΔT_{span}=15.4 K at U=0.5. The experimental investigation was conducted in a medium-scale rotary device at KTH Royal Institute of Technology. The La(Fe,Mn,Si)$_{13}$H$_y$ materials were bonded with 2.3 wt. % epoxy by Vacuumschmelze GmbH, Germany. The experimental results and numerical modeling are in good agreement.

Keywords: Magnetocaloric, refrigeration, epoxy-bonded, layered regenerator, AMR, numerical modelling.

1. INTRODUCTION

Magnetocaloric materials (MCM) that exhibit a first order phase transition (FOPT) are associated with a giant magnetocaloric effect (MCE). Thus, they are a very attractive option to be used in refrigeration technologies for near room temperature applications. However, FOPT materials are accompanied by many practical challenges. For example, the materials exhibit brittleness and a volume change during cyclic (de)magnetization (Brück et al., 2004). Additionally, the temperature region where a giant MCE occurs is much narrower for FOPT materials than for those that exhibit a second order phase transition (SOPT). The latter issue can be solved by layering different materials in one regenerator (Richard et al., 2004), (Rowe et al., 2014) and (Zimm et al., 2005). A number of numerical studies suggest how to design multilayered regenerators so that the maximum cooling power or maximum zero-load temperature span would be achieved (Lei et al., 2015), (Monfared and Palm, 2015) and (Lei et al., 2017). Lei et al., (2015) suggested in order to obtain 90 % of the maximum cooling power, the practical temperature difference between the transition temperatures of two materials in a regenerator beds should be 2.5 K. However, later it was pointed out that insufficient absolute layer thickness in a regenerator leads to significant reduction in performance (Govindappa et al., 2017).

An experimental investigation of a fifteen-layer epoxy-bonded La(Fe,Mn,Si)$_{13}$H$_y$ active magnetic regenerator (AMR) is presented in this study. The obtained experimental results are compared with results from a numerical model developed at KTH Royal Institute of Technology and explained in more details by Monfared et al., (2018).The developed novel approach of AMR modeling consists of three parts: a model of internal and external magnetic field, a model of the parasitic heat transfer, and a model of the active magnetic regeneration cycle. The model was previously verified against experimental data obtained for SOPT materials – Gd and its alloys.

2. EXPERIMENTAL PROCEDURE

Irregularly shaped La(Fe,Mn,Si)$_{13}$H$_y$ particles in a size range from 600 μm to 800 μm were bonded with 2.3 wt. % epoxy into a plastic housing (Figure 1 (a)). The housing was 150 mm long and consisted of 12 beds. The cross-sectional area of each bed was 207 mm^2. Two beds, 90 degrees apart, were filled with fifteen layers

---

of manually sorted La(Fe,Mn,Si)$_{13}$H$_y$ particles. Monfared and Palm, (2016) explained the sorting procedure in more details.

(a)	(b)
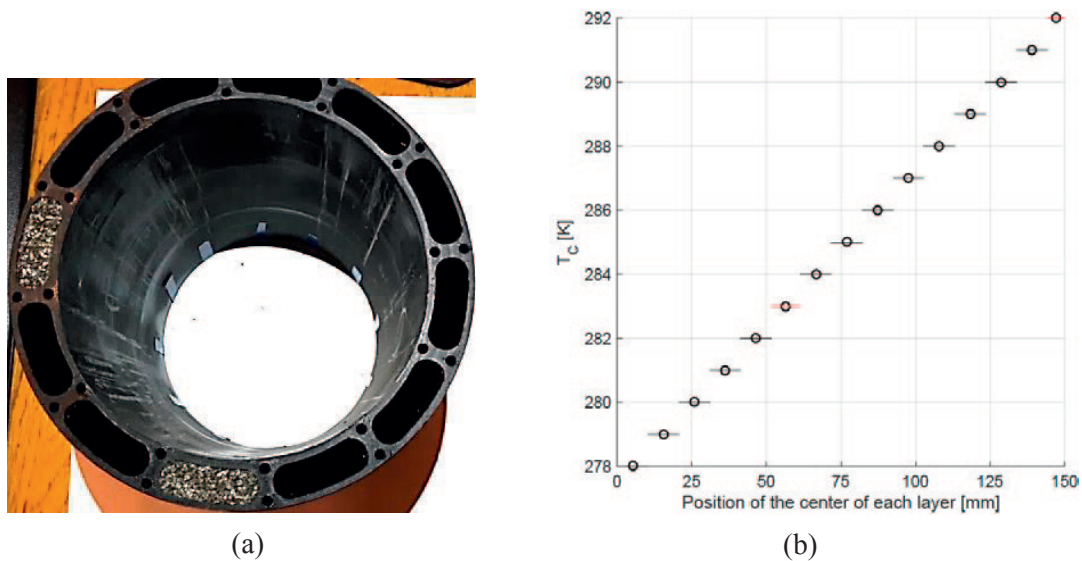
Figure 1. a) The housing with two regenerator beds with fifteen layers of La(Fe,Mn,Si)$_{13}$H$_y$ installed. The beds separated by 90°. b) T_C distribution over the regenerator beds. The horizontal guidelines represent each layer thickness. The red guidelines represent layers containing smaller mass fraction of La(Fe,Mn.Si)$_{13}$H$_y$.

The Curie temperature range of the epoxy-bonded particles is from 278 K to 292 K in steps of 1 K. Figure 1 (b) shows the T_C distribution over one regenerator bed (it is assumed that both beds are identical). The layer thickness is calculated knowing the mass of solid material and epoxy used in each bed and assuming that porosity is uniform over the entire regenerator. The T_C distribution over the regenerators is nearly linear. However, one can see that the sixth and the fifteenth layers are shorter than the remaining thirteen layers. This is due to the significantly smaller mass fraction of the sorted material in the two short layers, which is 6.36 % and 2.10 %, respectively, while the mass fraction of the remaining layers is 7.04 % each.

The regenerator was mounted into the medium-scale rotary device (Figure 2 (a)) described in more details by Monfared and Palm, (2016). Figure 2 (b) shows the schematic of the flow system of the device. The housing with regenerators is mounted on an iron yoke. The permanent magnet, which generates a 0.75 T magnetic field, is placed concentrically inside the yoke and the housing. An electrical motor rotates the magnet and a rotary valve. A gear system mounted on a connecting shaft synchronizes the magnet rotation and flow direction of the heat transfer fluid through the regenerators. A pump (1) pushes heat transfer fluid through the heat exchanger (7) and then to the rotary valve (8). There the fluid is directed to the magnetized regenerator. The regenerators are connected in series, thus the fluid from the magnetized regenerator flows to the demagnetized one and comes back to the rotary valve and is pushed to an expansion vessel (5). From there the fluid is pumped through a flow meter back to the pump and the loop closes. To simulate a cooling load, a system of cartridge heaters is placed at the cold side of regenerators. The system is controlled by software written in LabVIEW. The measurement data are logged by Agilent VEE software. The fluid flow rate is controlled by changing drive frequency of the pump. The cycle frequency is modified by changing operating frequency of the motor that drives the magnet in LabVIEW. The device is placed in a climate chamber to allow variation of the operating temperature.
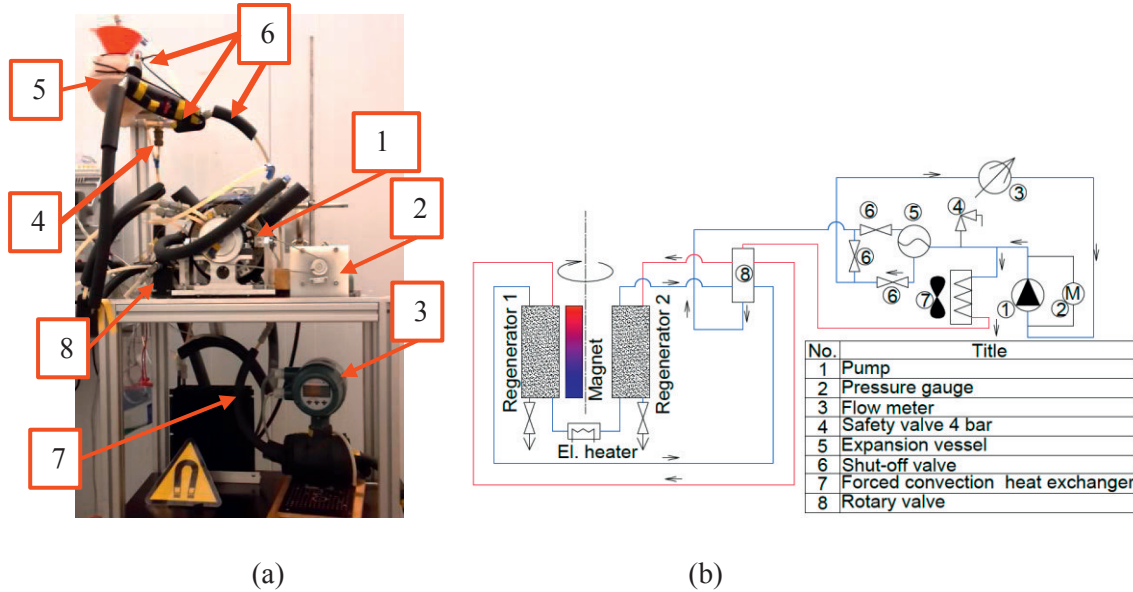
Water with a 2 vol.% solution of FNE ENTEK was used as a heat transfer fluid. The porosity of the regenerators was both estimated using the data provided by Vacuumschmelze, GmbH and measured experimentally. The porosity ε was estimated based on information from the supplier using Eq. 1

$$\varepsilon = 1 - \frac{\frac{m_s}{\rho_s} + \frac{m_e}{\rho_e}}{V_h}$$

Eq. (1)

where V_h is the total inner volume of the housing in m³, m_s and m_e are the masses of the solid and epoxy in kg, respectively, and ρ_s and ρ_e are the densities of the solid and epoxy in kg m⁻³, respectively. The values for ρ_s and ρ_e are 7000 kg m⁻³ and 1250 kg m⁻³, respectively.

The housing with the dry regenerators was weighed. Then one regenerator was filled with heat transfer fluid and the housing was weighed again. Next, the other regenerator was filled with the heat transfer fluid and the housing was weighed again. The measured porosity of each regenerator is 40.9 % and 41.2 %. The porosity estimated using Eq. 1 is 38.9 %. The difference between measured and estimated porosity values might be attributed to the inaccuracies in measurements, variation in epoxy and manufacturing.

	No.	Title
	1	Pump
	2	Pressure gauge
	3	Flow meter
	4	Safety valve 4 bar
	5	Expansion vessel
	6	Shut-off valve
	7	Forced convection heat exchanger
	8	Rotary valve

(a)   (b)

Figure 2. (a) A photo of the medium-scale rotary device. 1 –the iron yoke with the regenerator and the magnet inside; 2 – the electrical motor, which rotates the magnet and the rotary valve (8), 3 – the flow meter; 4 – the safety valve (4 bar); 5 – the expansion vessel, 6 – shut-off valves (the shut-off valve, mounted in the connecting line is always closed); 7 – the forced convection heat exchanger, directly exposed to the ambient air; 8 – the rotary valve. (b) A schematic of the flow system of the medium-scale rotary device.

Utilization, U, is a factor that defines the ratio of heat capacity rates between the heat transfer fluid and the solid and is defined by Eq. 2.

$$U = \frac{m_f c_f}{m_{reg} c_s}$$

Eq. (2)

where m_f is the mass of the fluid pushed through the regenerator in kg, c_f the specific heat of the fluid, m_{reg} the mass of the regenerator in kg and c_s is the specific heat of the MCM in J kg⁻¹ K⁻¹. The values used for c_f and c_s are 4210 J kg⁻¹ K⁻¹ and 501 J kg⁻¹ K⁻¹, respectively.

Literature suggest that the optimal value of U is between 0.2 and 0.8 (Kitanovski et al., 2015). In order to determine the fluid flow rate of the initial experiments the $U = 0.5$ was chosen.

3. NUMERICAL MODEL

The numerical model developed at KTH Royal Institute of Technology consists of three parts: a 3D COMSOL model of the magnetic field, a 3D steady state COMSOL model of parasitic heat losses and, a 1D transient active magnetic regeneration (AMR) model in the MATLAB environment (Monfared, 2018).

The magnetic field model here is used to simulate the external magnetic field. To simplify the model, it is assumed that the external magnetic field is uniform. Since the properties of MCMs vary with an internal field,

the value of an external field, obtained by the developed model, is converted to an internal field and implemented in the simulation model of the AMR. This is done using Eq. 3 and Eq. 4.

$$H_{in} = H_{ex} - NM \qquad \text{Eq. (3)}$$

$$N = \frac{1}{3} + (1 - \varepsilon)\left(D_z - \frac{1}{3}\right) \qquad \text{Eq. (4)}$$

where: H is the magnetic field in A m^{-1}, N is the demagnetization factor, M is the magnetization in A m^{-1}, D_z is the demagnetization factor of the geometrical shape, the subscripts *in* and *ex* stands for internal and external, respectively. The validity and applicability of Eq. 3 on packed bed regenerators was proved by experimental and numerical works reported in (Bjørk and Bahl, 2013; Bleaney et al., 1941).

To simplify the parasitic heat loss model the following assumptions were made: 1) the temperature in the MCM beds varies linearly from the cold to the hot ends; 2) the non-cylindrical magnet assembly is modeled as a cylinder with the size of the volume swept by the magnet assembly and average thermal properties. The parasitic heat loss equations were implemented into a model in the form of the distributed load as a local heat flux through the boundary between a regenerator and its casing and the concentrated load, represented in Eq. 5 and Eq. 6, respectively.

$$q_{par,dist} = 20.55\left(T_{amb} - T_f(x,t)\right) - \left(3.29(\overline{T}_{warm\,end,f} - \overline{T}_{cold\,end,f}) - 3.64\right) \qquad \text{Eq. (5)}$$

$$Q_{par,c} = 0.0093(T_{amb} - \overline{T}_{cold\,end,f}) + 0.0646(T_{amb} - \overline{T}_{cold\,end,f}) \qquad \text{Eq. (6)}$$

where: q is the heat flux in W m^{-2}, Q is the rate of the total concentrated load in W, T is the temperature in K, $\overline{T}$ is the average temperature in K, the subscripts *par*, *dist*, *c*, *amb*, *f*, *cold end*, and *warm end* are parasitic, distributed, concentrated, ambient, heat transfer fluid, the cold end of a regenerator and the hot side of the regenerator, respectively.

The first term on the right hand side of Eq. 5 corresponds to the heat flux from the ambient to the cold end of the regenerator and the second term represents the heat transfer from ambient to the electrical heater and the connecting tubes (Monfared, 2018).

The AMR cycle is modeled using the modified partial differential equations suggested by Engelbrecht, (2008). Eq. 7 and Eq. 8 show the included modifications that allows the AMR to be simulated using the innovative method.

$$-(1 - \varepsilon)\rho_s T_s \frac{\partial s}{\partial B}\frac{\partial B}{\partial t} = -k_{ef,s}\frac{\partial^2 T_s}{\partial x^2} - h_{sf,corr}a(T_f - T_s) + (1 - \varepsilon)\rho_s c_{H,s}\frac{\partial T_s}{\partial t} \qquad \text{Eq. (7)}$$

$$\frac{p.q_{par,dist}}{A_c} + \frac{dP}{dx}V_D = \rho_f V_D c_{p,f}\frac{\partial T_f}{\partial x} - k_{ef,f}\frac{\partial^2 T_f}{\partial x^2} + h_{sf,corr}a(T_f - T_s) + \varepsilon\rho_s c_{H,s}\frac{\partial T_s}{\partial t} \qquad \text{Eq. (8)}$$

where: s is entropy in J kg^{-1} K^{-1}, B is magnetic flux density in T, t is time in s, k is thermal conductivity in W m^{-1} K^{-1}, h is convection heat transfer coefficient W m^{-2} K^{-1}, a is specific surface area in m^{-1}, A_c is cross section area of regenerator in m^{2}, V_D is volumetric flow rate divided by cross section area of regenerator in m s^{-1}, x is position along regenerator in m. The subscripts *s*, *ef*, *sf*, *corr*, *H*, and *p* are solid phase, effective, solid-fluid interface, corrected, constant magnetic field, and constant pressure, respectively.

4. RESULTS AND DISCUSSION

Firstly, the series of experiments to find the optimal operational point was run for a constant utilization while varying T_{hot}. The experiments were started at the T_{hot}=293.3 K, then the hot end temperature was lowered for each following test. The last experiment in this series was done at T_{hot}=294.3 K. Figure 3 shows the zero load performance of the fifteen-layer regenerator varying the hot end temperature where a maximum temperature span of 15.4 K was obtained. Shortly after the beginning of the experimental investigation, mechanical disintegration of the material started to develop, resulting in a significant increase in pressure drop of 1.5 bar

for the tested flow rates, which prohibited further investigation. This breakdown of the structure is attributed to mechanical failure of the particles during operation.

One can see from the Figure 3 (a) that the experiment and the simulation results agree quite well at higher temperatures. The reason for the disagreement between simulation and experimental results at lower temperatures is attributed to the disintegration of the regenerator. The mechanical changes in the regenerator must have started earlier than it was possible to notice them and clearly associate the phenomenon to the mechanical collapse rather than inappropriate working temperature. Based on this model's general good agreement with this device using Gd and similar devices using both Gd and La(Fe,Mn,Si)$_{13}$H$_y$, it is likely that the major source of disagreement between model and experiment is the mechanical breakdown of the regenerator rather than issues with the model.

To find out whether the regenerator really disintegrated, experiments were run at constant hot end temperature while varying the utilization. The dashed black curve in Figure 3 (b) shows that the performance of the regenerator decreases drastically regardless of the utilization (region from U=0.20 to U=0.41). Note, that the test at U=0.50 was performed first. The second study against different utilization was performed after the effect of different hot end temperature was investigated. To find out whether the disintegration progressed in time, a series of experiments were started. From Figure 3 (b) (red dotted line), one can see that the initial experimental points were replicated even with one intermediate point at U=0.25 falling into the curve. However, the second intermediate point at U=0.37 showed somewhat better performance. This could be explained by a potentially better alignment of particles in the inner structure of the regenerators at the specific flow rate. However, it was impossible to replicate the first experimental point at U=0.50 because the pressure drop increased too much and the safety valve with the safety point of 4 bar opened during testing, which bypassed fluid flow around the regenerators.
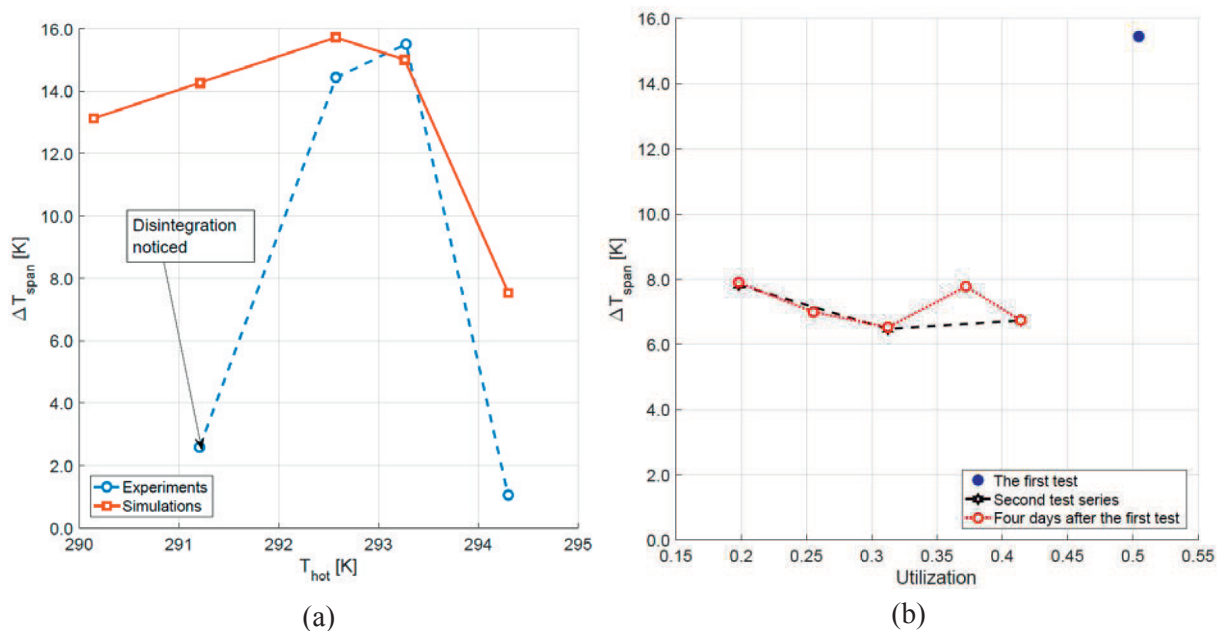
Figure 3. a) The steady state temperature span between the hot and the cold end as a function of the hot end temperature at zero load experiments and the corresponding simulation results. The experimental data points were obtained at 0.5 Hz cycle frequency and U= 0.5, which corresponds to 0.026 m³ h⁻¹ volumetric flow rate. b) The steady state temperature span between the hot and the cold end as a function of the utilization at zero load experiments. The data points were obtained holding the hot end temperature at 292 K. It was not possible to repeat the test at U=0.50 after four days due to the pressure drop increase.

5. CONCLUSIONS

A fifteen-layer La(Fe,Mn,Si)$_{13}$H$_y$ regenerator with 2.3 wt. % epoxy was experimentally investigated in this study. The obtained experimental results were compared with the numerical results. A maximum zero load temperature span ΔT_{span} of 15.4 K was obtained at U=0.50 for a hot end temperature of 292 K. Unfortunately, experiments had to be stopped after only a few experiments due to the mechanical disintegration of the material.

Finally, the experimental point at T_{hot}=293.3 K shows a good agreement with numerical modeling. Unfortunately, it was not possible further validate the model using the regenerator, presented in this study, due to mechanical failure of the material.

ACKNOWLEDGEMENTS

REFERENCES

Bjørk, R., Bahl, C.R.H., 2013. Demagnetization factor for a powder of randomly packed spherical particles. Appl. Phys. Lett. 103.

Bleaney, B., Hull, R.A., Hull R. A., 1941. The Effective Susceptibility of a Paramagnetic Powder, in: Series A, Mathematical and Physical Sciences. Royal Society, London, pp. 86–92.

Brück, E., Tegus, O., Zhang, L., Li, X.W., De Boer, F.R., Buschow, K.H.J., 2004. Magnetic refrigeration near room temperature with Fe_2P-based compounds. J. Alloys Compd. 383, 32–36.

Engelbrecht, K., 2008. A Numerical Model of an Active Magnetic Regenerator Refrigerator with Experimental Validation. University of Wisconsin-Madison, Wisconsin-Madison.

Govindappa, P., Trevizoli, P. V, Campbell, O., Niknia, I., Christiaanse, T. V, Teyber, R., Misra, S., Schwind, M.A., van Asten, D., Zhang, L., Rowe, A., 2017. Experimental investigation of $MnFeP_{1-x}As_x$ multilayer active magnetic regenerators. J. Phys. D. Appl. Phys. 50, 315001.

Kitanovski, A., Tušek, J., Tomc, U., Plaznik, U., Ožbolt, M., Poredoš, A., 2015. Magnetocaloric Energy Conversion. Springer, London.

Lei, T., Engelbrecht, K., Nielsen, K.K., Veje, C.T., 2017. Study of geometries of active magnetic regenerators for room temperature magnetocaloric refrigeration. Appl. Therm. Eng. 111, 1232–1243.

Lei, T., Nielsen, K.K., Engelbrecht, K., Bahl, C.R.H., Neves Bez, H., Veje, C.T., 2015. Sensitivity study of multi-layer active magnetic regenerators using first order magnetocaloric material La(Fe,Mn,Si)13Hy. J. Appl. Phys. 118.

Monfared, B., 2018. Design and optimization of regenerators of a rotary magnetic refrigeration device using a detailed simulation model. Int. J. Refrig. 88, 260–274.

Monfared, B., Palm, B., 2016. New magnetic refrigeration prototype with application in household and professional refrigerators, in: Seventh IIF-IIR International Conference on Magnetic Refrigeration at Room Temperature, Thermag VII.

Monfared, B., Palm, B., 2015. Optimization of layered regenerator of a magnetic refrigeration device. Int. J. Refrig. 57, 103–111.

Richard, M.A., Rowe, A.M., Chahine, R., 2004. Magnetic refrigeration: Single and multimaterial active magnetic regenerator experiments. J. Appl. Phys. 95, 2146–2150.

Rowe, A., Tura, A., Richard, M., Chahine, R., Barclay, J., 2014. An Overview of Operating Experience Using the AMR Test Apparatus 1721.

Zimm, C., Boeder, A., Chell, J., Sternberg, A., Fujita, A., Fujieda, S., Fukamichi, K., 2005. Design and Performance of a Permanent Magnet Rotary Refrigerator, in: 1st International Conference on Magnetic Refrigeration At Room Temperature.

C.2. Passive heat transfer enhancement in 3D corrugated tube

PASSIVE HEAT TRANSFER ENHANCEMENT IN 3D CORRUGATED TUBE

Kristina Navickaitė*, Kurt Engelbrecht, Christian Bahl
Technical University of Denmark, Department of Energy Conversion and Storage, Frederiksborgvej 399, 4000 Roskilde, Denmark
*knav@dtu.dk

Derek Noël
Ecoles de Mines de Nantes, 2 rue Alfred Kastler, Nantes, France

Abstract. An innovative hydraulic design was studied for corrugated tube geometry for a heat exchanger. An ellipse based double corrugation was used as a concept of the geometry. The hydraulic diameter (D_h) is maintained over the tube length while the shape of the cross section varies continuously along the flow direction. 38 corrugated tubes with a D_h of 5 mm were studied numerically with corrugation heights from 0.23 to 0.69 mm and corrugation periods from 5 to 50 mm for laminar flow with water. Computational fluid dynamics (CFD) is used as a tool to study the effect of corrugation geometry on heat transfer and fluid flow with a constant wall temperature and total pressure drop. The governing equations for these problems were solved using the Finite Element Method. The results of numerical modelling show significant increase in NTU for double corrugated tubes compared to a circular tube. The friction factor increases with increasing of severity index, which represents the degree of tube roughness.

Keywords: heat transfer enhancement, pressure drop, numerical simulation, 3D corrugated tube

1. INTRODUCTION

New solutions for more effective energy transfer are desirable due to increased demands for energy efficiency and compact systems. Improved heat transfer allows thermodynamic cycles to operate at conditions that are more efficient and opens new opportunities for alternative cycles and sustainable energy technologies. There are three techniques to enhance heat transfer: passive, active and compound (Kareem, *et al.,* 2015). The first one became the most frequent technique in most engineering applications, e.g. rippled and spirally corrugated tubes in systems for domestic hot water preparation using solar energy. Additionally, corrugated tubes give an advantage for more rapid thermal processing which is very important for retaining natural and organic properties of food (Barba, *et al.,* 2002).

The interest in the augmentation of heat transfer using corrugated tubes has increased significantly in the last five years (Kareem, *et al.,* 2015). Most of the research efforts were made on introducing spirally or transversally corrugated tubes, or techniques to increase heat transfer using fins or wavy strip tapes (Rainieri, *et al.,* 2014; Lazim, *et al.,* 2014; Dong, *et al.,* 2001; Talay Akyildiz, *et al.,* 2011). Srinivasan *et al.* (1994) studied numerically and experimentally the concept of fluted tube. The shape of the cross-section of the fluted tubes was defined by bore diameter, envelope diameter, flute depth, pitch and the helix angle, which depends on the number of flute starts. Thus, the investigated tubes had a different shape of cross-section area, e.g. a triangle shaped cross-section, a multi starts star shaped cross-section. Generally, all the analysed geometries showed an increase in Nusselt number with increasing Reynold number (*Re*) within the laminar flow regime. Hærvig *et al.* (2017) in the study of the spirally corrugated tubes concluded that increasing corrugation length increases the Nusselt number. Moreover, the same study showed that at high corrugation flow is radically different which results in slight increase in heat transfer, while pressure loss increases significantly (Hærvig, *et al.,* 2017).

In order to deform the thermal boundary layer more robust methods, such as artificial increase of wall roughness by inserting oblique teeth, have also been applied (Saha, 2010). All those approaches increase the surface area for heat transfer while also increasing pressure drop. To find the optimal geometry for the enhanced heat transfer with acceptable penalty of pressure drop numerous modelling and experimental studies have been done on corrugated tubes. The major part of the reported tubes are spirally corrugated. However, several studies reported performance of tubes which are shaped in sinusoidal manners (Hærvig, *et al.,* 2017; Mahmud, *et al.,* 2003; Phan-Thien & Khan, 1987; Tong, *et al.,* 2011). Most studies, both experimental and modelling, that investigated the heat transfer using the passive techniques were performed at low Reynolds number (Cao, *et al.,* 2014; Osley, *et al.,* 2013; Saha, 2013; Mills, *et al.,* 2014; Saha, 2010; Vicente, *et al.,* 2004; Mahmud, *et al.,* 2003; Zachár, 2010). Generally, it was found that the heat transfer in a corrugated tube of a given geometry increases in a certain range of *Re*. Further increasing *Re* decreases heat transfer.

This paper presents a novel geometry of a tube that is corrugated in both the transverse and annular directions, such that the hydraulic diameter (D_h) at any point in the flow direction is constant but that the aspect of the flow channel varies continuously in the flow direction. The variation of channel aspect causes the tube walls to constantly impinge on the area for fluid flow remains constant, the increase in pressure drop is minimized. The CFD (*Computational fluid dynamics*)

analysis was conducted in the laminar flow regime ($Re \leq 1500$) and constant pressure drop over the tube length. The problem of constant surface temperature (T_s) was analysed.

2. THE GEOMETRY OF DOUBLE CORRUGATED TUBES

A double corrugated tube geometry based on ellipses maintaining a constant hydraulic diameter has been conceived as shown in Figure 1 and the geometrical parameters of the representative tube are given in Table 1. Equation 1 defines the geometry of a tube along the z direction corrugated in x and y direction. The cross section of the tube at any point in the flow direction is defined as an ellipse with one axis equal to x and the other equal to y. At some points x and y are equal, and the cross section is circular.

$$\begin{cases} x=R_{\mathrm{h}}e^{\left(k_1\,sin\left(\frac{2\pi}{k_2}z\right)\right)}+R_{\mathrm{h}} \\ y=R_{\mathrm{h}}e^{\left(-k_1\,sin\left(\frac{2\pi}{k_2}z\right)\right)}+R_{\mathrm{h}} \end{cases} \tag{1}$$

where R_{h} is a hydraulic radius of a non-circular geometry, k_1 and k_2 are coefficients for corrugation height and corrugation length, respectively. There $k_1 \in [0.2; 0.8]$ and $k_2 \in [5; 50]$. The geometry of a tube might be modified by varying k_1, resulting in changes of a corrugation height (e), and k_2, resulting in changes of the corrugation period length (p). The severity index was proposed to measure the degree of tube roughness and it is defined as in Eq. 2.

$$\varphi=\frac{e^2}{pD_{\mathrm{h}}} \tag{2}$$

where D_{h} is the hydraulic diameter. Note that corrugation height corresponds to a depth of corrugation in this study, since the corrugation of the represented tubes changes by an exponential manner. As shown in Table 1, the corrugated tube has 25.9 % more surface area on the inner wall of the tube compared to a straight tube.
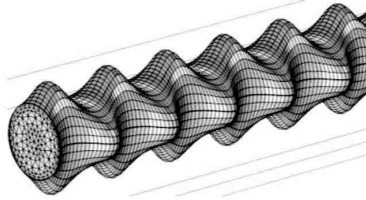

Figure 1. The isometric view of a double corrugated tube after being meshed in COMSOL.

Table 1. The geometrical data of the double corrugated tube, shown in Fig. 1 and the circular tubes.

Parameter	Length, mm	Hydraulic diameter, mm	Severity index, [-]	Corrugation length, mm	Corrugation height, mm	Inner surface area, mm^2
Corrugated tube	100	5	0.016	5	0.63	1968.2
Circular tube	100	5	0	∞	0	1570.8

The purpose of this study is to analyse the corrugation effect on flow rate and heat transfer while the geometrical parameters of are varied in a range $e \in [0.23; 0.69]$ mm and $p \in [5; 50]$ mm.

3. MATHEMATICAL FORMUALTION

3.1. Modelling and performance validation

Aiming to make the simulations computationally less expensive, only a quarter of the cross section of a tube one period long was modelled for each corrugated tube. A quarter of a circular tube with a corresponding length to each corrugated tube is modelled for a comparison. Thus, input pressure gradient is normalized by corrugation length – a period of a tube and the symmetry boundary condition (BC) is applied. The NTU method was used for the tube analysis. Since the problem of a constant wall temperature is analysed, the general assumption that the ratio of the heat capacity rates C_r is equal 0. Thus, Eq. 3 is used to evaluate the tubes. The comparison of the tube performance was made holding the length of tubes constant rather than the surface area, as the corrugations increase the surface area per length of tube.

$$q=\varepsilon\,C_{\min}(T_{\mathrm{h}}-T_{\mathrm{c}}) \tag{3}$$

where q is the heat transfer rate, T is the bulk fluid temperature, subscripts h and c denote hot fluid inlet and cold fluid, respectively, C_{min} is the minimum heat capacity rate, defined by Eq. 4, ε is the effectiveness, which is defined by Eq. 5.

$$C_{min} = \dot{m}\rho c_p \tag{4}$$

where $\dot{m}$ is the mass flow rate of the fluid, ρ is the density of water (1000 kg/m^3) and c_p is the specific heat of water (4.138 kJ/kgK). Then, the number of transfer units NTU is calculated as following.

$$\varepsilon = 1 - \exp(-NTU) \tag{5}$$

Equation 6 defines the average Nusselt number for the modelled tubes, $\overline{Nu}_D$, with a constant surface temperature:

$$\overline{Nu}_D = \frac{\bar{h}D}{k} \tag{6}$$

where D is the volume based diameter (Srinivasan, et al., 1994), k is the thermal conductivity of water (0.603 W/mK), and $\bar{h}$ is the average convection coefficient, defined by Eq. 7.

$$q_{conv} = \bar{h}A\Delta T_{lm} \tag{7}$$

where A is surface area, q_{conv} is the convective heat transfer, defined by Eq. 8, and ΔT_{lm} is the logarithmic mean temperature difference, defined by Eq. 9.

$$q_{conv} = \dot{m}c_p(\Delta T_i - \Delta T_o) \tag{8}$$

$$\Delta T_{lm} = \frac{\Delta T_o - \Delta T_i}{\ln\left(\frac{\Delta T_o}{\Delta T_i}\right)} \tag{9}$$

where $\Delta T_{o,i}$ is the temperature difference between the surface T_s and the outlet and the inlet of the tube denoted by subscripts o and i, respectively. The volume based Reynolds number Re_D is defined by Eq. 10 (Srinivasan, et al., 1994).

$$Re_D = \frac{\rho D u_m}{\mu} \tag{10}$$

where: u_m is the mean flow velocity, μ is the dynamic viscosity of water (0.0008 Pa-s).
To analyse the flow resistance the Darcy-Weisbach friction factor is calculated as defined by Eq. 11.

$$f = \Delta p \frac{2D_h}{\rho u_m^2 p} \tag{11}$$

where: Δp is the pressure drop.

3.2. Governing equations and boundary conditions

The commercially available CFD software package COMSOL was used to model the double corrugated tubes. The SIMPLE algorithm was used to couple the fluid dynamic and heat transfer equations. The Navier-Stokes equation for incompressible, laminar, pressure driven fully developed internal flow being solved (Eq. 12).

$$\mu\nabla^2 u = \frac{\partial p}{\partial z} \tag{12}$$

where: u is the fluid velocity in the z direction, $\frac{\partial p}{\partial z}$ is the pressure gradient in the z direction. No-slip boundary conditions (BC) are applied. To ensure that the flow is fully developed, a periodic BC with a pressure gradient is applied. The stationary heat transfer equation, neglecting pressure work, is solved as defined in Eq. 13.

$$\rho c_p \mathbf{u}\nabla T = \nabla \cdot (k\nabla T) \tag{13}$$

where: $\mathbf{u}$ is the flow velocity vector. The BC for modelling were derived for a circular tube which is 240 mm long and Reynolds number $Re = 1500$. The pressure drop in such a tube was calculated using Eq. 11 and normalised by the length of each of the modelled tubes. The modelling BCs are given in Table 2.
Table 2. The boundary conditions for flow dynamic and heat transfer simulations.

T_h	T_s	Δp	Pr	ρ	k	μ
303 [K]	281 [K]	59 [Pa]	5.5	1000 [kg/m³]	0.603 [W/mK]	0.0008 [Pa s]

3.3. Mesh selection and model validation

The swept mesh with triangular elements option is used to mesh all the modelled tubes, since it allows non-uniform element size over the geometry. A mesh independency study was carried out to ensure the reliability of the numerical modelling. Flow rate and heat transfer rate were selected as the quantities of interest. Ten different sizes of meshes with the element density from 408 to 4014 elements/mm³ were analysed. The term of element density is introduced since the geometry of the tubes varies with corrugation height and corrugation length. Thus, the concept of element density per geometry is used as a qualitative quantity to evaluate the consistency of a mesh over the different geometries. Relative errors (*err*) of the control quantities are calculated as described in Eq. 14 (Zachár, 2010).

$$err=100 \left| \frac{f_c - f_f}{f_f} \right| \tag{14}$$

where: *f* is the value of interest and subscripts c and f denote the coarsest and the fines meshes, respectively. Calculated results showed that the difference between flow rate as well as heat transfer rate on the finest and on the fifth finest mesh (element density is 2194 elements/mm³) is 0.015 %. The obtained *err* is less than 0.5 % thus, the accuracy of numerical models, when the selected mesh was used, was accepted. Furthermore, the values of the heat transfer rate, obtained during the study of mesh independency, follow the asymptotical behaviour. Thus, it is concluded that the study is mesh independent. Figure 2 shows the extreme geometry case meshed with the selected mesh.
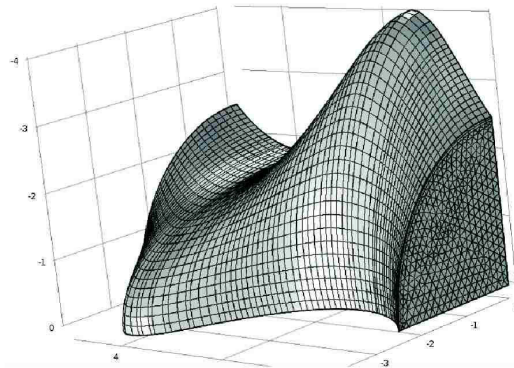

Figure 2. The extreme geometry case after being meshed in COMSOL.

The general model used in this study was validated by solving fluid flow problem in a circular tube assuming that the flow properties are following $Re = 1500$, $\rho = 1000$ kg/m³ and $\mu = 0.0008$ Pa-s. Figure 3 shows an excellent agreement between the analytical solution and modelling results, thus the model is valid.

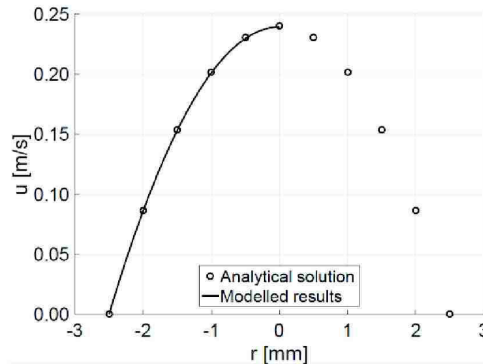

Figure 3. The velocity profile for a circular tube at the given flow conditions, solved analytically and obtained in a model.

4. RESULTS AND DISCUSSION

The heat flux for each tube was calculated and a representative case for both the corrugated and straight tube are shown in Figure 4. One can see that the heat transfer is taking place along the full length of the corrugated tube in Figure 4 a), while the intensity of heat transfer vanishes in a circular tube in the flow direction in Figure 4 b). The first results obtained by the models showed agreement with the hypothesis of the interrupted flow boundary layers.
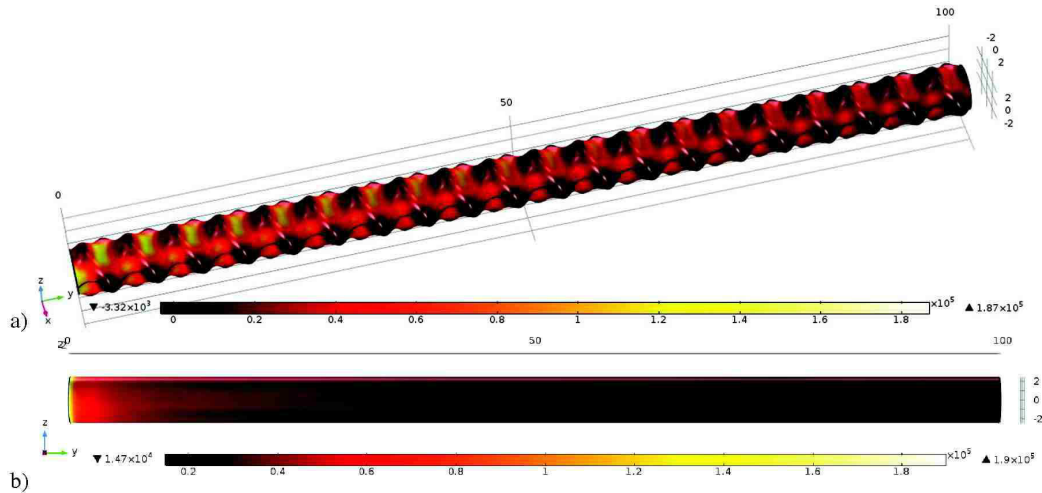

Figure 4. The scale bars show the modelling results for heat flux in W/m^2 at the same pressure gradient ($\Delta p = 13.6$ Pa) conditions in a) a double corrugated tube (flow rate 1.2e-6 m³/s) and in b) a circular tube (flow rate 2.5e-6 m³/s). The tube geometry is described in Table 1.

The data obtained using the modelling approach described in section 3 are presented further in this study. Figure 5 gives the fluid flow behaviour in a) circular and b) double corrugated tube with $e = 0.69$ mm and $p = 20$ mm. One can observe that the fluid in the double corrugated tube is compressed in the way that faster moving fluid is closer to the tube wall on the one side, while slower mowing fluid is closer on the other side. This phenomenon changes sides after each half period, and the both the thermal and hydraulic boundary layers are disturbed. Thus, warmer layers of the flow should be somehow closer to the wall for the corrugated tube than they are in the circular tube.

Figure 6, Figure 7, Figure 10 and Figure 9 represent the modelling results obtained for corrugated tubes, which are point by point normalised with the corresponding length of a circular tube. It is noticeable that the Darcy – Weisbach friction factor as well as the Reynolds number are constant for a circular tube independently of length of a tube. Quantities related to the heat transfer such as NTU and $\bar{h}$ are changing with the length of the tube, since the thermal entrance problem is solved in this study.
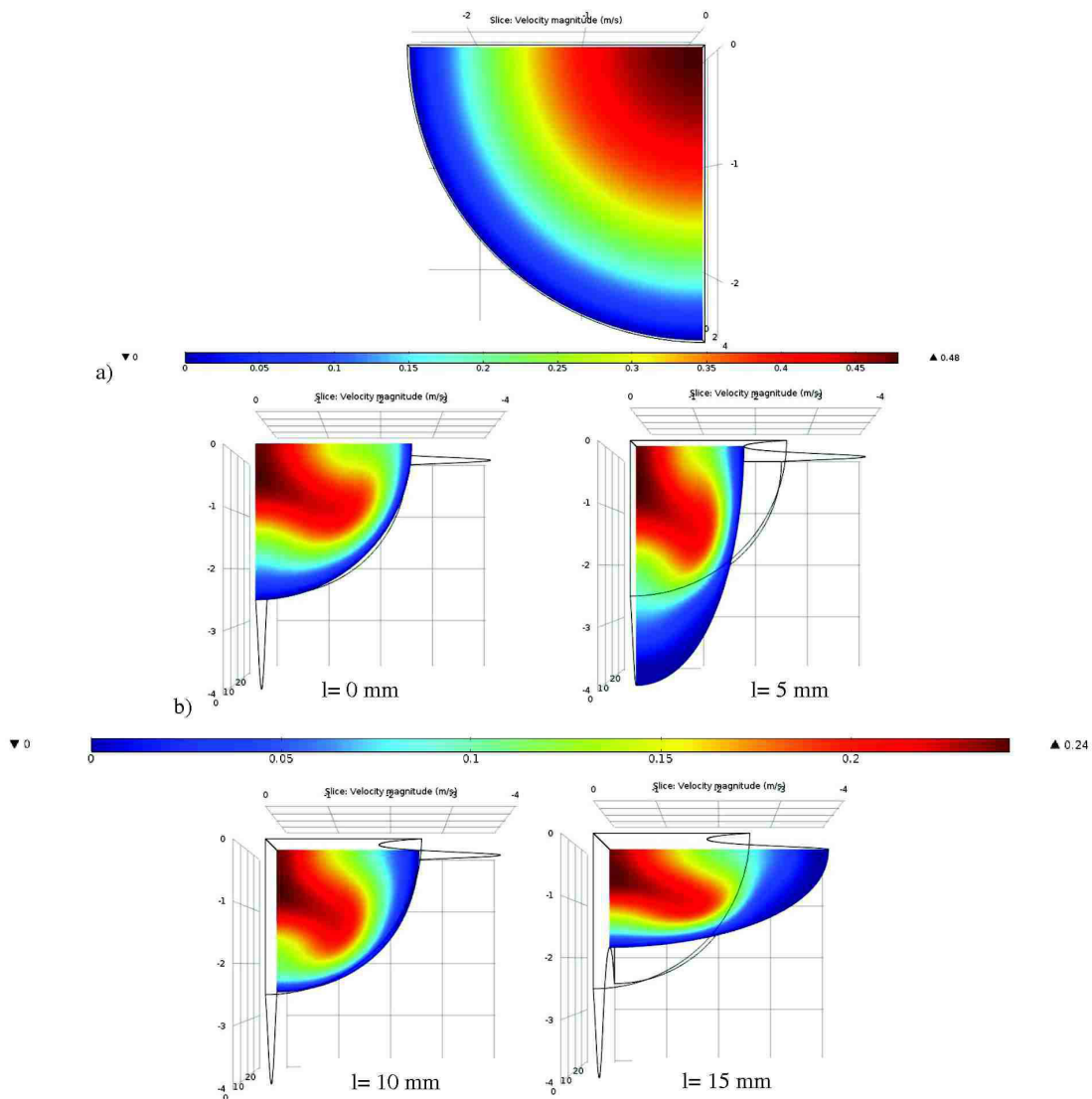
Figure 5. a) The cross-sectional view of the fully developed laminar flow in a circular tube. b) The cross-sectional view at different positions l after the inlet of the double corrugated tube ($e = 0.69$ mm, $p = 20$ mm). Note black lines here represents the edges of the geometry. The scale bar shows the fluid velocity in m/s.

Figure 6 shows the ratio of the surface area over the corrugated tubes with respect to corresponding circular tube. Even though the changes in the surface area of the corrugated tubes are presented per single period of a tube, it is given as a function of a corrugation length. This is because the surface area increases more for a short corrugation length than for a longer corrugation length, when the same corrugation height is considered. It is noticeable that even at the extreme geometry case – the highest corrugation height e and the shortest corrugation length p - the surface area does not increase more than 35 %. Moreover, the surface area increases less than 15 % for all the analysed cases when corrugation lengths are above 20 mm.
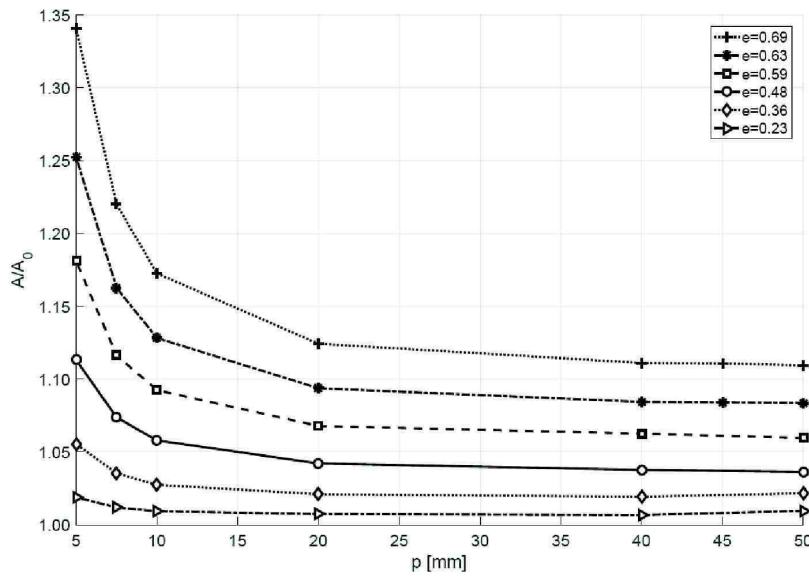
Figure 6. The inner surface area of corrugated tubes (A) in comparison with the circular tube (A_0) in a corresponding length as a function of corrugation length at several corrugation height.

Figure 7 shows the ratio between the friction factors over the modelled tubes in comparison with the circular tube. One can see that short corrugation periods (up to 10 mm) and small corrugation height (up to 0.36 mm) have a very small impact on friction factor, as if the diameter of a conventional circular tube would be smaller in the magnitude of double corrugation height. The corrugation effect starts having an impact on a fluid flow when the corrugation length or height is increased. It is also noticeable that the effect, caused by corrugation becomes lower when the corrugation length is increased. This is because the geometry approaches the plain tube. Mills *et al.* (2014) showed that flow at the high Reynolds number is insensitive for an intense corrugation with a short period. Thus, it is more convenient to use corrugated tubes with longer corrugation length for a flow at high Reynolds number.
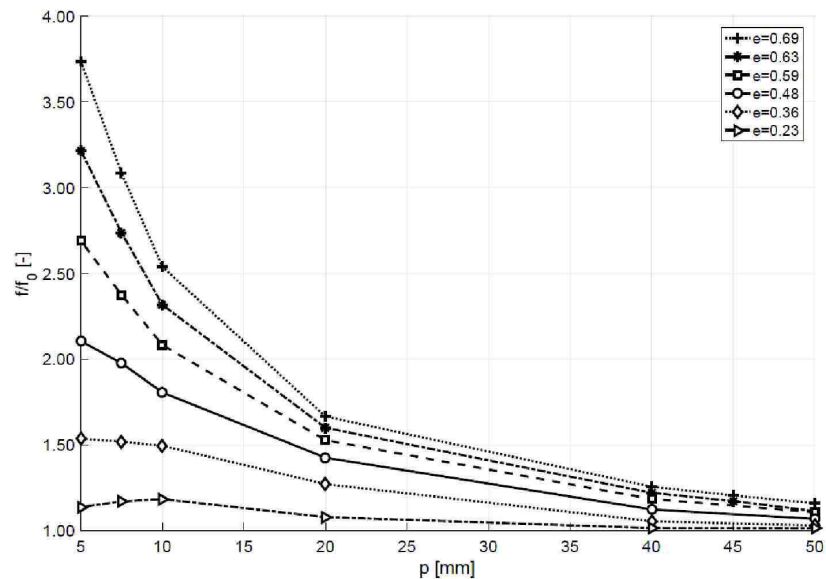
Figure 7. Friction factor in corrugated tubes (f) in comparison with the circular tube (f_0) in a corresponding length as a function of corrugation length at the same pressure gradient.

Figure 8 shows that, due to the same effect as described above, the Reynolds number has an inverse dependency on the corrugation length for the tubes with $e = 0.23$ mm and $e = 0.36$ mm with the corrugation length $p = 5$ mm and $p = 7.5$ mm. This phenomenon changes to linear behaviour when $p \leq 10$ mm for the same corrugation height. Other geometries

showed nearly linear behaviour all over the range of corrugation length. The Reynolds number increased with increasing corrugation length. It is interesting that the changes in Reynolds number with increasing corrugation height become less and less noticeable. For instance, difference in Reynolds number between tubes with $e = 0.36$ mm and $e = 0.48$ mm at $p = 20$ mm $\Delta Re_D = 120$, and for tube with $e = 0.48$ mm and $e = 0.59$ mm at the same corrugation length - $\Delta Re_D = 63$, even though the difference in corrugation height is approximately the same.
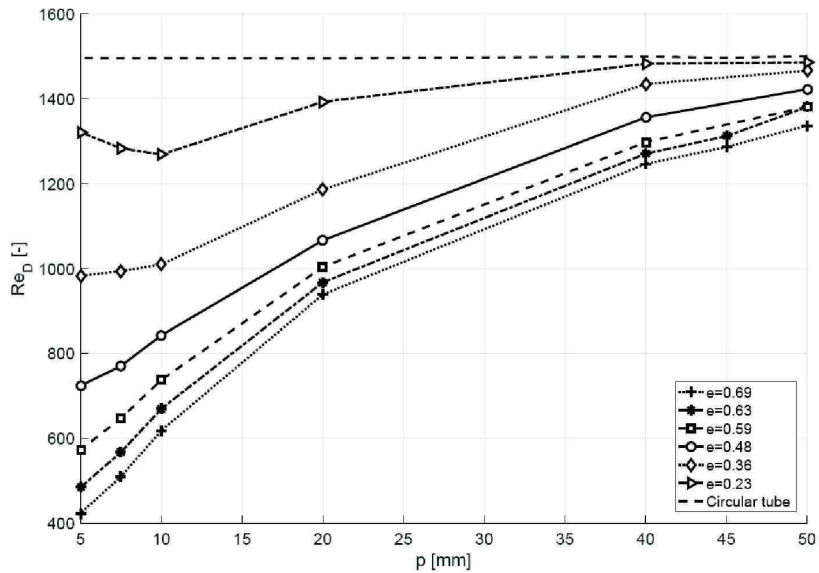
Figure 8. Volume based Reynolds number as a function of corrugation length at the constant pressure gradient.
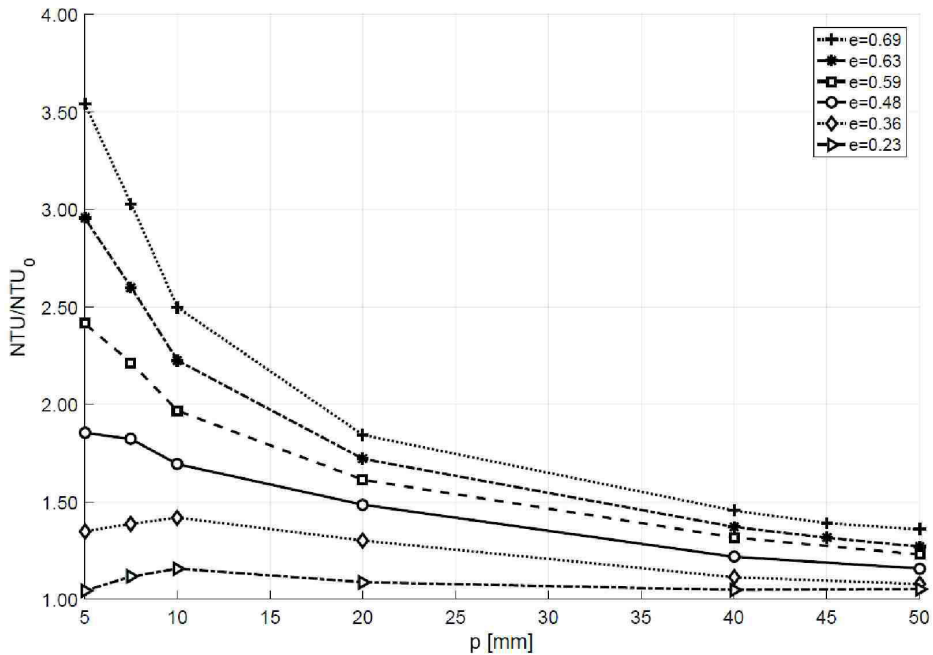
Figure 9. Ratio of NTU of the corrugated tubes (NTU) with the circular tube (NTU$_0$) as a function of corrugation length at the constant pressure gradient.

Figure 9 shows the NTU analysis of the corrugated tubes in comparison with the circular tube. Note that the flow rate in the corrugated tubes, at fixed pressure drop, is decreasing due to the increasing friction factor. NTU analysis shows that corrugation has a positive impact on heat transfer. However, the effectiveness of corrugation is diminished when the

corrugation length increases. This may be explained by a combination of several factors. Firstly, the flow rate in a corrugated tube in general is lower than in the corresponding circular one under the same pressure gradient, thus the transported amount of heat is lower. Secondly, disturbance of the thermal boundary layers becomes gentler when the corrugation length increases. Additionally, Vincente *et al.,* (2004) concluded that the higher the severity index is the larger the heat transfer is, at low Reynolds numbers. Indeed, analysing each series of tubes separately, the severity index decreases when the corrugation length increases and corrugation height is kept constant.

From Figure 10, one can see that the average Nusselt number at the thermal entrance region of tubes increases slightly when the corrugation length is $p \leq 10$ mm. The decrease in Nusselt number is significant at the intense corrugation case ($p = 5$ mm). However, the sharp peaks at p = 7.5 mm can be explained as a combination of low flow rates and much lower change in surface area of the corrugated tubes. The flow rate in the corrugated tubes increases to the value of the flow rate in corresponding circular tubes when the corrugation length increases. Nonetheless, the change in surface area decreases when the corrugation length increases. The ratio of surface area in the corrugated tubes and corresponding circular tubes decreases very sharply at short corrugation lengths and high corrugation height, while the change at long corrugation length is very modest. Thus, the sharp peaks in average Nusselt number can be explained as a combination of modest change in flow rate, while the change in the surface area is significant. Nevertheless, the phenomena at the $p = 7.5$ mm requires deeper investigations in the flow dynamics.

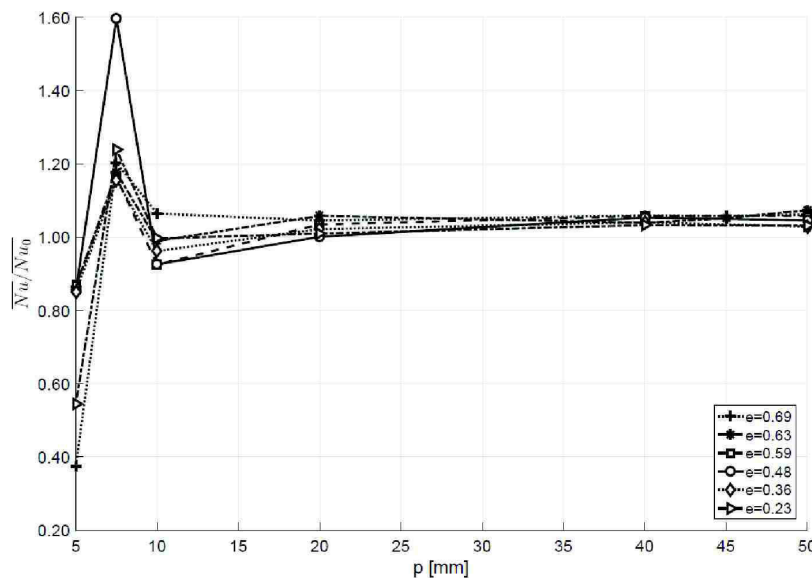Figure 10. Ratio of the average Nusselt number over corrugated tubes ($\overline{Nu}$) between the average Nusselt number over circular tube ($\overline{Nu}_0$) as a function of corrugation length at the constant pressure gradient.

However, to have a full picture of effectiveness of this type of corrugation, more analysis has to be done. The heat transfer in the corrugated tubes under the same flow rate and fully developed heat flow is of interest. Moreover, it would also be interesting to see what effect this type of geometry has on two-phase flow. Finally, an experimental investigation is necessary to validate the results of the modelling.

4. CONCLUSIONS

In this study, 38 double corrugated tubes were analysed under the same pressure gradient and constant wall surface temperature. We show that the novel geometry of double corrugated tubes affects the fluid flow in the way that the thermal boundary layer at the wall is not allowed to fully develop compared to a straight tube and the heat transfer through the tube is enhanced. Even at the same pressure gradient, NTU is increased more than three times at high corrugation with a short period. Moreover, the Nusselt number slightly increases in corrugated tubes, even though the flow rate is reduced significantly.

The friction factor increases sharply when the corrugation length decreases and corrugation height increases. We found that fluid at the high Reynolds number passes peaks in corrugation, when corrugation length is short, with a minor disturbance in the flow path. Thus, it is recommended to use an intense corrugation for flow with low Reynolds numbers. However, more investigation has to be done in order to fully characterize the corrugated tubes and derive recommendations for possible applications.

6. REFERENCES

Barba, A., Rainieri, S. & Spiga, M., 2002. Heat transfer enhancement in a corrugated tube. *International communicartion in heat and mass transfer,* 29(3), pp. 313-322.

Cao, Z. et al., 2014. Numerical simulation of modulated heat transfer tube in laminar flow regime. *International Journal of Thermal Sciences,* Volume 75, pp. 171-183.

Dong, Y., Huixiong, L. & Tingkuan, C., 2001. Pressure drop, heat transfer and performance of single-phase turbulent flow in spirally corrugated tubes. *Experimental thermal and fluid science,* Volume 24, pp. 131-138.

Hærvig, J., Sørensen, K. & Condra, T. J., 2017. On the fully-developed heat transfer enhancing flow field in sinusoidally, spirally corrugated tubes using computational fluid dynamics. *International journal of heat and mass transfer,* Volume 106, pp. 1051-1062.

Kareem, Z. S. et al., 2015. Passive heat transfer enhancement review in corrugation. *Experimental Thermal and Fluid Science,* Volume 68, pp. 22-38.

Lazim, T. M. et al., 2014. Heat transfer enhancement in spirally corrugated tube. *International review on modelling and simulations,* 7(6), pp. 970-978.

Mahmud, S., Islam, A. K. M. S. & Feroz, C. M., 2003. Flow and heat transfer characteristics inside a wavy tube. *Heat and mass transfer,* 39(5-6), pp. 387-393.

Mills, Z. G. et al., 2014. Onset of unsteady flow in wavy walled channels at low Reynolds number. *Physics of fluids,* 26(8), p. 1.4892345.

Osley, W. G., Droegemuller, P. & Ellerby, P., 2013. *CFD investigation of heat transfer and flow patterns in tube side laminar flow and the potential for enhancement.* 10.3303/CET1335166, Italian Association of Chemical Engineering - AIDIC, pp. 997-1002.

Phan-Thien, N. & Khan, M. M. K., 1987. Flow of an oldroyd-type fluid through a sinusoidally corrugated tube. *Journal of Non-Newtonian fluid mechanics,* 24(2), pp. 203-220.

Rainieri, S., Bozzoli, F. & Cattani, L., 2014. *Passive techniques for the enhancement of convective heat transfer in single phase duct flow.* Italian union of Thermo-fluid-dynamics, IOP Publishing.

Saha, S. K., 2010. Thermohydraulics of laminar flow through rectangular and square ducts with axial corrugation roughness and twisted tapes with oblique teeth. *Journal of Heat Transfer-transactions of the Asme,* 132(8), pp. 1-12.

Saha, S. K., 2013. Thermohydraulics of laminar flow through a circular tube having integral helical corrugations and fitted helical screw-tape insert. *Chemical Engineering Communications,* 200(3), pp. 418-436.

Srinivasan, V., Vafai, K. & Christensen, R. N., 1994. Analysis of heat transfer and fluid flow through a spirally fluted tube using a porous substrate approach. *Journal of heat transfer-transactions of the Asme,* 116(3), pp. 543-551.

Talay Akyildiz, F., Siginer, D. A. & Khezzar, L., 2011. Energy losses and heat transfer enhancement in transversally corrugated pipes. *International journal of heat and mass transfer,* Volume 54, pp. 3801-3806.

Tong, Z., Zhu, K., Lu, J. & Li, G., 2011. Numerical study of laminar flow and heat transfer characteristic in wave tubes based on sine curve. *Advanced material research,* 322(322), pp. 349-+.

Vicente, P., Garcia, A. & Viedma, A., 2004. Mixed convection heat transfer and isotermal pressure drop in corrugated tubes for laminar and transition flow. *International communication in heat and mass transfer,* 31(5), pp. 651-662.

Zachár, A., 2010. Analysis of coiled-tube heat exchangers to improve heat transfer rate with spirally corrugated wall. *International journal of heat and mass transfer,* 53(19-20), pp. 3928-3939.

C.3. Epoxy-bonded La(Fe,Mn,Si)$_{13}$H$_y$ as a multi layered active magnetic regenerator

EPOXY-BONDED La(Fe,Mn,Si)$_{13}$H$_z$ AS A MULTI LAYERED ACTIVE MAGNETIC REGENERATOR

Henrique Neves Bez[(a)], **Kristina Navickaitė** [(a)], **Tian Lei**[(a)], **Kurt Engelbrecht**[(a)], **Alexander Barcza**[(b)], **Christian R. H. Bahl**[(a)*]

[(a)] *Department of Energy Conversion and Storage – Technical University of Denmark, Frederiksborgvej 399, Roskilde, Denmark*
[(b)] *Vacuumschmelze GmbH & Co. KG, D-63450 Hanau, Germany*
[*]Corresponding author. E-mail: chrb@dtu.dk

ABSTRACT

The high magnetocaloric effect and tunability of the Curie temperature over a broad range makes La(Fe,Mn,Si)$_{13}$H$_z$ a promising magnetocaloric material for applications. Due to a volume change across the transition and the brittleness of the material as well as erosion due to fluid flow, the particles of the material may break apart during operation. In this context, we studied epoxy-bonded La(Fe,Mn,Si)$_{13}$H$_z$ regenerators, in a small versatile active magnetic regeneration (AMR) test device with a 1.1 T permanent magnet source. The magnetocaloric material was in the form of packed irregular particles (250-500 μm), which were mechanically held in place by an epoxy matrix connecting the particles, improving the mechanical integrity, while allowing a continuous porosity for the fluid flow. Water with 2 wt% ENTEK FNE as anti-corrosion additive was used as the heat transfer fluid for the epoxy-bonded regenerators. A series of AMRs was evaluated by varying the epoxy content in the range 1-4 wt%.

1. INTRODUCTION

Since the discovery of a material with a giant magnetocaloric effect two decades ago[1] there has been a desire to translate the very high entropy change observed into an increased performance in a magnetocaloric device. Since the first room temperature device presented by Brown in 1976[2] most magnetocaloric devices have used materials with a second order phase transition (SOPT). In these materials the transition between the ferromagnetic and the paramagnetic phase results in a smooth entropy change across a broad temperature range. Contrary to this, the discontinuous transition in materials with a first order phase transition (FOPT) results in a very sharp and narrow entropy change. However, the peak values of the entropy change are in general several times higher than those found in SOPT materials.

In order to improve performance, first order magnetic phase transition magnetocaloric materials may be used in the AMR. One of the most promising FOPT materials' series is La(Fe,Mn,Si)$_{13}$H$_z$[3]. This material has the Curie temperature, T_C, near room temperature, while it can be finely tuned by the Fe/Mn/Si ratio. Still, using FOPT materials instead of SOPT ones is not trivial and further considerations must be taken. Firstly, FOPT materials exhibit hysteresis [4], although it has been shown that for the La(Fe,Mn,Si)$_{13}$H$_z$ series it is rather small and in the range of 1 K [5]. Additionally, by definition FOPT materials exhibit a discontinuous phase transition over temperature and field, which is the reason that they exhibit large magnetocaloric effect. Nevertheless, the temperature range where there is a significant magnetocaloric effect is much narrower for FOPT materials. For example, the full width at half maximum of the Δs peak of Gd is about 30 K [6] for a field change of 1 T, while for La(Fe,Mn,Si)$_{13}$H$_z$ it can be as low as 7 K [5]. This brings forth the necessity of layering the regenerator with La(Fe,Mn,Si)$_{13}$H$_z$ with slightly different compositions along the direction of the temperature span, in such a way that the working temperature of each layer is optimized. This engineering is not straightforward and many complications have been shown elsewhere [7]. Furthermore, due to the necessity of interstitial H in order to bring the T_C to near room temperature without significant changes of the magnetocaloric properties, the shapeability of the material is compromised, as the hydrogenation process must be performed while the material is in the powder form and further sintering options remain limited [8].

Moreover, this material undergoes a volume change of ~0.9 vol% during the magnetic phase transition [8,9]. Given the brittleness of the material, microstructure and secondary phases, the volume change may lead to

cracking [10,11]. A method proposed to avoid cracking and erosion of the material under application is to bond the particles of the magnetocaloric material with epoxy, increasing the mechanical stability of the regenerator while still maintaining a continuous porosity [12].

In this context, we evaluate the performance of La(Fe,Mn,Si)$_{13}$H$_z$ epoxy-bonded double layer AMRs. The factors investigated here are: the effect of epoxy content; the heat transfer fluid; the effect of layering; and the utilization.

2. EXPERIMENTAL PROCEDURE

Fine particles of five slightly different compositions of La(Fe,Mn,Si)$_{13}$H$_{1.65}$ were used to make regenerators. The materials were produced by the same processing route[3] and will in the following be identified by their Curie temperature, measured by magnetometry.

Two types of regenerators were made: one with loose particles, held in place mechanically with a mesh at either end and a second where the particles were bonded together by a small amount of epoxy. In both cases the regenerators were cylindrical and made to fit into the versatile test device described previously[13,14]. The regenerator moves in and out of the 40 mm diameter bore of a 1.1 T permanent magnet Halbach cylinder. The device is placed in a temperature controlled cabinet, and the hot end temperature, T_{hot}, is fixed by a heat exchanger to be slightly above the ambient temperature in the cabinet, T_{amb}.

A table listing the regenerators tested is given below. The particle sizes were in a range of 250-500 μm and the regenerators had a porosity of 55%. The relatively high porosity is due to the relatively high irregularity of the shape of the particles, leading to a low packing density. The epoxy bonded regenerators were all fixed in 40 mm long pieces of Perspex tube, as shown in Fig. 1 all with masses of 95 g. The non-bonded regenerators were held in a custom container allowing filling with different amounts of material. Additionally, the viscosity and density of the transfer fluids were evaluated in an Anton Paar Lovis 2000 M/ME viscometer.

Name	Description	T_C	Mass
Single	Single layer regenerator with no epoxy	23.3 ℃	48 g
Double	Double layer regenerator with no epoxy	19.2 and 23.3 ℃	25 g each
Single4wt%	Single layer regenerator with 4 wt.% epoxy	22 ℃	95 g
Double1wt%	Double layer regenerator with 1 wt.% epoxy	23 and 26.6 ℃	95 g
Double2wt%	Double layer regenerator with 2 wt.% epoxy	23 and 26.6 ℃	95 g
Double4wt%	Double layer regenerator with 4 wt.% epoxy	23 and 26.6 ℃	95 g

Table 1: Description and properties of the regenerators for each given name.

Fig. 1 : Photo of an epoxy bonded regenerator, pen top for scale.

3. RESULTS AND DISCUSSION

For the regenerator tests we used two different corrosion protection additives, which have previously been shown to be effective for La(Fe,Mn,Si)$_{13}$H$_z$ type material, namely ethylene glycol based automotive antifreeze (EG) and Entek FNE (NT) [15]. Viscosity and density of water with different amounts of these additives were measured and compared to pure water, as shown in Fig. 2. The measurements were done at 20 ºC, which is close to the range the regenerators are tested in. Previous experience has shown that a concentration of around 15% of EG is needed for good corrosion protection, while concentrations in the order of 1-2% are sufficient when using NT. It is observed in Fig. 2 that the effect of the additive on the density and viscosity is much less for NT than for EG, presumably due to the much smaller concentrations. It can be noted that the change in viscosity per percent of additive is approximately the same while the effect on density is higher per percent of EG than NT. Also, while there is a significant change in the absolute viscosity of about 50% for EG and 20% for NT, the difference in density is only of the order of 3% for EG and less than 1% for NT.
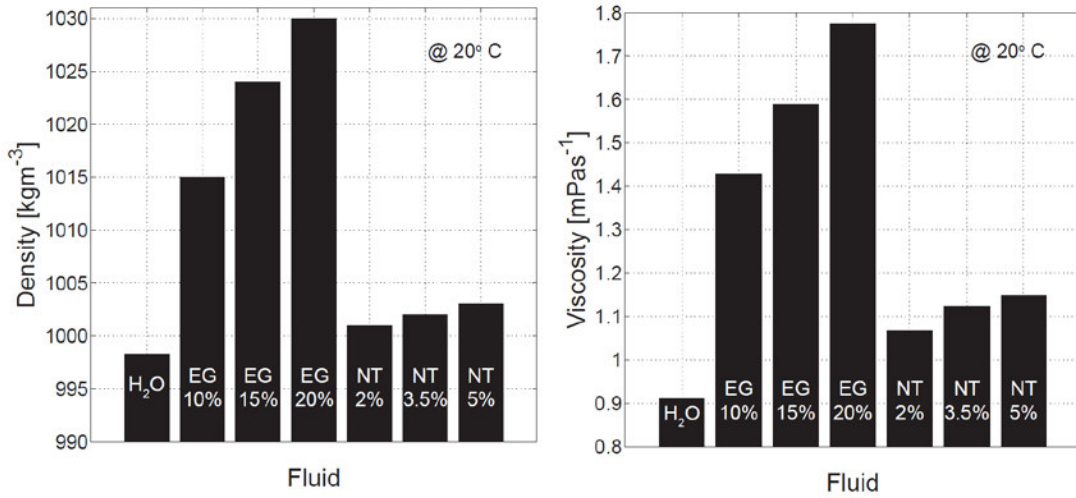

Fig. 2 : (a) The density and (b) the viscosity of the different fluids.

The apparent mechanical strength of the regenerators is generally good. However, during the regenerative tests the *Double1wt%* regenerator with just 1 wt.% of epoxy could not withstand the forces during operation and the regenerator broke apart.

We initiate the investigation of the regenerative performances by evaluating the influence of the utilization at a T_{hot} in the region of the maximum temperature span. The utilization, ϕ, is defined as

$$\phi = \frac{m_f c_f}{m_s c_s}$$

(1)

where m_f is the mass of the fluid pushed through the regenerator in one direction, c_f is the specific heat of the fluid, m_s is the mass of the solid regenerator and c_s is the specific heat of the regenerator material. The values used for c_s and c_f are 480 [5] and 4200 Jkg^{-1}K^{-1}, respectively.

Since the utilization is linearly proportional to the blown fluid mass, m_f, in Fig. 3 ΔT_{span} is shown as a function of the blown fluid mass. One can see that the trend of the span versus the m_f is approximately the same for the two regenerators without epoxy, independent of the number of layers and amount of material. The epoxy bonded regenerators have the peak at the same blown fluid mass as the ones without epoxy. Nonetheless, the mass of the solid regenerator is basically double of the ones without epoxy, and as we can see in equation (1) the effect will be to decrease the utilization by half.
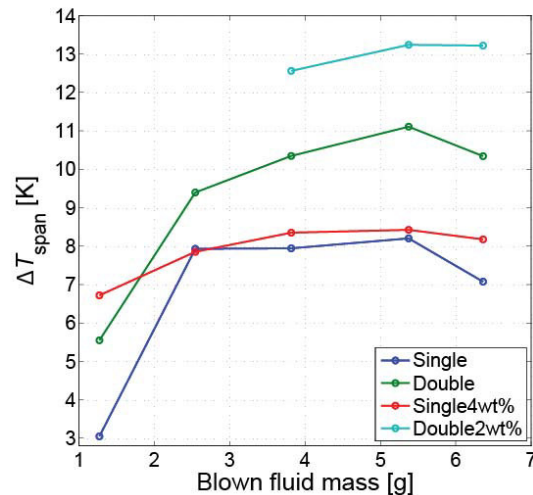
Fig. 3 : Temperature span as a function the blown fluid mass for three different regenerator at the region of maximum temperature span.

The temperature span as a function of the hot end temperature is shown in Fig. 4, where the left graph shows the results of the material without epoxy, while the right shows the results of the material with epoxy. It should be noted that the results of the regenerators without epoxy were done with water and 15 vol.% EG as the heat transfer fluid, while for the epoxy containing ones the fluid was changed to water with 2 vol.% NT. As discussed above these additives do change the viscosity, but only have a weak impact on the density. Due to the low frequency (0.13 Hz) the viscous dissipation is small when pushing the fluid through the regenerator, so even for the EG this will not have a large influence on the results. The regenerators were operated with the best resulting m_f, 5.4 g, which due to the difference of mass in the regenerators lead to different utilizations: 0.5 for the epoxy-bonded regenerators while those without epoxy were operated at a utilization of 0.9, in accordance with the results found in Fig. 3.

A feature common in all the results is a steady increase of temperature span with increasing T_{hot} up to a maximum at a temperature about 3-5 K above the highest T_C, then the span sharply decreases at higher hot end temperatures[7]. Additionally, it is observed that increasing the number of layers, from one to two, significantly increases the span, as expected. The measured temperature spans in the regenerators were not affected much by the epoxy-bonding. In fact they increased a little, as the dashed lines in Fig. 4 suggest. This, however, could be a combined effect of the different heat transfer fluids, differences in the mass of magnetocaloric materials and effects related to the epoxy itself. Additionally, the T_C spacing of the double layer regenerator without epoxy and the ones epoxy-bonded is slightly different. As it is shown in the literature[7], the temperature span can be heavily influenced by this spacing.

Although good performance was observed in the regenerators without epoxy, these regenerators were not mechanically stable. After three weeks of measurements, the regenerators started to release some very fine particles to the heat transfer fluid. These fine particles are believed to be the corners of the irregular particles, which are more susceptible to cracking. We believe that erosion during the fluid blow periods, coupled with the ~0.9% volume change that the material experiences at the transition [9, 11] result in breaking apart of the particles. Additionally, once this breaking apart starts, the packing of the regenerators is lost, and the particles are free to move inside the regenerator housing leading to further degradation of the regenerators. Indeed, this is what was observed. Shortly after the first fine particles were observed the number of particles in the fluid increased until the whole regenerators broke apart.

The reason for introducing the epoxy into the regenerator matrix was to enhance the mechanical stability and prevent breaking apart of the regenerators. As expected, the mechanical stability of the regenerators was increased significantly by epoxy bonding the particles. No degradation related to particles breaking was observed, even after 5 weeks of testing. By comparing the temperature span of regenerators *Double2wt%* and *Double4wt%* in Fig. 4 it is observed that increasing the amount of epoxy was detrimental to the span. So when epoxy bonding it is important to find the minimum amount of epoxy that can be used while still

maintaining the structural integrity of the regenerator. As discussed above the regenerator *Double1wt%* broke apart during initial testing, so the minimum amount of epoxy to avoid this seems to be 2 vol.%.
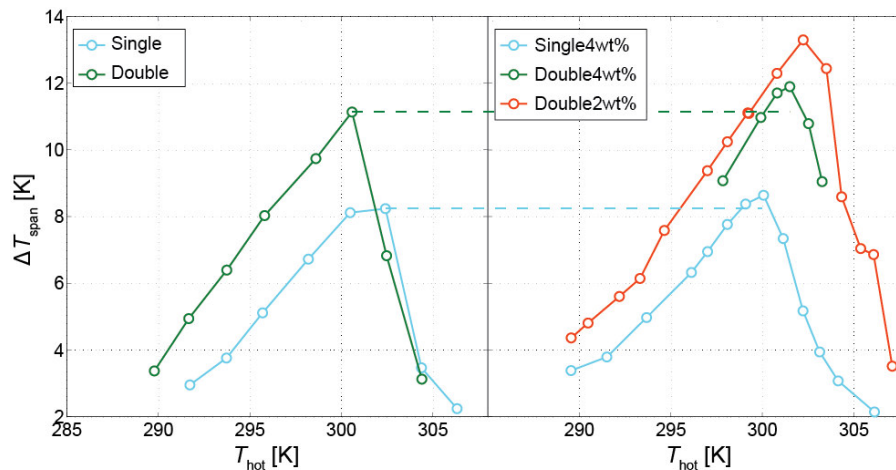

Fig. 4 : Temperature span as a function of the hot end temperature for different regenerators. The Dashed line is a guide to the eye.

4. CONCLUSIONS

The performance of La(Fe,Mn,Si)$_{13}$H$_z$ as an active magnetic regenerator is evaluated in a custom-built device. The results show that irregular particles of La(Fe,Mn,Si)$_{13}$H$_z$ deteriorate during application which would limit the use of this material as an AMR. By epoxy bonding the particles, the mechanical stability of the regenerators increased significantly and no deterioration due to particles breaking was observed. The temperature span reached by the epoxy-bonded regenerators suggest that 2 wt.% of epoxy maximizes the span, while still maintaining the mechanical integrity. The characterization of the transfer fluid showed that the Entek solutions have a lower viscosity and density then the ethylene glycol ones. Although the effect of a lower viscosity does not influence of the tests here done since the frequency is relatively low, this might play a very important role under high frequency operations.

ACKNOWLEDGMENTS

REFERENCES

[1]   V. K. Pecharsky and K. A. Gschneidner, Jr., "Giant Magnetocaloric Effect in Gd$_5$Si$_2$Ge$_2$," *Phys. Rev. Lett.*, vol. **78**, no. 23, pp. 4494–4497, 1997.

[2]   G. V. Brown, "Magnetic heat pumping near room temperature," *J. Appl. Phys.*, vol. **47**, no. 8, p. 3673, 1976.

[3]   A. Barcza, M. Katter, V. Zellmann, S. Russek, S. Jacobs, C. Zimm, "Stability and Magnetocaloric Properties of Sintered La(Fe, Mn, Si)$_{13}$H$_z$ Alloys," *IEEE Trans. Magn.*, vol. **47**, no. 10, pp. 3391–3394, 2011.

[4]   L. von Moos, C. R. H. Bahl, K. K. Nielsen, and K. Engelbrecht, "The influence of hysteresis on the determination of the magnetocaloric effect in Gd$_5$Si$_2$Ge$_2$," *J. Phys. D. Appl. Phys.*, vol. **48**, no. 2, p. 025005, 2015.

[5]   V. Basso, M. Küpferling, C. Curcio, C. Bennati, A. Barzca, M. Katter, M. Bratko, E. Lovell, J. Turcaud, and L. F. Cohen, "Specific heat and entropy change at the first order phase transition of La(Fe-Mn-Si)$_{13}$-H compounds," *J. Appl. Phys.*, vol. **118**, no. 5, p. 053907, 2015.

[6]   K. K. Nielsen, H. N. Bez, L. von Moos, R. Bjørk, D. Eriksen, and C. R. H. Bahl, "Direct measurements of the magnetic entropy change," *Rev. Sci. Instrum.*, vol. **86**, no. 10, p. 103903, 2015.

[7]   T. Lei, K. K. Nielsen, K. Engelbrecht, C. R. H. Bahl, H. Neves Bez, and C. T. Veje, "Sensitivity study of multi-layer active magnetic regenerators using first order magnetocaloric material

La(Fe,Mn,Si)$_{13}$H$_y$," *J. Appl. Phys.*, vol. **118**, no. 1, p. 014903, 2015.

[8]   S. Fujieda, a. Fujita, K. Fukamichi, Y. Yamazaki, and Y. Iijima, "Giant isotropic magnetostriction of itinerant-electron metamagnetic La(Fe$_{0.88}$Si$_{0.12}$)$_{13}$H$_y$ compounds," *Appl. Phys. Lett.*, vol. **79**, no. 5, p. 653, 2001.

[9]   H. N. Bez, K. K. Nielsen, P. Norby, A. Smith, and C. R. H. Bahl, "Magneto-elastic coupling in La(Fe, Mn, Si)$_{13}$H$_y$ within the Bean-Rodbell model," *AIP Adv.*, vol. **6**, no. 5, p. 056217, 2016.

[10]   J. Lyubina, R. Schäfer, N. Martin, L. Schultz, and O. Gutfleisch, "Novel design of La(Fe,Si)$_{13}$ alloys towards high magnetic refrigeration performance.," *Adv. Mater.*, vol. **22**, no. 33, pp. 3735–9, 2010.

[11]   A. Waske, L. Giebeler, B. Weise, A. Funk, M. Hinterstein, M. Herklotz, K. Skokov, S. Fähler, O. Gutfleisch, and J. Eckert, "Asymmetric first-order transition and interlocked particle state in magnetocaloric La(Fe,Si)$_{13}$," *Phys. status solidi - Rapid Res. Lett.*, vol. **9**, no. 2, pp. 136–140, 2015.

[12]   J. Lanzarini, T. Barriere, M. Sahli, J. C. Gelin, A. Dubrez, C. Mayer, M. Pierronnet, and P. Vikner, "Thermoplastic filled with magnetocaloric powder," *Mater. Des.*, vol. **87**, pp. 1022–1029, 2015.

[13]   K. Engelbrecht, K. K. Nielsen, and N. Pryds, "An experimental study of passive regenerator geometries," *Int. J. Refrig.*, vol. **34**, pp. 1817–1822, 2011.

[14]   C. R. H. Bahl, T. F. Petersen, N. Pryds, and a Smith, "A versatile magnetic refrigeration test device.," *Rev. Sci. Instrum.*, vol. **79**, no. 9, p. 093906, 2008.

[15]   D. Velázquez, M. Castro, E. Palacios, and R. Burriel, "Pratical Properties of LaFeCoSi Materials to Be Used in Magnetic Cooling Applications," in *Proceedings of Thermag VI*, 2014, pp. 133–134.